KU LEUVEN

ARENBERG DOCTORAL SCHOOL
Faculty of Engineering Science

# Multiscale modeling of cartilage mechanobiology: insights into degeneration and regeneration

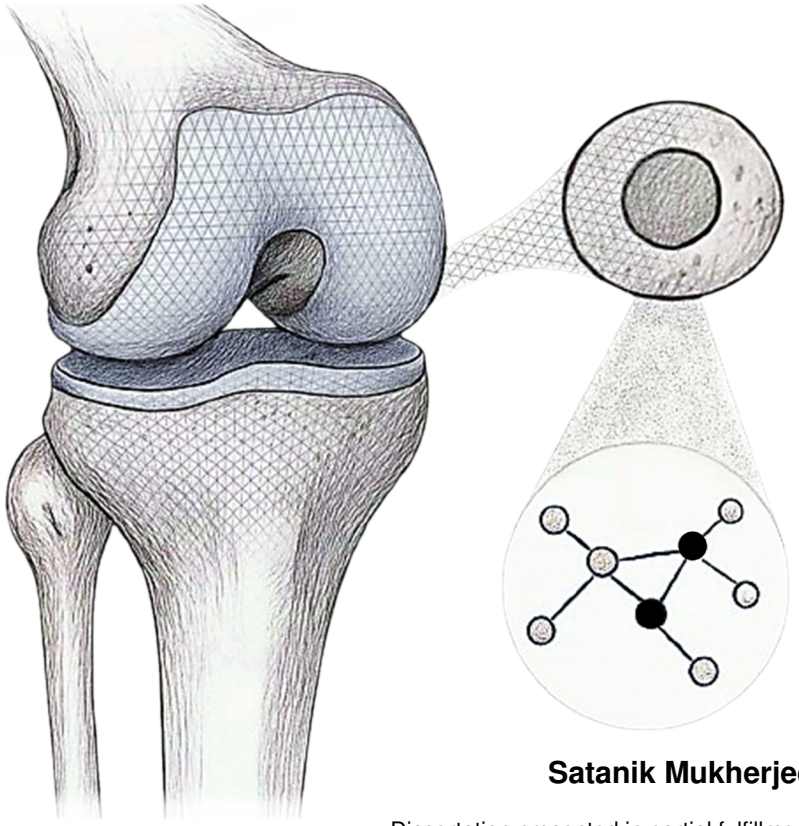

**Satanik Mukherjee**

Dissertation presented in partial fulfillment
of the requirements for the degree of
Doctor of Engineering Science (PhD):
Mechanical Engineering

Supervisor:
Prof. dr. ir. Liesbet Geris

April 2025

# MULTISCALE MODELING OF CARTILAGE MECHANOBIOLOGY: INSIGHTS INTO DEGENERATION AND REGENERATION

Satanik MUKHERJEE

Supervisor:
Prof. dr. ir. Liesbet Geris

Members of the
Examination Committee:
Prof. dr. ir.Jean Berlamont, chair
Prof. dr. Ilse Jonkers
Prof. dr. ir. Ioannis Papantoniou
Prof. dr. ir. Nele Famaey
Prof. dr. Gerjo Van Osch
(Erasmuc MC, Netherlands)
Prof. dr. Andrew Pitsillides
(Royal Veterinary College, UK)

Dissertation presented in partial fulfillment of the requirements for the degree of Doctor of Engineering Science (PhD): Mechanical Engineering

April 2025

© 2025 Satanik Mukherjee
Uitgegeven in eigen beheer, Satanik Mukherjee, Heverlee (Belgium)

Alle rechten voorbehouden. Niets uit deze uitgave mag worden vermenigvuldigd en/of openbaar gemaakt worden door middel van druk, fotokopie, microfilm, elektronisch of op welke andere wijze ook zonder voorafgaande schriftelijke toestemming van de uitgever.

All rights reserved. No part of the publication may be reproduced in any form by print, photoprint, microfilm, electronic or any other means without written permission from the publisher.

# Acknowledgements

As my PhD journey comes to a close, it feels like the right moment to pause and reflect on the experiences that have made this journey unforgettable. When I think back, the first thing that comes to mind is the incredible individuals I've had the privilege of crossing paths with during this time. Each of them has played a pivotal role, not only in the culmination of my research but also in shaping who I am today. This acknowledgment is my chance to express my heartfelt gratitude for their support, wisdom, and influence, which have been instrumental both in my academic journey and my personal growth.

First and foremost, my gratitude goes to Lies, my supervisor, without whom this thesis would not exist. Lies, you have inspired me more than you can imagine. Thank you for always believing in me, giving me the academic freedom to pursue my ideas, while at the same time ensuring that I kept the bigger picture in mind. Your passion for science and your strong resolve to make a difference in the *in silico* medicine community are exemplary. At the same time, your empathy and kindness have always stood out in the hyper-competitive world of academia. Lastly, one thing I can proudly say is that I am probably one of the few who have collaborated with you not only academically but also musically. I truly cherish the memories of our short concert performance at the CarBon consortium meeting in Genoa — you doing the vocals and me playing the violin. I hope we can share more moments like that in the future. Once again, thank you, Lies, for all your guidance. I look forward to continuing our collaboration for many years to come.

I was privileged to have some of my favorite professors in my examination committee, whose mentorship and guidance were immensely helpful throughout my PhD journey. Ilse, I am deeply grateful for your constant encouragement and support. Thank you for involving me in so many scientific discussions on cartilage research within your group — I learned a great deal from those exchanges. I also truly appreciated your warmth and guidance during the various conferences we attended together across the world. The research you're

leading in your group is incredibly exciting and inspiring, and I wish you all the very best in your future endeavors.

Ioannis, I would like to express my sincere thanks for your encouragement and the thoughtful questions you posed during many of my progress presentations. Your insights always gave me valuable food for thought and pushed me to view my research from new perspectives. Thank you for being such an important and engaged member of my supervisory committee.

Nele, thank you for your consistent and constructive feedback, particularly on the finite element (FE) aspects of my work. Your expertise and questions significantly enriched my understanding of this area. I also greatly appreciate the detailed feedback you provided on my thesis — it made a real difference.

Andy, where do I begin! You were first assigned as my academic mentor during the CarBon Consortium meeting in Dublin, and I'm privileged to say that you've now become my academic mentor for life (you have no choice!). Thanks to our countless discussions during the consortium meetings and beyond, I've gained so much clarity about my career path and research goals. Your insights and words of wisdom throughout my PhD have been instrumental in helping me discover myself as a researcher. I truly hope I'll continue to benefit from your mentorship and guidance in the years to come. Thank you for being such a valued contributor to my academic journey.

Gerjo, my first interaction with you was during the CarBon project, where you were the lead PI from the very beginning. I've always been inspired by your decisive yet empathetic leadership throughout the project. Over time, during CarBon meetings and beyond, I've consistently been enriched by your insightful comments on the biological aspects of my work. It was also a real pleasure to chair the Gordon Research Seminar on cartilage with you, while you served as chair of the corresponding GRC. I learned so much from those meetings and our discussions about organizing a scientific conference. Thank you once again for all your encouragement and support during my PhD.

I would also like to thank Prof. Jean Berlamont for chairing the examination committee of my thesis and for ensuring the smooth conduct of the private defense and all the related administrative procedures.

The research presented in this thesis would not have been possible without the generous support of several funding agencies. I am deeply grateful to the Marie Skłodowska-Curie Fellowship for supporting my doctoral research through the CarBon ITN project (grant agreement No. 721432). I also acknowledge funding from the European Research Council (ERC) under the European Union's Horizon 2020 research and innovation programme (ERC CoG grants No. 772418 and 101088919), the Research Foundation Flanders (FWO long stay travel grant

V441022N), and the European Society of Biomechanics through their Mobility Award.

Fernando, I consider myself incredibly lucky to have had you as a friend from the very first day I arrived in Leuven. It's quite uncanny that we not only share the same birthday, but also a lot in how we view the world and our likes and dislikes (astrologers, take note!). You are one of the very few people in the world with whom I could talk about anything and everything—from food to geopolitics to travel, and so much more. Thank you for being an excellent listener and for always offering advice and help throughout this PhD journey ("Mr. Dependable" really suits you!). I fondly cherish the memories of the many road trips we took together across different parts of the world (including being chased by the border police in Bosnia), and I look forward to more such adventures in the future. Thank you, Fernando, for being such a dependable friend and an elder brother.

Laura, you brought the Spanish sunshine into the lab the moment you arrived. I'm always moved by your warmth and your concern for the well-being of others. It's truly inspiring to see how beautifully you balance motherhood with Lucas and your professional life. I'm forever grateful for all the things you've done for me and for always being a pillar of support and encouragement. Special thanks for encouraging me to apply for the ESB Mobility Award—which I eventually won—and which made it possible for me to pursue a research stay in the University of Twente, Netherlands. I couldn't have asked for a more supportive lab mate and a dear friend. I wish you all the very best in your future endeavors.

Raphie, this PhD thesis would not have been possible without you. Coming from a mechanical engineering background, I had no prior knowledge of cartilage biology when I started my PhD. However, thanks to our many discussions and brainstorming sessions, I developed a real interest in the topic—something that's reflected in this thesis. Thank you for patiently explaining the nuances of systems biology to me, over and over again. And thank you also for all the great times outside of work—whether during the CarBon Consortium meetings or our many after-work dinners and drinks. I'm grateful to have you as both a friend and collaborator, and I wish you all the best for what's ahead.

Mojtaba (aka Moji), I have always been inspired by your passion for science and drinking. I'll never forget those lunch breaks at Alma where we'd talk about the cultural similarities between India and Iran, and our shared perspectives on the world. You've been a truly inspirational figure throughout my PhD, with your strong work ethic, deep insight, and collaborative spirit. Many thanks to you and Marz for being such welcoming hosts—I always enjoyed spending time at your place. I'm sure you're going to achieve great things in the field of

computational science, and my best wishes are always with you.

Ales, I vividly remember our first interaction, when you startled me by asking "Kemon acho?" (English: How are you?)—in perfect Bengali pronunciation! It was such a delightful surprise, and from that moment on, we quickly became close friends thanks to our shared interests in traveling, hiking, and photography. I truly cherish the memories we created while exploring and photographing the natural beauty of different parts of Europe. Thank you so much for hosting me in your hometown in the Czech Republic—an unforgettable trip that I will treasure for a lifetime. Though we've been in different countries these past couple of years, our friendship has remained strong despite the distance, and I'm confident it will continue in the future as well. Thank you, Ales, for being such a valuable friend in this journey.

Nicolas, you are an indispensable member of the Belgian trio of CarBon! I'm always amazed by your ability to bring humor and fun into any situation. It's always refreshing to talk to you—your warmth, humor, and positivity are truly infectious. I'm so happy to have you as a friend, and I wish you all the best in your exciting adventures with microscopy in the future.

Jurgen, thank you for being such a wonderful friend. You and Laura have always welcomed me warmly into your home and hosted me for many memorable gatherings. I fondly remember those evenings watching the Euro Cup matches at your place—it was such a great way to connect and have fun. I truly admire your calm demeanor and thoughtful insights, and I've learned a lot about Belgian culture and politics from you. My best wishes to you for all that lies ahead.

Ali, you were my 'cartilage buddy' throughout my PhD, and I truly couldn't have asked for a better collaborator and friend in this journey. I learned so much from the countless discussions we had—whether it was brainstorming about cartilage mechanobiology, exchanging ideas on simulations, or just sharing our thoughts on research challenges. Your curiosity, clarity of thought, and willingness to help always inspired me and made the process more enjoyable. I wish you the very best for all your future endeavors—both in science and beyond. I'm confident you'll continue to do amazing things!

To the members of the Biomechanics Research Unit in Liège, even though our meetings were limited, I truly enjoyed spending time with you during the team days. Many thanks to Marc, Sophie, Bingbing, Bernard, Margaryta, Loïc, Alessio, Luiz and others for the warm and friendly interactions.

Throughout my PhD, I was fortunate to work with amazing colleagues in the Biomechanics section at KU Leuven. I had the opportunity to interact with multiple generations of PhD students, and I truly enjoyed our lunchtime

conversations and the fun BME outings we shared. A big thank you to the former members—Tiago, Hannelore, Michel, Rebeca, Andrea, Klaas—and to the current members—Lauranne, Paulien, Jilmen, Pieter, Oriana, Sophie, Maikel, Kimberly and many others—for creating such a friendly and engaging atmosphere. Your camaraderie made my time in the lab both enjoyable and memorable. I'd also like to express my sincere gratitude to the BME secretaries—Rita, Jana and Kristel—for all your help with the administrative side of things, from booking flights to conference registrations. A special shoutout to the Matrix group—Hans, Jorge, Apeksha and Maxim—even though you were based in a different building, I always appreciated our interactions and collaborations, and the positive and welcoming vibe in your group. In the final phase of my PhD, the Indian community at BME grew from just me to four, with the addition of Anik, Vijay and Piyush. It was always refreshing to chat with you all and to have a slice of India at BME. I truly enjoyed our conversations during coffee breaks and wish you all the very best in your future endeavors.

I have been fortunate to also be part of the Tissue Engineering unit of SBE at the Gasthuisberg campus. The Prometheus data sessions there gave me valuable insights into the biology of skeletal tissues, which proved instrumental for my PhD research. At the same time, I truly enjoyed the company of some wonderful colleagues at SBE— Gabriella, Naomi, Marion, Hannah, Gabriele, Tim, Tom, Liesbeth, Kostas, Niki, Isaak, Przemko, Ruben, Eduardo, Ahmad, Ayse, Inge, Ehsan and many others. I have fond memories of the after-work drinks and the beach-volleyball sessions we shared during my time there. Thursdays quickly became one of my favorite days of the week—not just because I got to step away from my usual work in Biomechanics and gain a fresh perspective, but also because of the warm interactions with all of you. Our relaxed lunch breaks, and of course, the ritual of grabbing the very special 'Alma Burger', made those days especially memorable and enjoyable.

At this point, I must mention the dream CarBon team (a Marie Curie Consortium) that I was fortunate to be a part of during my PhD. I couldn't have asked for a more collaborative and collegial environment than what we had in CarBon. The experiences and memories from the CarBon consortium meetings will remain etched in my mind forever. The meetings struck an exceptional balance between science and fun. During the morning scientific sessions, I learned so much about cartilage biology through the presentations and the many in-depth discussions we had. And in the evenings, the friendships, laughter, and the joyful atmosphere we created together made those times truly special. That spirit was thanks to the amazing individuals who made up this consortium—both the fellow PhD students and the incredibly supportive PIs. Among the students, I was lucky to share this journey with Quique, Yannick, Mauricio, Cansu, Soraia, Kathy, Mengie, Claudio, Farhad, Raphie, Nicolas,

Martina and Dionysia. And I'm deeply grateful to the PIs—Frank, Bent, Linda, Danny, Roberta, Roberto, Gerjo, Erik, Andy, Lies and Christa—for their mentorship, warmth, and constant encouragement. I consider myself incredibly fortunate to have been part of this wonderful group, and I know that the bond we've built will last far beyond our time in the project. CarBon rocks!!

I am deeply grateful to Prof. Marcel Karperien for the opportunity to join his group for a research stay of three months in the University of Twente, and for his invaluable guidance. Many thanks to Jeroen, Laurens, Thanh, Carolina, Alexis, Janine, Castro, Niels and others for the friendly and collaborative atmosphere that you provided in the lab. During my time in Twente, I gained valuable hands-on experience with the experimental side research on the cartilage-on-chip setup. I will also fondly remember our fun badminton sessions, which made my time there even more enjoyable.

When living far away from home, it's easy to feel homesick—especially during the festive seasons. However, I was fortunate to find a slice of Bengal in Belgium through the Leuven Bong Club and Tero Parbon Belgium (the Bengali associations in Leuven and Brussels, respectively). Ashesh da, thank you so much for offering me a place to stay in this foreign land from the very first day I arrived in Leuven. Nachi da, Sayantan da, and Ipsita di—thank you for the memorable hikes and bike trips across Belgium. I'm also deeply grateful to Dwaipayan da, Gouri da, Arindam da, Sandip da, Papiya di, Mitali di, Monalisa di, Anamika di, Snigdha di, Sumedha di, Sabyasachi da, and many others who created a warm, welcoming space that truly made me feel at home away from home.

Doing research during a PhD can often be stressful and draining, but extracurricular activities offered a much-needed breath of fresh air and helped me recharge. In this regard, I am especially grateful to the photography club in Leuven—and in particular, to you, Ivan—for being my mentor in photography. Through our many discussions, I've not only learned a great deal about photography, but I've also been enriched by your broader insights about life and the world. Maverick is the word that comes to mind when I think of you. Thank you, Ivan, for being such a great friend and mentor.

Music has always been one of the most important forces that keeps me going in life. I'm deeply grateful to all the musicians I've had the pleasure of collaborating and performing with during my time in Leuven. These musical interactions enriched me immensely and gave me the strength to get through some of the more difficult moments of my PhD journey. I am especially indebted to my music mentors—Goswami Sir, Debasis Sir, Pankaj Kaku, and guruji, Arijit Mahalanabis. Despite being separated by continents, your consistent mentorship and guidance have shaped me not just into a better musician, but also a better

human being. I look forward to continuing this journey of learning with you in the years to come.

Devahita, words can hardly capture how much your love, patience, and strength have meant to me throughout this journey. Through every high and low, you stood by me with unwavering support, even when the path felt uncertain. Beyond the academic world, the music and dance we've shared have been our sanctuary—you, the dancer, and I, the musician—creating a space to breathe, express and connect. Our partnership, both on and off the stage, has brought rhythm and meaning to my life. This thesis carries echoes of your graceful movements, my melodies, and above all, your steady presence beside me. I couldn't have done this without you.

Lastly, and most importantly, to my parents and my sister, thank you for your endless love, support, and unwavering presence throughout this journey. Though we have often been separated by distance, your presence has never felt far. Your constant encouragement—through calls, messages, and the steadfast belief in my path—has been a source of strength in times of doubt and exhaustion. The values you've instilled in me, the warmth of our conversations, and the comfort of knowing you're always there have grounded me more than I can express. This milestone is not mine alone; it is deeply rooted in your sacrifices, your faith, and the foundation of love you have given me from the very beginning.

As I conclude this acknowledgment, I am reminded of the intricate, interconnected layers of friendship and support that have shaped my PhD journey—much like the multifactorial, multiscale model of cartilage that will follow in this thesis. Every facet, every layer, has played an essential role, and for that, I am deeply grateful.

Satanik
Leuven
April, 2025

# Abstract

Osteoarthritis (OA) is a common and painful degenerative joint disease that affects millions of people worldwide. It occurs when the cartilage—the smooth tissue that cushions the ends of bones—gradually breaks down, leading to joint stiffness, swelling, and reduced mobility. Despite its prevalence, understanding degradation of cartilage in OA and how to support its repair, remains a major challenge. This PhD thesis aimed to tackle this challenge by developing computational multiscale models integrating cartilage mechanics at different length scales with intracellular biochemical processes, to provide deeper insights into cartilage degeneration and regeneration. Firstly, a comparative study of bioreactor setups was conducted to evaluate their ability to replicate physiological joint mechanics. Subsequently, a multiscale modeling workflow for articular cartilage was developed spanning from the joint-tissue scale to the cell scale down to the intracellular scale. The cellular force from cell scale finite element model was coupled with intracellular regulatory networks using a Hill's function, bridging the gap between mechanical stimulation and biochemical response of the cell. The multiscale modeling workflow was calibrated and validated with respect to an *in vitro* study of dynamic compression of cartilage explants.

A multiscale model of the human knee joint model was then developed using the multiscale modeling workflow, to study the patho-physiology of knee cartilage following meniscectomy. The multiscale model successfully predicted catabolic responses in articular cartilage following meniscectomy. The catabolic processes followed a gradient which correlated with the gradient in mechanical loading across the thickness of cartilage. Furthermore, a novel *in silico-in vitro* framework was established in this thesis using a cartilage-on-chip device. Multiscale experiments were designed using the cartilage-on-chip device to study chondrocyte mechanobiology across multiple length scales, and the results were compared with predictions from the multiscale model. Finally, the multiscale workflow was implemented in a user-friendly model execution environment (MEE), providing an accessible tool for researchers to explore

cartilage mechanobiology and support future applications in *in silico* clinical trials and patient-specific studies.

This PhD thesis advances the field by integrating computational and experimental approaches, offering a comprehensive framework to study cartilage degeneration and regeneration at multiple length scales.

# Beknopte samenvatting

Artrose (OA) is een veelvoorkomende en pijnlijke degeneratieve gewrichtsaandoening die miljoenen mensen wereldwijd treft. Het ontstaat wanneer kraakbeen, het gladde weefsel dat de uiteinden van botten beschermt, geleidelijk afbreekt. Dit leidt tot gewrichtsstijfheid, zwelling en verminderde mobiliteit. Ondanks de hoge prevalentie hiervan, zijn het verschaffen van inzicht in de kraakbeendegeneratie bij OA en het ondersteunen van het regeneratieproces grote uitdagingen. Dit proefschrift gaat deze uitdaging aan door computationele multischaal modellen te ontwikkelen die de mechanica van kraakbeen op meerdere lengteschalen integreert met de intracellulaire biochemische processen. Het doel hiervan is beter inzicht krijgen in kraakbeendegeneratie en regeneratie. Hiervoor, is ten eerste een vergelijkende studie uitgevoerd naar de mate waarin bioreactor opstellingen in staat zijn fysiologische gewrichtsmechanica na te bootsen. Vervolgens werd een multischaal modellering werkstroom voor gewrichtskraakbeen ontwikkeld die van gewrichtsweefsel tot celniveau tot intracellulair niveau gaat. De cellulaire krachten afkomstig van het celniveau eindige-elementenmodel werden gekoppeld aan een intracellulaire regulatienetwerk met behulp van een Hill-functie. Hierdoor kon de kloof tussen de mechanische stimulatie en de biochemische respons van de cel worden overbrugd. De multischaal modellering werkstroom werd gekalibreerd en gevalideerd aan de hand van een *in vitro* studie die naar de dynamische compressie van kraakbeenexplanten keek.

Vervolgens werd een multischaal model van het menselijke kniegewricht ontwikkeld met behulp van de voorgenoemde multischaal modellering werkstroom. Dit is gedaan met het doel de pathofysiologie van kniekraakbeen na een meniscectomie te bestuderen. Het multischaal model voorspelde met succes katabole reacties in het gewrichtskraakbeen na een meniscectomie. De katabole processen volgden een gradiënt die correleerde met de gradiënt in mechanische belasting over de dikte van het kraakbeen. In dit proefschrift is ook een nieuw *in silico-in vitro* raamwerk ontwikkeld aan de hand van een kraakbeen-op-een-chip.

Multischaal experimenten zijn opgezet om de mechanobiologie van chondrocyten over meerdere lengteschalen met een kraakbeen-op-een-chip te bestuderen. De resultaten hiervan zijn vergeleken met de voorspellingen van het multischaal model. Tot slot werd de multischaal werkstroom geïmplementeerd in een zogeheten Model Execution Environment (MEE) om zo een gebruiksvriendelijk en toegankelijk hulpmiddel te creëren voor onderzoekers dat hen in staat stelt de mechanobiologie van kraakbeen te verkennen en hen ook kan ondersteunen in toekomstige *in silico* klinische onderzoeken en patiëntspecifieke studies.

Dit proefschrift bevordert het veld door computationele en experimentele benaderingen te integreren, en biedt een uitgebreid raamwerk voor het bestuderen van kraakbeen degeneratie en regeneratie op meerdere lengteschalen.

# List of abbreviations

| | |
|---|---|
| ACAN | Aggrecan |
| ACL | Anterior cruciate ligament |
| ADAMTS5 | A Disintegrin And Metalloproteinase with Thrombospondin motifs 5 |
| BCU | Bone cartilage unit |
| COLL | Collagen |
| DZ | Deep zone |
| FCD | Fixed charge density |
| GAG | Glycosaminoglycan |
| GRN | Gene regulatory network |
| HPC | High performance computing |
| IL | Interleukin |
| iNOS | Inducible nitric oxide synthase |
| LCL | Lateral collateral ligament |
| MCL | Medial collateral ligament |
| MEE | Model execution environment |
| MMP | Matrix metalloproteinases |
| MRI | Magnetic resonance imaging |
| MZ | Middle zone |
| NO | Nitric oxide |
| OA | Osteoarthritis |
| ODE | Ordinary differential equation |
| PCL | Posterior cruciate ligament |
| RVE | Representative volume element |
| RUNX2 | Runt-related transcription factor 2 |
| SOX9 | SRY-box transcription factor 9 |

| | |
|---|---|
| SZ | Superficial zone |
| TAK1 | Transforming growth factor $\beta$–activated kinase 1 |
| TAZ | Transcriptional coactivator with PDZ-binding motif |
| TE | Tissue engineering |
| TF | Transcription factor |
| TRPV4 | Transient receptor potential vanilloid-type 4 |
| YAP | Yes-associated protein |
| ZCC | Zone of calcified cartilage |

# Contents

**Abstract** ix

**Beknopte samenvatting** xi

**List of abbreviations** xiii

**Contents** xv

**List of Figures** xix

**List of Tables** xxiii

**1 General introduction** 1
- 1.1 Introduction . . . 2
- 1.2 Joint structure and its degenerative changes . . . 3
  - 1.2.1 Articular cartilage . . . 5
  - 1.2.2 Calcified cartilage . . . 7
  - 1.2.3 Subchondral bone . . . 8
  - 1.2.4 Ligaments . . . 9
  - 1.2.5 Meniscus . . . 10
- 1.3 Use of computational models to study joint degeneration . . . 10
  - 1.3.1 Musculoskeletal models . . . 11
  - 1.3.2 Finite element models . . . 12
  - 1.3.3 Gene regulatory network models . . . 20
  - 1.3.4 Multiscale models of joint degeneration . . . 22
  - 1.3.5 Data-driven approaches . . . 24
  - 1.3.6 Verification, validation and uncertainty quantification of computational models . . . 25
- 1.4 Discussion and Conclusion . . . 27

**2 Aims and Objectives** 29

2.1 General aims . . . 29
2.2 Specific objectives . . . 30
2.3 Outline of the thesis . . . 31

**3 From human joints to bioreactor setups: quantifying mechanical stimuli in cartilage physiology and regeneration 33**
3.1 Introduction . . . 34
3.2 Methods . . . 35
3.2.1 FE modeling of the human knee joint . . . 35
3.2.2 FE modeling of bioreactors for osteochondral plugs . . . 39
3.2.3 FE modeling of bioreactors for cartilage tissue engineered constructs . . . 43
3.2.4 Implementation . . . 44
3.3 Results . . . 45
3.3.1 FE analysis of the human knee joint . . . 45
3.3.2 Role of calcified cartilage and subchondral bone in unconfined compression of osteochondral grafts . . . 45
3.3.3 Differences in mechanics between osteochondral plugs and TE Constructs in unconfined compression . . . 48
3.3.4 Mechanical influence of combined dynamic compression and sliding rotation of ceramic ball . . . 49
3.3.5 Application of hydrostatic pressure elevates pore fluid pressurization . . . 50
3.3.6 Comparative analysis of the most-physiological cases from each bioreactor type . . . 52
3.4 Discussion . . . 56

**4 A multiscale modeling approach to study the role of mechanics and inflammation in pathophysiology of articular cartilage 61**
4.1 Introduction . . . 62
4.2 Materials and Methods . . . 64
4.2.1 General workflow of the multiscale modeling approach . 64
4.2.2 Calibration of the multiscale model with gene expression data from *in vitro* studies . . . 72
4.2.3 Application of the multiscale model to a patho-physiological scenario of meniscectomy in the human knee joint . . . 74
4.3 Results . . . 76
4.3.1 Results from the multiscale digital twin of the *in vitro* bioreactor setup . . . 76
4.3.2 Results from the multiscale digital twin of the human knee joint . . . 80
4.4 Discussion . . . 88

**5 A multiscale approach to study chondrocyte mechanobiology using a cartilage-on-chip setup 93**
5.1 Introduction . . . 94
5.2 Materials and Methods . . . 95
5.2.1 Description of the cartilage-on-chip setup . . . 95
5.2.2 Stress relaxation experiments on agarose hydrogel . . . 98
5.2.3 Inverse FE characterization of agarose hydrogel mechanical properties . . . 98
5.2.4 Multiscale experiments in cartilage-on-chip setup . . . 101
5.2.5 Post-processing of data from cartilage-on-chip experiments 103
5.2.6 Multiscale *in silico* model of the cartilage-on-chip device 106
5.2.7 Statistical analysis . . . 107
5.3 Results . . . 107
5.3.1 Inclusion of cells and beads reduce the stiffness of agarose hydrogel . . . 107
5.3.2 Inverse characterization of agarose hydrogel . . . 107
5.3.3 Membrane deformation in the cartilage-on-chip setup under pneumatic pressure . . . 108
5.3.4 Gradient deformation of the gel observed in both experiments and simulation . . . 108
5.3.5 Cell segmentation and projected area change under mechanical loading . . . 110
5.3.6 Influence of mechanical loading on chondrocyte behavior 110
5.4 Discussion . . . 112

**6 Implementation of the multiscale model in a model execution environment 115**
6.1 Introduction . . . 116
6.2 Overview of the model execution environment . . . 116
6.3 Implementation of the multiscale modeling workflow in the MEE 117
6.4 Proof-of-concept analysis of compression of cartilage explants in the model execution environment . . . 121
6.5 Discussion . . . 122

**7 General conclusions and future perspectives 125**
7.1 Thesis summary . . . 125
7.2 Main contributions of the thesis . . . 127
7.3 Limitations and perspectives for future research . . . 129
7.3.1 Computational aspects . . . 129
7.3.2 Experimental aspects . . . 131

**A Supplementary results from Chapter 3 133**

**B Detailed explanation of the pathways involved in the regulatory network** **141**
B.1 Mechanotransduction pathways . . . . . 141
B.1.1 Integrin mechanoreceptor and downstream pathways . . 141
B.1.2 Ion channel and calcium signaling . . . . . 144
B.2 Inflammatory pathways . . . . . 145
B.3 Interplay between pathways . . . . . 147

**C Mesh convergence studies** **159**

**Bibliography** **161**

**Curriculum Vitae** **193**

# List of Figures


1.1 Description of constitutive tissues in human knee joint . . . . . 4
1.2 Overview of different modeling approaches of joint degeneration 11
1.3 Fibril degeneration algorithm for cartilage . . . . . 16
1.4 Iterative fibril and proteoglycan degeneration algorithm for cartilage 18
1.5 Description of modeling framework for regulatory networks . . 21
1.6 Description of multiscale modeling framework for knee joint . . 23

2.1 Overview of thesis objectives . . . . . 31

3.1 FE model development of the human knee joint . . . . . 40
3.2 FE models of different bioreactor setups . . . . . 41
3.3 Results of FE analysis of stance phase of gait-part 1 . . . . . 46
3.4 Results of FE analysis of stance phase of gait-part 1 . . . . . 47
3.5 Distribution of maximum principal stress (in MPa) in different tissues of the OC plug and the TE construct for 10%, 20% and 30% strain applied in dynamic unconfined compression with 1Hz frequency. NoCC - No Calcified Cartilage. Scale bar = 5 mm. . 48
3.6 Results of dynamic unconfined compression in osteochondral plugs and TE constructs. . . . . 49
3.7 Distribution of fluid velocity in dynamic compression and ball rotation bioreactor . . . . . 51
3.8 Comparison of best case loading conditions in bioreactors with physiological condition . . . . . 55

4.1 Overview of the multiscale model workflow showing the different length scales involved for a human knee joint . . . . . 66
4.2 Results of the two-way sensitivity analysis of the regulatory network 77
4.3 Results of the calibration and validation process of the multiscale model. . . . . 79
4.4 Monte Carlo analysis to determine the stable states. . . . . 81

4.5 FE Analysis of the (mechanical) effect of meniscectomy in the human knee joint. . . . . 82
4.6 Results of meniscectomy on cell biomarkers: superficial zone . . 84
4.7 Results of meniscectomy on cell biomarkers: middle zone and deep zone . . . . . 85

5.1 Overview of the multiscale workflow for the cartilage-on-chip setup 97
5.2 Inverse characterization of agarose (a) Experimental setup; (b) FE model of the setup; (c) Comparison of reaction forces between experiments and the optimized FE model. . . . . 99
5.3 Overview of the control system used to actuate the cartilage-on-chip devices . . . . . 102
5.4 Schematic representation of the settings used for confocal microscopy of immunofluorescent stained samples . . . . . 104
5.5 Stress relaxation graphs showing reaction forces over time for agarose hydrogel. . . . . 108
5.6 Estimation of deformation of the hydrogel in cartilage-on-chip setup. . . . . 109
5.7 Image processing to perform cell segmentation. . . . . 111
5.8 Variation of *in silico* activity of biomarkers for three cells located in the cartilage-on-chip setup, and immunofluorescence staining from experiments . . . . . 112

6.1 MEE implementation overview . . . . . 118
6.2 Global model step in the MEE interface . . . . . 120
6.3 Cell model step in MEE interface . . . . . 120
6.4 Post-processing step in the MEE interface . . . . . 120
6.5 Visualization of results in the MEE . . . . . 122

A.1 Distribution of maximum shear strain in different tissues of the OC plug and the TE construct . . . . . 133
A.2 Distribution of pore fluid velocity (in mm/sec) in different tissues of the OC plug and the TE construct . . . . . 134
A.3 Distribution of maximum principal stress (in MPa) in OC plug and the TE construct for 4 different conditions of applied compression with ball rotation . . . . . 135
A.4 Distribution of maximum shear strain in OC plug and the TE construct for 4 different conditions of applied compression with ball rotation . . . . . 136
A.5 Distribution of pore fluid pressure (in MPa) in OC plug and the TE construct for 4 different conditions of applied compression with ball rotation . . . . . 137

A.6 Distribution of pore fluid velocity (in mm/sec) and pore pressure (MPa) in TE construct for applied dynamic hydrostatic pressure 138
A.7 Comparison of varus-valgus rotation between the FE model and the experimental measurements . . . . . 139

B.1 Snapshot of the mechanotransduction and pro-inflammatory signaling and their crosstalk in the in silico chondrocyte. . . . . 149

C.1 Mesh convergence study of knee joint . . . . . 159
C.2 Mesh convergence study for osteochondral plugs . . . . . 160
C.3 Mesh convergence study for agarose constructs . . . . . 160
C.4 Mesh convergence study for cell-level model . . . . . 160

# List of Tables

3.1 Table to describe the material parameters of the tissues and hydrogel used in the study . . . . . 38

4.1 Material parameters of the cartilage, extracellular matrix (ECM), pericellular matrix (PCM) and the chondrocyte used in this study(obtained from [220]) . . . . . 65
4.2 Cellular forces (in milli newton (mN)) as calculated from the cellular scale FE models in different zones, for both healthy (left) and meniscectomy (right) conditions . . . . . 83

# Chapter 1

# General introduction

Satanik Mukherjee[1], Majid Nazemi[2], Ilse Jonkers[3], Liesbet Geris[1,2,4]

[1]Biomechanics Section, KU Leuven, Leuven, Belgium
[2]GIGA Institute, University of Liege, Liege, Belgium
[3]Human Movement Biomechanics Research Group, Department of Movement Science, KU Leuven, Belgium
[3]Skeletal Biology and Engineering Research Center, KU Leuven, Leuven, Belgium

This chapter is adapted from previously published article: S. Mukherjee, M. Nazemi, I. Jonkers, and L. Geris. "Use of Computational Modeling to Study Joint Degeneration: A Review". English. *Front. Bioeng. Biotechnol.* 8 (2020). Publisher: Frontiers. DOI: 10.3389/fbioe.2020.00093

## 1.1 Introduction

Osteoarthritis (OA), a degenerative joint disease, is the most common chronic condition of the joints, which cannot be prevented effectively. In Europe, over 100 million people suffer from arthritis. In the United States, nearly 2 million people under the age of 45 have symptomatic knee OA [2]. In 2013, total medical costs and earnings losses due to arthritis were $304 billion in the U.S. (about 1 percent of the U.S. gross domestic product for 2013)[3]. OA is a disease prevalent predominantly in the elderly, but it can also affect younger patients following injury, overuse (due to sports activities) and overweight. With an aging population coupled with other risk factors like obesity, the impact of OA on the society is suggested to only increase in the near future.

Contrary to earlier belief that OA is a cartilage disease, modern studies [4–6] suggest that it is a disease of the whole joint involving not only cartilage but also other joint constituents like the subchondral bone and bone marrow, menisci, ligaments and synovium. Indeed, initiation and progression of OA is characterized by changes in both the cartilage and the subchondral bone. In addition to the fact that the cartilage and subchondral bone are mechanically connected [7], there are evidences in literature that suggest the possibility of a biological crosstalk between the cartilage and bone, that is further increased as OA progresses [8–10]. Thus, in order to study the initiation and progression of OA, the biomechanics of bone-cartilage unit need to be accounted for in the computational models.

It is also known that not all joints are equally prone to OA development. The joints that are most frequently affected by OA include the knee, hip, spine and the distal and proximal interphalangeal joints of the hand. Symptomatic OA does less frequently occur in the ankle, wrist, elbow and shoulder joints [5]. In these non-symptomatic joints, if degeneration of the articular cartilage occurs, it may be non-progressive, while in susceptible joints such a degeneration progresses to the OA state. For different joints, the kinematics and composition of the joint constituents are different, thereby resulting in different biomechanical joint environments. Also, the response of the chondrocytes in the cartilage and the underlying bone is different for different joints [5], which can also explain the susceptibility of certain joints to OA as compared to others.

It is already evident from the discussion above that in order to fully understand the onset and progression of OA, it is important to understand the biomechanical environment of anatomically complex joint structures like the knee joint. Since doing that experimentally is a challenging task, computational models can provide unique insights. Computational modeling of joint degradation can help to estimate the patient-specific progression of OA, which can aid clinicians

to estimate a suitable time for surgical intervention in osteoarthritic patients. Likewise, they might also help to estimate whether certain physiotherapeutic strategies could be effective for arresting joint degradation. Furthermore, modeling approaches can also be used to test different hypotheses related to the underlying mechanisms of joint degeneration. However, the robustness of computational models in predicting joint degeneration depends on their ability to incorporate all the relevant degeneration mechanisms across different length scales and their interplay. Hence, verification and validation of the models with relevant experimental and clinical data are crucial and important steps within the computational modeling workflow. The variability in *in vivo* and *in vitro* experimental data inherent to biological specimens further emphasizes the need of population-wide model validation.

The objective of this introduction chapter is to present an overview of different computational model formulations that have previously been used to study joint degradation. The advantages and shortcomings of each of these models, along with a comprehensive (yet non-exhaustive) set of examples of their use to study joint degeneration are discussed. The examples are focused on the knee joint since it is most prone to OA [11] and the bulk of literature in computational modeling of joint degeneration is focused on the knee joint. Nevertheless, the concepts used for modeling the knee joint (including the damage mechanisms) can be easily extended to other joints and therefore more generalized conclusions can be drawn from these examples.

The chapter is structured as follows: first, the different constituents of a joint are described as well as their changes with initiation and progression of OA. The following section describes the different computational model formulations that can be used to model joint degradation, including their advantages and disadvantages. The different computational models discussed include musculoskeletal models, finite element(FE) models (with different mechanisms of joint degeneration in the sub-sections), gene regulatory networks, multiscale models and data-driven approaches. Thereafter, the verification and validation aspects of these different computational models are discussed. Finally, some generalizable conclusions are drawn and suggestions for future work on further exploitation and integration of the different models are made.

## 1.2 Joint structure and its degenerative changes

To develop a computational model of a human joint, three main inputs are required: 1) the anatomical properties of the joint (Figure 1.1), 2) the mechanical properties of the involved tissues, and 3) loading parameters [12]. Obtaining

the anatomical properties of the joint is the first step in the modeling pipeline, in order to represent the geometry and arrangement of different tissues involved. The anatomical features are virtually reconstructed from CT images or MRI scans by manual or (semi-)automated segmentation and consist of the bones (tibia, femur with or without patella), articular cartilage lining at the contact interfaces of the bones, ligaments holding the bones together and other contact structures; like the meniscus. Depending on the research question, the modeler has to make a choice on the fidelity and level of detail of the anatomy to be included in the model. The purpose of the following section is to briefly introduce the different components of the tibio-femoral joint; their specific constituents and their degenerative changes as well as their functional role.

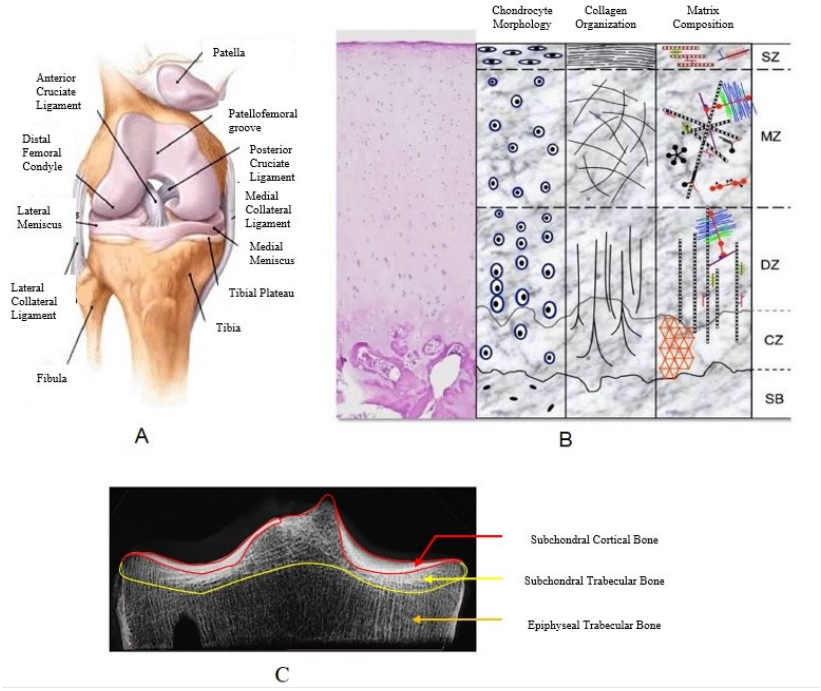


Figure 1.1: A detailed description of the human knee joint with the different constituents of the knee joint (A) (Islam), the different layers of articular cartilage showing variation in chondrocyte shape, collagen orientation and matrix distribution (B) (Di Bella et al., 2015) and the different regions of the subchondral bone (C) (modified from [13]). SZ,MZ,DZ-Superficial, middle and deep zone respectively. CZ-Calcified cartilage zone. SB-Subchondral bone.

### 1.2.1 Articular cartilage

Articular cartilage is the highly specialized connective tissue that covers the articulating ends of diarthrodial joints. Its primary function is to provide a lubricated, frictionless surface for smooth articulation and to act as a cushion to distribute mechanical loads during contact between two joint surfaces. The articular joint surface consists of hyaline cartilage and is 2 to 4 mm thick in humans [14]. Blood vessels, lymphatics and nerves are absent in the articular cartilage, and it is subject to high biomechanical loads. It is composed of a dense extracellular matrix (ECM) which is considered a biphasic material with a sparse distribution of cells called chondrocytes. Absence of vasculature limits its capacity for intrinsic healing and repair, therefore maintenance of its health is essential for joint health. The different constituents of articular cartilage are as shown in Figure 1.1B.

#### Water

Water is the primary constituent of articular cartilage, contributing up to 80% of its wet weight. A fraction of this water (approximately 30%) is contained in the intra-fibrillar space within the collagen, and a small fraction is contained in the intracellular spaces. The remainder water is contained in the voids of the porous ECM. The relative concentration of water increases from about 65% in the deep zone of cartilage to about 80% in the superficial zone [14]. The transport and distribution of nutrients to chondrocytes in the cartilage, and lubrication at the cartilage surface is aided by the flow of water through the cartilage and across the articular surface respectively. Applying a pressure gradient across the tissue or compressing the solid matrix causes flow of the inter-fibrillar water through the ECM. Due to low permeability of articular cartilage, the ECM offers high frictional resistance against its flow. This frictional resistance to water flow through the matrix results in flow-dependent viscoelastic behavior of cartilage. The flow-dependent viscoelasticity and pore fluid (water) pressurization within the matrix are the two basic mechanisms by which articular cartilage can withstand very high physiological compressive loads (up to several times body weight).

**Degenerative changes:** With progression of OA and subsequent loss of proteoglycans and collagen fibrillation, several studies have reported an increase in the water content and hydraulic permeability of the articular cartilage [15–18]. Mechanically, this increased permeability reduces the dynamic stiffness of the cartilage due to a reduction in interstitial fluid pressurization and consequent deficiency of the load support mechanism in the degenerated cartilage.

## Proteoglycans

Proteoglycans (PG) are an important constituent of the cartilage ECM which constitute approximately 30–35% of the dry weight of articular cartilage. They are large, complex biomolecules composed of a central protein core with negatively charged glycosaminoglycans (GAG) side chains [18]. These negatively charged groups produce a high negative charge density which is quantified as the fixed charged density (FCD). Due to the FCD, the concentration of ions inside the cartilage is higher than that in the surrounding synovial fluid. This excess of ion particles in the tissue leads to a higher osmotic pressure in the tissue as compared to the surroundings. As a result of this osmotic pressure difference, swelling of the tissue occurs. This osmotic swelling is critical as it enhances the ability of cartilage to resist compressive loads.

**Degenerative changes:** Depletion of PGs are observed during the progression of OA [18–20], especially in the superficial zone of articular cartilage. In the literature, two mechanisms underlying PG depletion are proposed: i) overloading of the cartilage, especially for post traumatic OA, resulting in death of chondrocytes and release of inflammatory cytokines, thereby inhibiting production of PG and leading to PG depletion [16, 21]; ii) damage to the collagen fibrils during early stages of OA leading to increased fluid flow velocity across the surface, thereby promoting loss of matrix fragments and loss of superficial PG [22, 23]. Mechanically, PG damage not only reduces the matrix stiffness but also increases the tissue permeability thereby reducing its dynamic stiffness. In addition, PG loss reduces the cartilage FCD and reduces the consequent osmotic swelling pressure.

## Collagen

Collagen is the most predominant structural macromolecule in ECM, constituting about 60% of the cartilage's dry weight. Type II collagen constitutes 90% to 95% of the collagen in ECM and forms fibrils and fibers intertwined with proteoglycan aggregates [14]. Collagen fibers offer resistance to tension. Hence, they provide resistance against swelling and tensile strains, but they do not offer significant resistance to compression. In the deep zone of cartilage, the collagen fibrils are perpendicular to the cartilage surface whereas in the superficial zone, they are parallel to the surface, thereby resisting shear deformation close to the surface.

**Degenerative changes:** Damage to the collagen network is one of the early signs of OA and has been recorded in many studies [24–26]. This has also been associated to the initial cartilage swelling observed in early OA [27]. Collagen

damage furthermore triggers loss of PGs and loss of tissue hydration as described in the previous section. Mechanically, damage to the collagen network causes a significant reduction in the tensile stiffness of the cartilage and enhanced swelling, since the collagen network helps constraining the swelling of the tissue.

#### Chondrocytes

Chondrocytes are the cells that reside in the articular cartilage. They are highly specialized cells which are metabolically active. They play a pivotal role in the development, maintenance, and repair of the ECM as well as its degeneration (in case of OA). Chondrocytes constitute only about 2% of the total volume of articular cartilage. The shape, number, and size of chondrocytes vary considerably across the thickness of the articular cartilage. The chondrocytes in the superficial zone of cartilage are flatter in shape and smaller in size and generally have a greater density than those present in the deeper zones in the matrix. They can sense and respond to a variety of stimuli, such as growth factors, mechanical loads and hydrostatic pressures. They do not easily proliferate in cartilage, which limits the healing capacity of the cartilage post injury or damage. An optimal chemical and mechanical environment is therefore critical to the survival of chondrocytes.

**Degenerative changes:** In OA, the balance between the anabolic and catabolic factors is disturbed, with an increase in the latter. During the early stages of OA, the levels of PG and collagen synthesis are largely increased [28, 29] to counterbalance the upregulated catabolic processes such as the increased production of matrix degrading metalloproteinases [30, 31]. In further stages of OA, chondrocyte apoptosis leads to the degradation of cartilage [32, 33]. Chondrocytes in OA have been shown to express hypertrophy markers such as type X collagen and MMP13 [34–36]. It is therefore hypothesized in some studies that during OA, articular chondrocytes lose their stable differentiated phenotype and behave like terminal differentiating chondrocytes as found in the growth plate of long bones, expressing hypertrophy-like changes [37–39].

### 1.2.2 Calcified cartilage

The zone of calcified cartilage (ZCC) acts as a transition zone from the softer cartilage to the stiffer subchondral bone region. The ZCC serves the important task of transmitting forces between the softer cartilage and the stiffer bone, thereby distributing the stresses across the bone-cartilage interface. The ZCC has intermediate stiffness with previous studies showing that the stiffness of the ZCC is about 100 times the overlying hyaline cartilage and 1/10 times

the underlying subchondral bone [40]. Apart from providing an intermediate stiffness, the ZCC is believed to act as a biochemical barrier preventing molecular exchange between the articular cartilage and the underlying bone marrow.

**Degenerative changes:** In OA, the ZCC is thought to cause thinning of the overlying articular cartilage by mineralization and advancement of the tidemark towards the articular cartilage layer [41, 42]. Thinning of articular cartilage further increases forces on the bone and thereby promote further degeneration. Some studies also suggests that vessels and channels that connect the subchondral bone with the calcified and the uncalcified cartilage become more abundant in the cartilage of patients with OA as compared to that of healthy individuals, thereby increasing the molecular cross-talk between the bone and cartilage cells [6, 43, 44].

### 1.2.3 Subchondral bone

There are different layers of bone beneath cartilage, the subchondral cortical bone, the subchondral trabecular bone, and the epiphyseal trabecular bone which are collectively regarded as the subchondral bone (Figure 1.1C). The subchondral cortical bone or subchondral cortical plate is a thin layer of compact bone beneath the calcified cartilage, separated from it by a thin layer of ductile material called the cement line, and is composed of about around 48% mineral, 31% organic matter, and 21% water in a healthy samples [45]. The thickness of subchondral cortical end-plate varies both within a sample and between different samples and could additionally be affected by OA. A range between 0.1 mm to 4.8 mm has been reported in the literature [13, 46–49], with increased thickness at the late stages of OA (subchondral sclerosis) [46, 50–52]. Likewise, a range of elastic moduli from 0.6 GPa to 20.0 GPa has been reported for the subchondral cortical bone [53, 54].

The subchondral trabecular bone is a layer of cancellous bone beneath the subchondral cortical bone. Subchondral trabecular bone layer thickness varies within and between samples with reported values ranging from 1 mm to 4 mm [55]. The apparent elastic modulus has been reported to vary between 6 MPa to 1670 MPa [56–60]. Under normal circumstances at the proximal tibia, mean bone volume fraction, trabecular thickness, trabecular spacing, and trabecular number are 0.296, 146 µm, 392 µm, and 2.07/mm, respectively [61]. The epiphyseal trabecular bone is a layer of cancellous bone which extends from the subchondral trabecular bone to the growth plate (Figure 1.1C). Compared to subchondral trabecular bone, epiphyseal trabecular bone has lower mean bone volume fraction and thinner trabeculae [61]. A range of elastic moduli

from 10 MPa to 2770 MPa has been reported for the epiphyseal trabecular bone [56, 60, 62, 63].

**Degenerative changes:** The subchondral cortical bone's composition is influenced by OA, leading to reduced mineral content and increased water content [45]. Subchondral bone tissue stiffness generally decreases with OA [58, 64, 65] which might be attributed to the lower mineral content (hypomineralization) [45, 54, 66, 67]. Increased subchondral trabecular bone volume fraction and thickness, and decreased trabecular spacing and degree of anisotropy have, however, been observed in the later stages of OA [66–69]. Animal studies have revealed decreased epiphyseal trabecular bone volume fraction with OA progression [70]. It is known that the microstructure and tissue density affects the apparent density and tissue modulus and microstructure affects the apparent modulus. Therefore, alterations of subchondral bone apparent density and modulus have been observed with OA progression. Various cadaveric and animal studies have shown decreased apparent density and modulus at early stages of OA [68, 71–73] which is thought to be due to elevated bone remodeling evidenced by vascular invasion at the cartilage-subchondral bone junction, and subchondral plate thinning and increased porosity [73, 74]. At the late stages of OA, however, apparent density and modulus have been reported to be significantly higher compared to normal subchondral bone [45, 54, 75]. The structural stiffness at the subchondral surface is a result of the specific spatial distribution of the apparent modulus and is thus expected to alter as OA progresses. Altered structural stiffness at the subchondral surface as the elastic foundation supporting the overlaying cartilage may influence the distribution of stress and strain in the cartilage leading to accelerated degeneration [76–78].

### 1.2.4 Ligaments

The primary function of the ligaments is to tie the bones of the joint together, thereby stabilizing its motions. Any injury or damage to the ligaments are known to trigger abnormal joint kinetics and kinematics, which may contribute to joint degeneration due to excessive shear forces [79, 80].

**Degenerative changes:** Injury to the anterior cruciate ligament (ACL) of the knee is known to increase the risk of OA. ACL deficiency results in disruption of the normal physiologic knee kinematics especially inducing increased internal tibial rotation and increased anterior tibial translation upon flexion. This has been associated with increased mean contact stresses in the posterior medial and lateral compartments of the knee joint under anterior and rotational loading which may trigger OA [80].

### 1.2.5 Meniscus

Menisci are located between the tibia and femur bone. They are two crescent-shaped pads of cartilage that evenly transfer load across the joint, absorb shocks during dynamic movement, and lubricate and help to stabilize the joint.

**Degenerative changes:** Injury, degeneration, or surgical removal (meniscectomy) of the entire or part of the meniscus is known to increase the risk of developing knee OA [81].

## 1.3 Use of computational models to study joint degeneration

Computational modeling of joint degeneration can be useful to predict the initiation and progression of degradation in the different components of the joint, thereby aiding clinicians in timely intervention (e.g. weight loss, surgery, rehabilitation). Computational models can range from joint level musculoskeletal models that evaluate abnormal whole joint loading conditions which may lead to joint degradation; FE models, which can evaluate tissue loading and predict their degeneration in response to mechanical loading; and gene regulatory network models, which can predict the fate of chondrocytes when subjected to abnormal mechanical or biochemical stimuli, thereby predicting the cellular processes underlying joint degradation. The choice of the specific modeling strategy depends on the specific research question that is to be answered. It is also evident from the discussion above that degradation happens due to interplay of factors which are active at different length scales. Therefore, multiscale modeling can be useful to combine the different length scales and to develop a more robust (computational) model of joint degeneration.

In this section, we will discuss the different computational modeling strategies used to date to study joint degeneration, a flowchart of which is shown in Figure 1.2. This section is structured as follows: firstly, musculoskeletal models are discussed with their advantages and disadvantages, followed by some examples from literature which involves the use of musculoskeletal models to study joint degeneration. Secondly, FE models are discussed with their advantages and disadvantages. The examples of FE models have been grouped based on the component of the joint that is being modeled for degeneration. Thirdly, gene regulatory network based models are discussed with their advantages and disadvantages, followed by some examples from literature which involves its use to study joint degeneration. Fourthly, multiscale models are discussed with their advantages and disadvantages, followed by some examples from literature which

involves the use of multiscale models in the perspective of joint degeneration. Finally, the use of data-driven approaches to study joint degeneration are discussed with their advantages and disadvantages and some examples.

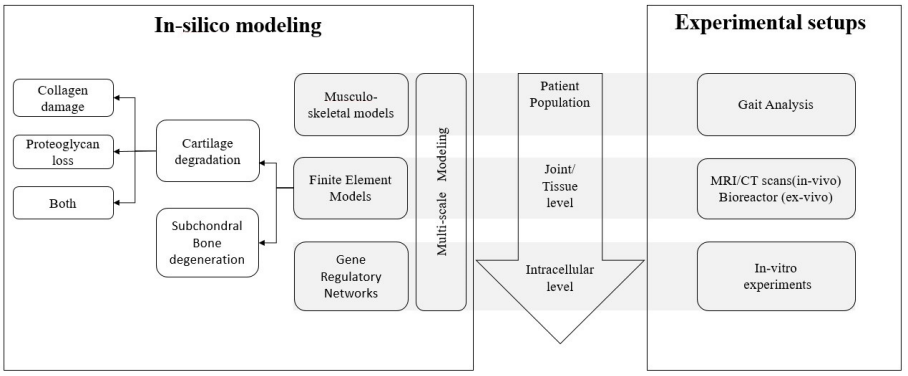


Figure 1.2: Overview of joint degeneration modeling approaches, length scales, and the link between *in silico* models and experimental setups.

### 1.3.1 Musculoskeletal models

Joint degradation is generally associated with altered gait patterns of the patient [52, 82, 83]. This altered gait kinematics and kinetics then increase the joint contact forces which will further promote the degeneration [84–86]. In this context, musculoskeletal computational models, with inputs from experimental motion and ground reaction force capture, can be used to quantify the joint contact forces and consequent pressures, which identify the presence of excessive loading at joint level and therefore predict the risk of damage initiation or progression.

**Advantages and limitations**

Musculoskeletal modeling provides a non-invasive way to calculate internal biomechanical loads from experimentally measured 3D body motions and contact forces in a wide range of conditions. These joint contact forces give an estimate on the presence of excessive loading and therefore the risk of damage initiation or progression. However, as these models only provide an overall estimate of joint loading, they cannot identify areas of damage initiation, nor progression as they do not quantify tissue-specific stresses and strains. The determination of the properties of a musculoskeletal model (such as bone lengths, muscle attachment

sites, joint centers etc.) is typically based on reference values from anatomic and cadaveric studies. This results in a generic musculoskeletal model which needs to be adapted and scaled to make it patient-specific. This is typically done using the information of 3D motion capture data. However, these linear scaling approaches can never mimic subject-specific geometries and therefore do not allow subject-specific predictions, thereby inherently limiting the use of this approach. On the other hand, medical imaging-based workflows using CT- or MR images have been developed allowing the introduction of patient-specific geometries in the musculoskeletal model [87]. Although the geometrical precision of these models clearly outperforms scaled generic musculoskeletal models, their application is usually cumbersome, expensive, time-consuming, dependent on a skilled operator and is therefore less feasible for large-scale studies. More recently, the use of population-based approaches (such as the MAP client) have been used to personalize generic musculoskeletal muscles, using a sparse data set of personalized geometrical features (e.g. from [88]).

**Examples**

It has been shown by Richards et al., [85] that for patients with medial knee OA, the knee adduction moment (KAM) is a strong predictor of the medial knee contact force (mKCF) at the first peak during normal walking. It was also reported in this study that walking with toe-in or wide-steps gait, modified the first peak KAM, but no reduction in mKCF was observed. However, the ratio of mKCF to total KCF, which represents the distribution of the loading, was reduced. This study demonstrated the potential of musculoskeletal models to not only identify markers that increase joint loading, thereby triggering more degeneration, but also to define modified gait strategies to reduce the joint loading in an already degenerated joint. In Meireles et al., [86] it was shown that the medial-lateral force and contact pressure distributions were already altered in early stages of medial knee OA during normal gait. No such trend was observed for a step-up-and-over motion.

### 1.3.2 Finite element models

The FE method has been used widely to calculate stresses and strains in the different joint tissues [12, 25, 89–91] . Since onset and progression of joint degradation are hypothesized to be a function of excessive tissue stresses and strains, FE models can be particularly effective in calculating the mechanical environment in the tissues that is expected to trigger degeneration. The steps that are generally followed to develop FE models of joint degeneration are as follows:

a) Representation of appropriate geometry of the joint and material properties

of the constituent tissues.
b) Input boundary conditions in terms of joint motions, loads and constraints, often derived from a musculoskeletal modeling workflow.
c) Identification of output modeling parameters relevant to joint degeneration.
d) Formulation of adaptive -degeneration- algorithms which relate the output parameters from the FE model to degeneration of the joint constituents.

Using such a workflow, the initiation and progression of degradation of knee joint structures have been quantified based on an iterative evaluation of the FE model-based stresses or strains and joint degeneration algorithms [19, 24, 92].

**Advantages and limitations**
With advancement in imaging technologies, FE models typically aim to incorporate the complex geometry of the different joint tissues as well as realistic material definitions. This increases the biofidelity of the FE models to emulate the *in vivo* mechanics of the joints. However, it is nearly impossible to obtain an accurate representation of the joint geometry due to lack of high resolution images, inaccuracies during the segmentation process as well as smoothing techniques commonly used to ensure better contact convergence in the joint. In addition, and comparable to our discussion on musculoskeletal modeling, manual segmentation of the geometry from imaging data to build a patient-specific model is a time consuming task, and hence is not suitable to be integrated in a routine manner in the clinic. There have been quite a few approaches to automate the process of segmentation [93–97]. However, most approaches are directed at automatic segmentation of the articular cartilage, while omitting the other significant tissues of the joint such as the ligaments or the meniscus (except for Dam et al. [94]), where meniscus was included), which restrict the accuracy of the *in silico* models to predict the *in vivo* conditions. Very sophisticated constitutive models have been developed for cartilage and other joint constituents [18, 91, 98], but obtaining sufficient experimental data to estimate the parameters for these models is quite a challenging task. In most cases, these parameters are estimated from *in vitro* experiments of cadavers, bovine or porcine joints, since determination of patient specific material properties is not always possible. Given that there is a huge variability in the material properties of biological samples, this approach leads to departure from patient-specificity of the developed models. Furthermore, limited tools are currently under development that allow non-invasive characterization of the material properties of the joint complex, which are necessary to develop FE models. Although MRI-based relaxometry is a promising technique [99], it merely is a qualitative more than quantitative imaging modality whose role in multi-scale modeling to predict patient-specific OA progression needs to be further confirmed [98]. Also, the constitutive models for cartilage tissue do not consider physical phenomena like buckling of the collagen fibrils, fibril-fibril

interactions and width of the collagen fibrils, nor fluid-pressurization-induced lubrication effects [98]. In addition, there are diverging opinions in literature on the FE output parameters to be used for the degeneration algorithms for the different joint constituents. Therefore, in the following examples, existing literature covering a variety of output parameters relevant for joint degeneration is discussed. Verification and validation of the degeneration algorithms with experimental data is also a challenging task and will be discussed in more details in section 1.4.

**Examples**
Since there are different models that exist in literature for the degradation of the different constituents of the joint, the examples have been grouped based on the constituent of the joint for which degeneration is being modeled using FE method. Hence, the names of the following subsections will be based on the constituent of the joint, keeping in mind that all the subsections involve the use of FE method as the common computational method (see breakdown in Figure 1.2).

**FE models of articular cartilage degeneration in OA:**
Articular cartilage is one of the primary load-bearing joint structures which may become damaged when cartilage is subjected to excessive mechanical loading, and such damage is likely to progress into OA. Early signs of OA include loss of PG and roughening of the cartilage surface. In the later stages, fibrillation of the cartilage occurs, with cracks on the surface penetrating deeper into the tissue [24, 100]. State of the art computational models include the different constituents of articular cartilage and account for fundamental mechanical properties such as collagen fiber reinforcement with physiological organization of the collagen structure, ground substance (ground matrix) stiffness and tissue swelling due to PGs, while accounting for a depth dependent collagen and PG density [18]. In consequence, their effects on the mechanical response of the cartilage can be numerically studied. This way, a holistic understanding of cartilage degeneration can be achieved, as damage in the individual components of cartilage, i.e. softening in the ground substance and damage to the collagen network, and the possible interaction between these two can be studied. As it is challenging to explore these effects experimentally, computational models provide unique insights. In the following subsections FE models for the degeneration of the different constituents of articular cartilage will be discussed.

*FE modeling of proteoglycan degeneration:* Loss of proteoglycans is one of the signs of early OA. Proteoglycans being the fixed charge carriers in cartilage, the degeneration of PGs has a two-fold effect: reducing the cartilage's compressive properties (due to increased permeability) and a decrease in the fixed charge density (FCD), resulting in reduced osmotic swelling pressure. In the paper by Orozco et al. [19], FCD loss was modeled in lesioned cartilage discs

under dynamic loading using a degeneration algorithm driven by fluid velocity, maximum shear strain and deviatoric strain separately. The fluid velocity driven algorithm was found to be most effective in predicting FCD loss when compared to experimental results. This 2D model incorporated only loss of FCD as a result of PG loss. No softening of the cartilage ground substance due to PG loss was considered, which is a shortcoming of this study. Another study [101] involving a 3D FE model of a lesioned cartilage disc, used similar degeneration algorithms, however with different parameters driving the degeneration algorithm, more specifically axial strain, shear strain, octahedral shear strain, maximum shear strain, minimum principal strain and maximum principal stress. A maximum shear strain-driven algorithm resulted in the maximum degeneration of fixed charges around the lesion. It was also observed that the choice of the degeneration thresholds for each of the cases as well as the choice of the loading regime largely influenced the degeneration of fixed charges around the lesion. Also, the collagen fibril stiffness was reduced and the permeability increased to model a more realistic case of loss of fixed charges, further increasing the FCD degeneration. It must be noted that both these models incorporated local damage theories, where the damage at an integration point was determined by the stresses or strains at that point only. This local damage theory could result in localization of damage which results in concentration of all damage in a vanishing volume. Based on past literature on damage mechanics [102, 103], this could cause an extreme brittle behavior of the material, with the material failing at almost zero energy [104]. In context of cartilage damage, it would mean that damage to cartilage occurs catastrophically as compared to a more gradual damage in physiological case. The solution to this problem would be to use non-local damage theories, such as the one used by Párraga Quiroga et al. [105].

*FE modeling of collagen fiber degeneration:* During the initiation phase of OA, an increase in the fibrillation of the collagen fibril network is observed. Hence, modeling the degradation of the collagen fibrils in articular cartilage as a result of repeated mechanical loading is an important step in the study of cartilage degeneration. In one study [92], a collagen degeneration algorithm was implemented for the first time in a human knee joint model, thereby representing damage accumulation in overweight patients during physiological gait loading. In this algorithm, the stiffness of the local collagen fibril network was reduced when the maximum principal stress in the tissue exceeded a threshold value based on a chosen criteria as shown in Figure 1.3. By performing 100 iterative simulations, the authors observed that fibril degeneration in the medial tibial cartilage was more pronounced for obese subjects compared to healthy humans. These results were also confirmed based on an experimental 4 year follow-up in patients. As such, this study was one of the first in its kind demonstrating the huge potential for simulation of patient-specific cartilage degeneration. In

another follow-up study [106], the same degeneration algorithm was used with patient specific FE models representative of different grades of OA involvement. The algorithm was able to predict OA progression when compared to the experimental follow-up data for different subjects. Maximum degeneration and degenerated volumes within the cartilage were found to be significantly higher in OA subjects as compared to healthy subjects.

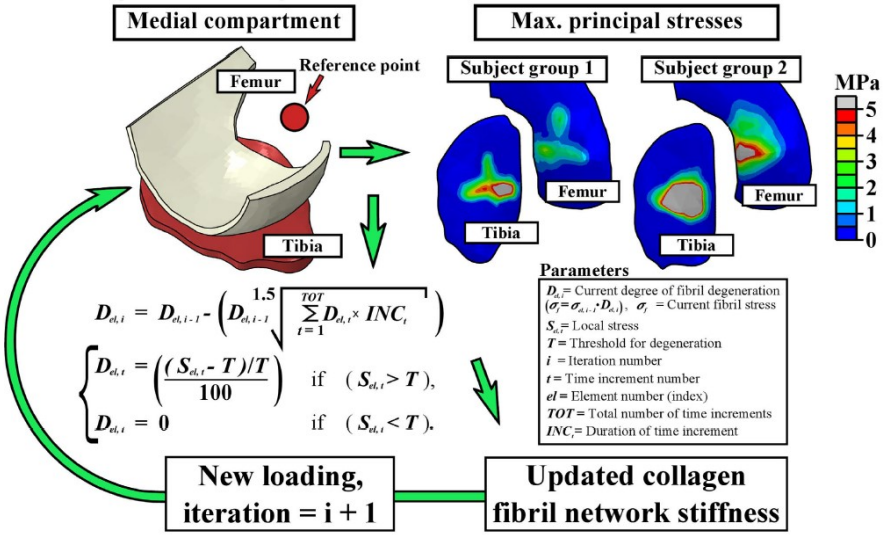


Figure 1.3: The fibril degeneration algorithm (shown in the left side) was based on excessive maximum principal stresses in the medial compartment of the knee joint. The stress distributions on the right are obtained at the first peak loading force of the stance phase of gait. The model was run iteratively to simulate gradual degeneration of the collagen fibril network. Adapted from [92].

Different opinions exist in literature regarding the physical parameters influencing the degeneration of collagen fibrils. In the aforementioned study [92], maximum principal stress in the tissue was considered to influence collagen damage, whereas in another study [107], it was shown that for relatively thick cartilage samples, collagen damage was caused by excessive shear strains along the collagen fibrils, whereas in thin samples, collagen damage was caused by both excessive shear strains along the collagen fibrils and collagen fibril tensile strains, at distinct locations. It was concluded that cartilage damage starts due to excessive shear strain along collagen fibrils and damage due to excessive fibrils strains occur at higher loads.

Apart from degradation of collagen fibrils, collagen network disorganization could progress following cartilage injury, which can lead to further cartilage degeneration [108]. Past works on computational modeling of collagen network disorganization in injured articular cartilage include studies by Tanska et al., [109] and Wilson et al., [107] . Tanska et al. [109] concluded that when the collagen reorientation algorithm was based on both tensile tissue stress or strain and tensile collagen fibril strain, substantial collagen reorientation was predicted locally near a cartilage defect and particularly at the cartilage–bone interface.

*FE modeling of combined degeneration of collagen fiber and proteoglycan:* Since the initiation and progression of OA is characterized by collagen fibrillation, and an increase in fluid fraction and proteoglycan depletion [19, 107, 110], there is a need to integrate all these mechanisms while developing a robust computational model of cartilage degeneration. In this context, a study by Hosseini et al. [24] aimed to understand the interaction between ground substance softening and fibril degeneration and their combined effect on overall cartilage degeneration. For the damage model, it was assumed that excess deviatoric strain in the ground substance beyond a particular threshold would lead to softening of the matrix. For the fibril network, it was assumed that strain in the direction of the fibers exceeding a threshold would lead to fiber softening. It was observed that under applied indentation loading, ground substance softening developed over a larger area than collagen damage. Damage to the ground substance caused cartilage softening earlier and to a greater extent than collagen damage. In a similar study by Mononen et al. [16], degeneration of collagen fibrils and PG content, combined with an increase in cartilage permeability of cartilage was modeled. While the degeneration of collagen fibrils was triggered by excessive and cumulative tensile stresses, degeneration of PG's was modeled by a reduction in the ground substance modulus due to excessive deviatoric strains. A decrease in the proteoglycan content was equated with an increase in the tissue permeability, leading to more fluid flow. The detailed schematics of the study is shown in Figure 1.4.

In another study, Parraga Quiroga et al.[105] investigated the effect of strain rate on cartilage damage. Given that cartilage is poro-viscoelastic, strain-rate dependent effects are indeed expected. The authors observed that with increasing strain rate collagen damage increased, whereas damage in the non-fibrillar matrix decreased. It must be noted that this study used the same damage evolution as in Hosseini et al. [24]. However, they incorporated a non-local damage theory, where, instead of using the local strain in each integration point for damage evaluation, a strain averaged over a specific volume around the integration point was used. The results showed that the local damage approaches result in larger damage areas, localized to specific elements, whereas the non-local approach shows lower damage values as a result of the weight-averaging

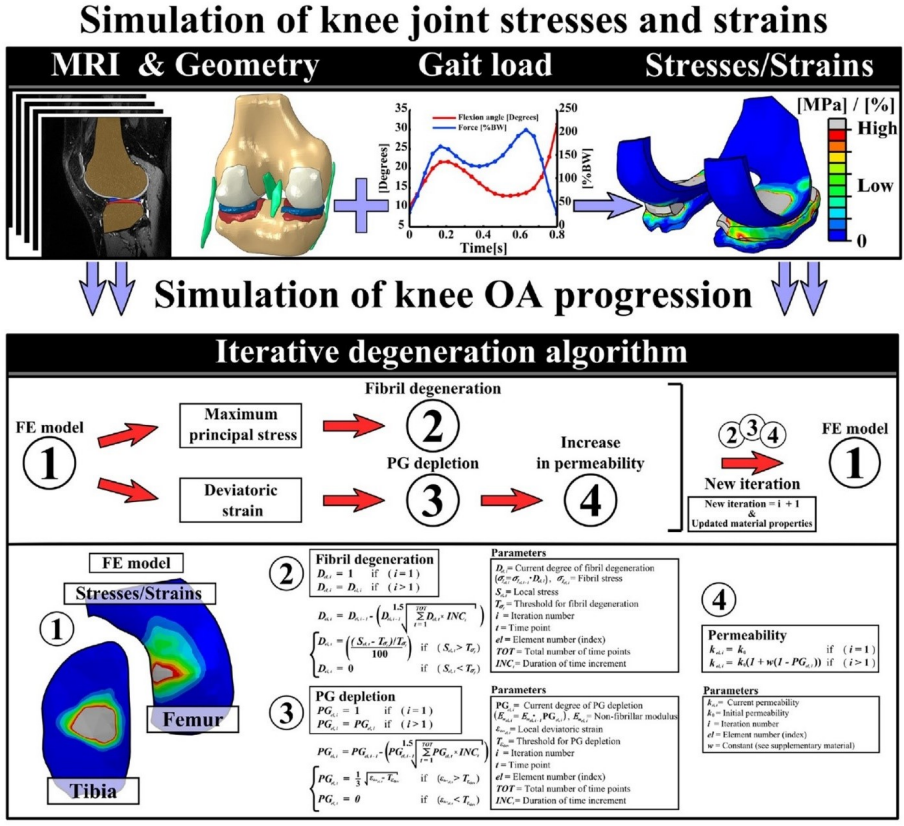


Figure 1.4: This figure presents the detailed workflow followed to implement an iterative degeneration algorithm. The top row describes the steps followed to develop the FE model to simulate knee joint stresses and strains. The middle row shows the different components of articular cartilage that are considered to be degenerating in the algorithm. The last row presents the mathematical formulations used in the algorithm to model collagen fibril degeneration, proteoglycan depletion and increase of permeability of the cartilage due to excessive stresses and strains. Adapted from [16].

damage based on Gauss function.

Alternatively, phenomenological models have also been developed to model the degradation of cartilage [111–113]. In one of these studies [112], a phenomenological mathematical damage model caused by mechanical action was developed. The model considered tissue failure as a result of chondrocyte death and matrix loss. It took into consideration different factors modifying fatigue resistance such as age, body mass index (BMI) and metabolic activity. These FE simulations were able to predict tissue failure at different loading frequencies, variations in damage magnitude and also different damage sites.

**FE models of subchondral bone changes in OA:**
Simplistic FE bone models have been developed to evaluate the structural role of subchondral bone in OA progression [56, 114]. Such models, however, disregard the intra-specimen spatial distribution of material properties and also the subtle geometric difference between subjects. QCT-FE models of subchondral bone have recently been developed to monitor alterations of local structural stiffness at the subchondral surface non-invasively and subject-specifically [115, 116]. In such models, the QCT provides information regarding the geometry and density of the imaged bone whereas FE calculates the integral contribution of all factors involved in the structural stiffness sensed at the subchondral surface. More advanced imaging techniques, e.g. MRI/CT imaging using contrast agents [117], could help to construct subject-specific FE models of the cartilage-subchondral bone complex.

**FE models coupling cartilage degeneration and subchondral bone remodeling in OA:**
Since degeneration of cartilage and remodeling of the subchondral bone progress hand-in-hand in case of OA [6], both the processes must be coupled in computational models for a more accurate (patho)physiological description. In a study by Stender et al. [118], the bone-cartilage unit (BCU) was modeled consisting of the articular cartilage, calcified cartilage, subchondral cortical bone and subchondral trabecular bone, however assuming a simple geometry. Bone remodeling was assumed to occur in the subchondral cortical and trabecular bone, and damage to articular cartilage could occur either via damage to collagen fibrils or degradation of GAGs. Results from spherical indentation on the articular cartilage surface of the bone-cartilage unit indicated that damage to articular cartilage occured at the articular surface. Furthermore, bone remodeling was also predicted to occur with a net stiffening of the subchondral bone plate. In another study involving poro-elastic properties of BCU [119], it was observed that the permeability of the articular cartilage governs the poro-mechanical response of the BCU while the permeability of calcified tissues exerts no appreciable effect on the force-indentation response of the BCU. With OA specific permeability properties for the bone and cartilage, higher fluid velocities

were observed. *In vivo*, this phenomenon would likely lead to chondrocyte death, tissue remodeling, alterations in joint lubrication, and the progression of OA.

### 1.3.3 Gene regulatory network models

Computer models can also provide a formal framework to study the dynamics of genetic programs happening inside a cell. Such computational approaches are highly relevant for systems biology, a field that has gained quite some importance in the field of tissue engineering and regenerative medicine over the last years. One family of models, the (gene) regulatory network (G)RN models, can be particularly interesting to decipher signaling and cell responses implied in cell fate decisions. Since the complex interplay of different factors present in signaling networks can impossibly be dealt with through human intuition, *in silico* models involving formal computer languages can provide unique insights. There exist quite some examples in literature [120–123] where *in silico* models were successfully used to decipher biological complexity and give new biological insights. The overview of different methods that can be used to generate the (G)RN models are shown in Figure 1.5 [124]. The first step is to generate a network graph, which provides a static (unchanging) representation of the biological processes under study. This network graph can be either inferred directly from the experimental data (data-driven approach) or derived from mechanisms and pathways already available in the literature (knowledge-based approach). Once a network is established, a dynamic analysis is performed to simulate the temporal evolution of the different network elements under specific conditions and to study the possible outcomes (stable states) of the established network. Various modeling approaches can be used to simulate the evolution of the network components over time. Quantitative models use ordinary differential equations (ODE) to describe the temporal evolution of species (cell density etc.) and can also include spatial resolution by using partial differential equations. Qualitative models on the other hand use logical statements to describe the evolution of species [125].

**Advantages and limitations**
Regulatory networks can be useful to study the molecular mechanisms of joint degeneration. In the adult stage, the chondrocytes in the articular cartilage remain in a stable phenotype characterized by a low rate of proliferation and the production of ECM rich in Col-II and Aggrecan. However, some degenerative diseases such as OA may lead to dysregulation of the stable cartilage phenotype, modifying the chondrocyte's proliferation rate and triggering its switch toward hypertrophy, thereby leading to abnormal ossification of the joints. (G)RN models of stable chondrocytes can be useful to study the intracellular activation of different pathways following mechanical and chemical signals,

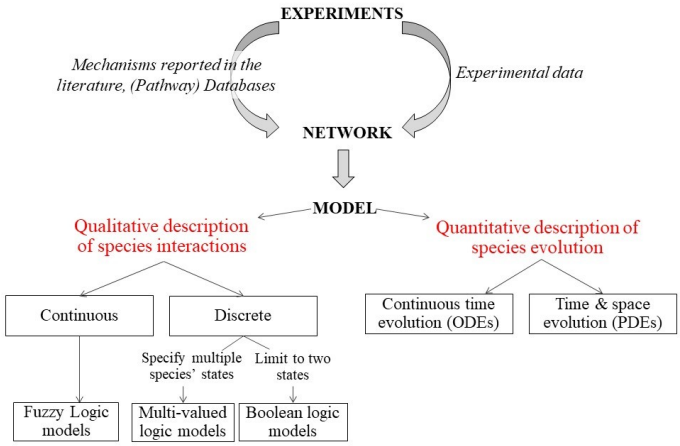


Figure 1.5: Description of modeling framework for regulatory networks. Firstly, a static network graph is generated from experimental data and mechanisms reported in literature. Then, various modeling approaches can be used to simulate the temporal evolution of the components of the network. Quantitative models use ordinary differential equations (ODE) to describe the temporal evolution of species (cell density etc.) and can also include spatial resolution by using partial differential equations. Qualitative models on the other hand use logical statements to describe the evolution of species. Adapted from [124].

thereby leading to cell phenotype changes due to cell dedifferentiation, inducing OA. Since these regulatory network graphs are sometimes constructed on the basis of experimental results published in literature (knowledge-based models), conflicting opinions in literature can lead to problems in decision making from the perspective of the model developer. Additionally, most of these (G)RN models are either qualitative or semi-quantitative in nature [126, 127], which makes it difficult to be integrated with quantitative methods like the FE method. Also, the ability for quantitative model predictions is limited.

**Examples**

In a recent study [128] using systems biology approaches combining experimental and computational findings, the mechanism by which TGF$\beta$ protects against pro-inflammatory responses and how this mechanism changes with age were studied. Computational modeling revealed that two independent mechanisms were needed to explain the crosstalk between TGF$\beta$ and pro-inflammatory signaling pathways. Further insights into the mechanisms that cause TGF$\beta$

signaling to change from a protective to a detrimental pathway in cartilage with ageing were provided. This systems biology approach suggested that the restoration of the protective role of TGF$\beta$ can be a potential therapy to prevent loss of cartilage in ageing patients. Similar studies to identify other factors leading to cartilage breakdown and identification of curative and protective targets can be found in [126, 129–133].

### 1.3.4 Multiscale models of joint degeneration

It is well known from literature that moderate mechanical loading is essential to maintain cartilage homeostasis [134–136] and excessive mechanical loading may trigger degeneration of cartilage. However, to understand the sequence by which mechanical signals are transferred from the joint level to the cellular level and how these signals trigger intracellular processes, multiscale modeling is necessary [137, 138]. A brief framework of multiscale modeling for articular cartilage is shown in Figure 1.6.

**Advantages and limitations**
Multiscale modelling can be an important tool to evaluate the intricately linked mechanical states of the tissue and the cells, which can lead to the onset and progression of OA. A feed-forward post-processing approach (translating from the macro-scale tissue level to the micro-scale cell level) for multiscale modelling has the advantage of being less computationally intensive because the micro and macro scale models need to be solved only once for a particular loading scenario. However, in a uni-directional feed-forward approach, the reverse direction (i.e. translating from the micro to macro scale) is generally not implemented, which is important when tissue properties may change due to tissue damage or regeneration as in OA. This step would involve a computational homogenization approach like Geers et al. [139] to infer the changes in the macro-scale tissue properties from the changes in micro-scale cartilage or bone properties due to intracellular processes. Such a homogenization procedure comes with specific computational challenges, a discussion of which is beyond the scope of this chapter.

**Examples**
Multiscale model using a post-processing approach have been developed in literature for the calculation of chondrocyte deformation due to physiological loading in the knee joint [140, 141]. In this post-processing approach, the macro-scale tissue level model was mechanically coupled to the micro-scale cellular model by passing the deformation gradient from the tissue level to the cell level. It was observed that micro-scale models calculated amplified deformations of the chondrocytes compared to those predicted at the macro-

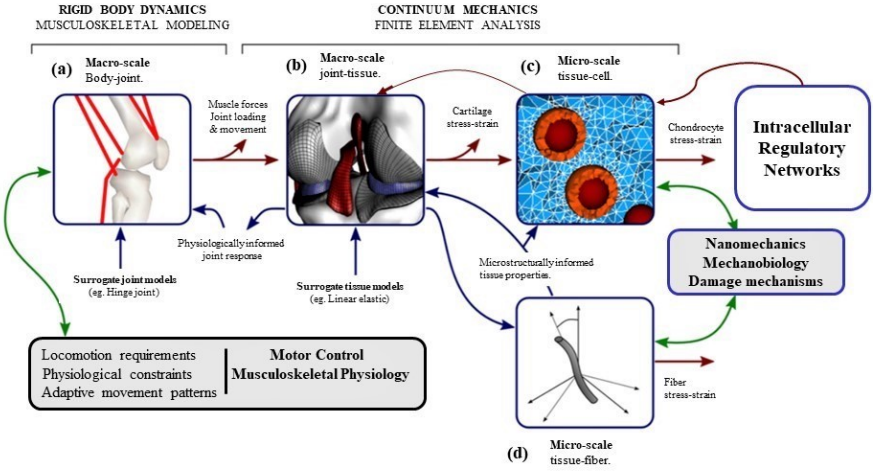


Figure 1.6: The pathway of mechanical signal from joint level to cellular (intracellular) level can be understood by developing computational models at different length scales which interact with each other. (A): Musculoskeletal (MSK) modelling approaches coupled with gait analysis can calculate the kinematics and the forces in the joint during locomotion. (B): Finite element (FE) analysis of the whole joint with inputs from MSK models can provide contact pressures and forces, and the macroscopic stresses and strains in the tissues. (C): Micro-scale FE analysis of chondrocytes in the extracellular environment, with inputs from macroscopic FE analysis of the tissue can produce deformations and stresses in the chondrocytes in their native environment. (D): Micro-scale fiber architecture and multiphase modeling can make the cellular-level models event more integrated. (E): The intracellular processes triggered by mechanical signals acting on the cell can be modeled by (Gene) Regulatory networks (modified from [137]).

scale when simulating one body weight compressive loading at the tibio-femoral joint. Also, it was observed in Sibole et al. [141] that first-order data passing (considering the first gradient of the deformation i.e. deformation gradient tensor, as the link between macro and micro scales) between the different spatial scales appeared to be sufficient for simplified loading conditions. In a similar study using a post-processing approach [142], a 3D multi-scale model was developed to compare chondrocyte and surrounding peri- and extracellular matrix responses under loading during gait in healthy and medial meniscectomy knee joints. Displacements and pore pressures at the nodes of a compartment level model (consisting only the medial compartment of knee joint) were used as boundary conditions for the cell level model. Medial meniscectomy per se was found not to alter chondrocyte deformations substantially during gait. However, abnormal joint loading following meniscectomy did expose the chondrocytes to higher magnitudes of fluid pressure and maximum principal strains. These changes might lead to loss of cell viability and contribute to the onset of OA. A different multiscale framework was developed by Fernandez et al. [79, 143], aiming at studying the initiation of OA at the bone-cartilage interface due to anterior cruciate ligament damage (ACLD). In the framework (shown in Figure 1.6), which was coded in CellML [144], the cell level model involved a bone remodeling algorithm [145] based on the RANK–RANKL–OPG pathway that predicted the number of active osteoblasts (to deposit bone) and osteoclasts (to absorb bone). Similarly, a cartilage damage prediction model was used (based on the work of Nam et al. [146])), which quantitatively described the action of NF-$\kappa$B signaling cascade under mechanical stimulation. Peak cartilage strains were used to excite IKK which activated the NF-$\kappa$B pathway, thereby inducing a number of pro-inflammatory genes. It was observed using this model that ACLD resulted in subchondral bone thickening with a reduction in cartilage thickness. Also increased peak cartilage strains of the ACLD knee resulted in increase of inflammatory cytokines in the medial femoral condyle. One of the main contributions of this multi-scale approach was its ability to incorporate the effect of subchondral bone remodeling on cartilage inflammation.

### 1.3.5 Data-driven approaches

Data-driven approaches such as machine learning [147–149] constitute a different modeling approach to predict OA progression. The difference between these approaches to the others discussed in previous sections is that these approaches are fed purely with data and do not rely on underlying physics-based modeling approaches. In this section, the examples will focus on models based on patient reported outcome measures (PROMs). Other areas where data-driven

approaches are commonly use are related to image processing and (G) RN inference.

**Advantages and limitations**
The data-driven approaches are designed to deal with uncertainty and imprecision which are commonly present in clinical data sets such as those from OA studies. Generally, such prediction models are developed using input and output variables, with input variables consisting typically of baseline demographic or imaging data [147, 150], and outcome variables consisting data related to the presence of knee OA as assessed by specific methods such as, Kellgren–Lawrence (KL) grade for classification of knee OA. The resulting model is then used to predict the outcome variables from a new data set (typically from independent patient data). The choice of the input variables is of great importance in this approach as it can affect the accuracy of the predictive models. Generally, known risk factors for OA are included in the list of input factors. The risk factors commonly include age, sex and BMI. Some other suggestions for risk factors can be pharmacological treatments, genetic factors, varus or valgus misalignment of the knee, ethnicity, physical activity etc. [148]. It is very important to identify the most important risk factors, as their inclusion will not only increase the accuracy of the prediction model but also reduce the number of redundant variables, thereby saving time and cost during the training phase of the model.

**Examples**
In Long et al. [151], a model for the prediction of knee OA was developed. Kinetic variables from the hip and knee and the quality of life outcome score were combined to create a prediction model for predicting the risk of knee OA in post-traumatic individuals (with the least prediction error of 0.02). Imaging-based information incorporated in machine learning-based prediction models were found to improve their performance [152]. In Ashinsky et al. [150], a disease classification model was developed using a machine learning algorithm to select features of articular cartilage from MRI (performed *in vivo*) indicative of OA progression. The selected features correlated with the Western Ontario and McMaster Universities Arthritis Index (WOMAC) score. The developed model predicted which patients would progress to having symptomatic OA with 75% accuracy.

### 1.3.6 Verification, validation and uncertainty quantification of computational models

Establishing credibility of *in silico* models of biological processes follows a series of well-defined steps, summarized by the abbreviation VVUQ: verification,

validation and uncertainty quantification. The verification step refers to ensuring that the simulation outcomes correspond to the mathematical model. This means, amongst others, ensuring that no mistakes were made in the implementation of the model, that proper convergence studies were executed and that the solution proposed by the software is correct. In the validation step, one has to demonstrate that the simulation results correspond to the physical reality. This requires running simulations to predict conditions, within the model's context of use, for which high-quality well-documented experimental data is available and performing the comparison between experimental and simulation results. For these first steps (verification & validation), a standard has recently been published for medical devices (ASME V&V, 40-2018)[153]. This standard allows to assess the amount of V&V that is necessary to include in regulatory filing of a medical device, depending on the influence and consequence of the *in silico* model on the functioning of the device. Recently, it was elaborated how these same concepts can be applied to physiologically-based pharmacokinetic-models typically used in the context of drug development [154]. Finally, in the uncertainty quantification step, the aim is to obtain an understanding of the impact of the assumptions that were made while establishing the model and its parameters on the model outcome. Several excellent reviews describe the process of VVUQ in further detail for a variety of models and medical applications, see for instance [155, 156] and references within. In the area of knee joint modeling, a recent paper by Erdermir et al. [12] explicitly addresses issues such as reproducibility, model training, standards and regulatory affairs.

For validating musculoskeletal models, the first step is to compare the outputs of the developed model (which is calibrated from experimental data) with independent data sets. Most commonly, electromyography (EMG) data is compared to calculated muscle activation and force profiles. Less common is the comparison of the calculated joint contact forces against available experimental measures of joint loading from instrumented implants [157]. Ideally, the simulation is based on the corresponding experimental data for which the measured joint loading is available. Unique data sets are currently available in the biomechanics community for this purpose. Alternatively, musculoskeletal simulation outcomes (i.e.. joint angles and moments, muscle activations and forces, muscle fiber and tendon velocities and internal joint loads) can be compared to the results obtained from previously validated published models, on the condition that identical input data (3D Motion capture and ground reaction force data) are used [158]. Verification of FE models involves a wide range of approaches including mesh convergence studies, and has been extensively reported in literature [159, 160]. For FE models aimed at studying the sensitivity of general outcomes to some input parameters, a detailed validation may not be necessary. While developing FE models of subject specific *in vivo* cases, such as the knee or the hip joint, validation can be quite challenging due to unavailability

of suitable experimental data (for example, measurement of joint contact forces *in vivo*) for both practical and ethical reasons. In such cases, partial validation of the *in vivo* model with experimental data for other specimens can be done. Non-invasive imaging techniques such as MRI can also be used to map the deformation of the cartilage, hence providing experimental data for validation. For validation of FE based degeneration models, one can use already established databases such as the OA initiative database, or use results from ongoing cohort studies. Since progression of OA is a long term phenomenon, in case of ongoing cohort studies, one has to wait for a long time to get the experimental data for the validation of prospective computational models. Some studies have used the OA database to compare their (retrospective) model predictions [92, 106], which provided confidence in the predictive capability of the models.

Validation of multi-scale models invokes the need for experimental setups which can capture deformations or changes in the micro-scale cellular level due to changes in inputs in the macro-scale. Such multi-scale experimental setups can use multi-photon laser microscopy to measure chondrocyte deformations in both osteochondral grafts as well as intact joints [21, 161]. Parameters such as cell aspect ratio, volume and height and width are generally used to validate the simulation results with experiments [140, 162].

## 1.4 Discussion and Conclusion

With a worldwide increase in OA prevalence, there is an urgent need of gaining a detailed understanding of the factors contributing to disease initiation, progression and remediation. The last decade, significant progress in the development of computational tools to study the complex biomechanical factors involved in OA was made, using computational models. Musculoskeletal and FE modeling [16, 24] as well as (gene) regulatory networks [79] were used to study the initiation and progression of damage in the joint. These computational modeling approaches are widely regarded as emerging technologies that can aid clinicians in planning timely interventions. Advanced imaging [163–165] coupled with sophisticated computer modeling techniques can help in achieving this goal. In terms of modeling approaches, FE models have been quite promising in predicting degeneration of different constituents of articular cartilage [24, 92] and the role of the subchondral bone in the disease process. However, there is still room for improvement in terms of the development of patient specific models. The primary bottleneck in developing patient specific *in silico* models of joint degeneration is the huge variability in joint geometry as well as mechanical properties of the corresponding tissues.

As evident from this literature review, algorithms for damage modeling of the different constituents of articular cartilage, i.e. the collagen fibrils, proteoglycans and permeability of ground matrix have evolved from simpler damage models triggered by principal or deviatoric strains [24] to more complex damage models that take into account the cumulative effect of loading [16], or use non-local damage theories [105]. These algorithms are coupled with FE models of the knee joint, and hence, are capable of predicting local cartilage degeneration due to biomechanical overloading of the joint. Another possible approach would be to add biomechanical factors into the statistical or machine learning-based predictive models. This would involve the use of data-driven methods with FE models and damage algorithms, which would provide information about the biomechanical factors in the model. However, this would require FE analysis of hundreds of subjects which is a cumbersome and time consuming task. Furthermore, statistical or machine learning methods can possibly reduce the level of subject-specificity in terms of geometry and mechanics of the joint, by approaching a template-based analysis.

In this chapter, we also considered the role of regulatory network models and their potential in predicting cell fate as a result of biomechanical and biochemical stimuli. To improve the robustness of such models, a complete description of the intracellular signaling pathways is needed thereby requiring unique experimental data that is increasingly made available from a range of microarray and RNA sequencing studies that describe the effect of mechanical loading on cell fate decisions. Also, if these regulatory networks were to be coupled with a larger multi-scale framework, the effect of abnormal joint loading on chondrocyte transcriptional activity and hence the phenotype change responsible for OA progression could ultimately be monitored. A major challenge in this field is to relate the changes in cell phenotype to macro level changes in the joint loading, which would require not only extensive experimentation to characterize the change in matrix constituents with change in cell phenotype, but also the application of computationally intensive homogenization methods for homogenization of micro-scale mechanical properties to the macro scale.

In conclusion, as described in this chapter, a substantial number of computational tools are available that can be used to model joint degeneration in OA. In the future, efforts should be made to integrate the different modeling techniques into a more robust computational framework that should not only be efficient to predict OA progression but also easily allow individualized risk assessment for use in screening in clinical practice.

# Chapter 2

# Aims and Objectives

This chapter presents the general aim and objectives of the thesis, followed by a brief outline of how the thesis addresses these objectives.

## 2.1 General aims

The previous chapter highlighted that cartilage degeneration is a multiscale process driven by the interplay of mechanical and biochemical factors across different length scales. *In silico* modeling offers a powerful tool to investigate this complexity. However, a gap remains in existing modeling approaches, which fail to integrate cartilage mechanics across multiple length scales with the intracellular biochemical processes influenced by mechanical and biochemical factors.

The aim of this PhD project is to develop a computational multiscale model that integrates cartilage mechanics with intracellular biochemical processes to enhance the understanding of cartilage degeneration and regeneration. Additionally, this PhD aims to establish methods for calibrating and validating the mutliscale model using suitable experimental approaches and apply it to investigate cartilage degeneration in a clinically relevant context.

## 2.2 Specific objectives

To achieve the general aims of the thesis, specific objectives were formulated as follows, each addressing a particular aspect of the overal aim. Figure 2.1 shows the overview of the objectives.

**Objective 1: Quantifying mechanical stimuli in cartilage and cartilaginous constructs across different environments, from human joints to bioreactor setups.**
To achieve this, finite element (FE) models of the human knee joint and bioreactor setups commonly used in cartilage research will be developed. These models will be used to perform FE analysis, quantifying the mechanical stimuli experienced by cartilage and constructs under various loading conditions, including the stance phase of gait in human knee joint and different bioreactor loading regimes.

**Objective 2: Development and calibration of a multiscale modeling workflow for articular cartilage.**
The multiscale modeling workflow will be developed by obtaining mechanical behavior across different length scales, from the tissue to the cellular level, using FE models, which will then be coupled with an intracellular gene/protein regulatory network. The coupling between the cellular forces obtained from cell scale FE model to a mechanical loading input to the semi-quantitative gene/protein regulatory network will be executed by using a Hill's function.The parameters of the Hill's function will be calibrated through optimization, using the difference between experimentally measured and simulated gene expressions from a dynamic compression setup of cartilage explants as the objective function.

**Objective 3: Application of the multiscale modeling workflow to study the pathological effects of meniscectomy in human knee joint.**
A multiscale model of the human knee joint will be developed following the workflow established in Objective 2. Meniscectomy will be simulated by removing the meniscus in the FE model, and its catabolic effects on relevant cartilage biomarkers will be analyzed using the multiscale approach.

**Objective 4: Development of a multiscale *in silico-in vitro* approach to study chondrocyte mechanobiology using a cartilage-on-chip device.**
To fulfill this objective, a multiscale experimental protocol will be devised in a cartilage-on-chip device, including the development of specific image processing algorithms to analyze the experimental data at different length scales. In parallel, a multiscale model of the cartilage-on-chip device will be developed using the multiscale workflow in objective 2. The results from the experiments and simulations at different length scales will then be compared, to provide further insights into the effect of mechanical loading on chondrocytes.

**Objective 5: Implementation of the multiscale modelling workflow in a model execution environment.**
The overall multiscale modeling workflow will be implemented in a model execution environment with a user-friendly graphical interface. This interface allows for easy input of cartilage geometry, cell number, and positioning, as well as streamlined result post-processing for efficient data analysis. In the longer term, this model execution environment can be utilized for *in silico* clinical trials and patient-specific modeling, enhancing its potential for personalized medicine and therapeutic applications.

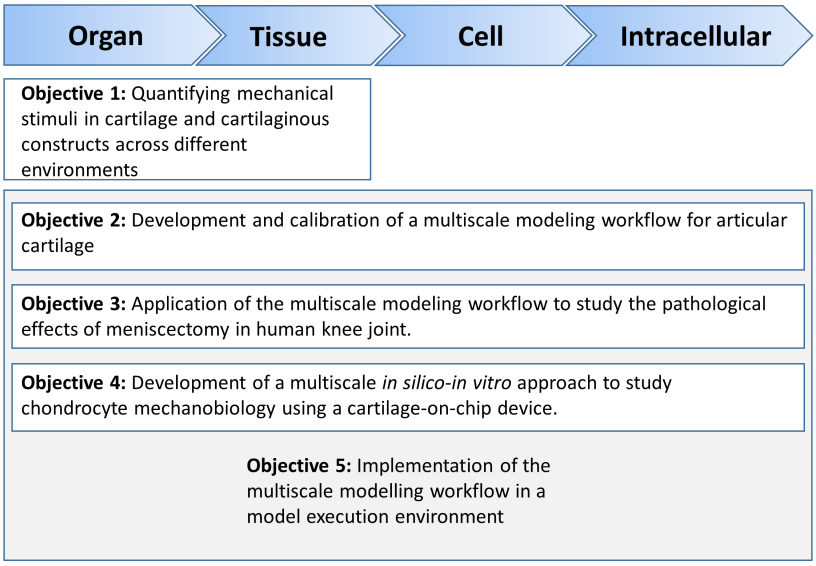


Figure 2.1: Overview of the objectives of the thesis, with the different length scales involved for each objective

## 2.3 Outline of the thesis

The objectives of the thesis are achieved in the subsequent chapters, a brief outline of which is provided herewith.

**Chapter 3** focuses on quantifying mechanical loading in cartilage and cartilage constructs, addressing **Objective 2** of this thesis. First, an FE model of the human knee joint is developed using geometry and material properties from the literature. Next, FE models are created for bioreactors that apply mechanical

loading to osteochondral grafts and tissue-engineered (TE) constructs. Finally, a comparative analysis is conducted to identify which bioreactor setup best replicates key aspects of the physiological loading conditions in the human knee joint.

**Chapter 4** aims to develop an integrated multiscale modeling workflow by combining FE models of articular cartilage at different length scales with a mechanistic intracellular module consisting of a gene/protein regulatory network, thereby achieving **Objective 2** of this thesis. The intracellular module captures key interactions between mechano-regulatory and inflammatory pathways influencing the chondrocyte phenotype. First, the study outlines the different length scales in the multiscale model, explaining their interconnections and the biological mechanisms incorporated. Calibration and validation are then performed to ensure model credibility. Finally, as an application, the model is employed to study the pathophysiology of the human knee joint following meniscectomy, thereby fulfilling **Objective 3** of the thesis.

**Chapter 5** focuses on developing an *in silico* and *in vitro* approach to study chondrocyte mechanobiology using a cartilage-on-chip setup, addressing **Objective 4** of this thesis. First, inverse characterization of the agarose hydrogel is performed to calibrate its material parameters for the *in silico* model. Next, multiscale experiments are conducted within the cartilage-on-chip setup to generate experimental data across different length scales under mechanical stimulation. Finally, a multiscale *in silico* model of the cartilage-on-chip system is developed, and numerical predictions at various length scales are compared with experimental results.

**Chapter 6** focuses on implementing the multiscale modeling workflow within a model execution environment (MEE), addressing **Objective 5** of this thesis. A user-friendly interface is developed, incorporating key features such as tissue geometry, cell location within the model, the specific zone of articular cartilage, and post-processing of the simulation results.

**Chapter 7** describes the relavant finding of the thesis and possible future research directions.

# Chapter 3

# From human joints to bioreactor setups: quantifying mechanical stimuli in cartilage physiology and regeneration

Satanik Mukherjee[1], Wouter Wilson[2], Liesbet Geris[1,3,4]

[1]Biomechanics Section, KU Leuven, Belgium
[2]TU Eindhoven, the Netherlands
[3]GIGA Institute, University of Liege, Belgium
[4]Skeletal Biology and Engineering Research Center, KU Leuven, Belgium

This chapter is based on a manuscript prepared to be submitted: S. Mukherjee, W.,Wilson and L. Geris. "From human joints to bioreactor setups: quantifying mechanical stimuli in cartilage physiology and regeneration."

## 3.1 Introduction

Mechanical loading plays a crucial role in maintaining articular cartilage homeostasis. Non-physiological mechanical loading, including both hypo-physiological loading, as seen during joint immobilization, and hyper-physiological loading, as encountered during traumatic joint injuries, are linked to degenerative changes in cartilage [134, 166, 167]. Articular cartilage is a biphasic tissue, consisting of a solid phase mainly composed of proteoglycans and collagen fibrils, and a fluid phase. In healthy cartilage, the majority of load-bearing is achieved through pore fluid pressurization. Additionally, there is an arcade-like pattern of collagen fibril orientation across the thickness of cartilage, especially in weight-bearing joints such as the hip and knee. This unique arrangement gives cartilage an anisotropic behavior, allowing it to resist shear forces along the surface. During daily activities, articular cartilage is subjected to a wide range of mechanical stimuli, creating a complex dynamic state of stresses and strains at various anatomical locations within the joint.

In cartilage tissue engineering (TE), bioreactors are used to culture tissue engineered constructs under controlled mechanical conditions. Bioreactors furthermore provide an *ex vivo* platform for studying the effects of mechanical loading on disease progression, such as osteoarthritis (OA) and possible therapeutic interventions. In literature, bioreactors used in context of cartilage (patho)physiology and regeneration can be broadly classified into dynamic compression, combined dynamic compression and shear, and hydrostatic pressure [168–170]. Each of these bioreactors is designed to mimic a certain aspect of the mechanics encountered *in vivo*. Despite the widespread use of these bioreactors in the literature, there is considerable variability in the corresponding mechanical loading protocols applied in these bioreactors, which can lead to inconsistencies in the outcomes of different studies. While multiple review articles exist that compare these different bioreactors (and loading conditions) to their respective outcomes in terms of cellular response [168–170], no such broad efforts have been made to compare quantitatively what are the differences in mechanics encountered in these different setups and how closely are they related to the *in vivo* physiological scenario.

Capturing the detailed mechanics of TE constructs or explants subjected to mechanical loading in bioreactors is very difficult using traditional experimental techniques due to the complexity of mechanical environment that exists within the specimens. In this context, *in silico* models have been established as an enabling technology to quantify the mechanical environment in these setups as well as human joints [171]. In particular finite element (FE) analysis has been widely used in literature to quantify the mechanics of constructs or explants in many bioreactor studies [172–175]. However, most of these studies focus on a

single type of bioreactor only, thereby making it difficult to make a comparative analysis across different types of bioreactors and corresponding loading protocols. Furthermore, these studies do not incorporate a model of the *in vivo* scenario which the bioreactor aims to recapitulate as a quantitative basis of comparison.

The present study aims to bridge this gap in literature by performing a comparative analysis of widely used bioreactor setups in the literature with a physiological human knee joint model, utilizing FE approaches. This study will not only provide a better understanding of the differences in mechanical environment across different bioreactor setups, but will also provide an extensive repository of bioreactor setups and loading conditions for experimentalists to choose from, depending on the research question to be studied. To achieve this aim, firstly, a FE element model of the human knee joint is developed using geometry and material properties obtained from literature. Secondly, FE models of bioreactors applying mechanical loading to osteochondral grafts and TE constructs are developed. Lastly, a comparative analysis is conducted between the optimal loading cases of each bioreactor type and the human knee joint. This analysis will help identify the loading regimes specific to each bioreactor setup that most closely mimics specific mechanical aspects of the physiological situation.

## 3.2 Methods

### 3.2.1 FE modeling of the human knee joint

#### Geometry and Meshing

The geometry of the tibiofemoral joint of a cadaveric right knee from a 70 year old female donor (77.1 kg, 1.68 m) was obtained from the Open Knee database [176] and imported in Abaqus 2023 (SIMULIA, Providence, RI, USA). The Open Knee joint geometry included geometric representations of the bones (femur and tibia), cartilage(femoral and tibial), menisci (medial and lateral), and ligaments (anterior and posterior cruciate, medial and lateral collateral). The segmented geometry of the lateral collateral ligaments in the database was incomplete. So, the collateral ligaments (both medial and lateral) were excluded from the simulations. Since the collateral ligaments are primarily responsible for side-to-side stability of the knee joint, and do not contribute to load-bearing in the joint, their exclusion are expected to not significantly alter the stresses in articular cartilage. The anterior and posterior ends of the menisci were attached to the tibial plateau by means of a series of linear springs with total stiffness of each meniscal attachment (also called meniscal horns) set to a 2000 N/mm

based on previous studies [91, 177]. The femoral and tibial cartilage were rigidly attached to the femur and tibia respectively using the 'Tie' constraint.

Articular cartilage were meshed with hexahedral pore pressure elements(C3D8P) and the other soft tissues were meshed with hexahedral linear elements (C3D8). The tibia and femur were meshed with rigid elements (R3D4). A mesh convergence study was conducted by varying the number of elements across the thickness of the articular cartilage from 7 to 12. These numbers were based on previous studies in literature that used similar fibril-reinforced poroviscoelastic (FRPVE) material model for knee joint, where the number of elements across the cartilage thickness ranged from 4-6 [91, 142]. This adjustment resulted in a total element count ranging from 60,837 to 104,292 for the coarser and finer meshes, respectively. No significant changes were observed in the distribution of the maximum principal stresses, pore pressures and contact pressures from the coarser to finer mesh as can be seen from Supplementary Figure C.1.

### Constitutive model of tissues

Articular cartilage was modeled as a fibril-reinforced poroviscoelastic material and implemented using UMAT subtroutine, as was described in previous studies [178, 179]. This biphasic material model consists of a solid and pore-fluid component, where the solid component consists of a fibrillar and non-fibrillar part. The fibrillar part models the collagen fibrils present in articular cartilage, whereas the non-fibrillar part mainly comprises proteoglycans. The total stress at an integration point was given by:

$$\boldsymbol{\sigma}_{\text{tot}} = \frac{n_{s,0}}{J}\left[\left(1-\sum_{i=1}^{\text{totf}}\rho_c^i\right)\boldsymbol{\sigma}_{\text{nf}} + \sum_{i=1}^{\text{totf}}\rho_c^i\boldsymbol{\sigma}_{\text{f iso}}^i\right] - p\mathbf{I} \tag{3.1}$$

where $\mathbf{I}$ is the unit tensor, $n_{s,0}$ is initial solid volume fraction, $J$ is the determinant of the deformation tensor $\mathbf{F}$, totf is the total number of fibrils considered at each integration point, $\rho_c^i$ is the volume fraction of the $i^{th}$ collagen fibrils with respect to the total volume of the solid matrix, $\boldsymbol{\sigma}_{\text{nf}}$ is the stress in the non-fibrillar matrix, $\boldsymbol{\sigma}_{\text{f iso}}$ is the stress in the collagen fiber network.
The strain-dependent permeability of cartilage was given by

$$k = \alpha(1-n_{\text{ext}})^{-M} \tag{3.2}$$

where $\alpha$ and $M$ are positive material constants.

**Non-fibrillar Part**: The non-fibrillar part of cartilage, which primarily consists of proteoglycans was modeled using a modified Neo-Hookean law

as in Heuijerjans et al.[180]. The stress in the non-fibrillar matrix $\boldsymbol{\sigma}_{\mathrm{nf}}$ was calculated as:

$$\boldsymbol{\sigma}_{nf} = -\frac{1}{6}\frac{\log(J)}{J}G_m\boldsymbol{I}\left[-1+\frac{3(J+n_{s,0})}{(-J+n_{s,0})}+\frac{3\log(J)Jn_{s,0}}{(-J+n_{s,0})^2}\right]+\frac{G_m}{J}\left(\boldsymbol{F}\cdot\boldsymbol{F}^T-J^{\frac{2}{3}}\boldsymbol{I}\right) \tag{3.3}$$

where $G_m$ is the shear modulus of the non-fibrillar part.

**Fibrillar Part**: The fibillar component consisted of 2 primary and 24 secondary collagen fibrils at each integration point. The primary fibrils followed an arcade-like structure along the cartilage depth, with the fibrils perpendicular to the bone-cartilage interface at the deep zone and parallel to the cartilage surface in the superficial zone of cartilage. The split-line patterns of the collagen fibrils in the femoral and tibial cartilage were implemented by using in-house codes developed in Matlab R2022b (The MathWorks Inc., Natick, Massachusetts). The stress in each fibril consisted of an isotropic component $\boldsymbol{\sigma}_{\mathrm{iso}}$ that accounts for the isotropic stiffness of the collagen fibers and a stretch activated component $\boldsymbol{\sigma}_{\mathrm{f}}$ along the fibril direction. The isotropic component of stress was calculated using the same Neo-Hookean material model as used for the non-fibrillar part, with the shear modulus of collagen fibers incorporated $Gm_f$. The stretch-activated directional component of the stress was calculated assuming a spring (S1) in parallel to a spring (S2) and dashpot ($\eta$) in series. The equations for the fibril stresses are as described below:

$$\boldsymbol{\sigma}_{\mathrm{f\ iso}} = \sigma_{\mathrm{f}}(\vec{e_f}\vec{e_f}) + \boldsymbol{\sigma}_{\mathrm{iso}} \tag{3.4}$$

$$\sigma_{\mathrm{f}} = \frac{\lambda}{J}P_f \tag{3.5}$$

$$P_f = P_1 + P_2; P_1 = E_1(e^{K_1\epsilon_f}-1); P_2 = E_2(e^{K_2\epsilon_e}-1) = \eta\dot{\epsilon_v} \tag{3.6}$$

where, $P_f$ is the total fibril stress, $\vec{e_f}$ is unit vector along the current fibril direction, $\epsilon_f$ is the total fibril strain, $\epsilon_e$ is the strain in spring S2 and $\epsilon_v$ is the strain in the dashpot. $E_1$, $E_2$, $K_1$ and $K_2$ are material constants, $\lambda$ is elongation of the fibril. The density of each collagen fibrils is given by

$$\rho_c = \rho_{c,tot}\frac{C}{2C+24} \text{ for primary fibrils,} \rho_c = \rho_{c,tot}\frac{1}{2C+24} \text{ for secondary fibrils} \tag{3.7}$$

where, $C$ is a positive constant and $\rho_{c,tot}$ is the total collagen fiber density.

Table 3.1 lists the values of the material parameters that were used for the simulations.

| Material | Parameter | Magnitude |
|---|---|---|
| Cartilage | Shear modulus of the non-fibrillar matrix $G_m$ [MPa] | 0.9 |
| | Shear modulus of the collagen matrix $G_{mf}$ [MPa] | 0.9 |
| | Material constants: $E_1$, $E_2$ [MPa] | 4.316, 19.97 |
| | Material constants: $K_1$, $K_2$ | 16.85, 41.49, |
| | Viscosity of collagen fibril $\eta$ [MPa-s] | 1.424 x $10^5$ |
| | Permeability constant $\alpha$ [$m^4$/(N-s)] | 1.767 x $10^{-15}$ |
| | Nonlinearity term of permeability $M$ | 1.339 |
| Calcified Cartilage | Elastic Modulus [MPa] | 320 |
| | Poisson ratio | 0.3 |
| Subchondral Cortical Bone | Elastic Modulus [MPa] | 3900 |
| | Poisson ratio | 0.3 |
| Subchondral Trabecular Bone | Elastic Modulus [MPa] | 1091 |
| | Poisson ratio | 0.3 |
| Cruciate Ligaments(ACL,PCL) | Elastic Modulus [MPa] | 300 |
| | Poisson ratio | 0.45 |
| Menisci | Elastic Modulus [MPa] | 59 |
| | Poisson ratio | 0.479 |
| Agarose Hydrogel | Shear Modulii: $\mu_1, \mu_2$ [MPa] | 0.0461, -0.0368 |
| | Material constants: $\alpha_1, \alpha_2$ | 7.512, 6.23 |
| | Material constants: $\beta_1, \beta_2$ | -0.1204, -0.194 |

Table 3.1: Table to describe the material parameters of the tissues and hydrogel used in the study

## Boundary Conditions and Contact Interactions

Time-dependent translations, rotations and forces were implemented as boundary conditions to the femur to simulate the stance phase of the gait cycle. The magnitude of joint axial force was scaled by a factor of 0.77 from the original values obtained from [91] to account for patient specific body weight. The boundary conditions were applied to a reference point located at the center of the medial and lateral femoral epicondyles as shown in Figure 3.1(b). The tibia was fixed in all directions. The gait cycle was simulated in the FE model in two successive steps as discussed below:

### Initial step

Since the segmented geometry of the knee was at full extension, an initial step was performed to adjust the initial axial force and rotations (internal–external and extension–flexion) to match the values at 0% of the gait cycle. Translations

were maintained at their initial positions. The initial step was assigned a duration of 0.1 seconds.

**Gait cycle step**
In this step, femoral translations (anterior-posterior) and rotations (internal–external and extension–flexion) were applied as time-dependent boundary conditions at the reference point using the smooth step option in Abaqus. The varus-valgus rotation was kept free to ensure continuity of contact between the femoral and tibial cartilage throughout the entire stance phase of the gait cycle. Also, by comparing the resulting varus-valgus rotation from simulations with respect to experimentally observed values, the role of supporting tissues (ligaments) in governing the passive motion of the knee joint during the stance phase could be elucidated. The medial-lateral translation was fixed to prevent the menisci from sliding out and losing contact with tibial cartilage in absence of collateral ligaments, which could lead to errors in contact convergence. Axial force variation during the stance phase was applied as a concentrated force at the reference point. The duration of a single stance was set to 0.6 seconds [181].

**Contact definition**
The general contact algorithm with selected surface pairs was used in Abaqus to define contact between the femoral and tibial cartilage, and the menisci. Frictionless behavior was assumed for the contacting surfaces. For the normal behavior, the penalty contact constraint enforcement method was used. The penalty stiffness was scaled by a factor of five times the default value, to minimize the interpenetration between contacting surfaces of the femoral and tibial cartilage.

### 3.2.2 FE modeling of bioreactors for osteochondral plugs

#### Geometry and Meshing

Three dimensional (3D) geometries of cylindrical osteochondral plugs were created in Abaqus. A diameter of 8 mm was chosen for the plugs based on studies in literature [182, 183]. The osteochondral plugs consisted of cartilage (2 mm thick considering average human cartilage thickness), calcified cartilage (0.2 mm thick [184]) and 4 mm of subchondral bone underneath. The subchondral bone was further subdivided into subchondral cortical bone (0.36 mm thick) and subchondral trabecular bone (3.64 mm thick) [185]). To assess the role of individual tissues in the stress response of osteochondral plugs, three cases were simulated by progressively excluding specific tissues (Figure 3.2):
(a) All: In this case all the constituent tissues as described above were considered.
(b) No calcified cartilage (NoCC): The calcified cartilage was removed from the

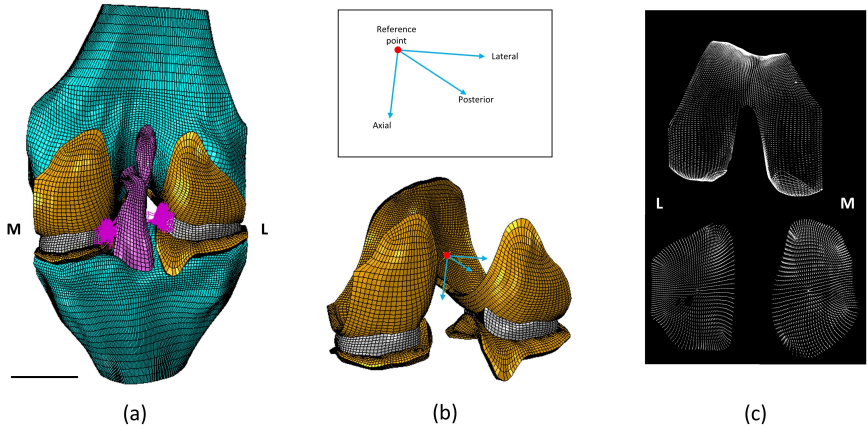


Figure 3.1: (a) FE model of the human knee joint with the different tissues and meniscal attachment springs (in pink), M-medial, L-lateral, Scale bar = 20 mm; (b) The reference point and the axes about which boundary conditions are applied for the FE model (ligaments and bones have been removed for visualization). In the inset box, a zoomed in view showing the reference point and axes with anatomical directions; (c) Orientation of the split-line patterns at the superficial zone as implemented in the FE model.

plugs, with all other tissues intact, to study the effect of calcified cartilage in load bearing.
(c) Only cartilage: This case consisted of only the cartilage of 2 mm thickness.

Cartilage was meshed with hexahedral pore pressure elements (C3D8P) while calcified cartilage and subchondral bone were meshed with hexahedral elements (C3D8). A mesh convergence study was performed to determine the final mesh density for the simulations (Supplementary Figure C.2)

### Constitutive model of tissues

Cartilage was modeled as a fibril-reinforced poroviscoelastic material as described in the previous section. Calcified cartilage, subchondral cortical and trabecular bone were modeled as linear elastic materials with material parameters obtained from literature [119], and mentioned in Table 3.1.

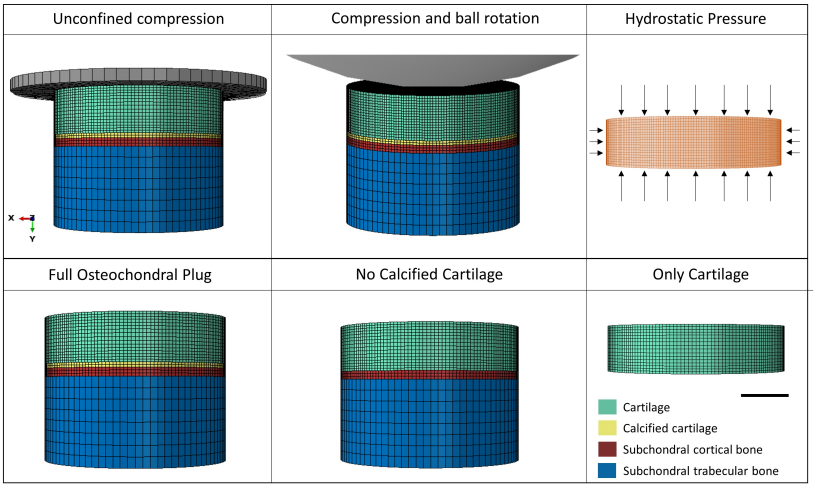


Figure 3.2: Top row: Different types of bioreactors used in the study. The first two from left show osteochondral plugs, while hydrostatic pressure was applied to only TE constructs. A portion of the ball is visualized in the compression and ball rotation case. Bottom row: FE models to study the role of different tissues in osteochondral plugs. Scale bar = 2 mm.

### Boundary Conditions and Contact Interactions

The osteochondral plugs were subject to mechanical loading in three different bioreactor setups that are commonly used in literature to apply unconfined compression, confined compression and combined compression and shear respectively. The boundary conditions that were applied to mimic mechanical loading in FE model of the bioreactors are described below (Figure 3.2) :

**(a) Dynamic unconfined uniaxial compression bioreactor:** This bioreactor is most commonly used in literature for its simplicity in design and ease of application of mechanical loading [52, 136]. Uniaxial dynamic compression was applied to the plugs in the FE model by using a rigid plate with a diameter of 12 mm. A haversine function with a frequency of 1 Hz and amplitudes of 10%, 20%, and 30% of the initial cartilage thickness was defined at the reference point of the rigid plate to impart dynamic compression to the plugs. The 1 Hz frequency closely resembles that of human gait. The loading amplitudes were selected to encompass the range of hypo to hyper-physiological loading regimes mentioned in literature [52, 186]. Vertical displacement of the the bottom surface of the plugs was constrained using the 'Ysymm' boundary

condition in Abaqus. Furthermore, to eliminate the possibility of any rigid rotations or translations of the plugs in lateral direction along the X-Z plane, two diametrically opposite nodes at the bottom surface of the plug were fixed in both the X and Z directions, respectively. This approach prevented rigid motions caused by numerical approximations without affecting the mechanics of uniaxial unconfined compression. To allow free fluid flow across the curved surface of the cartilage, a zero pore pressure boundary condition was prescribed at the nodes on that surface. A surface-to-surface contact was defined between the rigid plate and the top surface of cartilage with a 'hard' normal pressure-overclosure behavior. A friction coefficient of 0.003 [187] was applied between the contacting surfaces using the 'Lagrange Multiplier' friction formulation. For unaxial compression, all the 3 types of plugs were considered (all, no calcified cartilage and only cartilage) to do a comparative study of the contribution of different tissues to mechanical stress response. The corresponding tissues were rigidly attached to one another by using a 'Tie constraint'.

**(b) Dynamic multi-axial loading bioreactor:** Articular cartilage in the human knee joint is subject to a multi-axial state of loading during joint movements. To replicate this multi-axial loading in experimental settings, bioreactors were designed to apply a combination of shear and compressive forces to osteochondral plugs. One such bioreactor, as developed in studies from AO Davos, Switzerland [188, 189] used a commercially available ceramic hip ball (32 mm in diameter) to impart multi-axial loading. This was achieved by simultaneously applying axial compression through displacement and shear force by rotation of the ball about an axis perpendicular to the direction of axial compression. In the FE model of this setup, the ceramic ball was modeled as a rigid body due to its high stiffness as compared to cartilage. Four loading conditions were tested in this setup, with the boundary conditions applied to a reference point at the center of the ball: (1) 10% quasi-static compression for 10 seconds, (2) 10% quasi-static compression, followed by 10% dynamic loading at 1 Hz, (3) 10% quasi-static compression, followed by ±25 degree dynamic rotation at 1 Hz, (4) 10% quasi-static compression, followed by 10% dynamic loading and ±25 degree dynamic rotation at 1 Hz.
For the FE analysis of the three different types of bioreactors discussed above, dynamic loading was applied for five cycles. The results were then analyzed at the peak loading of the fifth cycle, by which the mechanical response of the cartilage had reached a steady-state.

### 3.2.3 FE modeling of bioreactors for cartilage tissue engineered constructs

#### Geometry and Meshing

The tissue-engineered (TE) constructs were modeled as discs of 8 mm diameter and 2 mm thickness. The diameter and thickness were kept consistent with those of the cartilage in osteochondral plugs to ensure dimensional conformity when comparing the simulation outcomes. The TE discs were meshed with hexahedral pore pressure elements (C3D8P). A mesh convergence study was performed to obtain the final mesh density as shown in Supplementary Figure C.3.

#### Constitutive model of TE construct

The TE constructs were assumed to be made of agarose, a hydrogel which is frequently used for cartilage TE in literature. Since agarose is known to behave as a compressible non-linear poroelastic material [190], a hyperfoam model with strain-dependent permeability was used to describe its nonlinear poroelastic behaviour as done in previous studies [191]. For the hyperfoam behavior, a modified Ogden-Hill strain energy potential (hyperfoam) available in Abaqus was used as given by the constitutive relation below:

$$W = \sum_{i=1}^{N} \frac{2\mu_i}{\alpha_i} \left[ \lambda_1^{\alpha_i} + \lambda_2^{\alpha_i} + \lambda_3^{\alpha_i} - 3 + \frac{1}{\beta_i} \left( J^{-\alpha_i \beta_i} - 1 \right) \right] \tag{3.8}$$

where $W$ is the strain energy density function and $\mu_i$, $\alpha_i$, and $\beta_i$ are material constants. $J$ is the determinant of the deformation gradient tensor and the principal stretches are given by $\lambda_1$, $\lambda_2$, $\lambda_3$. $N$ for agarose is $N = 2$.

Strain-dependent permeability for agarose was implemented as in Khoshgoftar et al. [191]:

$$k = k_0 \left( \frac{1 - n_{f,0}}{1 - n_f} \right)^M \tag{3.9}$$

where $k_0$ is the initial permeability, $M$ is a positive constant, and $n_{f,0}$ and $n_f$ are the initial and current fluid fractions respectively. Material parameters used for the simulations for 2% (w/v) agarose were derived from literature [191] and shown in Table 3.1. Hydraulic permeability parameters were $k_0 = 2.65 \times 10^{-12}$ ($\mathrm{m}^4$/N s) and $M = 4.1$ .

#### Boundary Conditions

The TE constructs were subject to mechanical loading in three different bioreactor setups that are commonly used in literature to apply unconfined compression, combined compression and shear, and hydrostatic pressure respectively. The boundary conditions applied to mimic mechanical loading for the first three cases were the same as those of the osteochondral plugs described in section 2.2 (boundary conditions **(a-b)**), with the only exception that the coefficient of friction between the compression plates (or rotating ball) and the TE construct was chosen to be 0.1 as derived from Geurds et al. [192].

**(c) Hydrostatic Pressure:** For knee articular cartilage *in vivo*, most of the compressive forces are transferred to hydrostatic pressure (HP) due to interstitial fluid pressurization, which acts as a primary load bearing mechanism in joints [193]. To harness this hydrostatic pressure to stimulate cartilage production in TE constructs, hydrostatic bioreactors have been used in literature imparting a wide range of loading magnitudes and frequencies [193–195]. In the present study, FE analysis of TE constructs subjected to static (0 Hz) and dynamic hydrostatic presure (at a frequency of 1 Hz) were performed. The loading magnitudes for hydrostatic pressure application were 0.5 MPa, 5 MPa, 10 MPa and 50 MPa, which were chosen to cover the wide range of magnitudes reported in literature [193]. The hydrostatic pressure was applied using a 'Pressure Load' in Abaqus.

### 3.2.4 Implementation

The development and analysis of FE models were performed using Abaqus. To implement the fibril reinforced poroviscoelastic model of cartilage, multiple user-defined subroutines in Fortran were used. In order to run simulations in parallel across multiple cores, the UMAT subroutines were made thread-safe by removing common blocks and UEXTERNALDB subroutines were developed to implement collagen fibril orientations. These improvements allowed simulations to be run in parallel, significantly reducing computation time. All simulations were performed on the wICE high-performance computing (HPC) cluster at the Flemish Supercomputing Center (VSC), KU Leuven. The cluster consists of 172 IceLake nodes, each equipped with two Intel Xeon Platinum 8360Y CPUs (2.4 GHz, 36 cores per CPU, 1 NUMA domain, and 1 L3 cache per CPU), 256 GiB RAM, and 960 GB SSD local disk. The default memory per core is 3400 MiB. Job submissions were managed via Slurm scripts.

## 3.3 Results

### 3.3.1 FE analysis of the human knee joint

The results of FE simulations of stance phase of gait in the human knee joint revealed that at the first peak loading (at 20% of the stance phase of gait), contact pressures were balanced between the medial and lateral compartments of the joint as observed in Figure 3.3. During the second peak loading (at 81.7% of the stance phase of gait), the contact pressures were higher on the lateral compartment of the tibial and femoral cartilage, suggesting a shift in load bearing towards the lateral compartment during the second peak loading of the gait cycle. This observation goes in line with previous observations in literature [91], where a gradual shift in load from the medial to the lateral compartment was observed as well. Similar trends were observed for maximum principal stress, pore pressure, pore fluid velocity and maximum shear strain as seen in Figures 3.3, 3.4. On further inspection across the thickness of the medial tibial and femoral cartilage at a cross-section taken at the contact region between the femoral and tibial cartilage in Figure 3.8, it was observed that highest values of maximum principal stress occurred at the superficial and middle zone of the cartilage, whereas highest values of maximum shear stress occurred at the surface of cartilage at the point of contact between the femoral and tibial cartilage. The varus-valgus rotations obtained from the simulations were within the range that was observed in experimental studies (Supplementary Figure A.7).

### 3.3.2 Role of calcified cartilage and subchondral bone in unconfined compression of osteochondral grafts

The removal of calcified cartilage from the osteochondral plug (noCC case) in simulations led to higher maximum principal stresses being transferred from the cartilage to the subchondral cortical bone for all three magnitudes of uniaxial compression (ranging from 10% to 30% strains) as compared to the intact osteochondral plug (all tissues present) (Figure 3.5). Additionally, there was an increase in the maximum principal stresses, pore fluid pressure, and fluid velocity around the cartilage circumference near the junction due to the absence of calcified cartilage. In the simulation of unconfined compression using only cartilage plugs, the lack of bone-cartilage interface resulted in a more uniform distribution of shear strains compared to the previous two cases. In the cartilage-only case, a spike in pore fluid velocity was observed at the top circumference of the cartilage, whereas, in the other two cases, the spike occurred in the cartilage

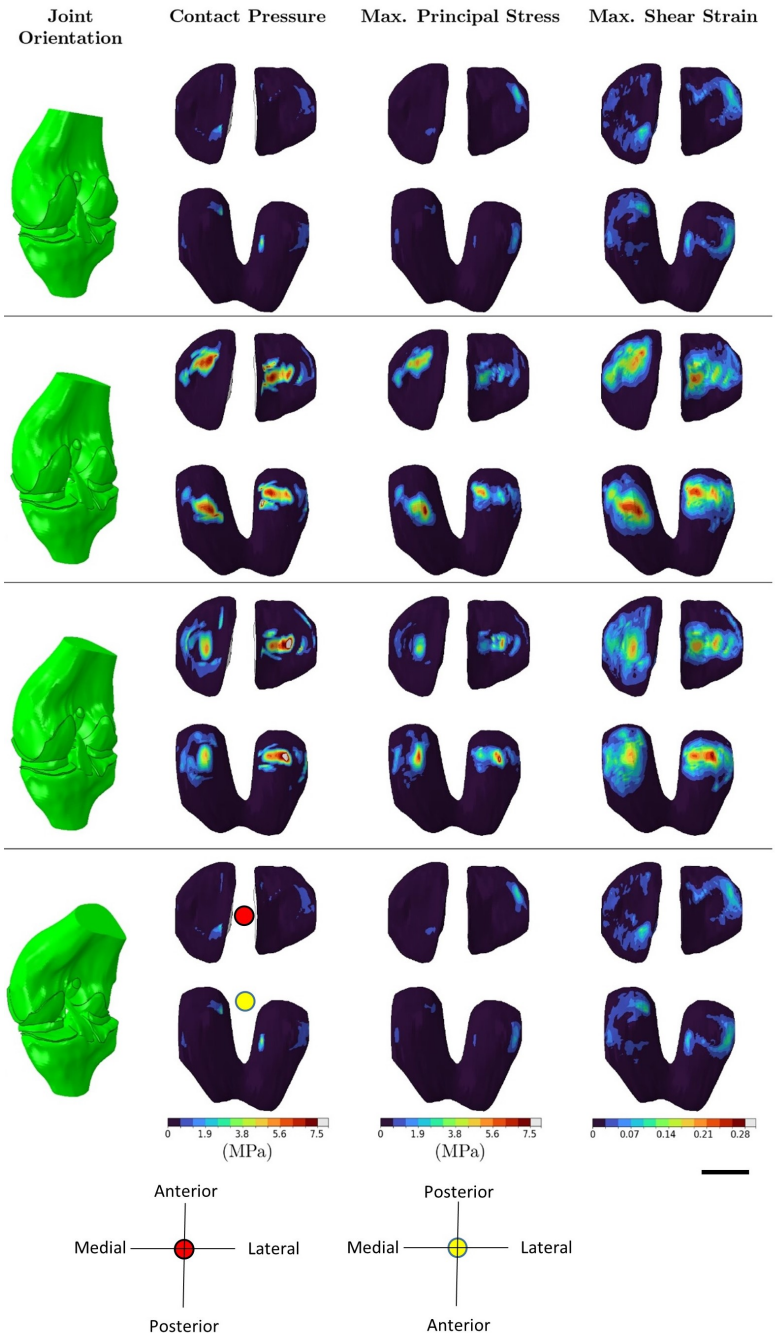


Figure 3.3: FE analysis of human knee joint during stance phase of gait showing results at fraction of stance 0, 0.2, 0.82, 1 starting from the top. Joint orientation is shown at the corresponding stance fraction. Red and yellow dots are used as indicators to show the relevant anatomical direction in context of the figures, where the tibial and femoral cartilage are displayed. Scale bar = 20 mm.

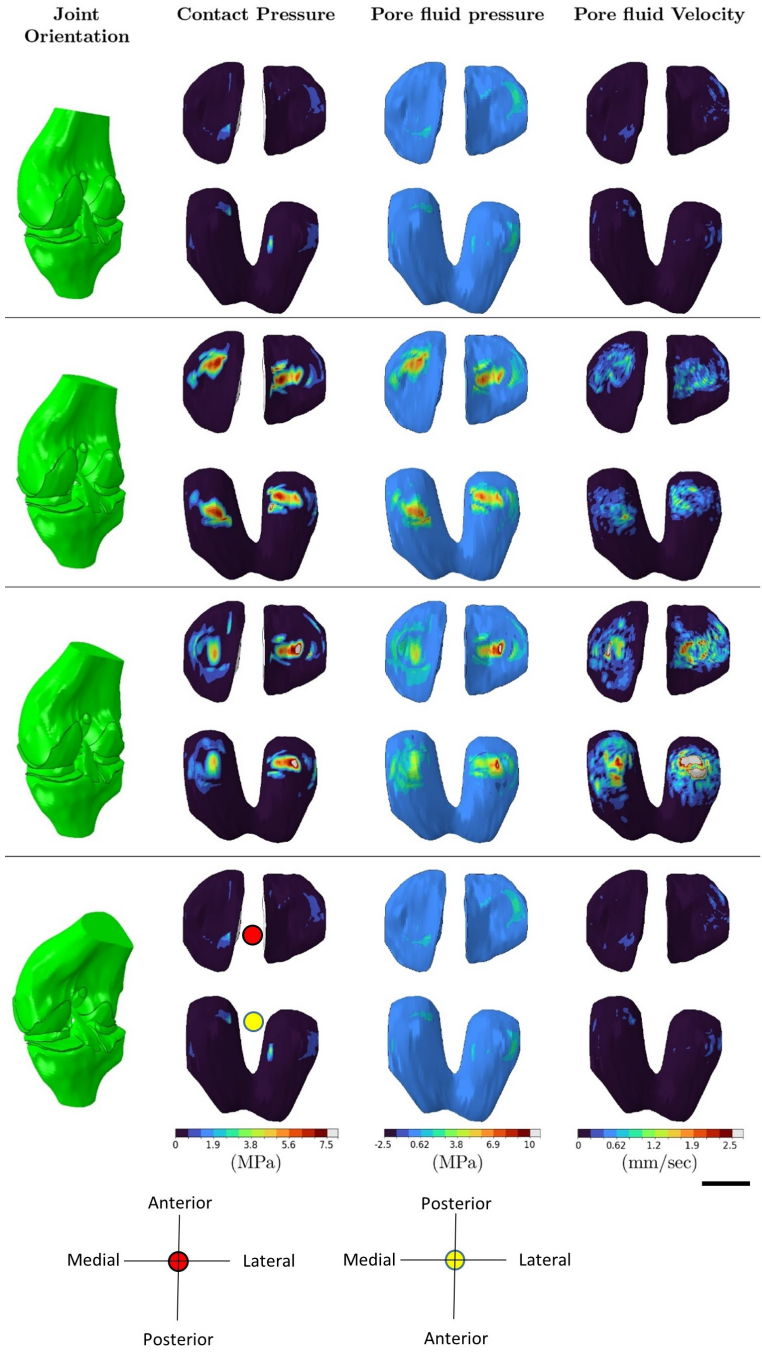


Figure 3.4: FE analysis of human knee joint during stance phase of gait showing results at fraction of stance 0, 0.2, 0.82, 1 starting from the top. Joint orientation is shown at the corresponding stance fraction. Red and yellow dots are used as indicators to show the relevant anatomical direction in context of the figures, where the tibial and femoral cartilage are displayed. Scale bar = 20 mm.

circumference at the cartilage-bone interface (Figure 3.6). The cartilage-only case also exhibited higher overall maximum principal strains, as there was no strain transfer to the underlying tissues. Overall values of pore pressure were consistently higher for the no CC case as compared to the OC plugs consistently across the 3 loading regimes.

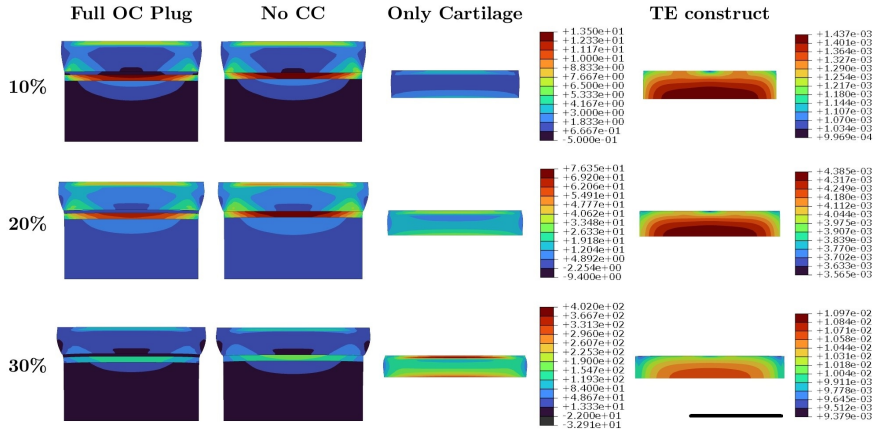


Figure 3.5: Distribution of maximum principal stress (in MPa) in different tissues of the OC plug and the TE construct for 10%, 20% and 30% strain applied in dynamic unconfined compression with 1Hz frequency. NoCC - No Calcified Cartilage. Scale bar = 5 mm.

### 3.3.3 Differences in mechanics between osteochondral plugs and TE Constructs in unconfined compression

For unconfined compression of OC plugs, the highest values of maximum principal stresses occurred in a region below the superficial zone (SZ) at the interface with the middle zone (MZ). This observation corresponds to studies in literature that report high strains and sub-surface delamination of cartilage at the SZ-MZ interface due to repetitive compressive forces [196–198]. On the contrary for TE construct, maximum principal stresses were highest at a central region near to the bottom Figure 3.5. Due to the higher permeability of the TE construct as compared to cartilage (by 3 orders of magnitude), fluid velocity was 1 order of magnitude higher and pore pressure 3-4 orders of magnitude lower (increasing order with increased strain from 10-30%) for the TE construct as compared to the native cartilage (Figure 3.6, Supplementary FigureA.2). The difference in pore fluid pressurization between the cartilage only plug and TE

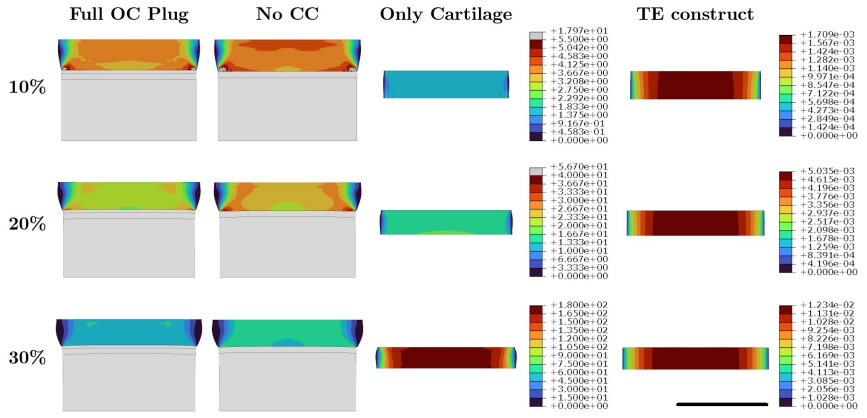


Figure 3.6: Distribution of pore fluid pressure (in MPa) in different tissues of the osteochondral (OC) plug and the tissue engineered (TE) construct for 10%, 20% and 30% strain applied in dynamic unconfined compression with 1Hz frequency. NoCC - No Calcified Cartilage. Scale bar = 5 mm.

construct also correlated with the 3-4 order of magnitude difference in maximum principal stresses, highlighting the important role of fluid pressurization in the load bearing capacity of cartilage as compared to the highly permeable agarose TE construct. Difference in shear stresses (both maximum and octahedral) were minimal between the cartilage plug and TE construct as seen in Supplementary Figure A.1.

### 3.3.4 Mechanical influence of combined dynamic compression and sliding rotation of ceramic ball

During compression of the specimens, the ceramic ball made contact with the central region of the specimen's top surface, leading to higher Maximum Principal Stresses in this region for both the OC plugs and TE constructs. Similar to unconfined compression in section 3.3, the highest maximum principal stresses in the cartilage were observed at the SZ-MZ interface. Pore fluid pressures were also highest at the central region of the specimens below the point of contact with the ceramic ball. Pore fluid velocity was highest at the edge of the contact between the ceramic ball and the top surface of the specimens (Supplementary Figure A.5). Since there was no pore fluid flow allowed at the contact surface between the non-permeable ceramic ball and the cartilage (or TE construct), the trapped pore fluid underneath the contact surface could only

flow out of the cartilage (or TE construct) surface at the edge of the contact surface where contact ends, leading to higher fluid velocities in this region. There was also a spike in pore fluid velocity observed around the circumference of the cartilage at cartilage-calcified cartilage interface, and similarly at the bottom circumference of the TE construct. This was because there was no fluid flow allowed between the cartilage-calcified interface or the bottom surface of the TE construct, leaving the circumference as the only region from where the fluid could flow radially out of the specimen. Due to the higher permeability of the TE construct as compared to cartilage (3 orders of magnitude), fluid velocity was 1 order of magnitude higher and pore pressure 3-4 orders of magnitude lower (increasing order with increased strain from 10-30%) for the TE construct as compared to the native cartilage, similar to what was described for unconfined compression in section 3.3.3.

The dynamic rotational motion of the ceramic ball had minor effects on the mechanics of cartilage across all the simulations of the osteochondral plugs as seen in Supplementary Figure A.3. Slightly higher effects in mechanics were seen for the TE construct as compared to the cartilage, due to the higher friction coefficient between the ceramic ball and agarose TE construct. As a result of the ball's rotation, an asymmetric distribution of maximum principal stress, pore fluid pressure and velocity was observed at the base of TE construct. The magnitudes of these three variables were higher in the leading direction of the ball's rotation as seen in Figure 3.7 and Supplementary Figure A.5. Maximum and octahedral shear strains were highest in the region below the contact with the ball for all specimens(Supplementary Figure A.4). The distribution and magnitude of the shear strains were not significantly altered due to the rotation of the ball for all the simulations.

### 3.3.5 Application of hydrostatic pressure elevates pore fluid pressurization

In previous sections, it was observed that due to the high permeability of the agarose TE construct, compression alone was not sufficient to generate pore fluid pressures comparable to those seen in native articular cartilage. Applying external hydrostatic pressure to the TE constructs resulted in pore fluid pressures equal to the applied pressure (ranging from 0.5 to 50 MPa) as seen in Figure A.6. However, dynamic hydrostatic pressure application produced much lower fluid flow velocities, on the order of $10^{-8} - 10^{-6}$ mm/s, compared to the higher fluid flow velocities observed during compression, which ranged from $10^{-3} - 10^{-2}$ mm/s.

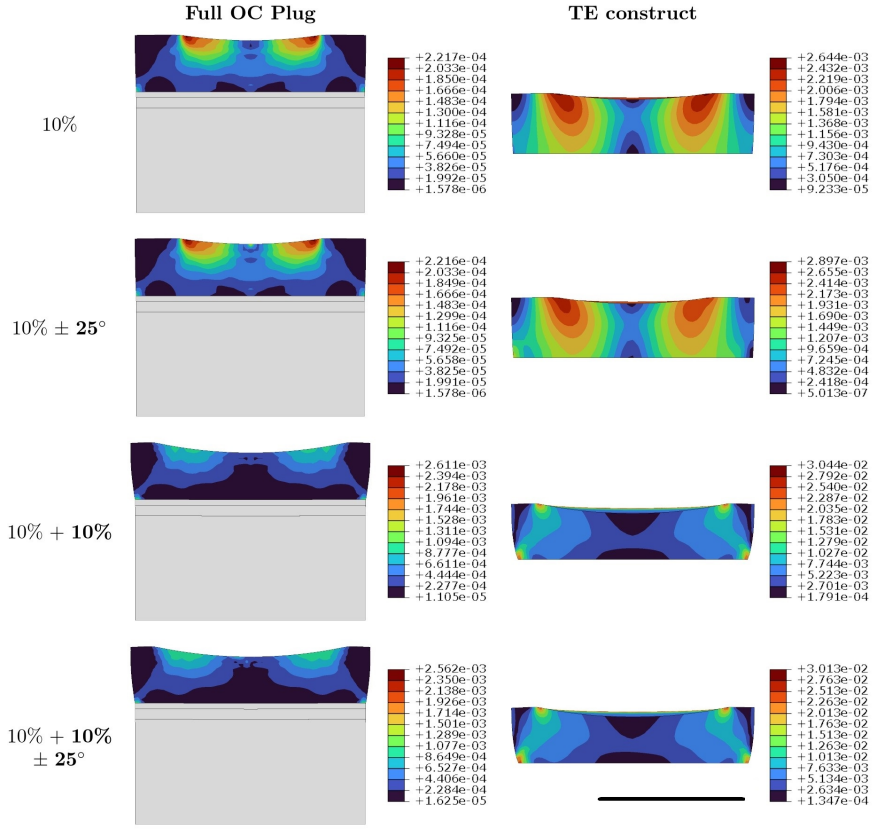


Figure 3.7: Distribution of pore fluid velocty (in mm/sec) in OC plug and the TE construct for 4 different conditions of applied compression with ball rotation. Values in bold in the first column represents a dynamic boundary condition with 1Hz frequency, while normal fonts are for quasi-static. Scale bar = 5 mm.

### 3.3.6 Comparative analysis of the most-physiological cases from each bioreactor type

The mechanical loading conditions for each type of bioreactor that mimics closest the mechanics of *in vivo* knee joint articular cartilage at the first peak loading of the stance phase of gait were selected for a comparative analysis as shown in Figure 3.8. For the comparison, 4 mechanical variables were chosen: maximum principal stress, maximum shear strain, pore fluid pressure and pore fluid velocity. The medial tibial and femoral cartilage at the first peak loading was considered for the comparative analysis since the maximum magnitudes of mechanical variables were observed in the medial compartment during the first peak loading, when the compressive joint forces were maximum.

**Unconfined compression of OC plugs:** For 10% unconfined compression of OC plugs, the maximum principal stresses had the same magnitude and distribution as the medial knee cartilage, with the highest values of stresses concentrated in the superficial zone in both the cases. Furthermore, there was a similarity in distribution of the stresses observed in the deep zone close to the cartilage-calcified cartilage interface. In a central region near to the interface, vertically under the area of contact of the articular surfaces and analogously at the central region of the cartilage in the OC plug, maximum principal stresses were low. This central region was surrounded on both sides by a region of high stresses. The high stresses were due to the constraints to displacements imposed by the rigid attachment of the cartilage with the underlying tissues of relatively high stiffness (calcified cartilage and bone for the OC plug and the knee joint respectively), thereby leading to stress buildup in that region.

The maximum shear strains also followed a gradient, with magnitudes decreasing relatively from the top surface to the deeper zones of cartilage for both the *in vivo* and *in vitro* conditions. The maximum shear strain distribution followed a more gradual gradient and was not concentrated in the superfical zone as was observed for maximum principal stress. This was because the maximum principal stress in the superficial zone primarily resulted from the stretching of the collagen fibers, which run parallel to the surface in this zone, and are modeled to resist tension. Contrarily, shear strains are modulated by the shear modulus of the proteoglycans in the cartilage matrix and follows a more gradual distribution across the thickness of the cartilage.

Pore pressure distribution for 10% unconfined compression of the OC plug was also similar to the physiological reference, with the pore pressures reaching towards zero for a region just outside the area of contact between the tibial and femoral cartilage in the knee and on the curved, free draining surface of cartilage in the OC plug. However, the magnitude of pore pressure was lower in

the cartilage of OC plug as compared to that in the knee cartilage. Pore fluid velocity was observed to be highest close to the cartilage surfaces in a region around the area of contacting cartilage in the knee. However, for the OC plug, the highest pore fluid velocities occurred through the curved surface from which free draining of the pore fluid could occur due to the applied zero pore pressure boundary condition.

**Dynamic compression and sliding motion applied to OC plugs:** Out of the four conditions of dynamic compression and ball rotation that were simulated in this study, a quasi-static compression of 10% followed by a 10% dynamic compression and simultaneous $\pm 25^\circ$ dynamic rotation of the ball was chosen for comparison with the knee articular cartilage. The values of all the 4 mechanical variables obtained from this bioreactor condition were higher in magnitude than the ones observed for knee cartilage. High maximum principal stress and pore fluid pressure distributions were observed at a region in the center of cartilage under the contact area of the ball with the cartilage, similar to the area underneath cartilage to cartilage contact in the knee joint. Highest values of maximum principal stress and maximum shear strain were located in the superficial zone. Pore fluid velocity in the OC plug followed similar distribution and magnitude, with highest magnitudes occurring towards the edge of the contact and close to the top surface, similar to the knee cartilage.

**Unconfined compression of TE constructs:** Due to lower stiffness of agarose used for the TE constructs, stresses were lower in the TE construct by 2 orders of magnitude, even when a high value of compression of 30% was chosen. Also, the maximum principal stress was uniformly distributed across the thickness of construct, contrary to compression of knee articular cartilage where higher stresses were observed in the superficial zone due to the effect of collagen fibrils, as discussed in the previous sections. The high value of compression (30%) led to significantly higher maximum principal strains (double that of cartilage), and also followed a uniform distribution. The fluid velocities observed were higher by 1 order of magnitude and the pore pressure lower by 2 orders of magnitude in the TE construct when compared to the corresponding knee cartilage. However, the distribution (rather than the magnitude) of these 2 physical variables showed resemblance to that of the corresponding variables for knee.

**Dynamic compression and sliding motion applied to TE constructs:** For this bioreactor type, a quasi-static compression of 10% followed by a 10% dynamic compression and simultaneous $\pm 25^\circ$ dynamic rotation of the ball applied to the TE construct was chosen for comparison with the knee articular cartilage. The maximum principal stresses were lower by 50% than that obtained for 30% of unconfined compression. The values of maximum shear strain close to the construct surface was significantly higher (around double) than that

observed for knee joint cartilage. Distribution of both maximum principal stress and maximum shear strain followed a gradient across the construct thickness with higher values closer to the contacting surface, similar to what is observed in knee articular cartilage. The magnitudes of pore fluid pressure and velocity followed similar trends as observed for the unconfined compression described above.

**Dynamic Hydrostatic pressure application to TE constructs:** The application of 5 MPa dynamic hydrostatic pressure produced a uniform distribution of pore pressure of 5 MPa in the TE construct, which resembled closely in magnitude to the pore pressuure obtained in the knee cartilage in the region under the contacting surfaces. This resemblance, due to the high permeability of the TE constructs, was very difficult to achieve with all the other bioreactor setups. However, magnitudes of all other variables were significantly lower when compared to the knee articular cartilage. This observation elucidates that applied dynamic hydrostatic pressure can mimic only the pore pressure environment of the physiological reference (knee cartilage) in the TE constructs, which was very difficult to achieve with all the other bioreactor setups due to the high permeability of the TE constructs.

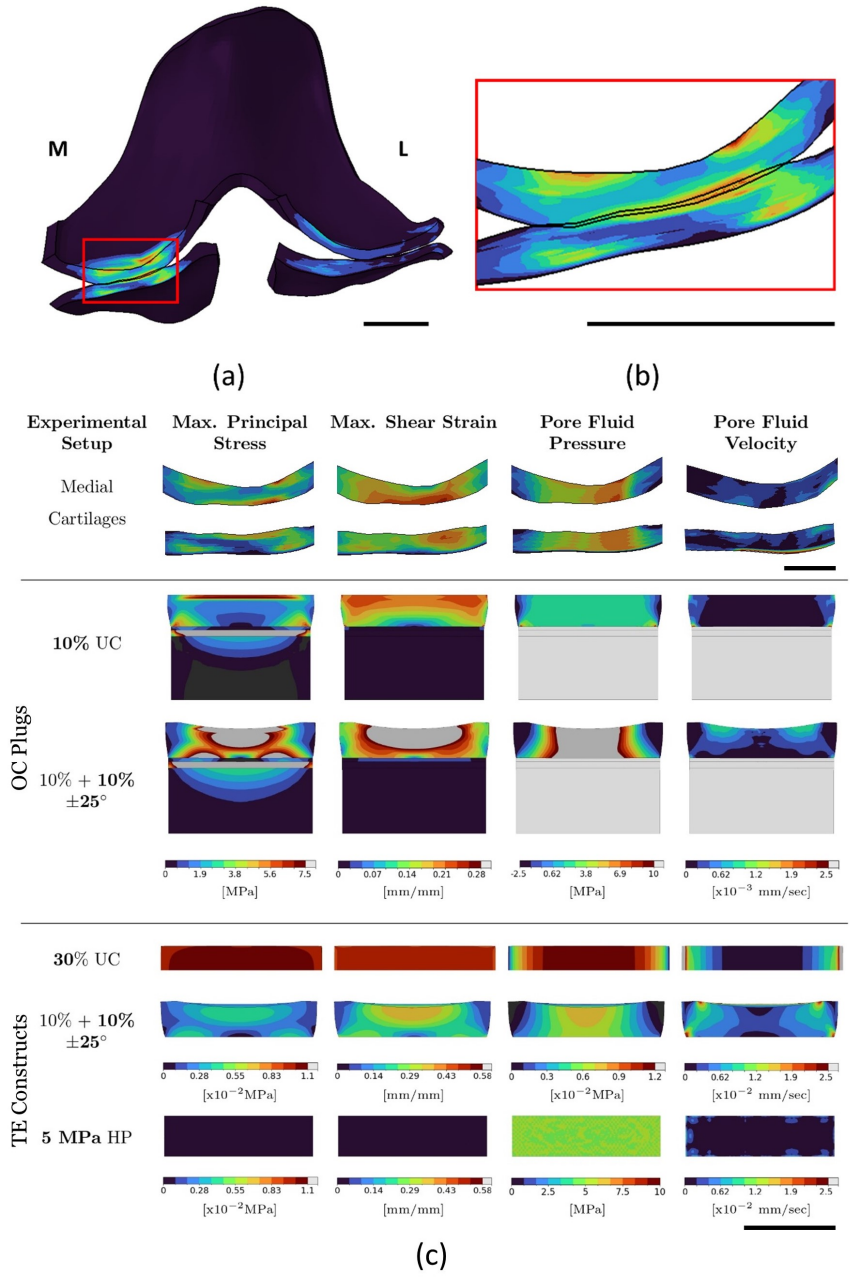


Figure 3.8: (a) Cut section of the knee joint at the first peak loading, the red box shows region of medial cartilage under contact, for which results were analyzed, Scale bar = 10 mm; (b) Zoomed in view of the contact region in (a), Scale bar = 10 mm; (c) Comparison of physical variables between the different conditions of mechanical loading of OC plugs and TE constructs with the medial cartilage region selected as in (a),(b). UC- Unconfined Compression, HP- Hydrostatic Pressure, applied at a frequency 1 Hz. Scale bar = 5 mm.

## 3.4 Discussion

In this study, a comparative analysis was performed between widely used bioreactor setups designed to apply mechanical stimulus to osteochodnral explants or cartilage TE constructs. The study involved comparing the finite element (FE) analysis of different mechanical loading protocols in these bioreactor setups with an FE model of the human knee joint developed within the study. While there exist studies in literature which separately look at mechanics in individual bioreactor setups [172, 174, 175, 199], the current study makes a unique and significant contribution to the field by comparing the different bioreactors with an *in vivo* scenario of the stance phase in human knee joint, thereby quantifying which mechanical loading scenario in the different bioreactor setups corresponds closest to the physiological reference.

The analysis across several bioreactors revealed that there is no single bioreactor or culture condition that successfully mimics all the mechanical variables both in terms of magnitude and distribution. However, the results of this study can help experimentalists make an informed choice about a bioreactor and a corresponding loading condition, depending on the research question. For example, while a 10% unconfined compression of cartilage explant could mimic maximum principal and shear stresses and pore pressures, the distribution of pore fluid velocities were dissimilar between the cartilage in the knee joint and the osteochondral plug. For TE constructs, the maximum principal stresses and pore pressures during unconfined compression (upto 30%) were lower by two to three orders of magnitude as compared to knee cartilage. A hydrostatic pressure of 5 MPa was able to mimic similar pore pressures in the TE construct and knee cartilage. However, the corresponding strains in the TE constructs were much lower than that in knee cartilage.

For the verification of the FE models developed in this study, mesh convergence analyses were conducted, which are reported in Appendix C. For validation of the results FE analysis of the knee joint, the varus-valgus rotations obtained from the simulations were compared with the corresponding values observed in literature (Supplementary Figure A.7). For the other bioreactor setups, there were no experimental data available to validate each of the loading conditions tested. However, the mechanical behavior of the materials were sourced from literature, where the material parameters were calibrated from experimental data.

An FE model of the human knee joint was developed in this study using the geometry from the open source project OpenKnee [176] and employing a realistic material description of the articular cartilage including collagen fibril orientation and depth-wise variation of proteoglycan, collagen and fluid content

[18]. To simulate the stance phase of the gait cycle, kinetic and kinematic boundary conditions were applied, derived from previously published data [91]. While similar material models had been implemented for human knee joint simulations in previous studies, a key innovation in this work was the ability to run simulations in parallel across multiple cores. This was achieved by optimizing existing UMAT subroutines to be thread-safe, removing common blocks, and using UEXTERNALDB subroutines to implement collagen fibril orientation in the Abaqus workflow. These improvements allowed simulations to be run in parallel, significantly reducing computation time.

For the OC plugs simulated in the study, the choice of 8 mm diameter was based on the fact that the area of contact between the knee cartilage surfaces during the first peak loading of the gait cycle had a diameter ranging from 6 to 10 mm, assuming a circular contact area. *In vivo*, the region adjacent to the cartilage-to-cartilage contact was surrounded by native cartilage, which resisted lateral deformations and free fluid flow. In contrast, the free lateral surface of the OC graft allowed fluid to drain freely from the sides and permitted unconstrained lateral bulging of the cartilage when compression was applied. As a result, during unconfined compression of the plugs, higher fluid velocities were observed from the lateral surface of the cartilage. This 'edge effect' could have led to the loss of matrix constituents from the lateral surface due to fluid flow as observed in some *in vitro* studies [52], especially since harvesting of the plugs by drilling it from the joints would have already caused damage to edges of the OC plug. The highest values of maximal principal stresses during unconfined compression of OC plugs were observed just below the superficial zone (SZ), at the interface with the middle zone (MZ). This aligns with previous studies reporting high strain concentrations and subsurface cartilage delamination at the SZ-MZ interface due to repetitive compressive loading [196–198]. For the combined compression and ball rotation simulations, though the effect of ball rotation on cartilage mechanics was negligible, it was still considered for the comparative study since ball rotation mimics the sliding motion between the knee articular cartilage during gait, which is known to trigger lubricin production in the superficial zone of cartilage. Lubricin is responsible for maintaining the low friction coefficients of cartilage [188].

This study also elucidated the importance of calcified cartilage layer in firstly, reducing stress transfer to the underlying subchondral bone during compression and secondly, acting as an intermediate layer between bone and cartilage to reduce interfacial stresses in cartilage. Calcified cartilage in the study was modeled as a linear elastic material, since permeability of calcified cartilage is not well-defined experimentally. Some studies in the literature have characterized it as entirely impermeable, while others have reported its permeability to be lower or comparable to that of articular cartilage [200]. In

future studies, experimentally determined permeability of calcified cartilage should be incorporated into the poroelastic FE analysis of OC grafts to simulate fluid (and thereby molecular) cross-talk between the cartilage and bone through the calcified cartilage. This cross-talk is expected to influence and potentially alter the progression of cartilage degeneration in osteoarthritis [6].

The FE analysis of mechanical stimulation of agarose TE constructs in different bioreactors highlighted that lower maximum principal stresses were developed in the constructs due to the relatively compliant behavior of hydrogel as compared to articular cartilage. Furthermore, the TE constructs were homogeneous without any anisotropy, which resulted in a more uniform distribution of stresses as compared to cartilage where the anisotropy of collagen fibrils led to higher stresses in the superficial zone. The FE analysis also revealed that TE constructs developed lower pore pressures and higher pore fluid velocities for the same magnitudes of mechanical loading as compared to cartilage. The lower pore pressure meant lower load bearing capacity of the construct, which would restrict its application when implanted *in vivo* in a cartilage defect. High pore fluid velocities can have a two-fold effect. On the one hand, it might facilitate better distribution of the nutrient rich medium throughout the construct, thereby favoring cartilage regeneration [201]. On the other hand, high fluid flows might disrupt the nascent matrix secreted by the embedded cells in the hydrogel, thereby leading to matrix loss and weakening of the construct. This was supported by a study by Orozco et al. [202], which demonstrated that initiation of loss in the fixed charge density of proteoglycans in native cartilage occurs at a fluid velocity threshold of 0.03 mm/sec, while complete breakdown of the proteoglycans was assumed to occur at a velocity of 1 mm/sec.

In the OC plugs, the cartilage was attached rigidly to the underlying calcified cartilage and subchondral bone. This constraint resulted in stress concentration at the interfacial region for cartilage. However, for the unconfined compression of TE constructs, the bottom of the construct was unconstrained only in the vertical direction, which led to free lateral spreading of the construct, thereby altering the deformation field as compared to native cartilage. To prevent this from happening, and also to reduce fluid flow from the lateral sides of the construct, partial confinement of half the thickness of the construct from the bottom had been suggested in a previous study in literature by Thorpe et al. [203]. Furthermore, restrictions imposed by the partial confinement on fluid flow and lateral deformations would result in higher pore pressures and also would create a gradient of the mechanical environment that would more closely mimic the *in vivo* mechanics of cartilage.

In the present study, dynamic hydrostatic pressure was the only condition that could effectively mimic pore pressures in the TE construct similar to those in articular cartilage *in vivo*. However, it is important to note that literature

suggests that the regulation of cartilage matrix synthesis in these TE constructs, due to hydrostatic pressure, depends not only on the magnitude of the applied pressure but also on the interactions between the cells and the matrix (hydrogel, in this case). For example, the study by [204] found that a fibrin hydrogel promoted greater accumulation of glycosaminoglycans compared to an agarose hydrogel when mesenchymal stem cells embedded in the gels were subjected to the same hydrostatic pressure protocols. The difference in cell attachment to the hydrogel likely led to distinct mechanotransduction pathways being activated, which may explain this discrepancy. However, long-term culture in agarose hydrogels showed hydrostatic pressure to be favorable for cartilage regeneration [205]. These complex interactions are not accounted for in the present finite element (FE) analysis, and it is important to be aware of these complexities when selecting loading protocols for a bioreactor setup.

This study successfully compares various bioreactor setups with a generic knee joint model. It is also important to note that the FE model of the human knee joint in this thesis was developed using geometry, material properties, and gait cycle data from different literature sources rather than a single patient. The knee joint model in this context was meant to provide a quantitative basis of comparison of what constitutes the physiological mechanical environment of the joint articular cartilage. Importantly, while the knee joint model was based on generalized assumptions and hence not patient-specific, these choices did not undermine the validity of the conclusions. Rather, they allowed for a robust analysis that could still offer meaningful insights into mechanics of knee cartilage and compare it with bioreactor performance across different loading conditions. This ensured that the results remained broadly applicable and relevant for future research applications. The medial collateral ligaments were excluded from the study due to insufficient data from the geometry, which might explain the higher loads in the lateral cartilage as compared to the medial part. However the varus-valgus rotations which were obtained as outcome of the simulations were within the range measured in previous experiments [206] (Supplementary Figure A.7). The contact behavior between opposing cartilage surfaces was assumed to be frictionless, since the friction coefficients are very low (in the order of 0.001) for intact cartilage. It is known for cartilage and hydrogels (which are both porous solids), that friction coefficients are inversely related to the interstitial fluid pressurization [207]. Such load varying friction behavior might be implemented in future studies for more realistic model predictions.

Finally, in the current study, mechanics of articular cartilage and TE constructs were studied at the macro-scale, tissue-level resolution. This approach provided valuable insights into the distribution of physical variables across different setups and under varying loading conditions. However, the present study did not consider any cell-matrix interactions, which is known to influence behavior

of cells to mechanical stimuli [208]. In the future, efforts must be made to develop multiscale models, that links the tissue-level mechanics (as done in this study) with micro-scale cellular mechanics, and subsequently the intracellular mechanotransduction processes that are triggered as a result of mechanical stimuli sensed by individual cells which are located at different regions of the cartilage or TE construct. Such a multiscale modeling framework would provide more granularity while quantifying loading protocols across different bioreactor setups to facilitate tissue regeneration.

To conclude, this study provides a robust framework for comparing bioreactor loading conditions with *in vivo* joint mechanics, offering valuable insights for optimizing cartilage tissue engineering strategies. By bridging the gap between experimental and physiological conditions, the findings will contribute to improving bioreactor design, enhancing regenerative medicine approaches, and advancing treatments for cartilage repair.

# Chapter 4

# A multiscale modeling approach to study the role of mechanics and inflammation in pathophysiology of articular cartilage

Satanik Mukherjee[1], Raphaelle Lesage[1], Liesbet Geris[1,2,3]

[1]Biomechanics Section, KU Leuven, Belgium
[2]GIGA Institute, University of Liege, Belgium
[3]Skeletal Biology and Engineering Research Center, KU Leuven, Belgium

This chapter is based on a manuscript prepared to be submitted: S. Mukherjee, R. Lesage and L. Geris. "A multiscale modeling approach to study the role of mechanics and inflammation in pathophysiology of articular cartilage."

## 4.1 Introduction

Mechanical loading is a critical factor that regulates the health of chondrocytes, the primary cells residing in articular cartilage. While physiological mechanical cues are essential for chondrocyte homeostasis, supra-physiological mechanical cues, such as those occurring during joint traumatic injuries, can disrupt stable cartilage homeostasis, leading to catabolic processes that contribute to osteoarthritis (OA) [166]. OA is the most prevalent degenerative joint disorder, affecting over 595 million people globally [209]. With a global prevalence of 23%, OA most commonly occurs in the knee joint [210]. Knee OA (KOA) is a leading cause of disability among older individuals, contributing to a significant socioeconomic burden that accounts for 1-2.5% of the annual gross national product and results in a loss of 15 million Quality-Adjusted Life Years annually. As populations age and obesity rates increase, the prevalence of OA is expected to rise in the future and is projected to reach 1 billion people by 2050 [209].

Understanding the mechanobiology of chondrocytes not only helps in identifying factors that contribute to cartilage degeneration in OA but also provides insights into how mechanical cues can be used to stimulate chondrocytes for cartilage regeneration in tissue engineering applications. Mechanical signal transduction in cartilage is inherently a multiscale process. Mechanical loads experienced by the joints during daily activities, propagate from the tissue to the cells, specifically the chondrocytes. Chondrocytes are capable of sensing mechanical stimuli through mechanosensitive receptors like integrins and ion channels such as TRPV4 and Piezo 1/2 [211–213], which initiate a cascade of intracellular biochemical processes via mechanotransduction pathways. The effect of mechanical loads on cartilage matrix biosynthesis or degradation during OA likely stems from intracellular biochemical changes at the chondrocyte level. Indeed, matrix and collagen network damage is typically first observed around the cells in the pericellular region, before progressively extending into the extracellular matrix (ECM) [214].

In addition to being mechanosensitive, chondrocytes can also respond to biochemical pro-inflammatory cues. Unlike rheumatoid arthritis, OA is generally characterized by low-grade synovitis, and is not typically considered an inflammatory disease [215, 216]. However, the molecular pathways that transduce signals from pro-inflammatory cytokines (e.g., IL-1$\beta$, TNF-$\alpha$) play a crucial role in regulating chondrocyte function. Multiple studies have shown their involvement in the onset and progression of cartilage degradation during OA [217, 218]. Moreover, mechanoregulatory and inflammatory signals are strongly interconnected in cartilage. Experimental evidence supports the existence of a threshold below which increased loading magnitude can reduce the cytokine-induced inflammatory response. Conversely, beyond this threshold, a further

increase in loading exacerbates the inflammatory pathways [146]. This threshold effect also resonates with the relationship between mechanical loading and cartilage degradation [52].

Gaining a comprehensive understanding of the intricate regulatory interactions between biomechanical and inflammatory signals is essential for deciphering OA mechanisms and proposing therapeutic interventions, including mechanical adjustments and selective pharmacological targeting. However, studying the complex interplay between mechanical and biochemical factors in cartilage is challenging to achieve solely through *in vivo* or *in vitro* experiments, given the limitations in precisely controlling and isolating these multiscale and multifactorial processes. *In silico* models, on the other hand, offer a powerful tool to integrate these diverse mechanisms, enabling a deeper understanding of how mechanical and inflammatory cues interact to regulate chondrocyte behavior and cartilage homeostasis.

Therefore, modeling the impact of mechanical loading on local intracellular reactions and cellular metabolism, and linking these processes to the ECM or cartilage mechanical properties, could help unravel the underlying mechanisms. This challenging task requires the integration of cell regulatory networks into tissue mechanical models across multiple length scales [219]. Previous models of chondrocyte mechanotransduction or multiscale cartilage models were often linear, deterministic, or phenomenological regarding the intracellular component [79, 146] and/or lacked detailed cell regulatory networks [202].

The present study aims to develop an integrated multiscale modeling workflow by combining a multiscale finite element (FE) model of articular cartilage with a mechanistic chondrocyte intracellular module. The intracellular module aims to capture relevant mechanisms for studying the interplay between mechano-regulatory and inflammatory pathways and their influence on chondrocyte phenotypic changes. Investigating this crosstalk was necessary for further understanding how mechanical loading influenced cartilage tissue. This study is organized as follows: firstly, the different length scales involved in the multiscale model are described with explanations on connecting the length scales and a brief description of the biological mechanisms integrated into the intracellular regulatory networks. Then, calibration and validation of the multiscale model are presented, that were performed to ensure model credibility. Lastly, as an application of the multiscale modeling workflow, the pathophysiology of the human knee joint due to meniscectomy is studied using a multiscale model of the human knee joint.

## 4.2 Materials and Methods

### 4.2.1 General workflow of the multiscale modeling approach

The general multiscale modeling framework developed in this study consisted of three different *in silico* models encompassing three length scales respectively as shown in Figure 4.1. The models were mechanically coupled with each other using a post-processing approach, such that the outputs from a larger scale were used as inputs to drive a smaller scale model. The general overview of models are described below in descending order of length scales.

#### Organ and tissue scale

The largest length scale of the multiscale model workflow comprises of the organ and tissue scale. Organ is a general term used in the workflow to refer to either a human joint (such as the knee joint) or an *in vitro* setup that mimics the physiological mechanical loading in a joint. The tissue scale focuses on articular cartilage, which is the primary tissue of interest in this study.

In this scale, FE models were developed for: i) a uniaxial dynamic compression bioreactor with a cartilage explant, and ii) a human knee joint with tibial and femoral cartilage. The geometry and boundary conditions used in these two FE models were described in detail in Sections 4.2.2 and 4.2.3, respectively. Articular cartilage was modeled as a fibril-reinforced poroviscoelastic (FRPVE) material, as described in previous studies [178, 179]. A detailed implementation of the constitutive model was provided in Chapter 3 of the thesis. Briefly, this biphasic material model consisted of a solid and a pore-fluid component, with the solid component further divided into fibrillar and non-fibrillar parts. The fibrillar component consisted of two primary and 24 secondary classes collagen fibrils at each integration point. The primary fibrils followed an arcade-like structure along the cartilage depth, with fibrils perpendicular to the bone-cartilage interface in the deep zone and parallel to the cartilage surface in the superficial zone. The non-fibrillar part of the cartilage, which primarily consists of proteoglycans, was modeled using a modified Neo-Hookean law, as described in [180]. The total stress at an integration point was given by:

$$\boldsymbol{\sigma}_{\mathrm{tot}} = \frac{n_{s,0}}{J}\left[\left(1-\sum_{i=1}^{\mathrm{totf}}\rho_c^i\right)\boldsymbol{\sigma}_{\mathrm{nf}}+\sum_{i=1}^{\mathrm{totf}}\rho_c^i\boldsymbol{\sigma}_{\mathrm{f\ iso}}^i\right]-p\mathbf{I} \tag{4.1}$$

where $\mathbf{I}$ is the unit tensor, $n_{s,0}$ is initial solid volume fraction, $J$ is the determinant of the deformation tensor $\mathbf{F}$, totf is the total number of fibrils

considered at each integration point, $\rho_c^i$ is the volume fraction of the $i^{th}$ collagen fibrils with respect to the total volume of the solid matrix, $\boldsymbol{\sigma}_{\mathrm{nf}}$ is the stress in the non-fibrillar matrix, $\boldsymbol{\sigma}_{\mathrm{f\ iso}}$ is the stress in the collagen fiber network. The material model was implemented using the UMAT subroutine in Abaqus 2023 (SIMULIA, Providence, RI, USA)

Table 4.1 lists the values of the material parameters that were used for the simulations.

| **Parameter** | **Cartilage/ECM** | **PCM** | **Chondrocyte** |
|---|---|---|---|
| Shear modulus of the non-fibrillar matrix $G_m$ [MPa] | 0.9 | 0.9 | 0.017 |
| Shear modulus of the collagen matrix $G_{mf}$ [MPa] | 0.9 | 0.9 | - |
| Material constants: $E_1$, $E_2$ [MPa] | 4.316, 19.97 | 0.4316, 1.997 | - |
| Material constants: $K_1$, $K_2$ | 16.85, 41.49 | 16.85, 41.49 | - |
| Viscosity of collagen fibril $\eta$ [MPa-s] | 1.424 x $10^5$ | 1.424 x $10^5$ | - |
| Permeability constant $\alpha$ [$m^4$/(N-s)] | 1.767 x $10^{-15}$ | 1.767 x $10^{-15}$ | 2.6 x $10^{-10}$ |
| Nonlinearity term of permeability M | 1.339 | 1.339 | - |

Table 4.1: Material parameters of the cartilage, extracellular matrix (ECM), pericellular matrix (PCM) and the chondrocyte used in this study(obtained from [220])

### Connecting tissue scale to cellular scale

To mechanically couple the tissue scale model with the cellular scale model, a node-based submodeling technique was utilized in Abaqus. Given the biphasic material behavior of cartilage, the global displacements and pore pressure obtained from the tissue scale model simulation were applied as boundary conditions to drive the cellular sub-model. This post-processing method for connecting length scales enables simulations of cellular scale models at various locations within the tissue scale model.

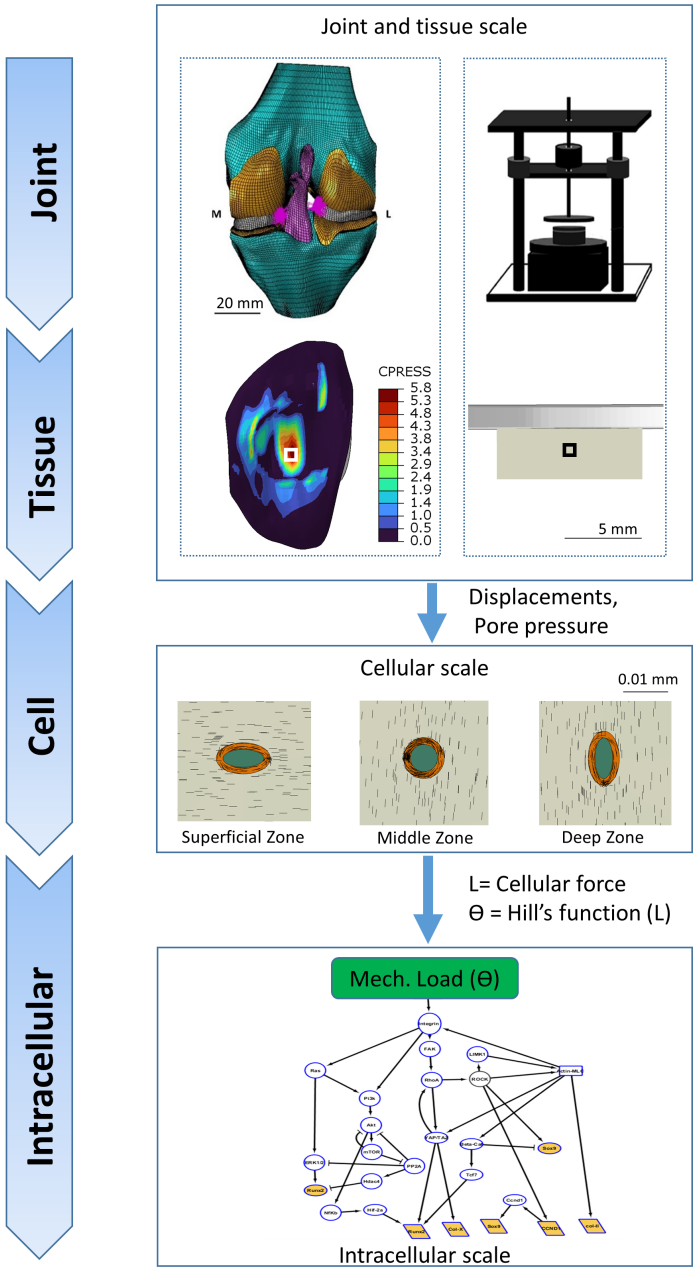


Figure 4.1: Overview of the multiscale model workflow showing the different length scales involved for a human knee joint and an *in vitro* setup for cartilage compression. The white box in the tissue scale for both the knee and the cylindrical cartilage construct indicates the location of the chondrocyte used in the calculation of the results shown in this study. Red arrows in the cellular scale denotes the fibril orientations in the different zones. The density of fibrils in the figure is reduced from actual implementation for better visualization.$\theta$=Mechanical loading input to networks, L=Cellular force from FE model.

### Cellular scale

The cellular scale was modeled as a cube of edge length 100 $\mu$m, consisting of a chondrocyte (predominant cell in articular cartilage) at its centroid, surrounded by its pericellular matrix (PCM) and extracellular matrix (ECM). To approximately satisfy mechanical consistency across spatial scales, the following considerations were made: firstly, the extracellular matrix (ECM), which comprised 99.9% of the total volume of the cube, was assigned identical properties to those of the articular cartilage in the tissue-scale model. This choice was made to maintain consistency in the material properties between the ECM and the cartilage at the macroscale level. Secondly, the choice of a 100 $\mu$m representative volume element (RVE) for the cube was based on previous studies in the literature [140, 141, 221]. This size was selected to ensure that the inclusion of the cell and pericellular matrix (PCM) does not significantly alter the deformation field at the boundaries of the cube.

The 2.5 $\mu$m thick PCM layer was modeled as a FRPVE material, with the 2 primary collagen fibrils oriented tangentially to the cell surface [222, 223] as shown if Figure 4.1. Since the diameter of type VI collagen fibers, predominantly present in the PCM is less than that of type II collagen predominantly found in the ECM [224], the collagen fibril stiffness in the PCM was assumed to be 10% as that in the ECM [142, 220].

The chondrocyte itself was modeled as a homogeneous, poro-hyperelastic solid using the same modified neo-Hookean material model as used to describe the mechanical behavior of non-fibrillar matrix of cartilage (section 4.2.1). The anatomical variation in chondrocyte shape, based on its location across the thickness of articular cartilage, was incorporated in the model. In the superficial zone, the chondrocyte was modeled as an ellipsoid with its major axis parallel to the cartilage surface, while in the deep zone, the chondrocyte was ellipsoid with its major axis perpendicular to the bone-cartilage interface [225, 226]. For the ellipsoidal chondrocytes the major and minor diameter was 15 $\mu$m and 6.5 $\mu$m respectively. In the middle zone, the chondrocyte was spherical with a diameter of 10 $\mu$m. The ECM, PCM and chondrocyte were connected to each other using the tie constraint in Abaqus, which ensured continuity of displacements and pore pressures across the ECM-PCM and ECM-cell interfaces. A mesh convergence study was performed for the cellular scale model as shown in Supplementary Figure C.4

### Connecting cellular scale to intracellular scale

In the FE model at the cellular scale, the total force (L) transmitted to the cell via the PCM was determined by summing the magnitude of forces acting on the nodes of the cell that were connected to the PCM using the tie constraint. However, the total force obtained could not directly be applied as the mechanical load input to the intracellular regulatory network in the multiscale modeling workflow. This was because the regulatory network is semi-quantitative in nature (with activity of each biomolecule representing a node in the network ranging from 0-1), whereas the cellular force calculated in FE model was purely quantitative in nature (measured in newtons). To translate the cellular forces (L) from the FE model to a mechanical loading input ($\Theta$) to the intracellular network, a Hill's function was chosen as shown below:

$$\Theta = \Theta_0 + \frac{(1 - \Theta_0)}{1 + \left(\frac{K_a}{[L]}\right)^n} \tag{4.2}$$

$\Theta_0$ represents the basal level of mechanical load sensed by the chondrocyte which is the mechanical load in the absence of any external mechanical stimulus. Since chondrocytes can detect extracellular matrix stiffness through focal adhesions via integrins [227], this basal load was assumed to be 0.1. L is the total force acting on the cell in the FE model, $K_a$ and n are constants for the Hill's function. Physically, $K_a$ represents the magnitude of cellular force L, at which the mechanical loading input $\Theta$ is halfway between its basal value ($\Theta_0 = 0.1$) and its maximum possible value (which is 1). $K_a$ indicates the sensitivity of the cellular mechanosensors (primarily the integrins, as will be discussed in following section) to the mechanical force. A lower $K_a$ means the cell is more sensitive to smaller magnitudes of mechanical loading. The value of n affects how sharply the mechanical loading input curve $\Theta$ changes as the L increases. The values of constants $K_a$ and n were calibrated using experimental data as is discussed in section 4.2.2

### Intracellular scale: Gene and protein regulatory network

The intracellular pathways triggered by mechanical loading were modeled using a gene and protein regulatory network. In this network, nodes represent key biological components (proteins or genes) involved in chondrocyte biology. Directed edges between nodes signify interactions or activating/inhibitory influences between source and target proteins, or between transcription factors (TFs) and their target genes. Annotations, descriptions, and cross-references for each network node and its interactions can be explored in two interactive

layers of the network: one focused on protein signaling and the other on gene regulation. The protein signaling network layer spans from the binding of growth factors to their respective receptors, down to the TFs entering the nucleus. The gene regulatory network (GRN) layer illustrates how transcription factors regulate the expression of target genes, which in turn code for proteins involved in the signaling network. These two network layers are interconnected, as each biological component is represented by both a gene in the GRN layer and its corresponding protein in the signaling network layer. Together, the two network layers form an interactive knowledge base for chondrocyte signaling.

The mathematical modeling of this network consisted of two distinct steps: first, constructing the network by representing the topological information of intracellular biochemical processes as a directed graph, and second, developing a framework to simulate the dynamics of the network. An explanation of these two steps are provided below.

**Construction of the gene and protein regulatory network**
The regulatory network was constructed using both knowledge-driven and data-driven approaches. The knowledge-based regulatory network was complemented with data-driven network inference to uncover *de novo* regulatory links, reveal previously unstudied or undiscovered interactions, and minimize bias associated with human literature curation. A detailed methodology of the regulatory network construction can be found in Lesage et.al. [228]. In the present study, extensions were made to the previously published regulatory network in Lesage et.al. [228], to include biochemical mechanisms related to mechanotransduction, inflammatory pathways, and their crosstalk in chondrocytes.

***Mechanotransduction pathways:*** In the modelled pathways, mechanical load ($\theta$) is transduced into biochemical cascades by integrins and focal adhesion kinase (FAK) complexes, activating RhoA/ROCK signaling that regulates actin cytoskeleton assembly and contractility, which influences cell differentiation and response to mechanical stimuli. This pathway also affects transcription factors like SOX9, which promotes ECM production, and YAP/TAZ, which regulate chondrogenic phenotypes and prevent hypertrophy. Additionally, the mTOR pathway is incorporated, linking integrins to PI3K/AKT/mTOR signaling, which regulates factors like GLI2 and RUNX2, contributing to chondrocyte mechanosensitivity.

In addition to integrins, chondrocytes also rely on mechanosensitive ion channels for mechanosensing and mechanotransduction, collectively referred to as the "channelome" [229]. This study incorporated the cation channel TRPV4 (transient receptor potential vanilloid 4), which plays a key role in the chondrocyte's metabolic response to dynamic mechanical loading [212]. Recent research [230] suggests that TRPV4 activation in chondrocytes occurs

due to osmotic fluctuations caused by the deformation of the chondrocyte's osmotically active microenvironment. Since the exact mechanistic link between deformation to osmotic changes to TRPV4 activation is very complex and not fully established in literature, it was assumed that the mechanical load ($\theta$) on the chondrocytes was directly responsible for TRPV4 activation. This assumption was based on the fact that mechanical load is directly proportional to the deformation of the microenvironment, as chondrocytes are directly attached to the extracellular matrix via focal adhesions. Supplementary data B contains a detailed explanation of the mechanotransduction pathways that were included in the current study.

***Inflammatory pathways:*** Inflammation plays a crucial role in OA onset and progression, driven by an auto-activating inflammatory loop. In this network, we simplified pro-inflammatory signaling by representing key mediators (e.g., IL-1$\beta$ or TNF-$\alpha$) with a single pro-inflammatory 'cytokines' node that activated an inflammation receptor ('R-inflam'). This was an important simplification allowing us to focus on the intracellular interplay between mechanotransduction and inflammation rather than the role of specific receptors and signaling molecules. In the network, pro-inflammatory 'cytokines' node induces matrix degradation, suppresses matrix biosynthesis, and amplifies its own production through feedback loops involving signaling cascades like TAK1, NFKB, and MAPKs. These pathways include activation of iNOS, which further fuels inflammation, and Wnt signaling, which also contributes to NFKB activation. Negative feedback loops, including SOCS proteins and the inhibition of TAK1, help regulate this auto-inflammatory response, with IGF signaling also playing a role in modulating inflammation and promoting tissue repair. Appendix B contains a detailed explanation of the mechanotransduction pathways that were included in this study.

***Mechano-inflammatory crosstalk pathways:*** Pathways involved in mechanotransduction and inflammation are interconnected, as shown by Madhavan et al. [231], who found that cyclic tensile strain suppresses pro-inflammatory gene induction by IL-1B, TNF-A, and LPS. In the current model, we described several direct molecular mechanisms linking mechanical loading and inflammation. For instance, integrin downstream signaling, particularly through $\alpha_5\beta_1$, upregulates MMP13 expression in chondrocytes when combined with inflammatory cues like IL-1B. Additionally, the model accounts for the interaction between YAP/TAZ and NFKB, where mechanical signals at physiological levels inhibit NFKB activation. Finally, ECM degradation products (DAMPs) activate inflammatory cytokine receptors and integrins, while mechanosensitive calcium signaling (TRPV4/Ca2+) inhibits ADAMTS5, highlighting the complex crosstalk between mechanical and inflammatory

pathways. Appendix B contains a detailed explanation of the mechano-inflammatory crosstalk pathways that were included in this study.

The complete network consisted of 74 nodes and 299 interactions. Important interactions and crosstalks related to the mechanotransduction and inflammatory pathways are reported in an activity flow diagram for illustration purposes in Supplementary Figure B.1. It represents a non-exhaustive part of the full interactome integrated in the model, the complete list of interactions in (and between) the gene and protein layers is available in Lesage et al. 2021.

**Simulating the dynamics of the regulatory networks**
The developed regulatory network was translated into a mathematical model using the additive formalism with priority classes developed by Kerkhofs et.al. [127]. In this approach, biological interactions were considered to occur on two distinct time scales: the fast (protein signaling) and the slow (gene regulation) levels. Consequently, each biological entity or node in the network could have both fast and slow upstream regulators. The global protein activity of a biological entity was calculated as the product of its gene expression level and its protein activation/inhibition level. The activity of a biological entity at the gene and protein levels was determined by the addition of upstream activators, which upregulate its effects, and the subtraction of inhibitors, which suppress its function.

### Implementation of the multiscale model

The development and analysis of FE models were performed using Abaqus. The primary collagen fibril orientations in articular cartilage of the knee joint (including the split-line patterns), and in the extracellular and pericellular matrix of the cell, were determined using Matlab scripts developed in-house. Subsequently, to implement the fibril reinforced poroviscoelastic model of cartilage, extracellular matrix and pericellular matrix, multiple user-defined subroutines in Fortran were used. In order to run simulations in parallel across multiple cores, existing UMAT subroutines were made thread-safe by removing common blocks, and UEXTERNALDB subroutines were developed to implement collagen fibril orientations. These improvements allowed FE simulations to be run in parallel, significantly reducing computation time. All FE simulations were performed on the wICE high-performance computing (HPC) cluster at the Flemish Supercomputing Center (VSC), KU Leuven. The cluster consists of 172 IceLake nodes, each equipped with two Intel Xeon Platinum 8360Y CPUs (2.4 GHz, 36 cores per CPU, 1 NUMA domain, and 1 L3 cache per CPU), 256 GiB RAM, and 960 GB SSD local disk. The default memory per core is 3400 MiB. Job submissions were managed via Slurm scripts. For the simulation

of intracellular gene/protein regulatory network, in-house Matlab scripts were developed.

### 4.2.2 Calibration of the multiscale model with gene expression data from *in vitro* studies

An important step in establishing the credibility of the multiscale model is its calibration with experimental data. As described in Section 4.2.1, the FE models at individual length scales already used calibrated material parameters from the literature, and regulatory network was developed from experimental data and its predictive value investigated by comparison with *de novo* experiments. However, the constants for the Hill's function—used to translate cellular forces (L) on the cellular-scale FE model into mechanical loading input ($\theta$) for the regulatory network—still needed calibration with experimental data.

#### Multiscale digital twin of the *in vitro* bioreactor setup

For this calibration, an *in vitro* dynamic compression study of cartilage explants by Li et al. [52] was chosen, which applied varying levels of dynamic compression (10% strain to 30% strain) to bovine cartilage explants from the superficial zone. This study also examined the combined effect of dynamic compression and the pro-inflammatory cytokine TNF-$\alpha$ on gene expression, making it ideal for calibrating our multiscale model. Hence, a multiscale digital twin of the experimental setup was developed (Figure 4.1), which incorporated three distinct length scales, with specific details for each scale outlined below:

**i) Organ and tissue scale:** An FE model of the cylindrical cartilage explant of 3 mm diameter and 1 mm thickness was done in Abaqus. The model was meshed with C3D8P elements and a mesh convergence study was performed to determine the optimum mesh density. FRPVE material properties as described in section 4.2.1 were assigned to the cartilage explant, with the primary collagen fibers parallel to the flat surface since the explants were harvested with the superficial zone intact. To simulate unconfined dynamic compression, the vertical displacement of bottom surface of the explant was fixed using a YSYMM boundary condition and a zero pore pressure boundary condition was applied to side of the cylinder to simulate free flow of pore fluid across this surface. Furthermore, displacement of two diametrically opposite points on the x and z axis at the bottom surface was constrained in the z and x direction respectively, to stop any rigid body motion along the x-z plane without compromising on the mechanics. Dynamic compression was applied to the explant using a rigid disc with a diameter of 8 mm, modeled as a discrete rigid body in Abaqus and

meshed with R3D4 elements. The loading protocol for dynamic compression was based on the experiment by Li et al. [52], and was applied to a reference point on the rigid disc. First, a pre-strain of 10% of the cartilage thickness was applied over 1 second, and the strain was held constant for an additional 10 seconds to allow for stress relaxation. Following this, dynamic compression of 10%, 20%, and 30% was applied using a haversine waveform (0.5 Hz, 40% duty cycle).

**ii) Cellular scale:** The cellular scale model for the superficial zone was used for this study (as described in section 4.2.1) and was positioned at the center of the cartilage plug, 0.5 mm from its top surface . The central position of the cell in the plug was chosen to capture an intermediate mechanical behavior that would be representative of the whole plug, given the gradient of mechanical stimuli present across its thickness.

**iii) Intracellular module:** The intracellular gene and protein regulatory network used for this study was as mentioned in section 4.2.1.

### Sensitivity analysis of the network

Sensitivity study of the network was performed using a two-factor full factorial design, by perturbing the pro-inflammatory cytokine and mechanical loading nodes of the network from 0 to 1 in steps of 0.1 (total of 121 simulations). Perturbations were applied for an indefinite period of (computational) time steps and the new phenotypes were assessed after the system had settled in stable states accounting for the perturbed environment. During the perturbation, the system could settle in slightly different final states under the imposed environmental perturbations because of the stochastic nature of the model. Therefore, each perturbation simulation was repeated 100 times and a weighted average destination profile was computed. The weights reflected the number of occurrences of the destination, or final profiles, among the 100 repetitions.

### Optimization using Genetic Algorithm approach

The constants of Hill's function, specifically $K_a$ and n, as described in section 4.2.1, were calibrated by minimizing the difference in gene expression levels of COL-II and ADAMTS5 between the experimental data and the multiscale model under 20% dynamic compression of the cartilage plug. Peak cellular force (L) from the 3rd cycle of dynamic compression was used to perturb the intracellular pathways using the same approach as in section 4.2.2. This was done to obtain an intermediate magnitude of forces between the first cycle

(where the forces were highest) and the successive cycles where the mechanics of the cartilage reached a steady state. The minimization was performed using a genetic algorithm approach in Matlab R2022b (The MathWorks Inc., Natick, Massachusetts). In the experiments by Li et al. [52], gene expressions were normalized with respect to a control case with no external loading. For consistency, the *in silico* gene expressions were also normalized to the control case, which assumed a zero external load condition (L=0; $\theta$=0.1) as input to the regulatory networks. The objective function (f) for the optimization was as follows:

$$f = \frac{1}{2}\left[\left(\frac{\text{COL-II}_i - \text{COL-II}_e}{\text{COL-II}_e}\right)^2 + \left(\frac{\text{ADAMTS5}_i - \text{ADAMTS5}_e}{\text{ADAMTS5}_e}\right)^2\right] \tag{4.3}$$

Subscripts $i$ and $e$ are for *in silico* and experimental values respectively. To prevent bias in the optimization due to differing gene expression magnitudes, each gene expression difference in the objective function was normalized by its corresponding experimental value, ensuring equal contribution from each gene.

### 4.2.3 Application of the multiscale model to a patho-physiological scenario of meniscectomy in the human knee joint

The calibrated multiscale model workflow was applied to a patho- physiological case of meniscectomy in the human knee joint, to qualitatively validate the multiscale model predictions against long term longitudinal studies of patients with menscectomy. This case was chosen due to extensive clinical evidence linking meniscectomy to cartilage degeneration and OA in many patients [232–235]. For this application, a multiscale digital twin of the human knee joint was developed following the same workflow as mentioned in section 4.2.1. The details of the length scales in the multiscale workflow are as follows:

**i) Organ and tissue scale:** An FE model of tibiofemoral joint of a cadaveric right knee from a 70 years old female donor (77.1 kg, 1.68 m) that was previously developed in Chapter 3, was used in this study. The geometry for the model was obtained from the Open Knee database [176]. The FE model included the geometric representations of the bones (femur and tibia), cartilage(femoral and tibial), menisci (medial and lateral), and ligaments (anterior and posterior cruciate). The anterior and posterior ends of the meniscii were attached to the tibial plateau by means of a series of linear springs with total stiffness of each meniscal attachment (also called meniscal horns) set to a 2000 N/mm based on previous studies [91, 177]. The femoral and tibial cartilage were rigidly attached to the femur and tibia respectively using the tie constraint. Articular cartilages

were meshed with hexahedral pore pressure elements (C3D8P) and the other soft tissues were meshed with hexahedral linear elements (C3D8). Following a mesh convergence study, a fine mesh of 12 elements across the cartilage thickness was chosen for the simulations. The tibia and femur were meshed with rigid elements (R3D4). Articular cartilage was modeled as an FRPVE material as mentioned in section 4.2.1. Time-dependent translations, rotations, and forces during the stance phase of the gait (scaled by 0.77 from the original values in Mononen et al. [91] to account for the difference in body weights of the patients from which the geometry and gait data were respectively sourced) were applied as boundary conditions to the femur. These were implemented through a reference point at the center of the medial and lateral femoral epicondyles.The tibia was fixed in all directions. The gait cycle was simulated in the FE model in two successive steps with the first step of 0.1 seconds to adjust initial kinematics and kinetics to the beginning of gait cycle. A second step of 0.6 seconds was used to implement the boundary conditions for the stance phase. To simulate bilateral meniscectomy in the FE model, the menisci and meniscal horns were removed from the healthy knee joint.
Table 4.1 lists the values of the material parameters that were used for the simulations.

**ii) Cellular scale:** A cellular-scale model was created for each of the three zones in the medial tibial cartilage—superficial, middle, and deep zone (SZ, MZ, DZ)— as described in section 4.2.1. The cells were positioned in the region of the medial tibial cartilage where the highest tibio-femoral contact pressures were observed, at normalized depths of 0.085, 0.3, and 0.8 from the cartilage surface for the superficial, middle, and deep zones, respectively. This location for the cell was chosen due to expected maximum changes in mechanics resulting from meniscectomy. It must be noted that to ensure convergence in spite of the higher stresses an strain rates encountered in menisectomy, time scaling by multiplication with a factor of 1.43 (making the total simulation duration 1 sec instead of 0.7 sec) was done for the SZ and MZ chondrocytes. Given the viscoelastic nature of cell and is microenvironment, the cellular forces obtained from the time-scaled models were also scaled by multiplying with a factor of 1.43 to compensate for the reduction in cellular forces due to time scaling.

**iii) Intracellular scale:** Two types of *in silico* analyses were conducted for each cell located in the different zones of cartilage using the intracellular regulatory network. Firstly, a canalization analysis was performed using a constrained Monte Carlo approach. In this analysis, the mechanical loading input ($\theta$) to the network was constrained with a value depending on the cell's location, while the other nodes were free to be updated. The results were reported as an average of 10,000 random initializations of the network, while respecting the constraints on the mechanical loading input ($\theta$). The purpose of this analysis

was to identify cell-specific stable states of the intracellular model under the predefined mechanical environments experienced by cells in different zones of the cartilage during their healthy state. Secondly, a perturbation analysis was carried out to investigate the effects of meniscectomy. The mechanical loading input ($\theta$) based on peak cellular forces (L) during gait for both healthy and meniscectomized cases was used to perturb the intracellular regulatory network. It was assumed that the cells initially resided in their stable healthy state (as determined from the Monte Carlo analysis) before the perturbation was applied. The external perturbations for the state transition study were applied for an indefinite number of computational time steps, and the new phenotypes were assessed after the system had settled into stable states under the perturbed environment. Due to the stochastic nature of solving the dynamics of the network, each perturbation simulation was repeated 100 times. A weighted average of the destination profiles was computed, with the weights reflecting the frequency of each final profile among the 100 repetitions. Additionally, weighted standard deviations were evaluated to quantify variability.

## 4.3 Results

### 4.3.1 Results from the multiscale digital twin of the *in vitro* bioreactor setup

#### Sensitivity analysis of the network reveals a complex interplay of mechanical and pro-inflammatory mediators

The sensitivity analysis of the network revealed a biphasic relationship between mechanical loading and the global activity of key cartilage matrix proteins, COL-II and ACAN, for pro-inflammatory cytokine levels below 0.7 (Figure 4.2). Specifically, mechanical loading in the range of 0.3 to 0.8 resulted in high global activity of ACAN and COL-II. However, when mechanical loading was either below 0.3 or above 0.8, the activity of these matrix proteins decreased. For higher pro-inflammatory cytokine levels (greater than 0.7), mechanical loads above 0.5 caused a significant reduction in the global activity of the matrix proteins, with the extent of this catabolic effect directly proportional to the increase in pro-inflammatory cytokine levels. This reduction in matrix proteins was accompanied by a drastic increase in the global activity of matrix-degrading enzymes, such as ADAMTS5 and MMP13, due to the combined effect of high mechanical loads and elevated pro-inflammatory cytokines. For cytokine levels below 0.7, the global activity of SOX9 increased monotonically with the increase in mechanical loading. However, when cytokine levels exceeded 0.7, mechanical

loads greater than 0.5 led to a drastic reduction in SOX9 activity. The global activity of RUNX2, a marker for pro-hypertrophic chondrocytes, was negligible under most conditions, except when both pro-inflammatory cytokine levels and mechanical loading were high.

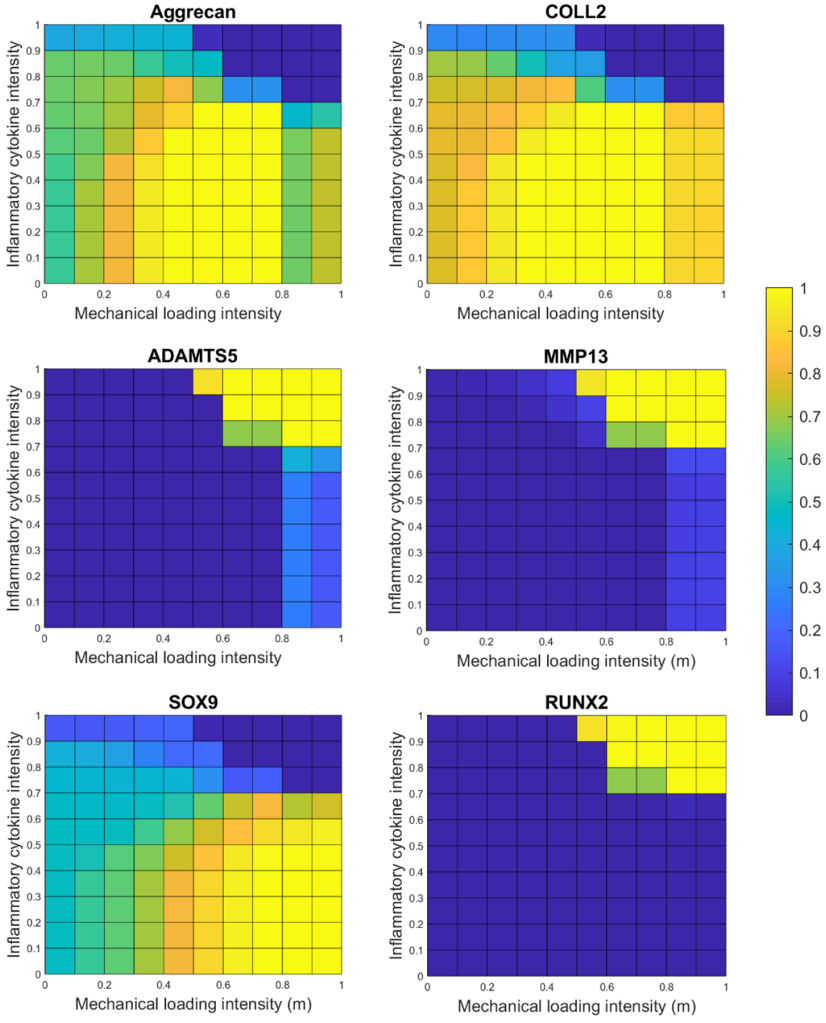


Figure 4.2: Results of the two-way sensitivity analysis of the network and its connection to the cellular level, showing the variation of relevant biomarkers resulting from a change of mechanical load and pro-inflammatory cytokines

### Calibrated *in silico* multiscale model captures the gene expressions of COL-II and ADAMTS5

The calibrated values of Ka and n for the Hill's function were 0.001656 and 1.870793 respectively which was obtained at 72nd generation of the genetic algorithm. Upon comparing the optimized numerical gene expressions with experimental values for the 20% strain case, a close match was observed for the genes ADAMTS5 and COL-II as in Figure 4.3. However, the gene expression of ACAN was overpredicted by the numerical model. For the 10% strain case, which was an independent dataset not used for calibration, the numerical models overpredicted the expressions of COL-II and ACAN. This was accompanied with an underprediction of ADAMTS5 expression.

### *In silico* model predicts sGAG loss from cartilage

To further validate the predictions of the numerical model, cumulative sGAG loss from cartilage explants to the medium after 8 days of treatment, as measured in experiments by Li et al. [52], was compared with the numerically calculated proteoglycan loss under the corresponding treatment conditions. The numerical value of proteoglycan loss for each condition was measured as difference in global values of the proteoglycan variable between the culture condition and the corresponding value at the baseline stable chondrocyte attractor. The results, shown in Figure 4.3(d), revealed that the numerical model overpredicted the sGAG loss for the "no load, no cytokine" condition and the "20% dynamic loading with cytokines" condition. In contrast, for the "no load with cytokine" condition and the "10% dynamic loading with cytokine" condition, the model underpredicted sGAG loss compared to the experimental data. Furthermore, the numerical model exhibited a biphasic response to mechanical loading, similar to what was observed in the experimental study. In the numerical study, the "10% dynamic loading with cytokines" condition restored sGAG loss to near baseline values (no load, no cytokines) levels, whereas 20% dynamic loading led to an increase in sGAG loss. In the experimental studies, however, the "20% dynamic loading with cytokines" condition most effectively reduced sGAG loss.

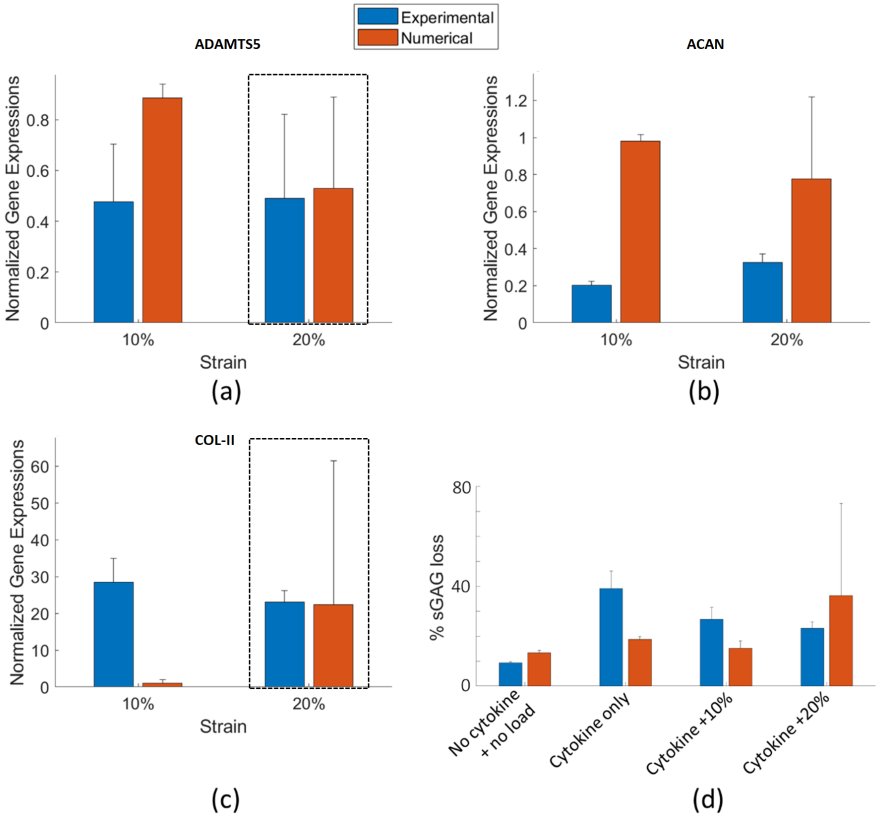


Figure 4.3: Results of the calibration and validation process of the multiscale model. (a-c) Normalized gene expressions of ADAMTS5, ACAN, COL-II respectively. The dotted lines indicate the conditions included in the calibration, and the rest of the conditions were used for validation, (d) additional validation of the multiscale model by comparing the s-GAG loss measured in experimental studies with the predicted value of Aggrecan from the model.

### 4.3.2 Results from the multiscale digital twin of the human knee joint

#### Monte Carlo analyses reveal that the stable states of the network is dependent on the location of the chondrocyte

The Monte Carlo analysis for screening the system's state space was performed for cells located in the SZ, MZ and DZ respectively in tibial cartilage during a typical gait cycle, with cellular forces specific to each chondrocyte's location as a fixed input. For all three chondrocyte types, two possible basal stable states were calculated from the model: a SOX9-positive (SOX9+) state, comparable to a healthy stable chondrocyte, and a RUNX2-positive (RUNX2+) state, comparable to a pro-hypertrophic chondrocyte (pro-HP) (Figure 4.4).

Generally, for all the 3 chondrocytes in the pro-hypertrophic state, high activity of pro-hypertrophic and catabolic markers such as RUNX2, Col-X, MMP13, ADAMTS5 and cytokines were observed. This was accompanied with high activity of relevant catabolic pathways such as the WNT, BMP, IHH, MAPK/ERK and FGF. In the non-hypertrophic (no HP) state, high activity of the markers of stable chondrocyte such as SOX9, Col-II and ACAN were observed. This was accompanied with high activity of relevant anabolic pathways such as PTHRP, TGF$\beta$ and IGF. However, different canalization and profiles were obtained for the SZ, MZ, and DZ chondrocytes, as shown in Figure 4.4. Specifically, for the SZ chondrocyte, 21% of the initial states led to the SOX9+ state and 79% to the RUNX2+ state, whereas for the MZ chondrocyte, these values were 11% and 89%, respectively, and for the DZ chondrocyte, they were 44% and 56%, respectively. When comparing SZ, MZ and DZ chondrocytes, no significant differences were observed in the activity of signaling pathways and genes for the pro-hypertrophic (pro-HP) state. However, for the healthy state, activity of the mechanotransduction related genes such as integrins and YAP/TAZ, and mechanotransduction pathways like the RhoA/Actin and TRPV4/Ca2+ were highest for the MZ and lowest in the DZ. Activity of cytokines and inflammation related pathways also followed a similar trend, with highest values in the MZ and lowest in the DZ. This Monte Carlo analysis therefore highlights how the gradient of mechanical load experienced by chondrocytes, depending on their spatial location, can influence their basal stable states.

| | | Superficial Zone | | Middle Zone | | Deep Zone | |
|---|---|---|---|---|---|---|---|
| | | **pro-HP** | **Healthy** | **pro-HP** | **Healthy** | **pro-HP** | **Healthy** |
| Signaling pathways | **WNT** | 0.94 | 0.00 | 0.94 | 0.00 | 0.91 | 0.00 |
| | **BMP** | 0.92 | 0.00 | 0.92 | 0.00 | 0.92 | 0.01 |
| | **WNT antagonit** | 0.00 | 0.84 | 0.00 | 0.84 | 0.00 | 0.80 |
| | **BMP antagonist** | 0.00 | 0.95 | 0.00 | 0.99 | 0.00 | 0.83 |
| | **FGF** | 0.67 | 0.00 | 0.67 | 0.00 | 0.67 | 0.00 |
| | **IHH** | 1.00 | 0.40 | 1.00 | 0.43 | 1.00 | 0.36 |
| | **PTHRP** | 0.00 | 0.83 | 0.00 | 0.85 | 0.00 | 0.77 |
| | **IGF** | 0.00 | 0.69 | 0.00 | 0.66 | 0.00 | 0.72 |
| | **TFGB** | 0.07 | 0.85 | 0.07 | 0.83 | 0.07 | 0.86 |
| | **MAPK/ERK** | 0.88 | 0.13 | 0.88 | 0.14 | 0.88 | 0.13 |
| TF | RUNX2 | 1.00 | 0.00 | 1.00 | 0.00 | 1.00 | 0.00 |
| | SOX9 | 0.00 | 0.95 | 0.00 | 0.99 | 0.00 | 0.83 |
| | NKX3.2 | 0.00 | 1.00 | 0.00 | 1.00 | 0.00 | 0.90 |
| ECM | MMP13 | 1.00 | 0.00 | 1.00 | 0.00 | 1.00 | 0.00 |
| | ADAMTS5 | 1.00 | 0.00 | 1.00 | 0.00 | 1.00 | 0.00 |
| | Col-X | 1.00 | 0.00 | 1.00 | 0.00 | 1.00 | 0.00 |
| | Col-II | 0.00 | 1.00 | 0.00 | 1.00 | 0.00 | 1.00 |
| | Aggrecan | 0.00 | 1.00 | 0.00 | 1.00 | 0.00 | 1.00 |
| Mechanotransduction | Loading | 0.54 | 0.54 | 0.62 | 0.62 | 0.38 | 0.38 |
| | Integrins | 1.00 | 0.36 | 1.00 | 0.41 | 0.92 | 0.25 |
| | YAP/TAZ | 0.00 | 0.61 | 0.00 | 0.71 | 0.00 | 0.42 |
| | **RhoA/Actin** | 1.00 | 0.61 | 1.00 | 0.71 | 0.92 | 0.42 |
| | **TRPV4/Ca2+** | 0.00 | 0.25 | 0.00 | 0.29 | 0.00 | 0.17 |
| Inflammation related | SOCS | 0.00 | 0.32 | 0.00 | 0.31 | 0.00 | 0.33 |
| | IKB-A | 0.00 | 0.39 | 0.00 | 0.29 | 0.00 | 0.51 |
| | FOXO1 | 0.00 | 0.30 | 0.00 | 0.27 | 0.00 | 0.34 |
| | Cytokines | 1.00 | 0.10 | 1.00 | 0.14 | 1.00 | 0.05 |
| | **Inflammation** | 1.00 | 0.09 | 1.00 | 0.11 | 0.97 | 0.05 |
| | **CANALIZATION** | **86%** | **14%** | **89%** | **11%** | **56%** | **44%** |

| Label | Variables included in average values |
|---|---|
| **WNT** | (WNT, DSH, B-Cat, LLEF/TCF, Frizzled) |
| **BMP** | (BMP, R-SMADs,SMAD_complex |
| **WNT antagonist** | (DKK1, FRZB) |
| **BMP antagonist** | GREM1 |
| **FGF** | (FGF, FGFR1, FGFR3) |
| **IHH** | (IGHH, GLI2) |
| **PTHRP** | (PTHrP, PKA, PPR, PP2A) |
| **IGF** | (IGFI, IGF-IR, [1-IFGBP]) |
| **TFGB** | (TGF, SMAD3, [1-SMAD7 ]) |
| **MAPK/ERK** | (ERK, RAS, P38, JNK) |
| **RhoA/Actin** | (Rhoa/ROCK, Actin-MLC) |
| **TRPV4/Ca2+** | (TRPV4, Ca2+) |
| **Inflammation** | (Rinflam, TAK1, NFKB, iNOS, NO) |

Figure 4.4: Monte Carlo analysis to determine the stable states (healthy vs pro-hypertrophic(pro-HP)) for chondrocytes in Superficial, Middle and Deep Zone of the human knee joint. The values shown are average values from the different factors shown to belong to a particular label.

### Meniscectomy leads to higher stresses in cartilage

FE analysis of the human knee joint revealed that meniscectomy resulted in significantly higher stresses within the articular cartilage compared to the healthy knee. Specifically, the maximum von Mises stress in the medial tibial cartilage at the cartilage-to-cartilage contact region increased from 5.03 MPa in the healthy knee to 6.78 MPa after meniscectomy, observed at the second peak loading during the stance phase of the gait cycle (Figure 4.5(b,c)). Additionally, contact pressures in the medial tibial cartilage also rose from 5.77 MPa to 7.93 MPa as a result of meniscectomy, as shown in Figure 4.5(a). This study also recorded increase in fluid pressure in the cell due to meniscectomy (for example, from 5.87 MPa in healthy to 8.25 MPa for meniscectomy for the MZ chondrocyte). Furthermore, simulations at the cellular level within a multiscale modeling framework demonstrated that meniscectomy led to an increase in cellular forces across all zones of the cartilage, as seen in Table 4.2.

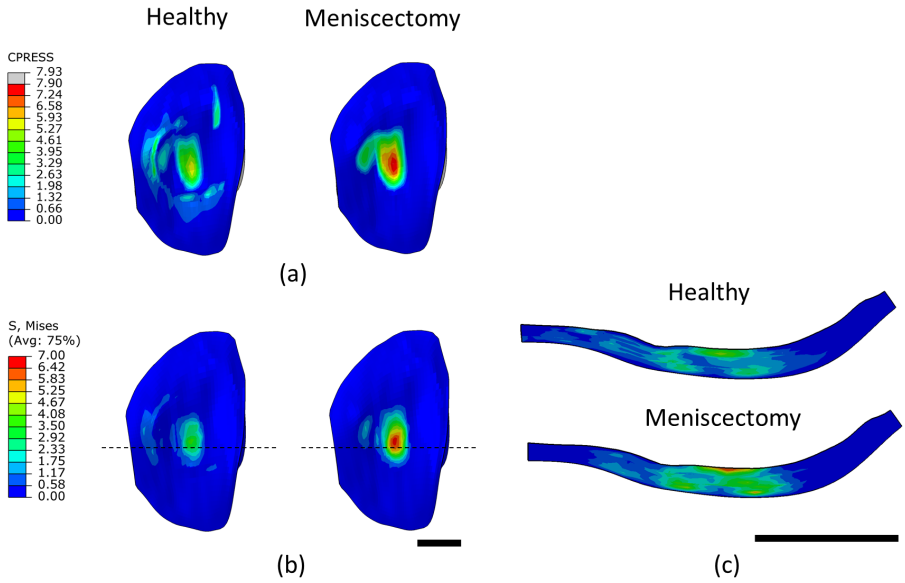


Figure 4.5: FE Analysis of the (mechanical) effect of meniscectomy in the human knee joint. (a) Contact Pressures (MPa), (b) von Mises' Stress (MPa), (c) von Mises' Stress (MPa) across the section where highest magnitude of contact pressure was observed, which was selected as the location for the cellular scale model, shown by dotted line in (b).

| | Healthy | Meniscectomy |
|---|---|---|
| **Superficial Zone** | 1.62 | 2.84 |
| **Middle Zone** | 1.96 | 3.22 |
| **Deep Zone** | 1.07 | 1.43 |

Table 4.2: Cellular forces (in milli newton (mN)) as calculated from the cellular scale FE models in different zones, for both healthy (left) and meniscectomy (right) conditions

### Meniscectomy induces catabolic and pro-inflammatory response in chondrocytes

To mimic the effect of a pathological mechanical signal due to meniscectomy on presumably healthy chondrocytes, the SOX9+ state (healthy) from each zone was used as an initial state. Subsequently, perturbation from the initial state was performed with abnormal mechanical load ($\theta$) due to meniscectomy, with zone-specific values calculated from the cellular-scale model (Table 4.2). The average profiles of the perturbations were reported based on 100 repeated simulations, as shown in Figures 4.6,4.7.

The increased mechanical load in the superficial zone (SZ), middle zone (MZ), and deep zone (DZ) chondrocytes following meniscectomy led to an upregulation of genes involved in mechanotransduction pathways, such as Actin-MLC, YAP/TAZ, and TRPV4/Ca2+, compared to their respective basal healthy states (Figures 4.6,4.7). Notably, the DZ chondrocytes exhibited the least increase in mechanotransduction gene activity, likely due to the comparatively lower mechanical load they experienced. In addition to the mechanotransduction pathway activation, meniscectomy induced a decrease in the expression of extracellular matrix-related genes like COL-II and ACAN, accompanied by an increase in matrix-degrading enzymes (MMP-13 and ADAMTS5) in the SZ and MZ chondrocytes, with a more pronounced effect in the MZ. In the DZ, however, matrix-related proteins showed negligible changes.

Meniscectomy also led to heightened activity of inflammatory genes (e.g., NFKB, TAK1, NO, and iNOS) in the SZ and MZ chondrocytes. Alongside this, there was an increase in the activity of pro-inflammatory cytokines (represented by the 'Cytokine' variable) and the receptor for inflammation (R-inflam) in the SZ and MZ. Despite these alterations, all three chondrocyte zones showed high expression of the stable chondrocyte marker SOX9 and low to negligible expression of pro-hypertrophic markers RUNX2 and COL-X. This suggested that the first iteration after meniscectomy induced some pro-inflammatory and catabolic changes, especially in the SZ and MZ, without triggering a full shift towards hypertrophy.

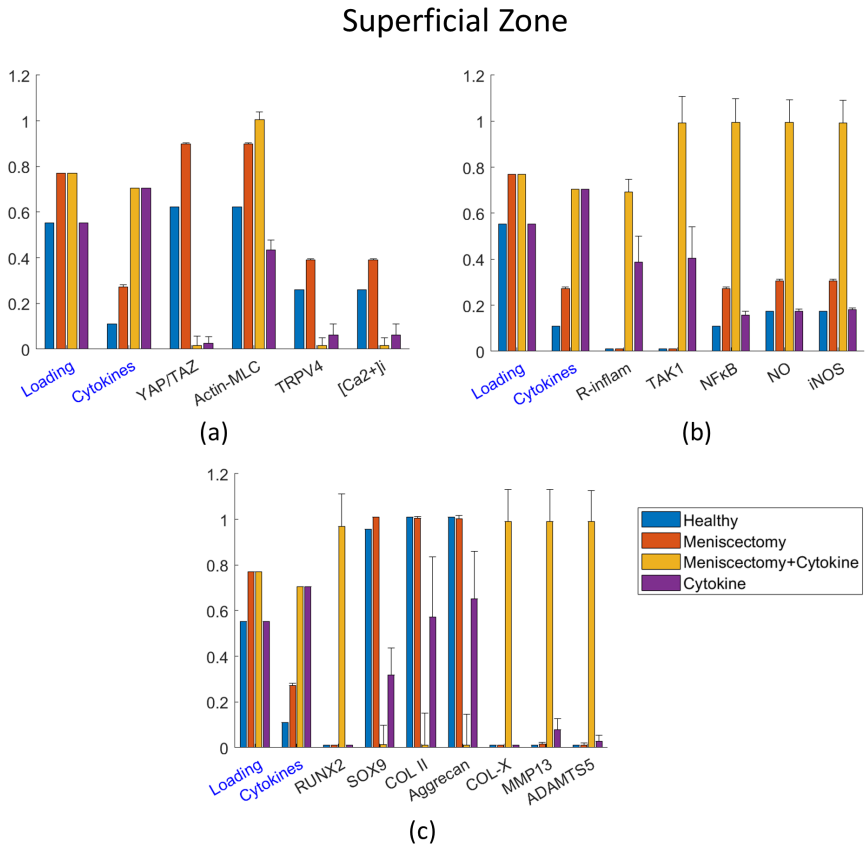


Figure 4.6: Analysis of interplay of meniscectomy-induced increased loading and inflammation in human knee joint using the multliscale model for superficial zone(SZ) chondrocyte. (a) Mechanotransduction biomarkers, (b) Inflammation biomarkers, (c) Extracellular Matrix biomarkers.

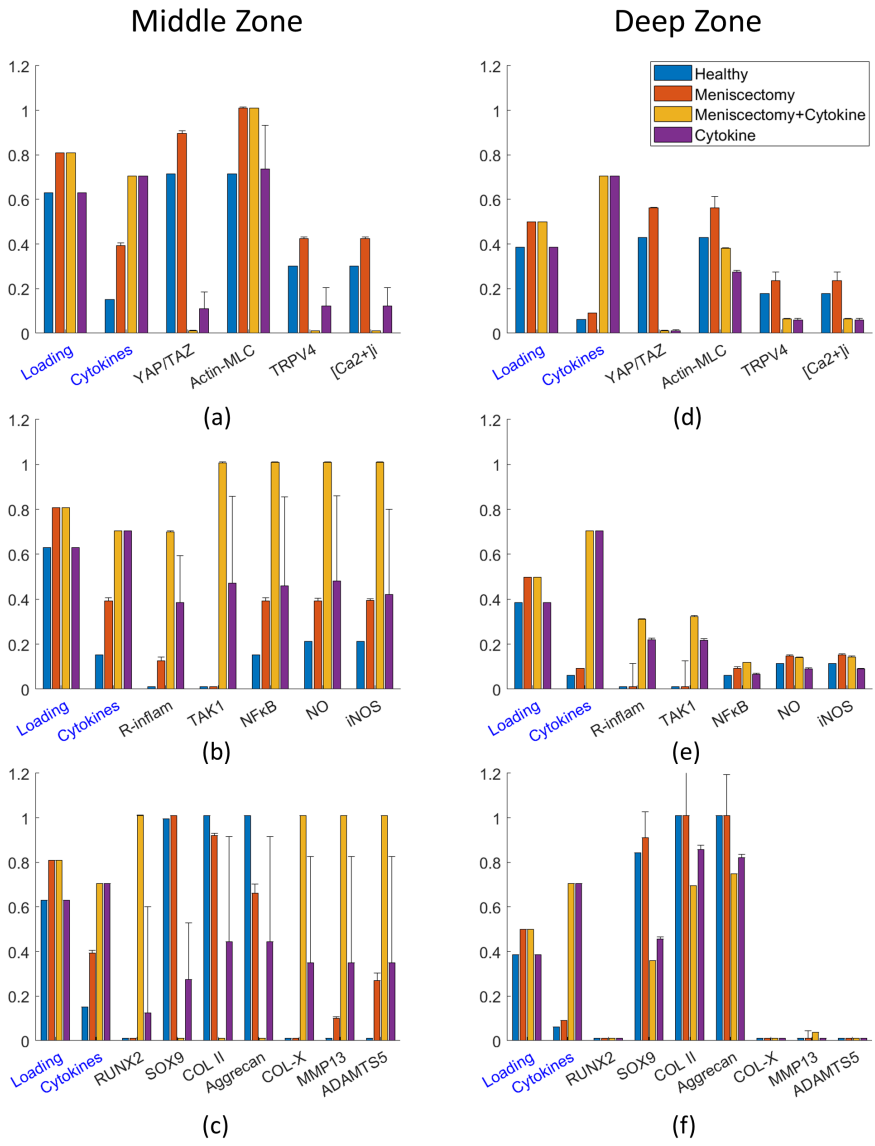


Figure 4.7: Analysis of interplay of meniscectomy-induced increased loading and inflammation in human knee joint using the mutltiscale model for middle (MZ) and deep zone(DZ) chondrocyte. (a,d) Mechanotransduction biomarkers, (b,e) Inflammation biomarkers, (c,f) Extracellular Matrix biomarkers.

### Build-up of pro-inflammatory cytokines further aggravate catabolic processes in meniscectomized knee joint

Since the first meniscectomy iteration in the multiscale model triggered a pro-inflammatory response and cytokine production as mentioned in the section 4.3.2, follow-up simulations were performed using the multiscale model to study the long-term effects of meniscectomy on the knee joint, including the buildup of pro-inflammatory cytokines over time and across repeated iterations. Several experimental studies have reported elevated levels of pro-inflammatory cytokines in plasma or synovial fluid from OA patients compared to non-OA patients [236].

To simulate the iterative buildup of cytokines to an elevated level, the cytokine variable in the regulatory network was set to a value of 0.695 based on the sensitivity analysis of the network described in section 4.3.1. Two conditions were simulated: first, the higher mechanical load due to meniscectomy was combined with elevated level of cytokines (values fixed to 0.695, i.e. about 7 times higher than in the basal situation in SZ). Second, a condition of healthy mechanical load combined with elevated level of cytokines. These conditions were simulated to evaluate the relative contribution of the different co-variables (mechanical loading and pro-inflammatory cytokines) and to better understand their interplay.

The combination of elevated mechanical cues and cytokines in the SZ and MZ fully activated pro-inflammatory pathways (NFkB, NO, iNOS and TAK1, represented by yellow bars in Figures 4.6,4.7) and triggered a transition to pro-hypertrophic state, as evident from the large increase of RUNX2, COL-X, MMP13 and ADAMTS5, and a decrease of SOX9, COL-II and Aggrecan (Figure 4.6,4.7, yellow bars). The pathological inflammation with meniscectomy also led to a sharp decrease of YAP/TAZ and TRPV4/Ca2+, which are relevant genes for mechanotransduction.

The sharp catabolic effect observed in SZ and MZ due to the combination of both elevated mechanical load and pro-inflammatory cues was not so distinct when the condition of normal mechanical load with pathological pro-inflammatory cytokines was applied as seen in purple bars in Figures 4.6,4.7. The pro-inflammatory cytokines alone disturbed the healthy phenotype as observed from the level of the master transcription factors (downregulated SOX9, and upregulated RUNX2) and ECM proteins (Figure 4.6,4.7, purple bars), but SZ and MZ still maintained some level of COL-II and Aggrecan. Most importantly, a greater standard deviation was observed in the final states of MZ chondrocytes following perturbations with cytokines condition alone, compared to meniscectomy plus cytokines (Figure 4.7 b). The large standard

deviation in the average profile was due to a variety of final states possibly reached (out of 100 repetitions) under the perturbation during state transition study. Overall, these findings suggest that pathological mechanical cues in the SZ and MZ sensitize chondrocytes, further aggravating the catabolic response to pro-inflammatory signals. This progression of catabolic processes from SZ and MZ to the DZ mirrors clinical observations following meniscectomy, where patients often develop OA with significant damage in the SZ and MZ, as documented in several longitudinal studies [232–235].

### Gradient of mechanical stimuli across cartilage zones leads to differential effect of meniscectomy

Most of the catabolic effects observed following meniscectomy were present in chondrocytes across all zones, though the effects were smallest in the DZ and largest in the MZ. This pattern was consistent with the mechanical load acting on the cells in the corresponding zones. In the DZ, the impact of increased mechanical loading was more subtle, as the forces acting on the DZ chondrocytes were much lower than in the other two zones (Figure 4.7). Despite this mild effect, some noticeable differences were still observed between the three zones. For example, in the DZ, COL-II and Aggrecan expression remained unchanged after meniscectomy, while they were reduced in the SZ and MZ. This response was likely facilitated by increased activity in mechanotransduction pathways and the absence of ECM-degrading enzymes (MMP13 and ADAMTS5) (Figure 4.7, d,f). Although some pro-inflammatory mediators were present in the DZ due to meniscectomy, their levels were not as high as the SZ or MZ chondrocytes (Figure 4.7).

Additionally, DZ chondrocytes appeared less sensitive to elevated pro-inflammatory cytokines compared to SZ chondrocytes. When exposed to the same level of elevated pro-inflammatory cytokines (0.695), the levels of cytokine receptors (R-inflam) and downstream effectors (TAK1) in the DZ increased to $0.32 \pm 0.004$ and $0.33 \pm 0.003$, respectively. In contrast, in the MZ, these levels reached $0.7 \pm 0.004$ and $1.0 \pm 0.003$, respectively. In the DZ, the effects on ECM-related proteins and inflammatory pathways in the meniscectomy + cytokine condition appeared to be largely driven by the cytokine co-variable (Figure 4.7). Moreover, for all simulated conditions in the DZ, no sharp transition to hypertrophy was observed (as evidenced by negligible activity of pro-hypertrophic markers RUNX2 and COL-X). This contrasted with the pro-hypertrophic behavior observed in SZ and MZ chondrocytes due to the combined effects of meniscectomy and elevated cytokines.

Another key difference was observed in the mechanoregulatory pathway involving

Actin-MLC. This pathway was over-activated in both the meniscectomy and meniscectomy + cytokine conditions in the SZ and MZ, while it was over-activated by meniscectomy and inhibited by meniscectomy + cytokine condition in the DZ. These results demonstrate the ability of the multiscale model to capture subtle differences in chondrocyte metabolism resulting from a crosstalk of pro-inflammatory and mechanical cues.

## 4.4 Discussion

In this study, a multiscale modeling workflow was developed for articular cartilage by coupling the mechanics at multiple length scales (from tissue to cell) with an intracellular gene/protein regulatory network. While there are studies in the literature that individually study either the multiscale mechanics of cartilage [140, 142, 221] or intracellular regulatory networks for cartilage [127, 132, 133, 228, 237], the present study makes a unique contribution to the field by coupling these two classes of models together, thereby resulting in a more robust and integrated multiscale approach to study different aspects of cartilage mechanobiology. The modeling workflow was calibrated and validated with respect to independent experimental data from the literature. As a further application, the multiscale modeling workflow was utilized to study the pathophysiology of the human knee joint during meniscectomy. The model predicted a catabolic response in articular chondrocytes driven by increased mechanical loading and inflammation following meniscectomy. These catabolic effects were particularly evident in the superficial and middle zones of the cartilage, where chondrocytes were exposed to higher mechanical forces. This study highlights the effectiveness of the multiscale modeling approach in capturing the complex interplay between mechanical loading and inflammation in articular cartilage. The integration of tissue, cellular, and intracellular scale models, as done in this study, provides a comprehensive and accurate framework for exploring cartilage mechanobiology, offering critical insights into cartilage pathophysiology.

Multiscale simulation of meniscectomy in this study showed an increase in fluid pressure in the cell due to meniscectomy (for example, from 5.87 MPa in healthy to 8.25 MPa for meniscectomy for the MZ chondrocyte), a trend which was also observed in previous studies in literature [142]. Furthermore, simulations from the intracellular network revealed that pathological mechanical cues in the SZ and MZ sensitize chondrocytes, further aggravating the catabolic response to pro-inflammatory signals. This progression of catabolic processes from SZ and MZ to the DZ mirrors clinical observations following meniscectomy, where patients often develop OA with significant damage in the SZ and MZ, as

documented in several longitudinal studies [232–235]. These findings highlight the importance of elevated mechanical cues in cartilage due to meniscectomy and the subsequent inflammatory response, which plays a key role in the development of OA.

In the tissue and cellular scale FE model developed in this study, a fibril-reinforced poroviscoelastic constitutive model [178] was used to describe the mechanical behavior of bulk cartilage, as well as the PCM and ECM. The simulations were run in parallel using multiple cores on a high-performance computing (HPC) cluster to reduce computational time. Furthermore, while previous FE models of chondrocytes [140, 142, 220, 221] employed a uniform spherical shape of chondrocytes across all cartilage zones, the present study incorporated zone-specific chondrocyte shapes in the cellular scale FE models, thereby capturing more closely the appropriate cellular scale mechanics and its variation across the thickness of cartilage.

In the present study, the knee joint FE model assumed the subchondral bone to be a rigid body. This assumption was made due to the significant difference in stiffness between the cartilage and the underlying subchondral bone [119], with the primary focus of the study being the pathophysiology of cartilage. However, for future studies, incorporating the subchondral bone and calcified cartilage could provide valuable insights (as elucidated in chapter 3 of the thesis), given their emerging role in the progression of OA in the knee joint [6]. It is also important to note that the FE model of the human knee joint in this thesis was developed using geometry, material properties, and gait cycle data from different literature sources rather than a single patient.

This study included integrin-mediated mechanosensing as the primary mechanism of mechanical signal transduction in chondrocytes, with the TRPV4 ion channel being another mechanosensor. The choice of integrin-mediated mechanotransduction was because it is a well-studied molecule with significant evidence in the literature regarding its role in mechanosensing [211, 238]. Even though there are multiple subunits of integrins, too few studies distinguish the downstream cascades and effects specific to each integrin subunit. Thus, for simplification, all integrin subunits were lumped into a single integrin node in the regulatory networks in this study. In reality, integrin-mediated focal adhesions are localized at specific regions in the cell with a complex binding dynamics [239]. However, a uniform attachment of the cell with the pericellular matrix using a 'Tie' constraint was assumed. This assumption was based on previous studies in the literature [240], where immunofluorescent staining of integrins in chondrocytes showed a uniform distribution of integrins around the chondrocyte.

Recent studies in the literature have shown the importance of Piezo channels

(especially Piezo 1 and 2) as another mechanosensor for the chondrocyte, especially for high-strain scenarios [169, 213, 241], which are not incorporated in the present study. In the future, as more downstream pathways of Piezo channels are delineated, incorporating Piezo channel-mediated mechanotransduction pathways could be a valuable addition to the present multiscale workflow. Furthermore, future studies could also incorporate the transport of nutrients, growth factors, and inflammatory cytokines across the cartilage, as was done in Eskelinen et al. [242], to obtain a spatial distribution of these factors, which are known to influence cartilage metabolism.

It is important to note that the intracellular regulatory network for chondrocyte mechanotransduction and inflammation was developed using a combined data-driven and knowledge-based approach. For the data-driven component, a set of microarray databases from studies on mice was used [228]. It is worth mentioning that a detailed database specifically for human cartilage did not exist in the literature. While developing the network, it was ensured that the pathways included in the final model were common across species. For calibration and preliminary validation, the experimental study by Li et al. [52] was considered, which used bovine cartilage explants. Since gene expression in that study was obtained using qPCR experiments, no spatial data of gene expression was available for comparison with the corresponding numerical models. In the future, the use of spatial transcriptomics will provide spatial gene expression data of cartilage for a more detailed validation of the numerical multiscale model [243].

For the verification of the FE models developed in this study, mesh convergence analyses were conducted for both the tissue and cell scale, which are reported in Appendix C. Subsequently, the sensitivity of the regulatory network to changes in mechanical loading and cytokines was studied using a two-way full factorial design. To validate the overall predictions of the multiscale model, the gene expression of ACAN, COL-II and ADAMTS5 due to 10% loading of cartilage explants (in section 4.2.2) was compared with that measured in experiments by Li et al. [52]. Furthermore, sGAG loss measured in the same study for different loading conditions were compared with the loss of Aggrecan predicted by the multiscale model (Figure 4.3). The next step in validation of the multiscale model will be to separately validate the individual length scales and their connections. To do so, in the future, multiscale experiments need to be performed that can measure both the mechanics at the tissue and cell scales simultaneously, as well as capture intracellular behavior by measuring the cellular response in terms of gene expressions and cell-secreted factors. Doing such experiments in a traditional bioreactor setup can be difficult. An alternative could be the use of microfluidic devices, such as those developed by Paggi et al. [244, 245] and Occhetta et al. [246], which can provide precise experimental data across multiple length scales. Another alternative could be

the use of laser scanning microscopy approaches, as developed in [247–249], which enable real-time measurement of chondrocyte deformations during loading of cartilage explants.

Lastly, the multiscale modeling workflow developed in this study is unidirectional in nature, where the information flow is from the tissue scale to the intracellular scale via the cellular scale. In the future, efforts can be made to complete the feedback loop, i.e., to incorporate how changes in intracellular behavior can, in turn, affect the cellular microenvironment and thereby change the global mechanical behavior at the tissue scale. However, this approach presents multiple challenges. Firstly, a calibrated profile needs to be developed that can relate cell-level gene expression to actual changes in the cellular microenvironment in terms of the quantity and mechanical properties of deposited extracellular matrix components. Secondly, advanced computational homogenization techniques are needed to enable bidirectional coupling between tissue- and cell-scale models, synchronously solving problems at both scales while exchanging information at each time step [139]. In this approach, the constitutive behavior at each higher scale integration point is determined by the average stress from a corresponding lower-scale problem, which accounts for micro-scale heterogeneity. The boundary conditions of the lower scale are modified iteratively based on the higher scale, driving new simulations. The degree of non-uniformity in displacement and fluid pressure fields affects the accuracy of data passing schemes, and future implementations for biphasic cartilage problems may benefit from second-order data passing (which assumes a second-order mapping of the displacement and pore pressure between the tissue and cell scale), as mentioned in Sibole et al. [141]. Additionally, the size of the cellular-scale model must be verified as a representative volume element (RVE), as RVE size impacts the accuracy of the data-passing process [250].

In conclusion, the multiscale modeling workflow developed in this study proves to be a powerful tool in understanding the complex interplay of mechanics and inflammation in articular cartilage. By integrating tissue, cellular, and intracellular scale models, it provides a more comprehensive and accurate framework for studying cartilage mechanobiology. This approach facilitates a deeper understanding of the pathophysiology of OA and provides valuable insights that can guide the development of targeted therapeutic strategies.

# Chapter 5

# A multiscale approach to study chondrocyte mechanobiology using a cartilage-on-chip setup

Satanik Mukherjee[1], Raphaelle Lesage[1], Laurens Spoelstra[4], Thanh Le[4], Carlo A. Paggi[4], Jorge Barrasa-Fano[1], Hans Van Oosterwyck[1], Marcel Karperien[4], Liesbet Geris[1,2,3]

[1]Biomechanics Section, KU Leuven, Belgium

[2]GIGA Institute, University of Liege, Belgium

[3]Skeletal Biology and Engineering Research Center, KU Leuven, Belgium

[4]Department of Developmental Bioengineering, University of Twente, Netherlands

This chapter is based on a manuscript prepared to be submitted: S. Mukherjee, R. Lesage, L. Spoelstra, T. Le, C. A. Paggi, J. Barrasa-Fano, H. Van Oosterwyck, M. Karperien and L. Geris. "A multiscale approach to study chondrocyte mechanobiology using a cartilage-on-chip setup."

## 5.1 Introduction

Understanding chondrocyte mechanobiology is crucial for unraveling the complex processes underlying cartilage health, disease, and regeneration. Chondrocytes, the primary cells in articular cartilage, are highly responsive to mechanical stimuli, which regulate their behavior, metabolism, and functionality. Disruptions to normal mechanical loading, such as those seen in joint injuries or diseases like osteoarthritis (OA), can lead to chondrocyte dysfunction and cartilage degradation [166]. In contrast, tissue engineering approaches leverage mechanical stimulation to activate chondrocytes or chondroprogenitor cells, promoting cartilaginous matrix formation [251, 252]. While traditional *in vivo* models have provided valuable insights into chondrocyte biology [253], their limitations in replicating human-specific responses and controlling environmental factors have spurred the development of more advanced experimental platforms.

Recent advances in microfluidic technology have led to the development of cartilage-on-chip models, which offer the potential to replicate the *in vivo* microenvironment of articular cartilage in a controlled, reproducible setting [244–246, 254]. These microfluidic devices allow precise manipulation of mechanical and biochemical cues, such as nutrients, growth factors, and drugs, to study chondrocyte behavior under various conditions. Made from optically transparent materials like polydimethylsiloxane (PDMS), these devices enable longitudinal, real-time imaging, allowing visualization of cell and tissue responses to stimuli, even at the single-cell level. By combining this *in vitro* approach with multiscale *in silico* modeling, it is possible to explore the mechanobiology of chondrocytes at multiple scales, from the cellular to the tissue level. Additionally, these devices use small volumes (in the microliter range), reducing the need for large quantities of reagents and cells compared to traditional 2D and 3D cell culture models.

Despite their potential, tuning the wide range of parameters (mechanical, biochemical, etc.) in cartilage-on-chip devices to address specific research questions can be time-consuming and resource-intensive. In this context, multiscale *in silico* modeling, such as that described in Chapter 4, can serve as an enabling tool to optimize these parameters. Conversely, the high-resolution imaging capabilities of the chips can be used to validate the various length scales of the *in silico* model, providing feedback to improve its accuracy. By integrating *in vitro* experiments with multiscale simulations, a comprehensive platform can be created for studying chondrocyte mechanobiology. This approach would allow researchers to investigate cell-level responses to varying mechanical forces while capturing broader tissue-level effects on cartilage function.

The aim of this chapter was to develop a combined *in silico-in vitro* workflow,

that would enable researchers to investigate the chondrocyte mechanobiology using a cartilage-on-chip setup. The workflow was developed based on pilot experimental data, which enabled validating the different length scales in the workflow. Further detailed experimentation would be necessary to obtain biological insights using the workflow, which is beyond the scope of this thesis. The structure of this study was as follows: First, inverse characterization of the agarose hydrogel was performed to calibrate its material parameters for the *in silico* model. Next, multiscale experiments were conducted within the cartilage-on-chip setup to obtain experimental data across different length scales, driven by mechanical stimulation applied within the device. Finally, a multiscale *in silico* model was developed for the cartilage-on-chip system, and numerical predictions at various length scales were compared with the experimental results.

## 5.2 Materials and Methods

### 5.2.1 Description of the cartilage-on-chip setup

The cartilage-on-chip device used in this study is a microfluidic device that was developed by Paggi et.al. [244, 254]. It consists of a rectangular culture chamber (1260 $\mu$m $\times$ 4000 $\mu$m) designed to accommodate cartilage explants or engineered tissue constructs. This chamber is separated from an adjacent perfusion channel (4400 $\mu$m $\times$ 500 $\mu$m) by an array of pillars (100 $\mu$m $\times$ 100 $\mu$m cross-section) with an inter-pillar spacing of 100 $\mu$m, allowing controlled nutrient and waste exchange (Figure 5.1). On the opposite side of the culture chamber, three pneumatic actuation chambers are integrated to apply mechanical stimulation. These chambers are separated from the culture chamber by a thin PDMS membrane (50$\mu$m thick), which deforms in response to pressure changes within the actuation chambers. Each actuation chamber is equipped with a single inlet (1 mm diameter) for pressure control. A continuous 50-$\mu$m gap along the membrane connects the three actuation chambers, enabling uniform actuation. A particular feature of this device is the ability of generate a wave-like deformation field in the construct by independently varying the pressures in the three actuation chambers, thereby mimicking the multiaxial loading that is encountered in the articular cartilage of the human knee joint. The height of all microfluidic structures within the device is either 200 or 220 $\mu$m.

A typical experiment started by seeding primary human chondrocytes (1.5 million cells/mL) in low-melting temperature agarose (2% w/v), together with fluorescent beads (3.17 $\mu$m diameter, 5 millions/mL) and injected in the cartilage-on-chip device at day 0. After one minute, chondrocyte proliferation medium was introduced into the perfusion channel. At day 1, to promote

extracellular matrix formation, the chondrocyte proliferation medium was replaced with a chondrocyte differentiation medium. The differentiation medium consisted of Dulbecco's Modified Eagle Medium (DMEM) supplemented with 1× insulin–transferrin–selenium (ITS) premix, 100 U/mL penicillin, 100 $\mu$g/mL streptomycin, 4 mM proline, 50 $\mu$g/mL ascorbic acid 2-phosphate, 1× sodium pyruvate, 20 ng/mL TGF-$\beta$3, and $10^{-7}$ M dexamethasone based on previous studies by Paggi et al. [254]. Medium was changed daily throughout the culture period. Subsequently, different experimental regimes were applied by varying the duration of loading (section 5.2.4).

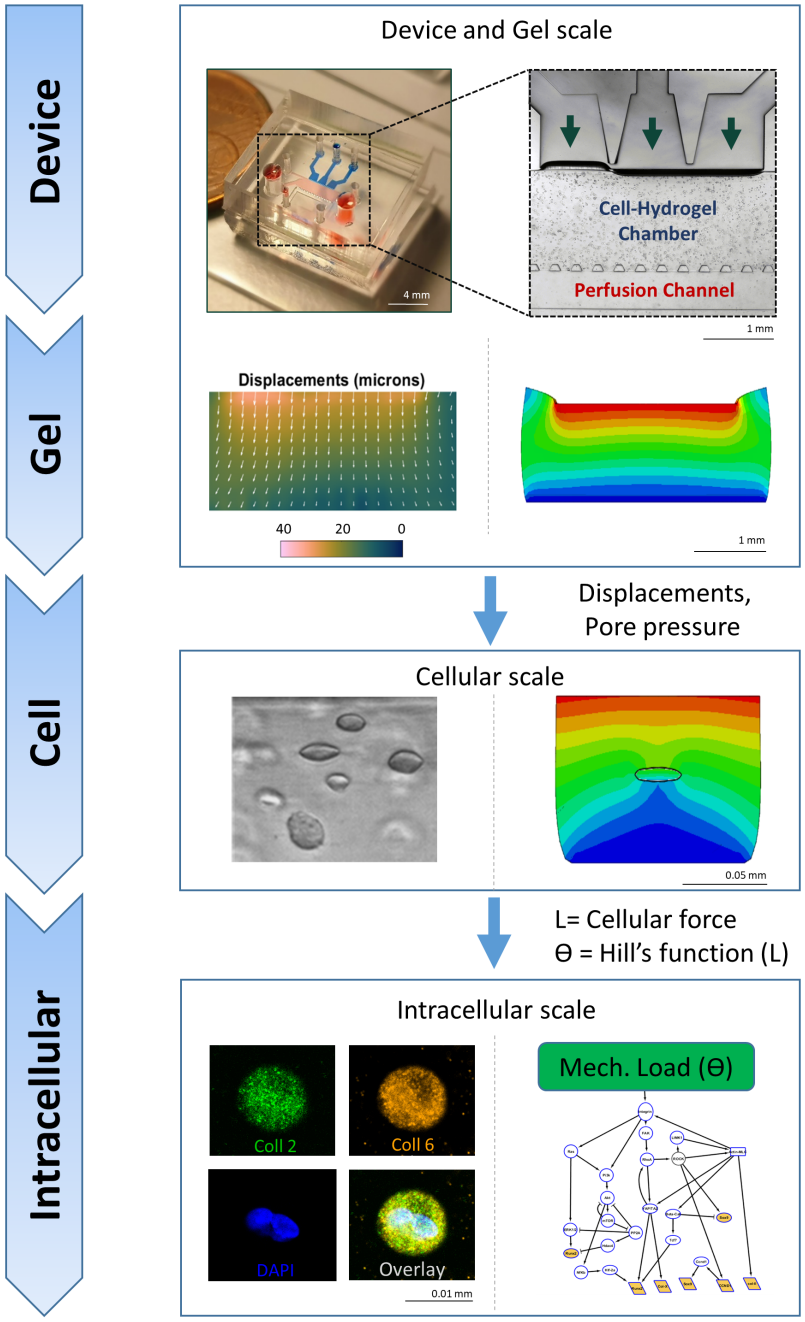


Figure 5.1: Overview of the multiscale model workflow illustrating the different length scales involved in the cartilage-on-chip setup (left) and their corresponding *in silico* models (right).

### 5.2.2 Stress relaxation experiments on agarose hydrogel

To develop a digital twin of the cartilage-on-chip setup, a precise mechanical characterization of the agarose hydrogel was performed in order to calibrate the mechanical parameters required for developing the corresponding finite element (FE) model.

For this purpose, cylindrical agarose constructs with a diameter of 8 mm and a thickness of 1.5 mm were prepared, using an agarose concentration of 2% w/v. Since subsequent experiments in the cartilage-on-chip setup involved cells and fluorescent beads embedded in agarose (see Section 5.2.4), various combinations of bead diameters and bead densities were studied by embedding them in the agarose constructs, together with chondrocytes. This was done to examine the influence of the beads and chondrocytes on the global mechanical behavior of the hydrogel. Two bead densities (1.5 million/mL and 10 million/mL) were studied for fluorescent beads of diameter 3.3$\mu$m. The density of the chondrocytes was kept to 1.5 million/mL as was used in the cartilage-on-chip experiments.

To measure the mechanical behavior of the hydrogels, a two-step uniaxial compression and stress relaxation protocol was devised based on previous studies in the literature [186, 255]. The experiments were performed on a Rheometer (HR20, TA Instruments Inc., New Castle, Delaware, USA) (Figure 5.2(a)). First, a tare load of 0.02N was manually applied to ensure contact between the flat plate of the compression device and the agarose constructs. Subsequently, a 2% compression was applied with a speed of 0.01 mm/sec followed by a stress-relaxation step of 300 seconds. Next, a 20% compression of the construct was performed at a loading rate of 0.16 mm/sec (corresponding to strain rate of 2%/sec) followed by stress-relaxation step up to a total time of 1500 seconds.

### 5.2.3 Inverse FE characterization of agarose hydrogel mechanical properties

#### FE model development for agarose material characterization

A FE model of the agarose construct was developed in Abaqus 2023 (SIMULIA, Providence, RI, USA) to perform inverse characterization of the material behavior of agarose (Figure 5.2(b)). The cylindrical construct, with a diameter of 8 mm and thickness of 1.5 mm, was discretized using 3D 8-node reduced integration brick elements (C3D8P). A rigid compression disc, with a diameter of 12 mm, was meshed using 3D 4-node rigid elements (R3D4). The loading

protocol, as described in the previous section, was applied to a reference point located on the rigid disc.

A frictionless node-to-surface contact interaction was defined between the compression disc and the agarose construct using the penalty method for constraint enforcement. To simulate the free flow of pore fluid, a zero pore pressure boundary condition was applied to the curved surface of the cylindrical construct. Additionally, vertical displacement was constrained at the bottom of the construct using a 'Zsymm' boundary condition to replicate the uniaxial compression condition.

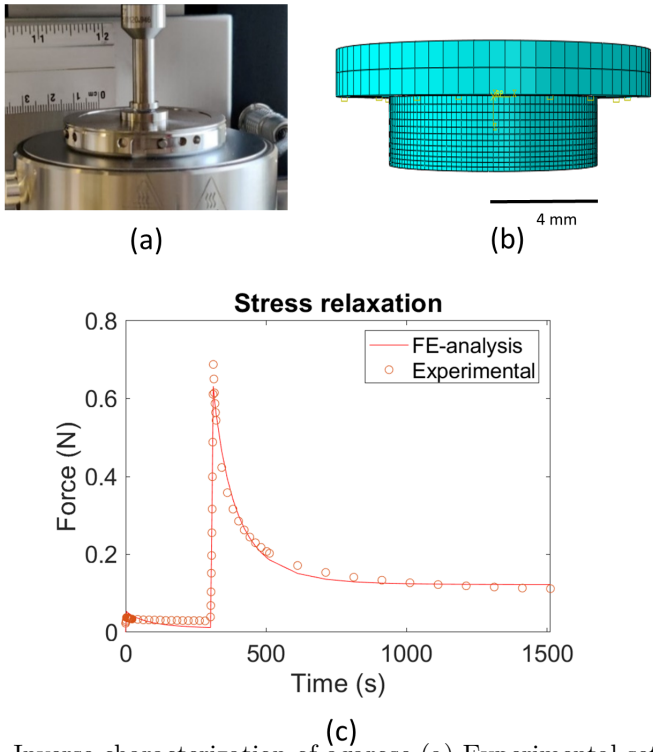


Figure 5.2: Inverse characterization of agarose (a) Experimental setup; (b) FE model of the setup; (c) Comparison of reaction forces between experiments and the optimized FE model.

### Constitutive model of agarose hydrogel

The agarose hydrogel was modeled using a poro-viscoelastic constitutive framework within Abaqus 2023, to effectively capture the coupled mechanical and fluid transport behavior of the agarose hydrogel under compression. The fluid flow within the agarose hydrogel followed Darcy's law:

$$\mathbf{q} = -k\nabla p, \tag{5.1}$$

where $\mathbf{q}$ iss the fluid flux, $k$ is the permeability, and $\nabla p$ is the pressure gradient. The total stress $\sigma_{\text{tot}}$ in the material is given by:

$$\sigma_{\text{tot}} = \sigma_{\text{ve}} - p\mathbf{I}, \tag{5.2}$$

where $\sigma_{\text{ve}}$ represents the viscoelastic stress, $p$ the pore pressure, and $\mathbf{I}$ the identity tensor.

The viscoelastic behavior of the agarose hydrogel was described using a one-parameter Prony series for the deviatoric deformations:

$$G_R(t) = G_0\left(1 - g_1(1 - e^{-t/\tau_1})\right), \tag{5.3}$$

where $G_R(t)$ represents the time-dependent shear modulus, $G_0$ the instantaneous shear modulus, $g_1$ the Prony series parameter, and $\tau_1$ the relaxation time. The instantaneous shear modulus $G_0$ was related to the instantaneous elastic modulus $E_0$ and Poisson's ratio $\nu_0$ by:

$$G_0 = \frac{E_0}{2(1+\nu_0)}. \tag{5.4}$$

Since there was no possibility to measure lateral deformations in the experimental setup, the value of the Poisson's ratio $\nu_0$ was assumed to be 0.12 based on literature [256]. The key parameters governing the poro-viscoelastic behavior included the permeability $k$, the instantaneous elastic modulus $E_0$, and the Prony series parameters $\tau_1$ and $g_1$. These parameters were determined through an inverse FE characterization approach, as described in the next section.

### Optimization algorithm to evaluate the mechanical parameters

To determine the mechanical parameters ($k$, $E_0$, $\tau_1$ and $g_1$) of the agarose hydrogel, an optimization approach was employed in Matlab R2022b (The MathWorks Inc., Natick, Massachusetts) using a least squares objective function. The optimization process aimed to minimize the difference between experimentally measured reaction forces and those obtained from FE simulations.

The objective function was defined as:

$$F = \frac{1}{N} \sum_{i=1}^{N} \left( R_i^{\mathrm{FE}} - R_i^{\mathrm{exp}} \right)^2 \tag{5.5}$$

where $R_i^{\mathrm{FE}}$ represents the reaction force obtained from the FE model at the $i$-th data point, $R_i^{\mathrm{exp}}$ is the corresponding experimentally measured reaction force, and $N$ is the total number of data points. The optimization was performed using Matlab's `fminsearch` function, which employs the Nelder-Mead simplex algorithm. This algorithm does not require gradient information, making it suitable for problems where the objective function is nonlinear and potentially non-differentiable. The function was initialized with an initial guess for the mechanical parameters, including permeability ($k$), instantaneous elastic modulus ($E_0$), and Prony series parameters ($\tau_1, g_1$). The optimization procedure iteratively adjusted these parameters to minimize the objective function. Convergence was assumed when the relative change in function value between iterations fell below a predefined tolerance. The optimized parameters were then validated by comparing the predicted reaction forces with experimental data, ensuring an accurate representation of the hydrogel's mechanical behavior.

### 5.2.4 Multiscale experiments in cartilage-on-chip setup

#### Mechanical stimulation of chondrocytes in cartilage-on-chip setup

Two distinct culture conditions were tested in the device, a static and a dynamic one. In the static condition, serving as the control condition, culture of the chondrocytes for a total of 14 days was performed in the device without any mechanical stimulation. For the dynamic compression stimulation regime, cyclic compression was applied after an initial week of static culture, using a pressure of 300 mbar at a frequency of 1 Hz, approximating the physiological loading frequency of walking. The pressure of 300 mbar was based on previous studies in the setup [254], where 300 mbar of pressure imposed a physiological level of strain in the hydrogel. Mechanical stimulation was initiated on day 7 of culture and applied for 1 hour per day over a total duration of 5 days (T7–T11). This was followed by an additional 2 days of static culture to allow sufficient time for accumulation of cell secreted factors in response to mechanical loading. On day 14, the samples were removed from culture for further analyses.

Mechanical actuation was controlled via a dedicated setup consisting of a positive pressure controller, a negative pressure source, and a system of two-way valves

(7-switch, Fluigent) for rapid pressure modulation as seen in Figure 5.3. The entire system was managed using AiO software, as previously described [254].

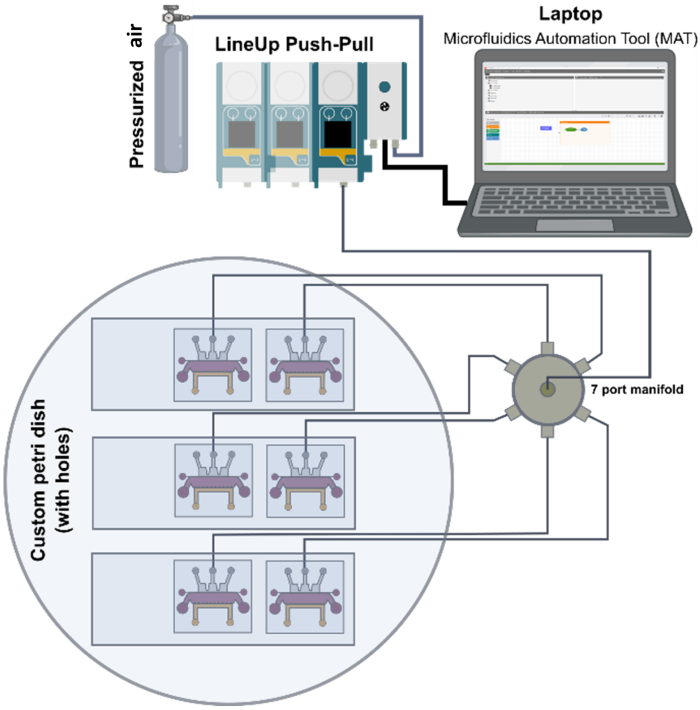


Figure 5.3: Overview of the control system used to actuate the cartilage-on-chip devices

### Measurement of hydrogel and cell deformation in the cartilage-on-chip

To assess the deformation of the hydrogel and embedded chondrocytes over multiple time points ($T_1$, $T_7$, $T_{11}$ and $T_{14}$) in the cartilage-on-chip device, controlled mechanical loading was applied using a pressure of 300 mbar. Brightfield and fluorescence microscopy images were acquired at both 0 mbar (unloaded) and 300 mbar pressures at 4× magnification to evaluate the deflection of the PDMS membrane and hydrogel deformation, respectively. In addition, imaging to measure cell deformations was performed. Each chip was imaged using brightfield and fluorescence microscopy at 40× magnification under both 0 mbar and 300 mbar pressure conditions. Multiple images were captured around the central region of the chip to ensure representative data collection. This region was selected because it experiences uniform membrane deformation, while

deformation is reduced near the edges due to membrane attachment. Images were systematically recorded and stored for subsequent analysis, enabling a comprehensive assessment of hydrogel and cellular deformation under mechanical stimulation.

This methodological approach provided insights into the time-dependent mechanical behavior of the hydrogel and its embedded chondrocytes, facilitating a detailed understanding of their response to mechanical loading.

#### Immunofluorescent staining and confocal imaging of mechanically stimulated samples in cartilage on chip setup

To assess deposition of matrix proteins due to mechanical stimulation in the device, immunofluorescent staining was performed for COL-VI (predominantly found in the chondrocyte pericellular matrix, PCM), DAPI (for nuclear staining), and COL-II (predominantly found in cartilage extracellular matrix). This was followed by 3D confocal imaging (Zeiss LSM880). Confocal imaging was performed to capture high-resolution z-stacks, using appropriate settings to achieve optimal signal-to-noise ratios for each fluorophore. Z-stacks were acquired with a minimum of 2-3 slices per cell (or "chondron", which is the chondrocyte and its surrounding pericellular matrix) to ensure sufficient resolution. The pre-defined imaging locations as shown in Figure 5.4 were chosen to be in the center of the gel to avoid edge artifacts. The collected data allowed for precise analysis of deposition of matrix proteins by the embedded chondrocytes within the gel, providing insights into the spatial deposition of matrix proteins in the different experimental conditions.

### 5.2.5 Post-processing of data from cartilage-on-chip experiments

#### Image processing to evaluate membrane deformations

To calculate the deformation of the membrane in the cartilage-on-chip device under a 300 mbar pressure applied in the actuation chamber, an in-house Matlab code was developed. The code utilized image processing algorithms to compare the undeformed and deformed brightfield images of the membrane at $4\times$ magnification as described in section 5.2.4. First, it enhanced the image contrast using adaptive histogram equalization, then converted the images to binary format to isolate the membrane. The Canny edge detection filter was applied to identify the edges of the membrane, and the deformation was subsequently calculated at the membrane's center. Measuring the membrane

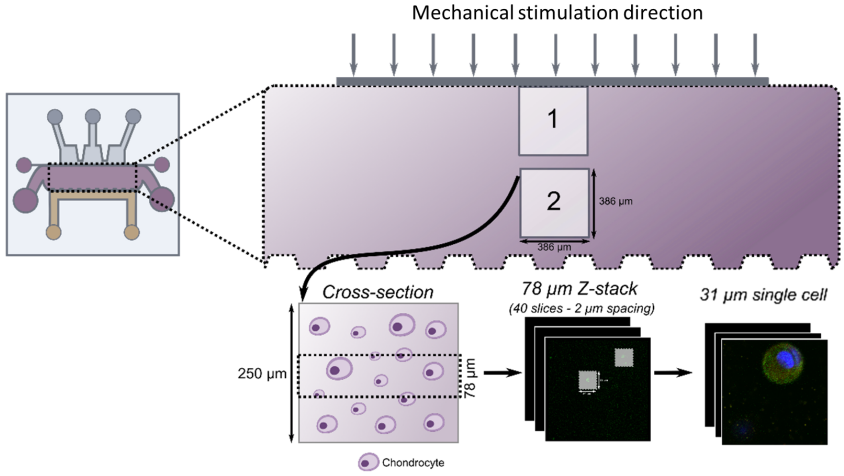


Figure 5.4: Schematic representation of the settings used for confocal microscopy of immunofluorescent stained samples

deformation was crucial, as it provided the input boundary condition for the FE model of the cartilage-on-chip device, as detailed in Section 5.2.6. Furthermore, changes in membrane deformation are expected to be sensitive to variations in the stiffness of the agarose construct, which will occur due to cartilage maturation over time. These changes in stiffness will likely be reflected in corresponding variations in membrane deformation, offering valuable insights into the progression of the maturation process.

### Non-rigid image registration technique to measure hydrogel deformation from bead displacements

To measure the deformation of the hydrogel under mechanical compression, fluorescent microscopy images at 4× magnification were acquired for both unloaded and 300 mbar pressure-loaded conditions, as described in section 5.2.4. First, a lowpass difference-of-gaussians (DoG) filter was applied to reduce background noise and enhance bead contrast. The remaining differences between the loaded and unloaded images were attributed to non-rigid displacements caused by the applied mechanical loading. To calculate these displacements, a B-spline-based free-form deformation (FFD) algorithm, as developed by Jorge-Peñas et al. [257], was used. In the FFD algorithm, the goal was to align the relaxed image, $I_r$, with the stressed image, $I_s$. A displacement field $u(x)$ was applied to warp $I_r$ using a transformation model $T$, and the alignment

was evaluated with a similarity metric $S$. The transformation parameters were updated iteratively until convergence. The transformation was defined by a deformable B-spline grid, where the parameters represented displacements of control points. The algorithm was implemented using in-house Matlab codes, which enabled estimation of the deformation field in the hydrogel.

### Image processing to evaluate cell deformations

To calculate the cell deformations from the brightfield images taken at 40× magnification, individual cells were segmented from the loaded and unloaded images using an image processing approach developed by Buggenthin et al. [258](Figure 5.7(a)). The approach, designed specifically for high-throughput segmentation of cells from brightfield images, included a series of steps for background correction, foreground object detection and segmentation of cells as discussed below:

**Background correction:** the raw image was divided into overlapping tiles (30×30 pixels), and the intensity distribution of each tile was analyzed. Using density-based clustering, tiles were classified as background or foreground. The mean intensity of background tiles was used to generate a background image, which was then used to correct the original image by dividing it by the background. Any 'halo' effect (brighter pixels than the background) was corrected by setting them to the background intensity.

**Foreground object detection**: maximally stable extremal regions (MSER) were used to identify foreground objects. MSER is a thresholding-based segmentation method, where each pixel was classified as part of the foreground or background based on intensity. Stable extremal regions were determined by iterating over different threshold values, and nested regions were merged. This resulted in a binary mask representing the foreground objects.

**Segmentation of chondrocytes:** a modified marker-based watershed algorithm was used to separate the chondrocytes from the hydrogel background. The raw image was inverted, and local intensity maxima (cell centers) were identified. These maxima were then imposed on a distance transform of the foreground mask. Watershed segmentation was applied, creating an initial segmentation of the cells.

**Over-segmentation correction:** to avoid over-segmentation, a rule-based 'split and merge' procedure was applied. Adjacent objects were checked for likely over-segmentation based on pixel likelihood to be foreground or background and the eccentricity of the objects. If objects met certain criteria, they were merged.

**Final object filtering:** small regions and regions with high eccentricity (greater than 0.99) were discarded, as they were unlikely to represent cells. Objects touching the image border were also removed. The final output was a binary mask of identified cells.

With final segmented cells, the change in area of the cells were calculated to define the deformation in terms of projected area change and compare it to the numerical studies.

### 5.2.6 Multiscale *in silico* model of the cartilage-on-chip device

In parallel with the multiscale experiments mentioned in the previous section, a multiscale *in silico* model of the cartilage-on-chip setup was developed, connecting the tissue, cellular, and intracellular scales, following the multiscale workflow developed in chapter 4 (Figure 5.1). The different length scales were incorporated as described below:

**Device and gel scale:** at the gel scale, a 3D FE model of the cell-laden agarose in the cartilage-on-chip device was developed. The agarose was modeled with poro-viscoelastic material behavior, with parameters calibrated in Section 5.2.2. A compression, equivalent to the average membrane deflection at day 7 (measured in Section 5.2.5), was applied to the top surface of the agarose, while vertical deformation of the bottom surface was restricted. Additionally, a zero pore pressure boundary condition was applied to the bottom surface to simulate the free flow of pore fluid. Lateral deformation was restricted on all the lateral surfaces.

**Cellular scale:** at the cellular scale, a 100 $\mu$m cube of agarose gel with a spherical chondrocyte (diameter 10 $\mu$m) at its center was modeled. The cell was treated as a poro-viscoelastic material, as described in Chapter 4. The cellular scale model was driven by displacements and pore pressure obtained from the tissue-scale model using the submodel feature in Abaqus.

**Intracellular scale:** cellular forces (L) obtained from the cellular scale were converted to mechanical loading input ($\theta$) for the intracellular scale using a Hill's function to map the total force to the intracellular regulatory network input. The intracellular scale focused on the gene and protein regulatory networks involved in mechanotransduction and inflammation. This network incorporated key pathways such as integrin-mediated mechanotransduction, inflammatory signaling, and their crosstalk. The network model integrates these pathways to simulate the chondrocyte response to mechanical loading and inflammation. For more detailed implementation and equations related to the biphasic material model and multiscale coupling, readers are referred to Chapter 4.

### 5.2.7 Statistical analysis

The experimental results from the stress-relaxation tests in agarose hydrogel was done for n=3 samples, and the mean and standard deviation of the data were calculated. To compare the membrane deformations at three time points (day 1, 7, 14), a one-way ANOVA test was performed to check for the statistically significant difference between the mean deformations at the respective time points. The data for change in cell projected area with distance from the membrane was fitted with a linear trendline using least squares regression to identify the overall trend.

## 5.3 Results

### 5.3.1 Inclusion of cells and beads reduce the stiffness of agarose hydrogel

Stress relaxation experiments revealed that the inclusion of chondrocytes (1.5 million/mL) reduced the instantaneous stiffness of the agarose hydrogel, as evidenced by a decrease in mean peak forces (out of n=3 samples) at the end of compression in Figure 5.5. Specifically, the mean peak force was reduced by 3.35% (from 0.867 N to 0.838 N). Similar effects have been reported in previous studies [259]. However, the relaxation times remained unchanged with the inclusion of chondrocytes. Further addition of beads, along with cells, led to a further reduction in stiffness, as indicated by a further decrease in peak forces by 17.20% during compression. Interestingly, increasing the bead concentration from 1.5 million/mL to 10 million/mL did not affect the peak force or stiffness. However, at higher bead densities, the relaxation times decreased, with denser bead concentrations leading to faster relaxation of the hydrogel.

### 5.3.2 Inverse characterization of agarose hydrogel

Inverse characterization of the agarose hydrogel resulted in a close match between the numerical and experimental results, as shown in Figure 5.2. The optimized values for the instantaneous elastic modulus ($E_0$), permeability ($k$), and Prony series parameters ($\tau_1, g_1$) for the hydrogel containing cells (1.5 million/mL) and beads (1.5 million/mL) were determined to be 0.041 MPa, $1.237 \times 10^{-12}$ $m^4$/N-s, 0.82234, and 106.08 seconds, respectively.

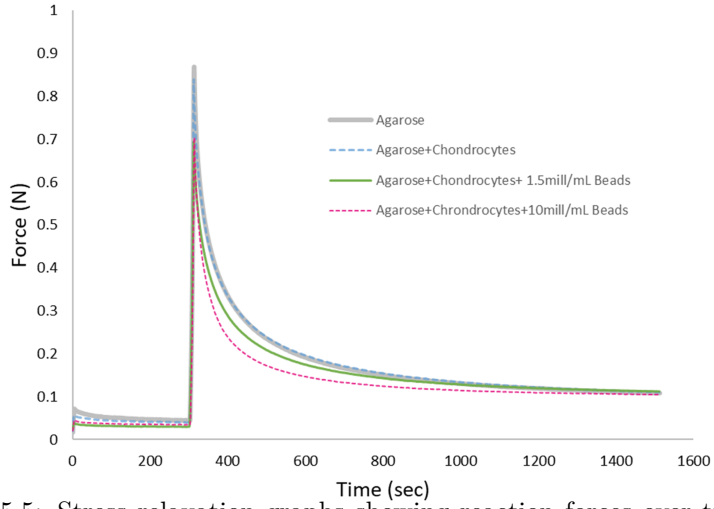


Figure 5.5: Stress relaxation graphs showing reaction forces over time after two-step loading till 20% strain. The conditions tested are: stress on agarose hydrogel, agarose hydrogel with chondrocytes (1.5 mill/mL), agarose hydrogel with chondrocytes (1.5 mill/mL) and beads (1.5 mill/mL and 10 mill/mL).

### 5.3.3 Membrane deformation in the cartilage-on-chip setup under pneumatic pressure

The deformation of the membrane in the cartilage-on-chip setup due to a pneumatic pressure of 300 mbar was measured at three time points: day 1, day 7, and day 14, from brightfield images (Figure 5.6(a-c)). Measurements taken from three chips showed mean deformations of 35.72, 36.26, and 30.21 $\mu$m at days 1, 7, and 14, respectively. However, a one-way ANOVA test indicated no statistically significant differences between the means at the 3 time points.

### 5.3.4 Gradient deformation of the gel observed in both experiments and simulation

Figure 5.6(d,e) shows the gel deformation at day 7 due to a 300 mbar pressure, tracked using fluorescent beads and non-rigid image registration. A gradient in deformation was observed, with the surface facing the membrane experiencing the most deformation. The FE model predicted a similar deformation pattern (Figure 5.6(f)). Comparing experimental and numerical displacements at the center of the gel (Figure 5.6(g)), the FE model showed higher displacements

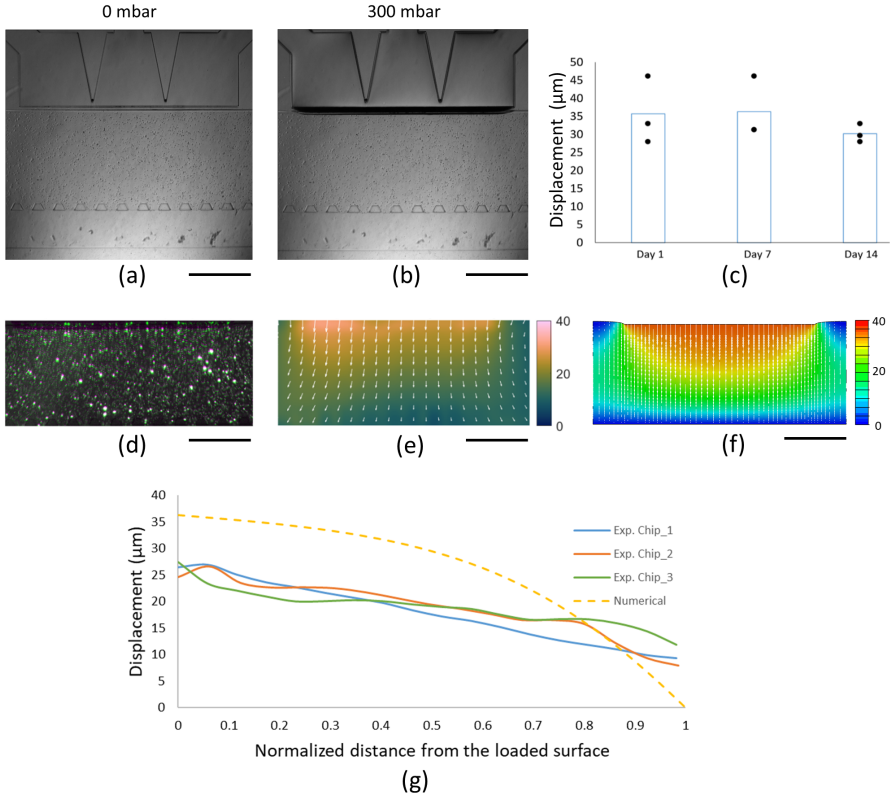


Figure 5.6: Estimation of the deformation of the hydrogel in the cartilage-on-chip setup. (a) Unloaded chip. (b) Loaded chip at 300mbar actuation pressure. (c) Mean of experimental membrane displacements at three time points. (d) Overlayed image of bead displacements obtained from fluorescence microscopy. Purple: unloaded, green: loaded. (e) Deformation (in $\mu$m) of the gel obtained by tracking the beads using a non-rigid image registration technique. (f) Deformation of the gel obtained from FE simulations (in $\mu$m). The white arrows show the direction of deformation for panels e and f. (g) Variation of deformation at different depths, compared between the experiments (solid line) and simulations (dashed line). Scale bar=1 mm.

in the top 80% of the gel, tapering to zero at the bottom due to the zero vertical displacement boundary condition. However, experiments showed non-zero displacement (8-10 $\mu$m) at the bottom of the gel. This was likely due to small movement through the gap between the micro-pillars at the bottom of the gel. When comparing the measured deformation of the gel with simulation

results, the simulations tended to overpredict deformations, particularly in the top 80% of the gel. Upon closer inspection, it was found that, especially after a week of culture, some gels had developed a small gap between the actuating membrane and the hydrogel due to hydrogel shrinkage over time. This gap had to be covered by the membrane before deforming the hydrogel, leading to a smaller effective compression in experiments than predicted by the simulations.

### 5.3.5 Cell segmentation and projected area change under mechanical loading

The cell segmentation algorithm successfully identified individual cells from the brightfield images, with the intermediate steps of segmentation shown in Figure 5.7(a). Next, the percentage change in the projected area of cells under 300 mbar mechanical loading was plotted against the relative initial position of the cell across the thickness of the chip. Results were gathered from cells in three separate chips, as shown in Figure 5.7(b). The decrease in projected cell area showed a trend (as depicted by the linear trendline obtained by fitting the data using least squares regression) with higher decrease for cells closer to the actuating membrane. Simulations of the cell-level FE model at three locations within the gel revealed that the cellular forces (L) obtained from the FE model followed a gradient, with the cells at the top, mid and bottom positions experiencing forces equal to $3.06\times 10^{-6}$ N, $2.38 \times 10^{-6}$ N and $1.17\times 10^{-6}$ N respectively.

### 5.3.6 Influence of mechanical loading on chondrocyte behavior

From cellular-scale simulations at three locations, the peak cellular force ($L$) was obtained, and the mechanical load ($\theta$) was computed using Hill's function (Chapter 4). This parameter was then used to simulate the intracellular gene regulatory network. Subsequently, expression of relevant biomarkers under mechanical loading were analyzed (Figure 5.8). Due to the low stiffness of agarose hydrogel compared to native cartilage, the mechanical load sensed by the cells remained low, resulting in minimal activation of mechanotransduction pathways (Figure 5.8a). Inflammatory marker activity was also low ($<0.05$) across all conditions (Figure 5.8b). Conversely, stable chondrocyte markers (SOX9, COL-II, and ACAN) showed high activity, while pro-hypertrophic markers were negligible, indicating a stable anabolic chondrocyte state. Confocal microscopy (Figure 5.8d) qualitatively confirmed significant deposition of COL-II and COL-VI after one week of static culture in the chips. This deposition further increased following an additional week of dynamic compression, highlighting

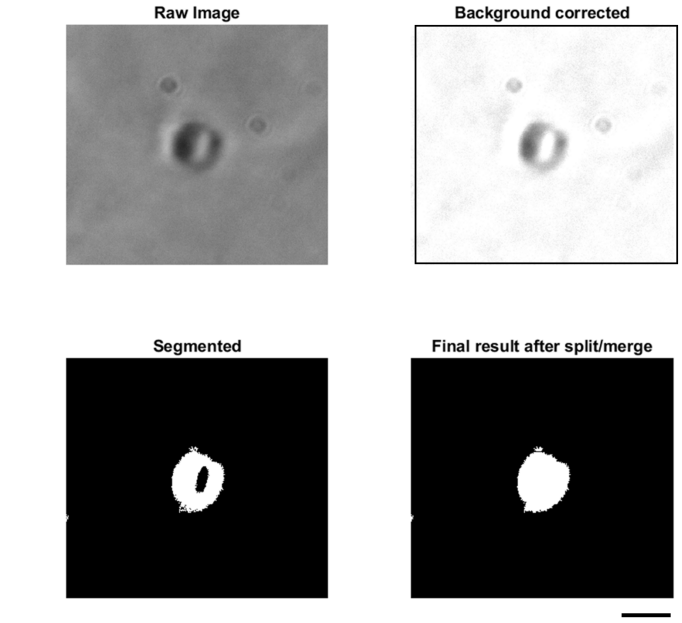


(a)

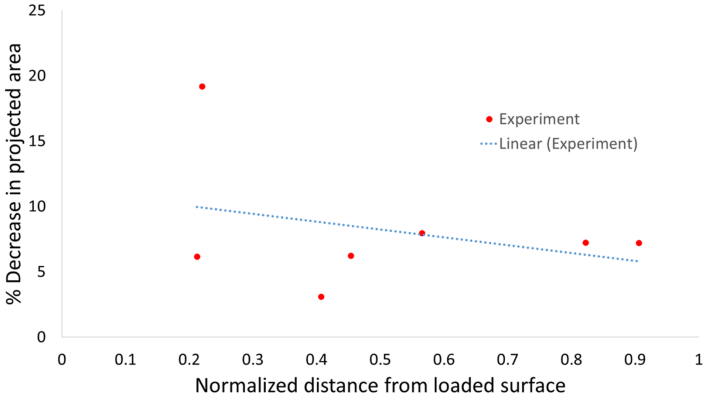


(b)

Figure 5.7: Image processing (a) The different steps of segmenting a single cell from the brightfield image; (b) Variation of decrease in area of projected cells across the thickness of the gel. The blue dotted line represents the linear trendline obtained by fitting the data using least squares regression. Scale bar=10 $\mu$m.

the role of mechanical loading in maintaining a stable chondrocyte phenotype in this experimental setup.

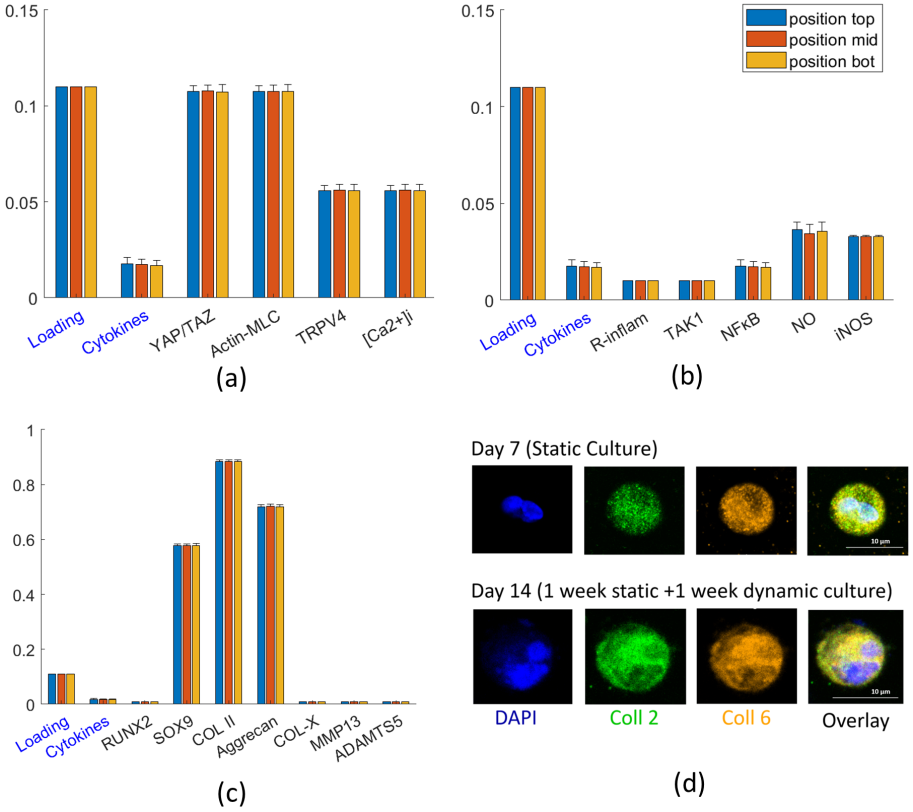


Figure 5.8: Variation of biomarkers in three cells located at the top, middle, and bottom of the gel at a normalized depth of 0.25, 0.5 and 0.75 from the top of the gel (a) Mechanotransduction biomarkers; (b) Inflammation biomarkers; (c) Matrix biomarkers; (d) Immunofluorescent staining for nucleus (DAPI) and matrix proteins Coll 2 and Coll 6. Scale bar: 10 $\mu$m.

## 5.4 Discussion

This study developed a combined multiscale *in vitro* and *in silico* approach to examine the effects of mechanical loading on chondrocyte behavior in a cartilage-on-chip device. Firstly, stress relaxation experiments and inverse

FE characterization were performed to optimize material parameters for agarose hydrogel with cells and beads, closely matching experimental data. The optimized parameters were then used to adapt the previously developed multiscale FE modeling framework. Subsequently, experimental data from different length scales (from device level to cellular level) were processed using relevant image processing algorithms and compared with corresponding simulation results. Intracellular gene regulatory network simulations indicated that the low stiffness of the hydrogel resulted in minimal mechanotransduction activation but maintained high expression of stable chondrocyte markers (SOX9, COL-II, and ACAN) while suppressing pro-hypertrophic markers. Immunofluorescence imaging confirmed substantial deposition of COL-II and COL-VI, after a week of static culture and a further week of dynamic culture. These findings suggest that the developed workflow provides a reliable and quantifiable approach to studying chondrocyte function and matrix production by integrating *in vitro* and *in silico* methods. This integrated framework creates an ideal setting to study chondrocyte mechanobiology, with promising applications in cartilage tissue engineering and research on osteoarthritis progression.

The optimized material parameters for agarose hydrogel in this study, specifically the instantaneous elastic modulus ($E_0$) and permeability ($k$), were 0.041 MPa and $1.237 \times 10^{-12}\,\mathrm{m}^4/\mathrm{N}\cdot\mathrm{s}$, respectively. These values are within the range reported in the literature [256], which noted 0.015 MPa for the elastic modulus and $2.65 \times 10^{-12}\,\mathrm{m}^4/\mathrm{N}\cdot\mathrm{s}$ for permeability. Notably, the elastic modulus of agarose is one to two orders of magnitude lower than that of cartilage (0.25 - 3 MPa) [260], resulting in cellular forces in the agarose hydrogel being three orders of magnitude smaller ($3.06\times10^{-6}$ N) compared to those experienced by chondrocytes in the superficial zone of tibial cartilage ($1.6\times10^{-3}$ N, from Chapter 4).

Despite the over prediction of gel deformation in the simulations, the overall deformation field predicted by the simulations matched the experimental results, validating the gel-scale of the multiscale model. Additionally, the deformation gradient observed in the hydrogel was similar to that in human knee joint cartilage, where the superficial zone experiences higher deformation than the deep zone, as shown in Chapter 3. The bead density of 5 million/mL in the hydrogel was an optimized value. For lower bead densities, the resolution of displacement due to non-rigid image registration was poor, whereas higher bead densities made the gel brittle by incorporating multiple flaws in the hydrogel, resulting in breakage of the hydrogel during mechanical stimulation in the chips.

In line with the gel deformations, the cellular forces from the cell-level FE models followed a gradient, with higher forces near the membrane. However, these forces were three orders of magnitude lower than those in native cartilage.

The Hill's function used to couple the cellular forces (L) obtained from FE analysis with non-dimensionalized mechanical loading ($\theta$) input to the regulatory network was calibrated for native cartilage. For agarose hydrogel, the lower forces had minimal impact on the mechanical loading input ($\theta$) parameter. Consequently, the mechanical load parameters for the three positions did not vary significantly, as the Hill's function was not sensitive to low loads. As a result, the biomarker activity from the regulatory networks did not differ much for the 3 cell positions, despite the difference in measured cellular forces. Additionally, while mechanical load plays a role, perfusion of the chondrocyte differentiation medium into the hydrogel may also influence cellular response. However, these effects were not considered in the multiscale model.

In the cellular-scale model, the agarose and cells were bound by a tie constraint. In reality, after a week of static culture, chondrocytes deposit a pericellular matrix that they bind to [254], forming adhesions through which intracellular mechanotransduction is triggered [227, 238]. Since the model did not include this pericellular matrix, future work should focus on modeling its growth and biomechanical role. To do so, longitudinal experimental measurements are needed to study the progressive development of the pericellular matrix in the chip.

In conclusion, this study introduces an innovative approach that integrates multiscale experiments within a cartilage-on-chip setup with a multiscale *in silico* model. This approach not only provides deeper insights into the mechanical behavior across different length scales but also holds the potential to shed light on the underlying biological processes triggered by mechanics. The established workflow provides interesting opportunities for future applications, offering a powerful platform allowing to disentangle the multiscale and multifactorial mechanisms that are important for the development of pharmaceutical drugs to arrest OA and the exploration of novel tissue engineering strategies aimed at regenerating cartilage.

# Chapter 6

# Implementation of the multiscale model in a model execution environment

Satanik Mukherjee[1], Karol Zajac[2], Piotr Nowakowski[2], Maciej Malawski[2], Liesbet Geris[1,3,4]

[1]Biomechanics Section, KU Leuven, Leuven, Belgium
[2]Sano Centre for Computational Medicine, Poland
[3]Skeletal Biology and Engineering Research Center, KU Leuven, Belgium
[4]GIGA Institute, University of Liege, Belgium

This chapter is based on a manuscript prepared to be submitted: S. Mukherjee, K. Zajac, P. Nowakowski, M. Malawski and L. Geris. "Implementation of a multiscale model of articular cartilage in a model execution environment."

## 6.1 Introduction

The multiscale modeling workflow developed in this thesis integrates finite element (FE) models at different length scales with an intracellular gene/protein regulatory network. To improve accessibility and usability, this study implements the workflow within a model execution environment (MEE) developed by SANO – Centre for Computational Personalized Medicine, Poland. The MEE provides a user-friendly interface for executing complex multiscale simulations on high performance computing (HPC) infrastructure, enabling researchers and clinicians to modify parameters and analyze results without requiring extensive expertise in computational modeling. The multiscale model developed in this thesis require multiple software tools, including Abaqus for FE analysis, Fortran subroutines for material behavior, and Matlab for intracellular simulations. Running these models across different platforms presents challenges, particularly for non-experts. Additionally, executing such high-computational-demand models on an HPC infrastructure requires specialized knowledge, limiting accessibility.

By integrating the multiscale workflow into the MEE, this study addresses these challenges, creating an intuitive and structured approach to executing simulations. This chapter introduces the MEE, details the steps taken to implement the multiscale model within this environment, and presents a proof-of-concept study on the dynamic compression of cartilage explants (chapter 4) to demonstrate its effectiveness.

## 6.2 Overview of the model execution environment

The overview of the features that are available in the MEE interface are described in this section below:
**Pipeline:** To execute computations within the MEE infrastructure, pipelines must be created. Pipelines consist of a series of computational 'steps' executed sequentially to produce a specific output. These 'steps' which can vary in scope and complexity. MEE utilizes Rimrock, a system that provides a REST API (Representational State Transfer Application Programming Interface) to simplify interaction with the infrastructure and facilitate the execution of computations.

**Pipeline Steps:** Each step within a pipeline defines a list of required inputs, which must be available in the patient input directory, pipeline input directory, or output directory before the computation can begin. This structured approach ensures efficient data processing and seamless execution of complex multiscale simulations. Pipeline steps allow running computations on the Ares

supercomputer (Academic Computer Center CYFRONET AGH, Poland) by submitting jobs using slurm scripts to a selected queue. Slurm, is a free and open-source job scheduler for Linux and Unix-like kernels, used by many of the world's supercomputers and computer clusters. A job is described by the slurm starting script, which can be generated by MEE from a template. The template and computation code should be stored in the git repository. Currently, MEE is integrated with GitLab and supports native git repositories.

**Patients:** This feature in the MEE environment allows for the personalization of pipelines for individual patients. Once a pipeline is created with specific steps, it can be customized by incorporating patient-specific input data at various steps of the pipeline. This enables tailored simulations that reflect individual patient characteristics, improving the accuracy and relevance of computational analyses. In the context of this thesis, each simulation case (dynamic compression of cartilage explant or human knee joint) will be considered as a patient in the MEE.

**Cohorts:** By utilizing this feature of the MEE, multiple patients can be grouped into specific cohorts based on predefined criteria, such as a pre-existing medical condition, sex, ethnicity, or other relevant characteristics. A cohort, in this context, is a group of individuals who share these specific traits or experiences and are observed over time to evaluate health outcomes, disease progression, or the effects of treatments. As this thesis focuses on building the framework rather than applying it to a cohort of patients, this feature was not used.

**Campaigns:** This feature is used to create a personalized pipeline for each patient in the cohort, thereby facilitating the execution of computations in a patient-specific manner. As this thesis did not involve a cohort of patients, the campaign feature was also not used in this thesis.

## 6.3 Implementation of the multiscale modeling workflow in the MEE

To implement the multiscale model in the MEE, a pipeline with 3 steps were configured as seen in Figure 6.1. The 3 steps are described as follows:

**1. Global model step:** This step was employed to facilitate the simulation of the joint (or device) and tissue(or gel) scale FE models of the multiscale workflow in the MEE (Figure6.2). The details of this step are discussed below:

- **User's choice:** Number of CPUs to be used. It refers to how many individual cores will be utilized for processing the simulation.
- **Inputs:**
  .inp Abaqus input file for simulation in Abaqus.
  .for Fortran subroutine for cartilage material behavior.
  .txt files for mesh information.
- **Output:** Global simulation results stored in .odb format for use in subsequent steps.
- **Software used:** Abaqus and Fortran 90 subroutines.

**2. Cell model step:** In this step, both the cell-level FE model and the corresponding intracellular gene/protein regulatory networks were incorporated (Figure 6.3). Although these models represented two separate scales within the multiscale framework, they were combined in this step to facilitate easy transmission of information from the cell to intracellular level. While each cell had to be simulated individually to incorporate cell-specific inputs into the regulatory network, the computational resources required for the cell-level model were sufficient to handle the regulatory networks as well. The details of this step are discussed below:

**Cellular scale model**

- **User's choice:** Number of CPUs to be used, number of cells to be simulated.
- **Inputs:**
  .odb file from the Global Model step. This was automated in the MEE, so

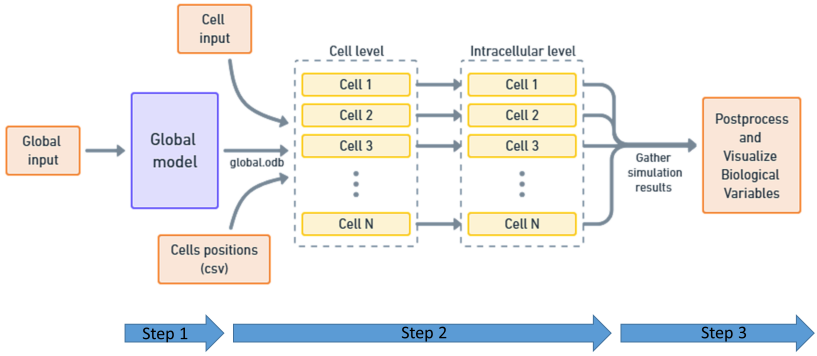


Figure 6.1: Overview of implementation of the multiscale modeling workflow in MEE

that once the global model step was complete, the .odb file was accessible to the cell model step.
.csv file containing the 3D coordinates of each cell's position in the global model.
.inp Abaqus input file for cell-specific simulation in Abaqus.
.for Fortran subroutine for cell, pericellular and extracellular matrix material behavior.
.txt files for mesh information.

- **Outputs:**
  .odb file containing cellular scale simulation results.
  .txt file containing cellular force obtained from the .odb file.
- **Software used:** Abaqus, Fortran 90 subroutines and Python.

**Intracellular regulatory network**

- **Inputs:**
  .txt files containing cellular forces obtained from the cellular scale model.
  .m Matlab scripts that are used to simulate the intracellular gene/protein regulatory network.
  .mat Matlab file that contains information about the wild-type attractors or stable states of the regulatory network.
- **Output:**
  .mat file containing details of each biomolecule's activity from simulating the regulatory network.
- **Software Used:** Matlab.

**3. Post-processing step:** The purpose of this step was to collect simulation results from the cell model step (which simulated multiple cells) and perform comprehensive post-processing to calculate and visualize biological variables (Figure6.4).

- **User's choice:** Selection of specific biological variables from a list, to be visualized in the results.
- **Inputs:**
  .mat Matlab files for each cell, that contain information about the wild-type attractors or stable states of the regulatory network. .m Matlab scripts that are used to post-process the data contained in the .mat files.
- **Output:** visualization of processed data for multiple cells.
- **Software Used:** Matlab.

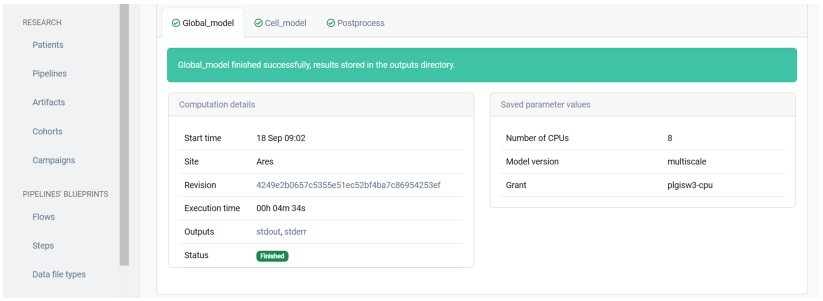


Figure 6.2: Global model step in the MEE interface.

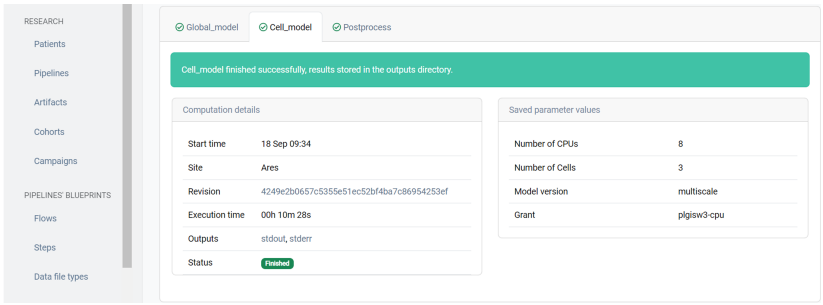


Figure 6.3: Cell model step in MEE interface.

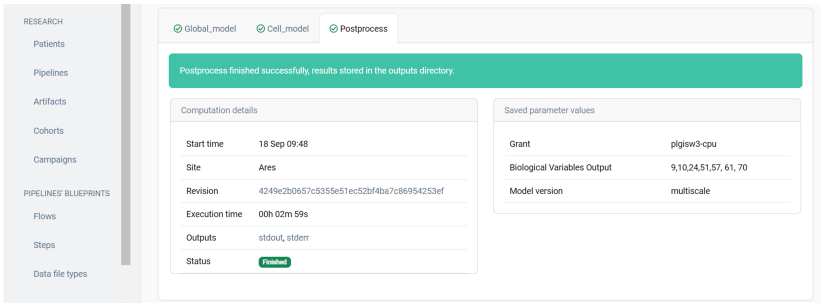


Figure 6.4: Post-processing step in the MEE interface.

## 6.4 Proof-of-concept analysis of compression of cartilage explants in the model execution environment

A proof-of-concept study was performed to demonstrate the use of multiscale modeling workflow in the model execution environment. The study simulated the dynamic compression of cartilage explants, that was already described in detail in chapter 4. A brief overview of the choices made during the study is provided below.
1) **Tissue-level FE model** of a bovine cartilage disc of 1 mm thick and 3 mm diameter, mimicking the in vitro experimental setup of dynamic compression of articular cartilage explants [52]. The cartilage was modelled as a fibril reinforced poroviscoelastic material [18] and subjected to dynamic compression of 20% strain (at 0.5 Hz frequency). To simulate this FE model, 8 CPU cores were used.
2) **Cell-level FE model**, consisting of a chondrocyte, pericellular matrix and extracellular matrix. For this study, 3 cells were chosen, and 8 CPU cores were used for simulation of each cell. The cells were positioned at the central region, halfway between the top surface and the bottom of the cartilage explant.
3) **Intracellular model**, which was an additive, semi-quantitative regulatory network for chondrocyte mechanotransduction and inflammation developed using a combination of knowledge-based and inference-based approach (as described in chapter 4).

The model was then run within the MEE, and results were processed during the post-processing step. A sample output is shown in Figure 6.5, which compares the expression of relevant user chosen biomarkers across the three simulated cells.

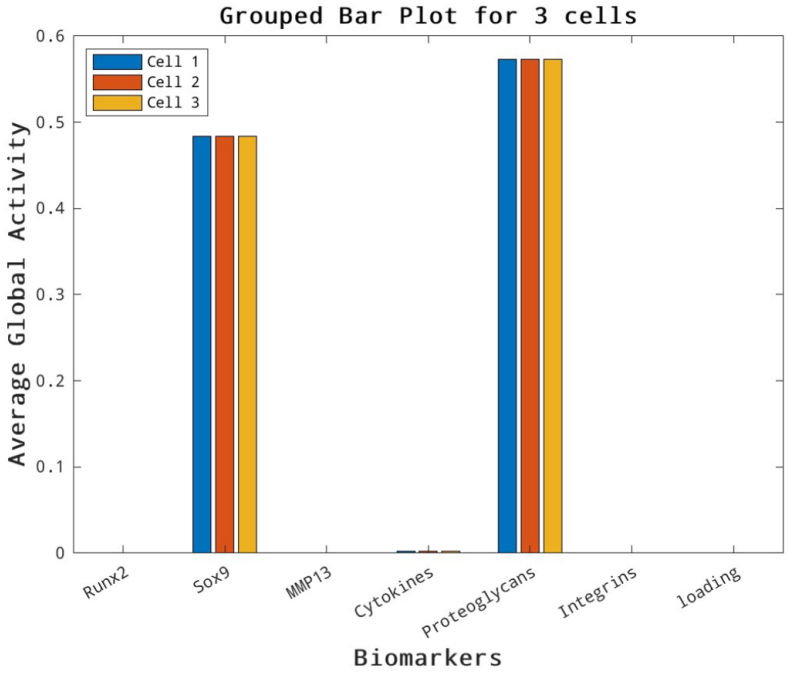


Figure 6.5: Visualization of results in the MEE for proof-of-concept study.

## 6.5 Discussion

In this chapter, the multiscale modeling workflow for cartilage developed in this thesis, was implemented in a user-friendly MEE. This implementation provided a simple platform for utilizing the multiscale model to address specific research questions. It also offered flexibility to the user, allowing them to select parameters such as the number of CPUs to be used, the number of cells to be simulated along with their location, and the biological variables to be visualized as outputs. Future studies in the MEE could explore several avenues to further enhance its capabilities and broaden its application. An immediate next step will be to incorporate the multiscale model of the human knee joint, already developed in chapter 4 of the thesis. This extension will allow for more realistic simulations of knee osteoarthritis, providing valuable insights into the progression of the disease and treatment outcomes.

The multiscale workflow developed in this thesis and incorporated into the MEE follows a unidirectional flow, progressing from the tissue level to the

intracellular level. In the future, completing the feedback loop by linking the intracellular regulatory networks with the cell-level model and subsequently back to the tissue level model could be a key improvement, enabling a more accurate representation of how cellular changes impact tissue behavior. However, to complete this feedback loop, multiple challenges need to be overcome. Firstly, a calibrated profile needs to be developed that can relate cell-level gene expression to actual changes in the cellular microenvironment in terms of the quantity and mechanical properties of deposited extracellular matrix components. In this context, the 'post-processing step' currently implemented in the MEE can be updated to include the calibration profile, that will feedback to the 'cell model step' in MEE. Secondly, advanced computational homogenization techniques are needed to enable bidirectional coupling between tissue- and cell-scale models, synchronously solving problems at both scales while exchanging information at each time step [139]. In this approach, the constitutive behavior at each higher scale integration point is determined by the average stress from a corresponding lower-scale problem, which accounts for micro-scale heterogeneity. The boundary conditions of the lower scale are modified iteratively based on the higher scale, driving new simulations. This bidirectional coupling between the cell and tissue-scale model can be implemented in the MEE in future studies, by incorporating a 'computational homogenization step' in between the 'tissue model' and 'cell model' step of the MEE.

Linking these components would complete the feedback loop offering a more dynamic and realistic simulation. Finally, the addition of a 'pre-processing step' in MEE for anatomical measurements and gait data will enable patient-specific simulations, paving the way for personalized OA models and/or in silico clinical trials. The current study forms a strong foundation for these future developments and holds promise for the uptake of the multiscale model in *in silico* clinical trials and patient-specific studies in clinical settings.

# Chapter 7

# General conclusions and future perspectives

This final chapter presents a comprehensive summary of the research conducted in this thesis. Since each chapter consists of an independent scientific study with its own discussion, this section describes the main contributions and overarching conclusions of the PhD research. Additionally, it outlines the limitations and challenges encountered throughout the project and explores potential directions for future research.

## 7.1 Thesis summary

The general aim of this PhD research was to develop a computational multiscale model that integrates cartilage mechanics with intracellular biochemical processes, providing deeper insights into cartilage degeneration and regeneration. To accomplish this, the research was structured around specific objectives, outlined in Chapter 2. Each chapter of this thesis contributes to achieving these objectives through targeted research and analyses. This section summarizes the general findings of each chapter of the thesis.

The introduction of this thesis (Chapter 1) provided an overview of various modeling approaches used to study different aspects of joint degeneration, with a primary focus on the knee joint. It first described the components of a healthy joint and the changes that occur in these structures during osteoarthritis (OA). The chapter then outlined different modeling techniques used to investigate

OA, including its etiology, progression, and potential treatments. These models were categorized based on their underlying assumptions and technologies, namely musculoskeletal models, finite element (FE) models, (gene) regulatory models, multiscale models, and data-driven models such as artificial intelligence and machine learning. The introduction concluded by emphasizing the need for future research to integrate these diverse modeling approaches into a comprehensive computational framework.

In chapter 3, a comparative study was conducted on widely used bioreactor setups designed to apply mechanical stimuli for mimicking joint mechanics in an *ex vivo* environment or for cartilage tissue engineering. The study compared FE analyses of different mechanical loading protocols in these bioreactor setups with an FE model of the human knee joint developed within the study. While previous research has examined mechanics in individual bioreactor setups, this study provided a novel contribution by comparing various bioreactors to an *in vivo* scenario of the stance phase in the human knee joint. This comparison allowed for the quantification of the bioreactors' mechanical loading regimes most closely replicating physiological conditions.

Subsequently, in Chapter 4, a multiscale modeling workflow for articular cartilage was developed, integrating mechanics across multiple length scales (from tissue to cell) with an intracellular gene/protein regulatory networks. The multiscale model was calibrated and validated using independent experimental data from the literature. The workflow was then applied to study the knee joint pathophysiology following meniscectomy, specifically predicting the catabolic effects on the knee joint, which were shown to be dependent on the cartilage zones. This approach uniquely combined multiscale cartilage mechanics and intracellular regulatory network modeling, providing a more comprehensive framework for studying cartilage mechanobiology.

Chapter 5 developed a combined multiscale *in vitro* and *in silico* approach to examine the effects of mechanical loading on chondrocyte behavior in a cartilage-on-chip device. Stress relaxation experiments and inverse FE characterization were performed to optimize the material parameters for agarose hydrogel loaded with cells and fluorescent beads. A multiscale model of the cartilage-on-chip setup was developed based on the previously developed multiscale modeling framework. Experimental data obtained from the different length scales were compared with simulation results from the multiscale model. Intracellular gene regulatory network simulations showed that the low stiffness of the hydrogel led to minimal mechanotransduction activation, maintaining a high expression of stable chondrocyte markers while suppressing pro-hypertrophic markers. This was confirmed experimentally by immunofluorescence imaging that showed COL II and COL VI deposition by the chondrocytes. The developed workflow can study the effects of mechanical loading on chondrocytes in a

comprehensive manner, integrating both *in vitro* and *in silico* approaches to evaluate chondrocyte behavior across multiple length scales.

The final chapter of the thesis focused on implementing the multiscale modeling workflow for cartilage in a user-friendly model execution environment (MEE). This implementation in MEE provided an accessible platform for addressing specific research questions, offering users flexibility in selecting parameters such as the number of CPUs, the number of cells to simulate, and the biological variables to visualize as outputs. Additionally, the platform provided a link to easy-to-use high performance computing (HPC) resources, enabling efficient execution of large-scale simulations.

## 7.2 Main contributions of the thesis

A significant challenge in the research presented in this thesis was its **highly interdisciplinary nature, encompassing both computational and experimental aspects**. On the computational side, the thesis developed the integration of FE models—accounting for complex constitutive behavior and geometries, ranging from a whole knee joint to individual cells—with a detailed systems biology model of gene and protein regulatory network. Additionally, substantial improvements were made to existing codes and subroutines to enable model parallelization, facilitating large-scale simulations on HPC systems. On the experimental side, **novel experiments were designed using a cartilage-on-chip model** to generate data across multiple length scales, which were then compared with corresponding results from the multiscale models. This **combined *in silico* and *in vitro* approach**, investigating cartilage behavior across multiple scales, harnesses and integrates the strengths of both modeling and experimental techniques, representing a major contribution of this thesis.

Another key contribution of this thesis was the comparative study conducted in Chapter 3, which examined widely used bioreactor setups designed to apply mechanical stimuli for mimicking joint mechanics in ex-vivo cartilage samples as well as cartilage tissue engineered constructs. The study **compared FE analyses of different mechanical loading protocols in these bioreactors with an FE model of the human knee joint**. Unlike previous studies that focused on individual bioreactor setups, this work uniquely compared all setups with an in-vivo knee joint scenario, quantifying which mechanical loading conditions most closely replicated physiological conditions. This contribution not only deepens the understanding of the mechanical differences across bioreactor setups but also provides a valuable resource for experimentalists in choosing the appropriate bioreactor and loading regimes for specific research questions.

Another contribution of this thesis was the **development of a multi-scale model of the human knee joint that incorporated zone-specific chondrocyte shapes and variations in extracellular and pericellular matrix composition** at the cellular scale. In addition, the tangential orientation of the collagen fibrils in the pericellular matrix adjoining the cells was also implemented in this study. Unlike previous multiscale models [140, 142, 220, 221] that used a uniform spherical chondrocyte shape across all cartilage zones, this approach aimed to capture more precisely the variation in cellular mechanical behavior across the thickness of the cartilage. The multiscale model successfully predicted the catabolic effects of meniscectomy on knee joint cartilage and demonstrated how zone-specific gradient of mechanical loading led to varied outcomes across the cartilage thickness.

One of the novel elements in this thesis was the development of a method to **couple the cellular forces from the cell-scale FE model with intracellular regulatory network**. This presented a challenge, as the regulatory network was semi-quantitative (with each biomolecule's activity ranging from 0 to 1), while the cellular forces in the FE model were purely quantitative (measured in newtons). To bridge this gap, a Hill's function was used to translate the cellular forces (L) into a mechanical loading input ($\Theta$) for the intracellular pathways. The parameters of the Hill's function were calibrated by optimizing relevant gene expressions obtained from simulating the network, ensuring alignment with the corresponding values measured in experiments.

In the multiscale modeling workflow developed in this study, the FE models at the joint/tissue and cell scale were computationally expensive. A key innovation in this work was **optimizing the FE models at the joint/tissue and cell scales to enable parallel simulations across multiple CPU cores**. This was achieved by making existing UMAT subroutines for material behavior thread-safe, eliminating common blocks, and using UEXTERNALDB subroutines to implement collagen fibril orientations in the Abaqus workflow. These improvements enabled large-scale simulations to run efficiently on HPC clusters, significantly reducing computation time.

To assess credibility of the *in silico* models developed in this study, appropriate **verification and validation** approaches were undertaken. For all the FE models developed, the verification step involved mesh convergence analyses, to determine the final converged mesh for the simulations. Validation of the knee joint FE model in chapter 3 was performed by comparing the varus-vagus rotations between the simulations and experiments. The overall multiscale model workflow developed in chapter 4 was validated with respect to gene expression and sGAG loss data from experimental studies. Lastly, for a validation of individual length scales in the multiscale workflow, a multiscale experimental approach was undertaken using a cartilage-on chip setup in chapter 5. Using

this approach, results from the different length scales from the device level to the intracellular level were compared between the simulations and experiments.

Fianlly, the multiscale modeling workflow for cartilage developed in the thesis, was **implemented in a user-friendly MEE**. This platform enables researchers to apply the multiscale model to specific questions without requiring extensive coding expertise. Its intuitive graphical interface allows users to adjust key simulation parameters, such as the number of CPUs for HPC, the number of cells simulated, and the biological variables visualized as outputs. With its flexibility and scalability, the implemented model holds promise for adoption in *in silico* clinical trials and patient-specific studies, facilitating integration into clinical environments in the future.

## 7.3 Limitations and perspectives for future research

While the discussion sections of each chapter have addressed their specific limitations, this section outlines the broader limitations of the thesis and offers perspectives for future research. These perspectives are categorized into computational and experimental aspects.

### 7.3.1 Computational aspects

The FE model of the human knee joint in this thesis was developed using geometry, material properties, and gait cycle data from different literature sources rather than a single patient, posing a potential limitation. This lack of coherence can be mitigated by utilizing open-source patient cohort databases, such as the Osteoarthritis Initiative, which provides longitudinal MRI images of knee joints. Additionally, advancements in non-invasive cartilage mechanical characterization from MRI (by using virtual fields methods for example) could further enhance patient specificity in knee joint modeling.

To develop a patient-specific FE model of the human knee joint, the knee joint geometry should be segmented from MRI images from the patient and thereafter appropriately meshed. This process of generation of the FE model is a cumbersome task, requiring significant time and effort. Therefore, in the future to upscale the usage of patient specific models, a template based modeling approach can be adopted as described by Mononen et al. [261] can be utilized. Such template based approaches scale a generic template of the knee joint based On patient specific anatomical measurements, thereby ensuring a level of patient specificity without needing significant effort.

In the multiscale analysis of the knee joint, the cell scale models were located in a region in the medial tibial cartilage where the highest stresses were observed. This was done because the most significant mechanical changes occurred in that region after meniscectomy. However, in the future, the multiscale analysis can be extended to multiple locations in the cartilage to gain a broader understanding of which regions are more affected by meniscectomy or other pathological conditions, such as ACL ruptures.

The representative volume element (RVE) of cellular scale models in the multiscale model consisted of a single cell, with its peri-and extracellular matrix. In future studies, multiple cells can be included in the RVE, so that the effects of cell-cell mechanical interactions can be included in the multiscale analysis.

In the multiscale modeling workflow, mechanics served as the primary factor linking multiple length scales to generate a cellular response. In the future, the model can be expanded to include the effects of soluble factors, such as nutrient transport, growth factors, and inflammatory cytokines, on chondrocyte response. These factors can be modeled using diffusion equations, as demonstrated by Eskelinen et al. [242], or coupled with the pore fluid flow (which was already implemented in the FE models in this thesis) to determine their spatial distribution and influence on cartilage metabolism.

Lastly, the multiscale modeling workflow developed in this study is unidirectional in nature, where the information flow is from the tissue scale to the intracellular scale via the cellular scale. In the future, efforts can be made to complete the feedback loop, i.e., to incorporate how changes in intracellular behavior can, in turn, affect the cellular microenvironment and thereby change the global mechanical behavior at the tissue scale. However, this approach presents multiple challenges. Firstly, a calibrated profile needs to be developed that can relate cell-level gene expression to actual changes in the cellular microenvironment in terms of the quantity and mechanical properties of deposited extracellular matrix components. Secondly, advanced computational homogenization techniques are needed to enable bidirectional coupling between tissue- and cell-scale models, synchronously solving problems at both scales while exchanging information at each time step [139]. In this approach, the constitutive behavior at each higher scale's integration point is determined by the average stress from a corresponding lower-scale problem, which accounts for micro-scale heterogeneity. The boundary conditions of the lower scale are modified iteratively based on the higher scale, driving new simulations. The degree of nonuniformity in displacement and fluid pressure fields affects the accuracy of data passing schemes, and future implementations for biphasic cartilage problems may benefit from second-order accuracy, as mentioned in Sibole et al. [141]. Additionally, the size of the cellular-scale model must be verified as a representative volume element (RVE), as RVE size impacts the accuracy of the data-passing process

[250].

### 7.3.2 Experimental aspects

In Chapter 3, the comparative analysis of bioreactors identified loading protocols for each bioreactor type that closely mimic physiological mechanics. Based on the findings of the *in silico* studies in this thesis, follow-up experiments can be conducted to assess whether these protocols effectively preserve native cartilage in ex vivo setups and promote cartilage regeneration in tissue-engineered constructs.

For calibration of the mutliscale model in chapter 3, the experimental study by Li et al. [52] on bovine cartilage explants was used. However, since gene expression in that study was measured using qPCR, no spatial data were available for direct comparison with the numerical models. In the future, use of spatial transcriptomics can provide spatial gene expression data of cartilage for a more detailed validation of the numerical multiscale model [243].

In Chapter 5, the cartilage-on-chip experiments provided valuable data for establishing a multiscale *in silico–in vitro* workflow to study chondrocyte mechanobiology. In the future, this workflow can be used to investigate the effects of hyperphysiological loading on chondrocyte behavior by applying higher mechanical stimuli within the chips. Additionally, the combinatorial effects of mechanics and pro-inflammatory mediators (such as TNF-$\alpha$ and IL-1$\beta$) can be explored using the cartilage-on-chip platform. The setup can also be leveraged to test the efficacy of pharmaceutical drugs in mitigating mechanically or inflammation-induced catabolic effects in chondrocytes. The *in silico* component of the workflow can help identify potential pathways and druggable targets, which can then be experimentally tested in the chips. This integrated approach holds significant promise for developing optimal treatment strategies to prevent cartilage degeneration.

# Appendix A

# Supplementary results from Chapter 3

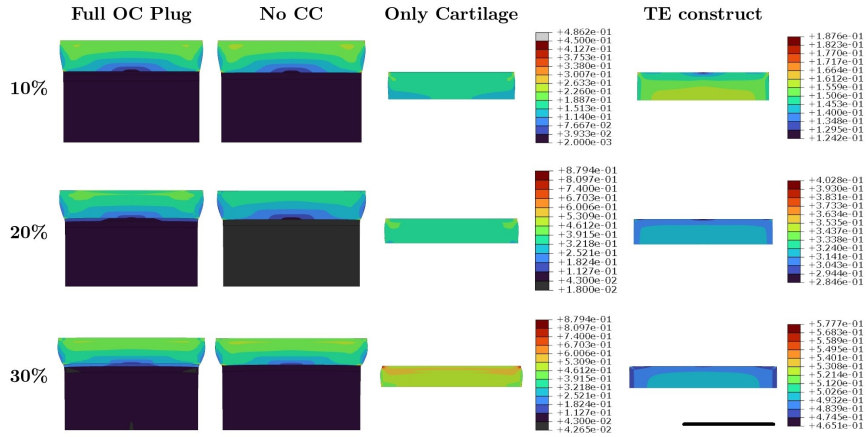


Figure A.1: Distribution of maximum shear strain in different tissues of the OC plug and the TE construct for 10%, 20% and 30% strain applied in dynamic unconfined compression with 1Hz frequency, NoCC - No Calcified Cartilage, Scale bar = 5mm

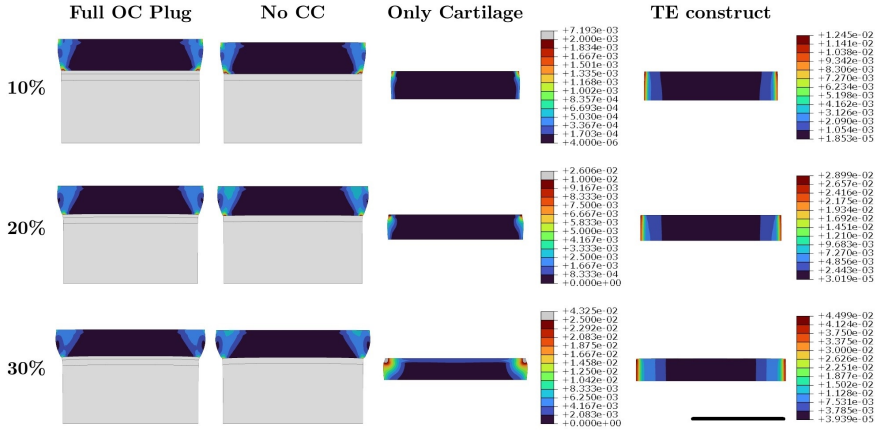


Figure A.2: Distribution of pore fluid velocity (in mm/sec) in different tissues of the OC plug and the TE construct for 10%, 20% and 30% strain applied in dynamic unconfined compression with 1Hz frequency, NoCC - No Calcified Cartilage, Scale bar = 5mm

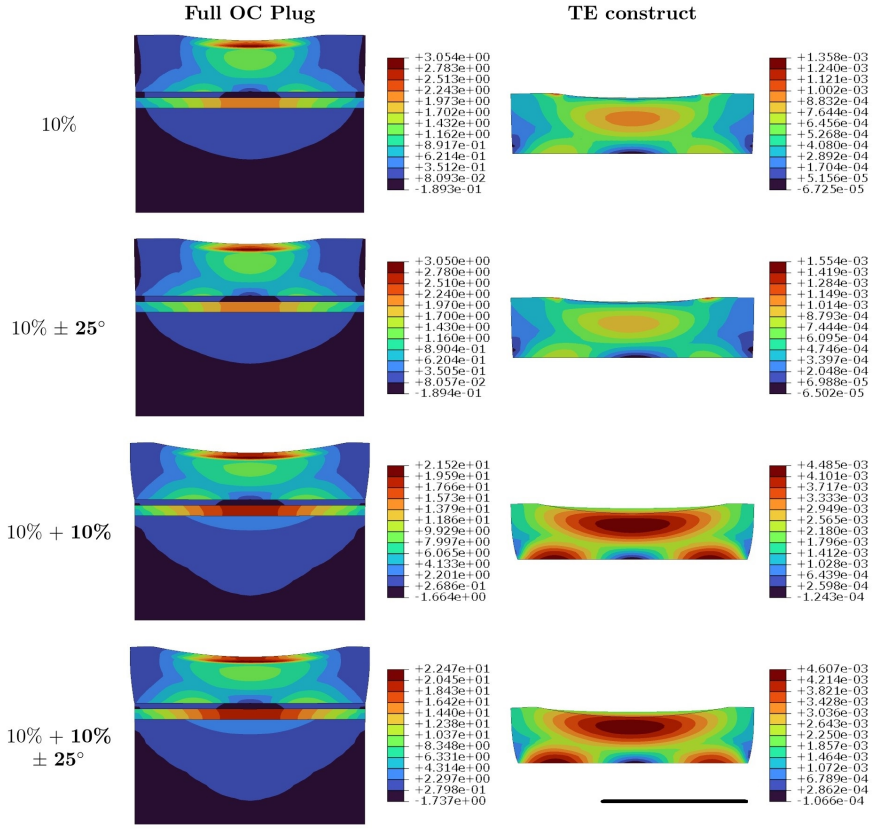


Figure A.3: Distribution of maximum principal stress (in MPa) in OC plug and the TE construct for 4 different conditions of applied compression with ball rotation. Values in bold in the first column represents a dynamic boundary condition with 1Hz frequency, while normal fonts are for quasi-static. Scale bar = 5mm

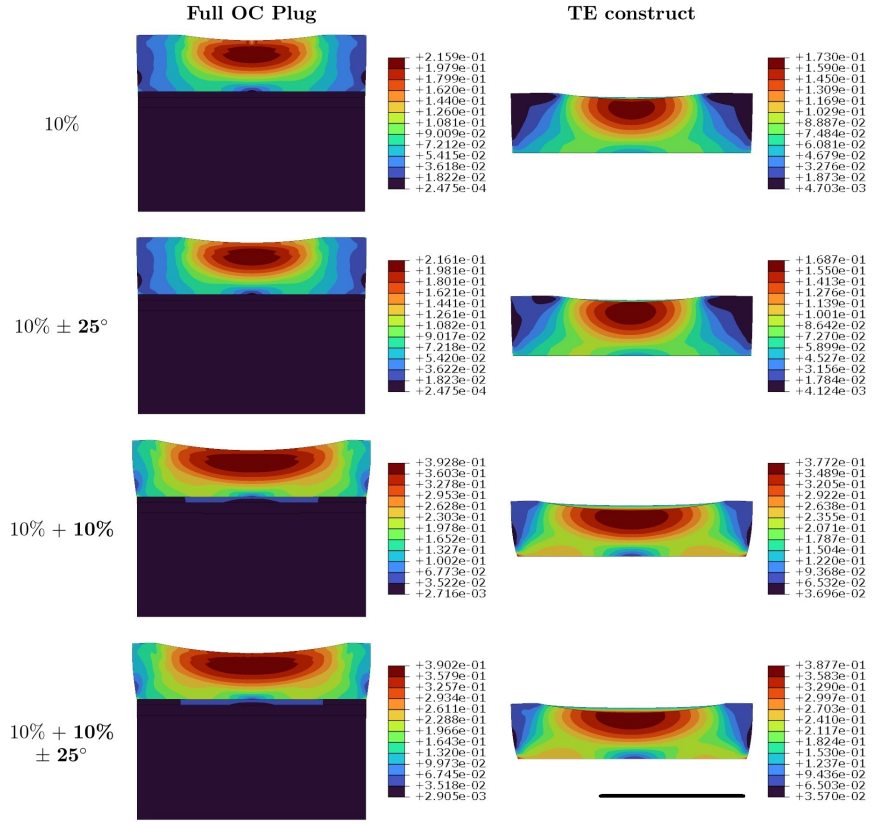


Figure A.4: Distribution of maximum shear strain in OC plug and the TE construct for 4 different conditions of applied compression with ball rotation. Values in bold in the first column represents a dynamic boundary condition with 1Hz frequency, while normal fonts are for quasi-static. Scale bar = 5mm

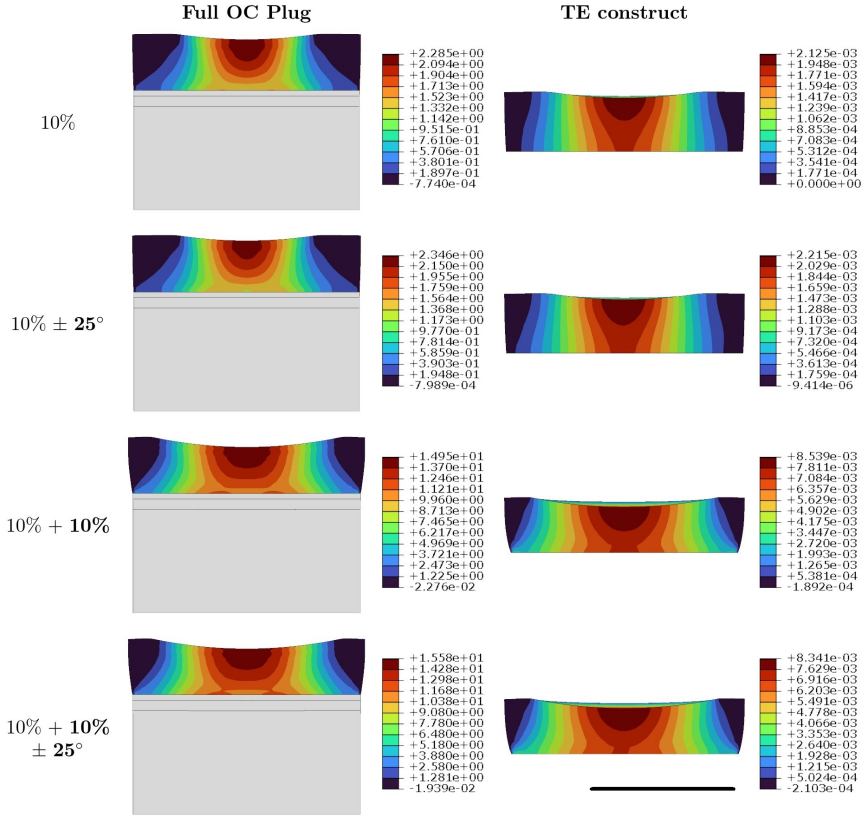


Figure A.5: Distribution of pore fluid pressure (in MPa) in OC plug and the TE construct for 4 different conditions of applied compression with ball rotation. Values in bold in the first column represents a dynamic boundary condition with 1Hz frequency, while normal fonts are for quasi-static. Scale bar = 5mm

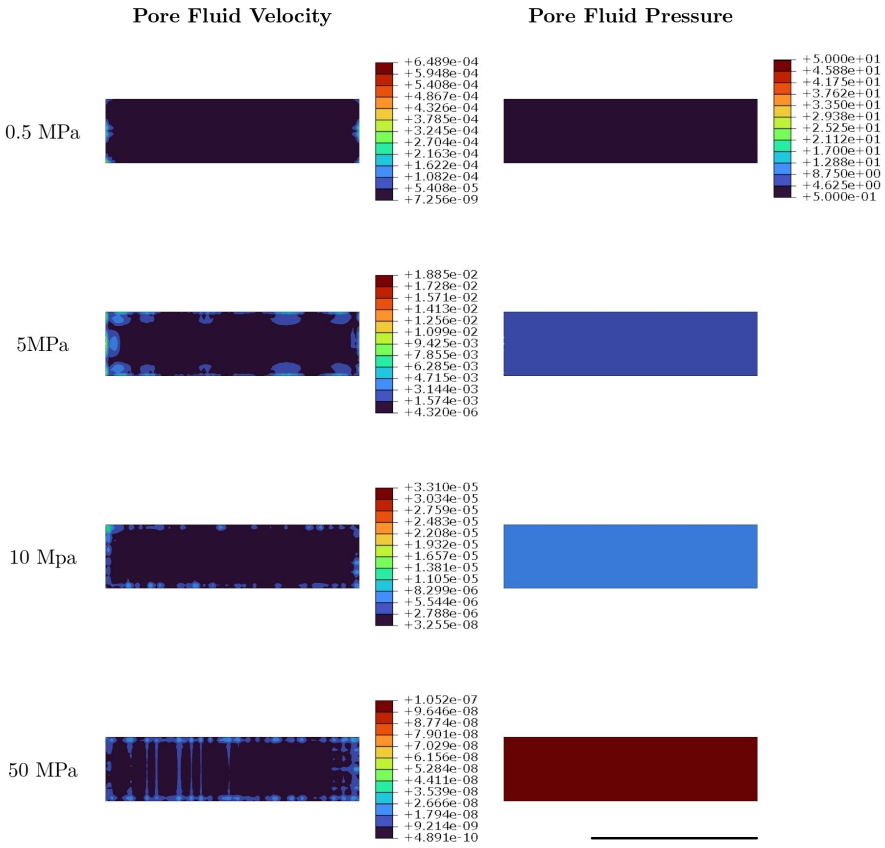


Figure A.6: Distribution of pore fluid velocity (in mm/sec) and pore pressure (MPa)in TE construct for 4 different conditions of applied dynamic hydrostatic pressure at 1Hz frequency. Scale bar = 5mm

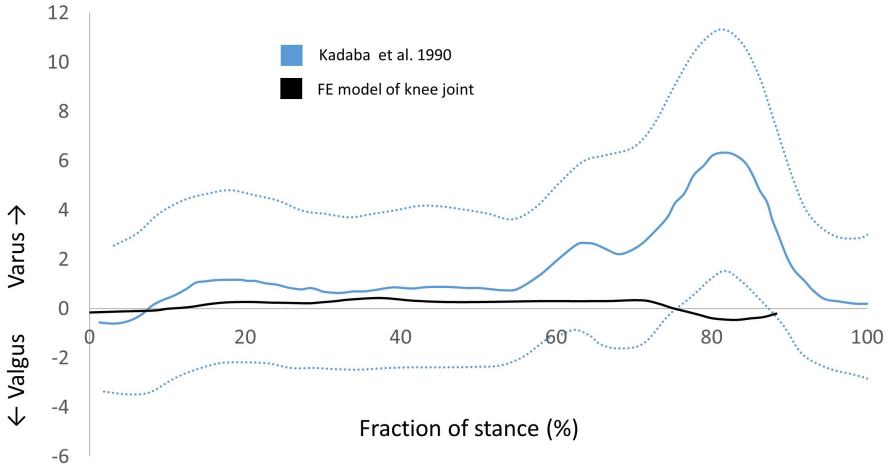


Figure A.7: Comparison of varus-valgus rotation between the FE model and the experimental measurements as was done in Kadaba et al.[206]. The blue dotted lines represent the standard deviation

# Appendix B

# Detailed explanation of the pathways involved in the regulatory network

This supplementary data contains detailed explanations of the different pathways included in the regulatory networks (adapted from Lesage et al. 2021)

## B.1 Mechanotransduction pathways

### B.1.1 Integrin mechanoreceptor and downstream pathways

One of the major sensor by which chondrocyte sense the external forces are the transmembrane integrin proteins and focal adhesion complexes. These complexes are made of integrins and other cytoplasmic molecules, which provides kinase activity to the complexes (14, 15). They mediate mechanical force transmission to downstream biochemical reaction cascades. There are several integrin isoforms and subunits that differs between species (e.g. $\alpha 1\beta 1$, $\alpha 5\beta 1$, etc..) and that have binding sites for different ECM fibers (e.g. collagen, fibronectin), which act as external ligands (16). The $\alpha 5\beta 1$subunint has been shown to be important for modulating the expression of MMPs in mouse chondrocytes (17), but too few studies distinguish downstream cascades and effects specific to each integrin subunits. Thus, the node representing integrins in the model is a general summarization of a receptor translating mechanical

cues into biochemical cascades, for sake of simplification. One specific human gene coding for this type of protein could be ITGB1, for instance. Generally speaking, focal adhesion kinases (FAK) are among of the main effectors of focal adhesion complexes, for signal transduction (18). More actors are involved to offer refined response to various loading regimen but, for sake of simplification, our model summarizes these molecular complexes by a single node named FAK. This type of kinases functions as a hub to transduce signals, including through phosphorylation of the RhoA GTPases, which are known to be involved in the regulation of cell response to mechanical cues (19). More particularly, these phosphorylation cascades are involved in the regulation of cell differentiation by mechanical cues in development and regenerative processes (20). RhoA proteins and the downstream ROCK1/2 proteins regulate the actin cytoskeleton assembly and contractility by phosphorylating myosin light chains (MLC) (21). This level of contractility and cytoskeleton assembly is represented by a single variable named Actin-MLC in the model. Evidences showed that RhoA and ROCK are involved in the suppression of hypertrophic chondrocyte differentiation (22), possibly in part through activation of the cyclin CCND1, a known suppressor of RUNX2 activity (22), which is accounted for in the model. Actin-myosin phosphorylation by the RhoA/ROCK axis also takes place through LIM-domain containing protein kinase and cofilin proteins (21, 23), but this side and redundant pathway that does not involve many crosstalk with other actors was not represented in the model for sake of simplification. Other downstream effectors below the RhoA/ROCK axis are multiple. First, ROCK would promote SOX9 phosphorylation, thereby promoting its transduction to nucleus in chondrocyte (24). SOX9 is commonly known to directly upregulate expression of the genes producing ECM proteins such as proteoglycans and type-II collagen (24). In other words, this axis can fairly be presumed as a mechanically induced pro-anabolic pathway, when considered in isolation of the full connectome. Second, the phosphorylation of the cytoskeleton stress fibers and MLC, which increases the stability and contractility of the cytoskeleton, regulates the transcriptional activity of various TFs (25). For instance, it promotes the nuclear translocation of $\beta$-catenin, an effector of the Wnt canonical pathway, thereby promoting the WNT/$\beta$-catenin axis (20). In the same way, it also promotes the activation of Yes-associated protein (YAP) and the transcriptional co-activator with PDZ-binding motif (TAZ). Actin contractility would also up-regulate ECM related genes such as COL2A1 and ACAN (or Aggrecan, a proteoglycan), but the exact nature of the involved TF is not clear. For that reason, we introduced a dummy TF in the model, for the transcriptional activity induced by the cytoskeleton-increased contractility (more details below). Mechanical stimulation of chondrocytes increased their sensitivity to mechanical cues, suggesting the involvement of a positive feedback loop. There are experimental evidences that cyclic loading increases integrin receptors

amount at the membrane after mechanical stimulation (26). We propose a mechanism in which, upon integrin stimulation, downstream pathways promote the integrin gene up-regulation, thereby increasing the abundance of integrin receptors. In the model, we assume that this positive transcriptional activity happens through the dummy-TF introduced earlier and lying downstream of the RhoA/ROCK/Actin-MLC pathway, the main force-transducing axis. A possible candidate for that dummy-TF could be serum response factor (SRF) because the Rho family of GTPase (RhoA, Rac1) as well as actin contractility are reported to promote the SRF transcription factor activation upon mechanical stimulation and that factor would regulate cell contractility related genes in return (15, 27, 28). In absence of specific information, this dummy-TF or SRF is not regulated at the transcriptional level, in the model. As mentioned previously, YAP and TAZ have been identified to be mechanosensitive and to be involved in the transduction of mechanical signals (29). They can be activated or deactivated according to the mechanical environment, such as ECM stiffness. YAP and TAZ are considered as analogous; nevertheless, downstream effects are often reported for YAP rather than TAZ, in literature (30). In the current model, we do not make any distinction between the two and they are represented by a single entity. YAP inactivation is induced by phosphorylation, which prevent its translocation to the nucleus and may even direct it toward proteasome degradation (31). Mechanically-induced YAP/TAZ activation, downstream of the RhoA/ROCK/Actin-MLC axis, would be independent from the often reported NF2/Hippo/LATS biochemical pathway (29). For that reason the Hippo pathway was not represented in the model. Furthermore, YAP and TAZ are involved in the regulation of chondrogenic phenotype in response to physical cues (20, 30, 32). For instance, YAP was reported to block hypertrophy during skeletal development (30) while the overall amount of YAP is reduced during OA (31). Mechanistically, YAP contributes to SOX6 upregulation and reduces RUNX2 activity by direct binding, eventually preventing RUNX2 to upregulate COL10A1 expression (30). Our mathematical model accounts for these mechanisms by letting YAP/TAZ increase SOX9 at genetic level, which represents the SOX trio (SOX9, 5 and 6), and decrease RUNX2 protein activation. With the lack of specific information about their transcriptional regulators in cartilage, YAP/TAZ are only modulated at the protein level and not at the transcriptional level in the present numerical model. Finally, mTOR is a well-known mechanosensitive gene that is activated by cyclic loading in chondrocytes (33). This mechanically induced activation was reported to happen downstream of the PI3K/AKT/mTOR cascade in osteoblasts. This axis being also active in chondrocytes we introduced an activation link directly from integrin to PI3K, in the model. Inhibition of mTOR have been shown to reduce OA severity (34) but the implications of mTOR in chondrocyte biology are manifold and we only introduced a few downstream effectors, in the model. We

modeled mTOR capacity to phosphorylate and help the nuclear translocation of GLI2 (35), the nuclear effector the IHH pathway. This interaction also accounts for the ability of mTOR to regulate the PTHrP pathway via GLI2 in chondrocytes (35) since GLI2 was already modelled as an upstream positive regulator of PTHrP expression. In addition, mTOR may enhance RUNX2 expression through indirect activation of the transcription factor DLX5 and GLI2 (36) and is capable of suppressing its own inhibitor PP2A in the model (37, 38), generating a positive feedback loop. The involvement of mTOR in different complexes (i.e. mTORC1 and mTORC2) was not considered and many mTOR-related mechanisms were disregarded in the current model.

### B.1.2 Ion channel and calcium signaling

Beside integrins, other important mechanosensors are expressed by chondrocytes, including the the so called chondrocyte "channelome". We focused on the cations channels entitled transient receptor potential vanilloid 4 (TRPV4), largely located at the cell membrane of articular chondrocyte (39). They are multimodally activated channels as they can transduce dynamic compressive loading signals and be activated by osmotic pressure variations as well as chemical signals (40, 41). TRPV4 plays a major role in the physiological response to cartilage loading by mediating intracellular calcium cations (Ca2+) influx (40). Functional mutation of the TRPV4 channel have been related to skeletal dysplasia and joint degenerative conditions such as osteoarthritis in human (40, 42). TRPV4 expression and activation was often related to SOX9 increased expression as well as overexpression of ECM related proteins such as type II-collagen and proteoglycans, as such, it is believed to be involved in chondrogenic differentiation (43). Importantly, Ca2+ signaling is an essential universal secondary messenger in articular chondrocytes and its regulation is reported to be highly complex and based on frequency of concentration oscillations (44, 45). The current model being discrete in time and semi-quantitative, it does not allow to represent this tightly regulated periodic flux, which could be subject to a dedicated time continuous model in itself. Instead, in our model, the TRPV4 entity can be activated with increased mechanical loading, based on the same forces that are sensed by integrins, it subsequently increases the activity of the node called Ca2+ representing the concentration or effective level of cytoplasmic Ca2+. In that sense, we can consider that the maximal value of the variable would correspond to the most optimal level and frequency of Ca2+ oscillations and the lower value to less physiological frequencies, since the spontaneous calcium signaling is known to be altered in disease (46). Actually, both intra (e.g. endoplasmic reticulum) and extra-cellular sources of Ca2+ exist but the current model focuses on the extracellular source

of influx as supported by this study (44) according to which Ca2+ signaling, either spontaneous or load induced, has to be initiated by the extracellular Ca2+ influx. cAMP response element-binding protein (CREB) is one of the downstream transcription factors which decipher the information encoded by Ca2+ concentration, this connection was represented by an activation link toward ATF4 (also known as CREB2), which was already present in the regulatory model. TRPV4 stimulation with dynamical mechanical loading or agonist treatment was reported to modulate ECM proteins biosynthesis. In particular, it increases COL2A1 expression and decreases the mRNA level of ADAMTS5, an ECM proteinase (40). The first observation was not directly encoded in the model but it is expected to be mediated by the activating effect of Ca2+ on the cytoskeleton contractility and on SOX9 expression in the model, as mentioned above. The second one is represented by an inhibitory edge relating Ca2+ activity and ADAMTS5 gene expression, even though that relationship is likely to be indirect and to involve an intermediary TF, which is not precisely identified, to our knowledge. Interestingly, this TRPV4-dependant mechanosensitive pathway can be modulated by, and interplay with, other pathways. For instance, N. Trompeter et al. have recently showed that the TRPV4 channel was regulated by the actin cytoskeleton through binding of F-actin to the Microtubule Associated Protein Binding 7 domain of TRPV4. They have also shown that TRPV4 activity is suppressed by IGF-1 treatment concluding that IGF-1 would modulate the activity of this channel through alteration in the actin cytoskeletal organization (47). Indeed, IGF-1 treatment in primary chondrocytes increased cell stiffness and F-actin formation (48, 49). In order to integrate this precise mechanism in the model, we made sure that concomitant activity of the IGF-1 receptor and F-Actin was able to decrease the TRPV4 protein activity (i.e. channel opening) by using a multiplicative factor in the equations. That way, the Actin-MLC can inhibit TRPV4 activity only if the IGF-1 receptor is activated by its ligand, and this in a dose dependent way. Moreover, this calcium signaling interacts with the Rho GTPase/Actin axis to promote F-actin stability and contractility (50), which is translated by an activation link between Ca2+ and RhoA/ROCK, in our model.

## B.2 Inflammatory pathways

Increasing evidences have highlighted the implications inflammatory events in OA onset and progression (51–53). Even though a relatively low synovitis grade is observed during OA, this pathology is characterized an auto-activating inflammatory loop. Indeed, in presence of some ECM degradation products or damage-associated molecular patterns (DAMPS), inflammatory receptors such as the Toll-like receptors trigger signal transductions resulting in pro-

inflammatory cytokine production by the chondrocytes, themselves (3, 54–56). In this section, we summarize the main inflammatory related pathways that we integrated in our model and the assumptions made. First, several pro-inflammatory mediators, for which chondrocytes expressed the specific receptors (e.g. Toll-like receptor), are responsible for inducing pro-inflammatory events. For the sake of simplification in the model, we represented a single pro-inflammatory cytokine entity (e.g. Interleukine-1 beta (IL1B) or Tumor Necrosis Factor (TNF)) that is able to signal through a unique receptor of inflammation (R-inflam). This is an important assumption allowing us to focus on the intracellular interplay between mechanotransduction and inflammation rather than the role of specific receptors and signaling molecules. In chondrocytes, IL1B increases the production of proteases responsible for matrix degeneration, suppresses matrix biosynthesis and induces pro-inflammatory mediators by controlling expression of genes such as inducible NO synthase (iNOS) or matrix metalloproteinases (MMPs) (51, 57). In addition, pro-inflammatory cytokines like IL1B promote their own production, which amplifies the immune response as a positive feedback loop (58), This may be mediated by several signaling cascades involving TAK1, NFKB, and MAPKs, we refer the reader to Chapter 1 for more details and we shortly recall the main axes in the paragraphs below. In particular, TAK1 is a critical point where signals generated by pro-inflammatory signals converge, notably to initiate NFKB signaling cascade and pro-inflammatory gene induction (58, 59). The canonical mechanism of action involves a double inhibition and the release of NFKB from its inhibitor, IKBA (56). Since the other upstream activators of NFKB are only able to activate it for nuclear translocation when it is free from IKBA, we devised a special term in which the sum of the upstream activators is multiplied by the term (1- [level of IKBA]) in the model's equation. In addition, there exists a negative feedback loop in which NFKB promotes the gene expression of its own inhibitor IKBA(56). iNOS is an enzyme that can be induced by pro-inflammatory cytokines and that promotes the production of nitrite oxide, a pro-inflammatory mediator feeding the inflammatory loop in abnormal situations (60, 61). Indeed, in cytokine-stimulated chondrocytes, induced-nitric oxide causes persistent activation of NFKB (60). The inflammation inducible effect was represented in the model by overexpression of iNOS by NFKB, since the promoter region of the iNOS gene contains an NFKB binding site (60, 62), and the loop feeding with the direct activation of NFKB by NO. Another path involved in the activation of chondrocyte inflammatory response is the Wnt signaling. Indeed, overexpression of TCF4, a WNT downstream effector, was shown to induce the expression of MMPs and the activation of NFKB in chondrocytes. TCF would directly bind to NFKB to help its nuclear translocation in articular chondrocytes (63). This was accounted for by a direct activation link between LEF/TCF and NFKB at the protein level. Nevertheless, the aforementioned auto-inflammation

loop does not function in a fully uncontrolled fashion. There exist suppressors of cytokine signaling (e.g. SOCS proteins), which are soluble inhibitors of pro-inflammatory cytokines receptors (Rinflam, in the model) (59). They prevent the downstream phosphorylation cascades that normally lead to NFKB activation and negatively regulate the cytokine induced-JAK/STAT pathway during osteoarthritis (64). SOCS proteins are upregulated by the FGF and IGFI pathways, which illustrates some of the crosstalk happening with other signaling pathways, in the model. Another way that IL1B-R mediated signaling can be terminated is by activating some negative feedback loops. For instance, the p38 MAPK induces the phosphorylation of TAB1, which inactivates TAK1, and NFKB can overexpresses its own inhibitor IKBA. Inflammatory signal also interplays with IGF signaling, in several ways. One way involves the IGF binding proteins, which bind to IGFI and prevent downstream signaling. These proteins are known to be up-regulated during hypertrophy and OA (65, 66). While IGFI signaling may act as a break to inflammatory signal via up-regulation of SOCS proteins, IL-1 promotes the production and release of IGFBPs (67), which is translated by the up-regulation of IGFBP expression by the nuclear effector NFKB in our model, although the real mode of action is not clear yet. Finally, FOXO is an important anti-catabolic TF modulated and downregulated by inflammation (68) and represented in the in silico model via its ability to promote proteoglycans and collagen production and downregulate MMP13 and ADAMTS5 (69).

## B.3 Interplay between pathways

Previously we compartmented pathways into the mechanoregulatory and inflammatory specific pathways but those cellular paths are actually interconnected. S. Madhavan et al. have showed that cyclic tensile strains suppressed pro-inflammatory gene induction induced by all the three inflammatory mediators, IL-1$\beta$, TNF-$\alpha$, and LPS (58). However, the exact relationship is complex and neither linear nor straightforward. Here we describe some of the most direct molecular mechanisms by which mechanical loading and inflammation influence each other and that are accounted for in the current computational model. First, signal transduction through integrin receptors such as integrin subunits $\alpha$5 and $\beta$1 have been shown to up-regulate MMP13 expression in chondrocyte, when associated with inflammatory cues. Indeed, that effect would likely be mediated through induction of IL1B (17, 26). It corroborates with the fact that excessive mechanical loading is thought to cause NFKB activation and OA development (10). However, this observation likely depends on the status of all other connected signaling pathways and the magnitude of the biomechanical signals since it was also repeatedly reported that mechanical

signals at lower or physiological magnitudes maintain healthy cartilage and are potent inhibitors of inflammation and degrading enzymes (10, 58, 70). The TAK1/NFKB pathway has been suggested as key player of this biomechanical signal-mediated anti-inflammatory effect (59). In normal physiological ranges, mechanical stimulations would block TAK1 phosphorylation, thereby preventing IKK phosphorylation and activation (58, 59, 71). A possible mode of action that was integrated in the model regards YAP/TAZ. Indeed, YAP and NFKB pathways reciprocally inhibit each other, possibly affecting cartilage degradation in OA (31). On the one hand IL1B and TNFA promotes YAP/TAZ degradation through TAK1-mediated phosphorylation (31). On the other hand, YAP directly binds with TAK1, thereby limiting NFKB activation by blocking reaction substrate accessibility (31). Second, iNOS and NO are in a central position for the mechano-inflammatory crosstalk. Indeed, the pro-inflammatory mediator iNOs is also mechano-inducible (72, 73). This is represented in the model by a direct activatory link between Actin-MLC, the most direct intracellular mechanical transducer, and iNOS at protein level. However, the exact mode of action is not Third, ECM degradation products, also called damage-associated molecular patterns (DAMPs) are generated in case ADAMTS5 proteinases are released by chondrocytes or in case of adverse events, as observed in OA(74). Those degradation products interact with membrane receptors of cytokines such as Toll-like receptors (TLRs) but also integrins, eventually increasing pro-inflammatory and catabolic products. In the model we shortcut the implication of these DAMPs and we added a link describing the indirect activation of inflammatory cytokine receptors and integrins by ADAMTS5, assuming that ADAMTS5 amounts and DAMPS were linearly related for simplification. However, calcium signaling (TRPV4/Ca2+), which is mechanosensitive, inhibits ADAMTS5 expression in chondrocytes. This is another illustration of the multiple and complex connections between mechanotransduction and inflammatory responses. In the end, cells integrate all the aforementionned signals and modify their secretary profile accordingly, which affects their the matrix mechanical properties and cells mechanobiological environement (75), eventually leading to new external cues.

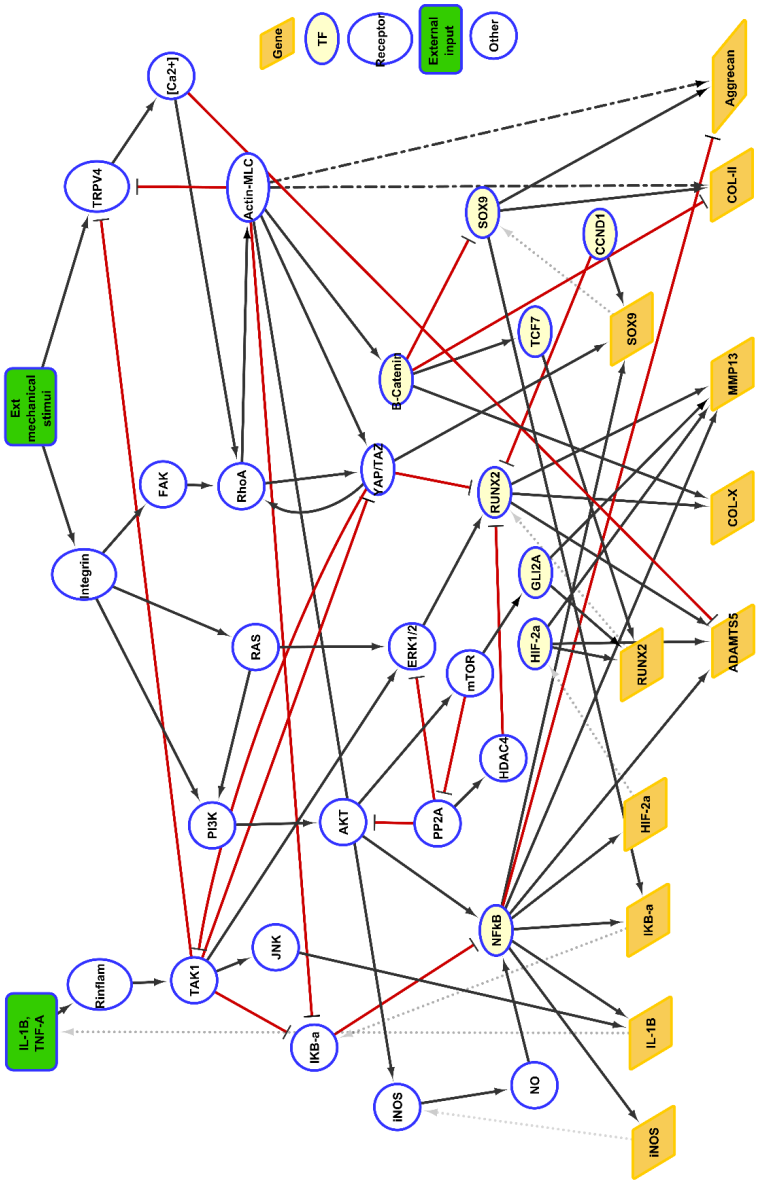


Figure B.1: Snapshot of the mechanotransduction and pro-inflammatory signaling and their crosstalk in the in silico chondrocyte. This activity flow diagram is an arbitrary selection of important crosstalk from the model and related to mechanotransduction or inflammation, for illustration. External cues (in green) are either the mechanical loading or pro-inflammatory cytokines. The signal is transduced through signaling molecules ('Other') up to transcription factors ('TF' in blue circled yellow ellipse), which up- or down-regulate the expression of downstream genes (yellow parallelograms). As a result, genes increase the amount of the corresponding upstream proteins (grey dotted lines). Black arrows (resp. red T-ended lines) represent activation (resp. inhibition) interactions or influences. Influences may be direct or indirect in chondrocytes, the dashed black lines represent interactions that involve an intermediary node in the model but that is unrepresented in the graph.

**References**

1. A. C. Lin, B. L. Seeto, J. M. Bartoszko, M. A. Khoury, H. Whetstone, L. Ho, C. Hsu, A. S. Ali, B. A. Alman, Modulating hedgehog signaling can attenuate the severity of osteoarthritis. Nat. Med. 15, 1421–1425 (2009).

2. Z. Fan, S. Söder, S. Oehler, K. Fundel, T. Aigner, Activation of interleukin-1 signaling cascades in normal and osteoarthritis articular cartilage. Am. J. Pathol. 171, 938–946 (2007).

3. J. H. Rosenberg, V. Rai, M. F. Dilisio, D. K. Agrawal, Damage-associated molecular patterns in the pathogenesis of osteoarthritis: potentially novel therapeutic targets. Mol. Cell. Biochem. 434 (2017), pp. 171–179.

4. M. Neidlin, S. Dimitrakopoulou, L. G. Alexopoulos, Multi-tissue network analysis for drug prioritization in knee osteoarthritis. Sci. Rep. 9 (2019), doi:10.1038/s41598-019-51627-6.

5. M. Kapoor, J. Martel-Pelletier, D. Lajeunesse, J. P. Pelletier, H. Fahmi, Role of proinflammatory cytokines in the pathophysiology of osteoarthritis. Nat. Rev. Rheumatol. 7 (2011), pp. 33–42.

6. J. Nam, B. D. Aguda, B. Rath, S. Agarwal, Biomechanical Thresholds Regulate Inflammation through the NF-$\kappa$B Pathway: Experiments and Modeling. PLoS One. 4, e5262 (2009).

7. Y. Li, E. H. Frank, Y. Wang, S. Chubinskaya, H. H. Huang, A. J. Grodzinsky, Moderate dynamic compression inhibits pro-catabolic response of cartilage to mechanical injury, tumor necrosis factor-$\alpha$ and interleukin-6, but accentuates degradation above a strain threshold. Osteoarthr. Cartil. 21, 1933–1941 (2013).

8. A. P. Hollander, I. Pidoux, A. Reiner, C. Rorabeck, R. Bourne, A. R. Poole, Damage to type II collagen in aging and osteoarthritis starts at the articular surface, originates around chondrocytes, and extends into the cartilage with progressive degeneration. J. Clin. Invest. 96, 2859–2869 (1995).

9. V. D. Sree, A. B. Tepole, Computational systems mechanobiology of growth and remodeling: Integration of tissue mechanics and cell regulatory network dynamics. Curr. Opin. Biomed. Eng. 15 (2020), pp. 75–80.

10. J. Nam, B. D. Aguda, B. Rath, S. Agarwal, Biomechanical thresholds regulate inflammation through the NF-$\kappa$B pathway: Experiments and modeling. PLoS One. 4 (2009), doi:10.1371/journal.pone.0005262.

11. V. B. Shim, P. J. Hunter, P. Pivonka, J. W. Fernandez, A multiscale framework based on the Physiome markup languages for exploring the initiation of osteoarthritis at the bone-cartilage interface. IEEE Trans. Biomed. Eng. 58,

3532–3536 (2011).

12. G. A. Orozco, P. Tanska, C. Florea, A. J. Grodzinsky, R. K. Korhonen, A novel mechanobiological model can predict how physiologically relevant dynamic loading causes proteoglycan loss in mechanically injured articular cartilage. Sci. Rep. 8 (2018), doi:10.1038/s41598-018-33759-3.

13. S. J. Millward-Sadler, D. M. Salter, Integrin-Dependent Signal Cascades in Chondrocyte Mechanotransduction. Ann. Biomed. Eng. 32, 435–446 (2004).

14. M. A. Wozniak, K. Modzelewska, L. Kwong, P. J. Keely, Focal adhesion regulation of cell behavior. Biochim. Biophys. Acta - Mol. Cell Res. 1692 (2004), pp. 103–119.

15. Z. Sun, S. S. Guo, R. Fässler, Integrin-mediated mechanotransduction. J. Cell Biol. 215 (2016), pp. 445–456.

16. R. F. Loeser, Integrins and chondrocyte-matrix interactions in articular cartilage. Matrix Biol. 39 (2014), pp. 11–16.

17. E. C. Arner, M. D. Tortorella, Signal transduction through chondrocyte integrin receptors induces matrix metalloproteinase synthesis and synergizes with interleukin-1. Arthritis Rheum. 38, 1304–1314 (1995).

18. N. Q. Balaban, U. S. Schwarz, D. Riveline, P. Goichberg, G. Tzur, I. Sabanay, D. Mahalu, S. Safran, A. Bershadsky, L. Addadi, B. Geiger, Force and focal adhesion assembly: A close relationship studied using elastic micropatterned substrates. Nat. Cell Biol. 3, 466–472 (2001).

19. J. Hoon, M. Tan, C.-G. Koh, The Regulation of Cellular Responses to Mechanical Cues by Rho GTPases. Cells. 5, 17 (2016).

20. K. H. Vining, D. J. Mooney, Mechanical forces direct stem cell behaviour in development and regeneration. Nat. Rev. Mol. Cell Biol. 18 (2017), pp. 728–742.

21. M. Amano, M. Nakayama, K. Kaibuchi, Rho-kinase/ROCK: A key regulator of the cytoskeleton and cell polarity. Cytoskeleton. 67 (2010), pp. 545–554.

22. G. Wang, A. Woods, S. Sabari, L. Pagnotta, L. A. Stanton, F. Beier, RhoA/ROCK Signaling Suppresses Hypertrophic Chondrocyte Differentiation. J. Biol. Chem. 279, 13205–13214 (2004).

23. M. Maekawa, T. Ishizaki, S. Boku, N. Watanabe, A. Fujita, A. Iwamatsu, T. Obinata, K. Ohashi, K. Mizuno, S. Narumiya, Signaling from Rho to the actin cytoskeleton through protein kinases ROCK and LIM-kinase. Science (80-. ). 285, 895–898 (1999).

24. D. R. Haudenschild, J. Chen, N. Pang, M. K. Lotz, D. D. D'Lima, Rho kinase-dependent activation of SOX9 in chondrocytes. Arthritis Rheum. 62, 191–200 (2010). 25. N. Wang, Review of cellular mechanotransduction. J. Phys. D. Appl. Phys. 50 (2017), p. 233002.

26. E. Lucchinetti, M. M. Bhargava, P. A. Torzilli, The effect of mechanical load on integrin subunits $\alpha 5$ and $\beta 1$ in chondrocytes from mature and immature cartilage explants. Cell Tissue Res. 315, 385–391 (2004).

27. E. N. Olson, A. Nordheim, Linking actin dynamics and gene transcription to drive cellular motile functions. Nat. Rev. Mol. Cell Biol. 11 (2010), pp. 353–365.

28. C. S. Hill, J. Wynne, R. Treisman, The Rho family GTPases RhoA, Racl, and CDC42Hsregulate transcriptional activation by SRF. Cell. 81, 1159–1170 (1995).

29. S. Dupont, L. Morsut, M. Aragona, E. Enzo, S. Giulitti, M. Cordenonsi, F. Zanconato, J. Le Digabel, M. Forcato, S. Bicciato, N. Elvassore, S. Piccolo, Role of YAP/TAZ in mechanotransduction. Nature. 474, 179–184 (2011).

30. Y. Deng, A. Wu, P. Li, G. Li, L. Qin, H. Song, K. K. Mak, Yap1 Regulates Multiple Steps of Chondrocyte Differentiation during Skeletal Development and Bone Repair. Cell Rep. 14, 2224–2237 (2016).

31. Y. Deng, J. Lu, W. Li, A. Wu, X. Zhang, W. Tong, K. K. Ho, L. Qin, H. Song, K. K. Mak, Reciprocal inhibition of YAP/TAZ and NF-$\kappa$B regulates osteoarthritic cartilage degradation. Nat. Commun. 9, 1–14 (2018).

32. W. Zhong, Y. Li, L. Li, W. Zhang, S. Wang, X. Zheng, YAP-mediated regulation of the chondrogenic phenotype in response to matrix elasticity. J. Mol. Histol. 44, 587–595 (2013).

33. Y. Guan, X. Yang, W. Yang, C. Charbonneau, Q. Chen, Mechanical activation of mammalian target of rapamycin pathway is required for cartilage development. FASEB J. 28, 4470–4481 (2014).

34. B. Pal, H. Endisha, Y. Zhang, M. Kapoor, mTOR: A Potential Therapeutic Target in Osteoarthritis? Drugs R D. 15 (2015), pp. 27–36.

35. B. Yan, Z. Zhang, D. Jin, C. Cai, C. Jia, W. Liu, T. Wang, S. Li, H. Zhang, B. Huang, P. Lai, H. Wang, A. Liu, C. Zeng, D. Cai, Y. Jiang, X. Bai, mTORC1 regulates PTHrP to coordinate chondrocyte growth, proliferation and differentiation. Nat. Commun. 7 (2016), doi:10.1038/ncomms11151.

36. Q. Dai, Z. Xu, X. Ma, N. Niu, S. Zhou, F. Xie, L. Jiang, J. Wang, W. Zou, MTOR/Raptor signaling is critical for skeletogenesis in mice through the

regulation of Runx2 expression. Cell Death Differ. 24, 1886–1899 (2017).

37. K. L. Posey, F. Coustry, A. C. Veerisetty, M. G. Hossain, M. J. Gambello, J. T. Hecht, Novel mTORC1 Mechanism Suggests Therapeutic Targets for COMPopathies. Am. J. Pathol. 189, 132–146 (2019).

38. L. Hui, V. Rodrik, R. M. Pielak, S. Knirr, Y. Zheng, D. A. Foster, mTOR-dependent suppression of protein phosphatase 2A is critical for phospholipase D survival signals in human breast cancer cells. J. Biol. Chem. 280, 35829–35835 (2005).

39. A. L. McNulty, H. A. Leddy, W. Liedtke, F. Guilak, TRPV4 as a therapeutic target for joint diseases. Naunyn. Schmiedebergs. Arch. Pharmacol. 388 (2015), pp. 437–450.

40. C. J. O'Conor, H. A. Leddy, H. C. Benefield, W. B. Liedtke, F. Guilak, TRPV4-mediated mechanotransduction regulates the metabolic response of chondrocytes to dynamic loading. Proc. Natl. Acad. Sci. U. S. A. 111, 1316–1321 (2014).

41. M. N. Phan, H. A. Leddy, B. J. Votta, S. Kumar, D. S. Levy, D. B. Lipshutz, H. L. Suk, W. Liedtke, F. Guilak, Functional characterization of TRPV4 as an osmotically sensitive ion channel in porcine articular chondrocytes. Arthritis Rheum. 60, 3028–3037 (2009).

42. C. J. O'Conor, S. Ramalingam, N. A. Zelenski, H. C. Benefield, I. Rigo, D. Little, C. L. Wu, D. Chen, W. Liedtke, A. L. McNulty, F. Guilak, Cartilage-Specific Knockout of the Mechanosensory Ion Channel TRPV4 Decreases Age-Related Osteoarthritis. Sci. Rep. 6, 1–10 (2016).

43. S. Muramatsu, M. Wakabayashi, T. Ohno, K. Amano, R. Ooishi, T. Sugahara, S. Shiojiri, K. Tashiro, Y. Suzuki, R. Nishimura, S. Kuhara, S. Sugano, T. Yoneda, A. Matsuda, Functional gene screening system identified TRPV4 as a regulator of chondrogenic differentiation. J. Biol. Chem. 282, 32158–32167 (2007).

44. M. Lv, Y. Zhou, X. Chen, L. Han, L. Wang, X. L. Lu, Calcium signaling of in situ chondrocytes in articular cartilage under compressive loading: Roles of calcium sources and cell membrane ion channels. J. Orthop. Res. 36, 730–738 (2018).

45. E. Smedler, P. Uhlén, Frequency decoding of calcium oscillations. Biochim. Biophys. Acta - Gen. Subj. 1840, 964–969 (2014).

46. X. Gong, W. Xie, B. Wang, L. Gu, F. Wang, X. Ren, C. Chen, L. Yang, Altered spontaneous calcium signaling of in situ chondrocytes in human

osteoarthritic cartilage. Sci. Rep. 7, 1–12 (2017).

47. N. Trompeter, J. Gardinier, V. DeBarros, M. Boggs, V. Gangadharan, W. Cain, L. Hurd, R. Duncan, bioRxiv, in press, doi:10.1101/2020.03.10.985713.

48. K. Novakofski, A. Boehm, L. Fortier, The small GTPase Rho mediates articular chondrocyte phenotype and morphology in response to interleukin-1$\alpha$ and insulin-like growth factor-1. J. Orthop. Res. 27, 58–64 (2009).

49. N. D. Leipzig, S. V. Eleswarapu, K. A. Athanasiou, The effects of TGF-$\beta$1 and IGF-I on the biomechanics and cytoskeleton of single chondrocytes. Osteoarthr. Cartil. 14, 1227–1236 (2006).

50. S. Pritchard, F. Guilak, Effects of interleukin-1 on calcium signaling and the increase of filamentous actin in isolated and in situ articular chondrocytes. Arthritis Rheum. 54, 2164–2174 (2006).

51. M. P. Vincenti, C. E. Brinckerhoff, Early response genes induced in chondrocytes stimulated with the inflammatory cytokine interleukin-1$\beta$. Arthritis Res. 3, 381–388 (2001).

52. Y. Y. Chow, K. Y. Chin, The Role of Inflammation in the Pathogenesis of Osteoarthritis. Mediators Inflamm. 2020 (2020), , doi:10.1155/2020/8293921.

53. M. B. Goldring, M. Otero, Inflammation in osteoarthritis. Curr. Opin. Rheumatol. 23 (2011), pp. 471–478.

54. M. Millerand, F. Berenbaum, C. Jacques, Danger signals and inflammaging in osteoarthritis. Clin. Exp. Rheumatol. 37 (2019), pp. 48–56.

55. T. Sillat, G. Barreto, P. Clarijs, A. Soininen, M. Ainola, J. Pajarinen, M. Korhonen, Y. T. Konttinen, R. Sakalyte, M. Hukkanen, P. Ylinen, D. C. E. Nordström, Toll-like receptors in human chondrocytes and osteoarthritic cartilage. Acta Orthop. 84, 585–592 (2013).

56. A. Weber, P. Wasiliew, M. Kracht, Interleukin-1 (IL-1B) pathway. Sci. Signal. 3 (2010), p. 1.

57. C. Lianxu, J. Hongti, Y. Changlong, NF-$\kappa$Bp65-specific siRNA inhibits expression of genes of COX-2, NOS-2 and MMP-9 in rat IL-1$\beta$-induced and TNF-$\alpha$-induced chondrocytes. Osteoarthr. Cartil. 14, 367–376 (2006).

58. S. Madhavan, M. Anghelina, D. Sjostrom, A. Dossumbekova, D. C. Guttridge, S. Agarwal, Biomechanical Signals Suppress TAK1 Activation to Inhibit NF-$\kappa$B Transcriptional Activation in Fibrochondrocytes. J. Immunol. 179, 6246–6254 (2007).

59. Choi, Jo, Park, Kang, Park, NF-B Signaling Pathways in Osteoarthritic Cartilage Destruction. Cells. 8, 734 (2019).

60. R. M. Clancy, P. F. Gomez, S. B. Abramson, Nitric oxide sustains nuclear factor kappaB activation in cytokine-stimulated chondrocytes. Osteoarthr. Cartil. 12, 552–558 (2004).

61. J. N. Sharma, A. Al-Omran, S. S. Parvathy, Role of nitric oxide in inflammatory diseases. Inflammopharmacology. 15 (2007), pp. 252–259.

62. K. Vuolteenaho, T. Moilanen, U. Jalonen, A. Lahti, R. Nieminen, H. M. Van Beuningen, P. M. Van Der Kraan, E. Moilanen, TGF$\beta$ inhibits IL-1 -induced iNOS expression and NO production in immortalized chondrocytes. Inflamm. Res. 54, 420–427 (2005).

63. B. Ma, L. Zhong, C. A. Van Blitterswijk, J. N. Post, M. Karperien, T cell factor 4 is a pro-catabolic and apoptotic factor in human articular chondrocytes by potentiating nuclear factor $\kappa$B signaling. J. Biol. Chem. 288, 17552–17558 (2013).

64. C. Malemud, Negative Regulators of JAK/STAT Signaling in Rheumatoid Arthritis and Osteoarthritis. Int. J. Mol. Sci. 18, 484 (2017).

65. R. C. Olney, K. Tsuchiya, D. M. Wilson, M. Mohtai, W. J. Maloney, D. J. Schurman, R. L. Smith, Chondrocytes from osteoarthritic cartilage have increased expression of insulin-like growth factor I (IGF-I) and IGF-binding protein-3 (IGFBP-3) and -5, but not IGF-II or IGFBP-4. J. Clin. Endocrinol. Metab. 81, 1096–1103 (1996).

66. J. Martel-Pelletier, J. A. Di Battista, D. Lajeunesse, J. P. Pelletier, IGF/IGFBP axis in cartilage and bone in osteoarthritis pathogenesis. Inflamm. Res. 47 (1998), pp. 90–100.

67. R. C. Olney, D. M. Wilson, M. Mohtai, P. J. Fielder, R. L. Smith, Interleukin-1 and tumor necrosis factor-$\alpha$ increase insulin-like growth factor-binding protein-3 (IGFBP-3) production and IGFBP-3 protease activity in human articular chondrocytes. J. Endocrinol. 146, 279–286 (1995).

68. A. M. Grabiec, C. Angiolilli, L. M. Hartkamp, L. G. M. Van Baarsen, P. P. Tak, K. A. Reedquist, JNK-dependent downregulation of FoxO1 is required to promote the survival of fibroblast-like synoviocytes in rheumatoid arthritis. Ann. Rheum. Dis. 74, 1763–1771 (2015).

69. T. Matsuzaki, O. Alvarez-Garcia, S. Mokuda, K. Nagira, M. Olmer, R. Gamini, K. Miyata, Y. Akasaki, A. I. Su, H. Asahara, M. K. Lotz, FoxO transcription factors modulate autophagy and proteoglycan 4 in cartilage

homeostasis and osteoarthritis. Sci. Transl. Med. 10, eaan0746 (2018).

70. J. Deschner, B. Rath-Deschner, S. Agarwal, Regulation of matrix metalloproteinase expression by dynamic tensile strain in rat fibrochondrocytes. Osteoarthr. Cartil. 14, 264–272 (2006).

71. A. Dossumbekova, M. Anghelina, S. Madhavan, L. He, N. Quan, T. Knobloch, S. Agarwal, Biomechanical signals inhibit IKK activity to attenuate NF-$\kappa$B transcription activity in inflamed chondrocytes. Arthritis Rheum. 56, 3284–3296 (2007).

72. B. Fermor, J. Brice Weinberg, D. S. Pisetsky, M. A. Misukonis, A. J. Banes, F. Guilak, The effects of static and intermittent compression on nitric oxide production in articular cartilage explants. J. Orthop. Res. 19, 729–737 (2001).

73. B. Fermor, J. B. Weinberg, D. S. Pisetsky, F. Guilak, The influence of oxygen tension on the induction of nitric oxide and prostaglandin E2 by mechanical stress in articular cartilage. Osteoarthr. Cartil. 13, 935–941 (2005).

74. J. Martel-Pelletier, A. J. Barr, F. M. Cicuttini, P. G. Conaghan, C. Cooper, M. B. Goldring, S. R. Goldring, G. Jones, A. J. Teichtahl, J. P. Pelletier, Osteoarthritis. Nat. Rev. Dis. Prim. 2 (2016), pp. 1–18.

75. L. G. Alexopoulos, L. A. Setton, F. Guilak, The biomechanical role of the chondrocyte pericellular matrix in articular cartilage. Acta Biomater. 1, 317–325 (2005). 76. A. Erdemir, Open knee: A pathway to community driven modeling and simulation in joint biomechanics. J. Med. Devices, Trans. ASME. 7, 1 (2013).

77. S. Mukherjee, R. Lesage, W. Wilson, L. Geris. Multiscale modeling to investigate the role of mechanical loading in articular cartilage. 14th World Congress in Computational Mechanics (WCCM) and ECCOMAS Congress 2020, 11-15 January 2021, Virtual Congress. (2021).

78. P. Julkunen, W. Wilson, J. S. Jurvelin, R. K. Korhonen, Composition of the pericellular matrix modulates the deformation behaviour of chondrocytes in articular cartilage under static loading. Med. Biol. Eng. Comput. 47, 1281–1290 (2009).

79. A. A. Young, S. McLennan, M. M. Smith, S. M. Smith, M. A. Cake, R. A. Read, J. Melrose, D. H. Sonnabend, C. R. Flannery, C. B. Little., Proteoglycan 4 downregulation in a sheep meniscectomy model of early osteoarthritis. Arthritis Res. Ther. 8 (2006), doi:10.1186/ar1898.

80. J. B. Thorlund, A. Holsgaard-Larsen, M. W. Creaby, G. M. Jørgensen, N. Nissen, M. Englund, L. S. Lohmander, Changes in knee joint load indices from

before to 12 months after arthroscopic partial meniscectomy: A prospective cohort study. Osteoarthr. Cartil. 24, 1153–1159 (2016).

81. S. Fu, H. Meng, S. Inamdar, B. Das, H. Gupta, W. Wang, C. L. Thompson, M. M. Knight, Activation of TRPV4 by mechanical, osmotic or pharmaceutical stimulation is anti-inflammatory blocking IL-1$\beta$ mediated articular cartilage matrix destruction. Osteoarthr. Cartil. 29, 89–99 (2021).

82. R. Potla, M. Hirano-Kobayashi, H. Wu, H. Chen, A. Mammoto, B. D. Matthews, D. E. Ingber, Molecular mapping of transmembrane mechanotransduction through the $\beta$1 integrin–CD98hc–TRPV4 axis. J. Cell Sci. 133 (2020), doi:10.1242/jcs.248823.

83. C. Ji, C. A. McCulloch, TRPV4 integrates matrix mechanosensing with Ca2+ signaling to regulate extracellular matrix remodeling. FEBS J. (2020), , doi:10.1111/febs.15665.

# Appendix C

# Mesh convergence studies

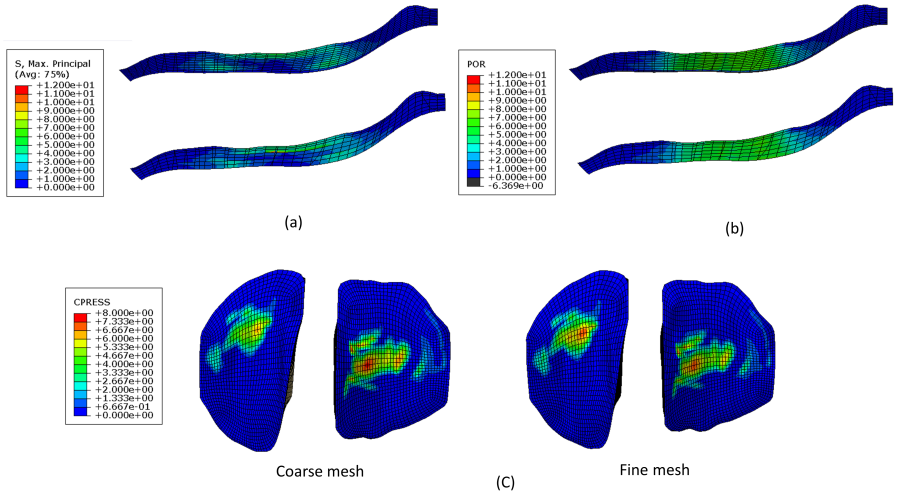


Figure C.1: Mesh convergence study of knee joint. (a) Maximum principal stress. (b) Pore pressure. (c) Contact pressure

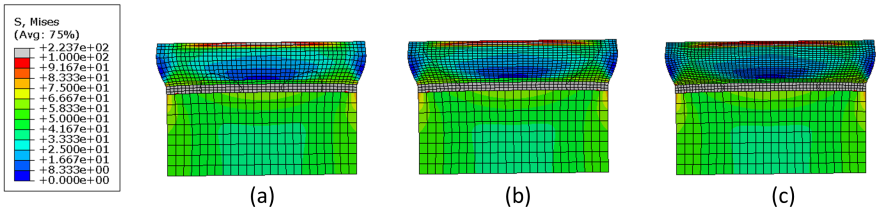


Figure C.2: Mesh convergence study for osteochondral plugs at 30% strain. (a) Mesh=32023 elements. (b) Mesh=50263 elements. (c) Mesh=91447 elements.

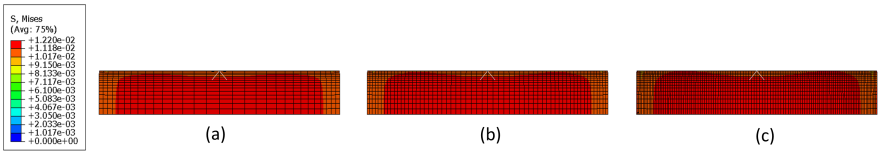


Figure C.3: Mesh convergence study for agarose constructs 30% strain. (a) Mesh=18297 elements. (b) Mesh=54672 elements. (c) Mesh=221127 elements.

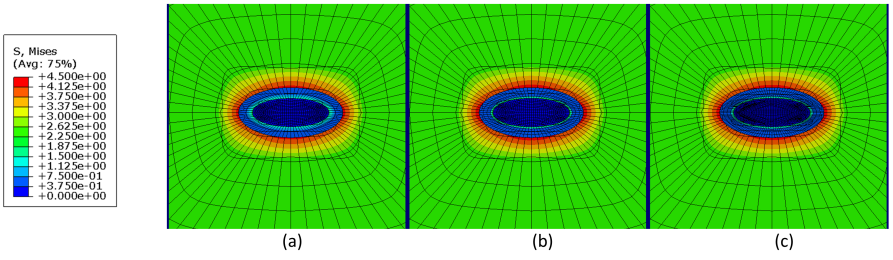


Figure C.4: Mesh convergence study for cell-level model 10% strain. (a) Mesh=29216 elements. (b) Mesh=32912 elements. (c) Mesh=59092 elements.

# Bibliography


[1] S. Mukherjee, M. Nazemi, I. Jonkers, and L. Geris. "Use of Computational Modeling to Study Joint Degeneration: A Review". English. *Front. Bioeng. Biotechnol.* 8 (2020). Publisher: Frontiers. DOI: 10.3389/fbioe.2020.00093.

[2] B. R. Deshpande, J. N. Katz, D. H. Solomon, E. H. Yelin, D. J. Hunter, S. P. Messier, L. G. Suter, and E. Losina. "Number of Persons With Symptomatic Knee Osteoarthritis in the US: Impact of Race and Ethnicity, Age, Sex, and Obesity". *Arthritis Care & Research* 68.12 (2016), pp. 1743–1750. DOI: 10.1002/acr.22897.

[3] L. B. Murphy, M. G. Cisternas, D. J. Pasta, C. G. Helmick, and E. H. Yelin. "Medical Expenditures and Earnings Losses Among US Adults With Arthritis in 2013". *Arthritis Care & Research* 70.6 (2018), pp. 869–876. DOI: 10.1002/acr.23425.

[4] K. D. Brandt, E. L. Radin, P. A. Dieppe, and L Van De Putte. *Yet more evidence that osteoarthritis is not a cartilage disease*. ISBN: 0003-4967. 2006.

[5] K. E. Kuettner and A. A. Cole. "Cartilage degeneration in different human joints". *Osteoarthritis and Cartilage* 13.2 (2005), pp. 93–103. DOI: 10.1016/j.joca.2004.11.006.

[6] R. J. Lories and F. P. Luyten. "The bone–cartilage unit in osteoarthritis". en. *Nat Rev Rheumatol* 7.1 (2011). Publisher: Nature Publishing Group, pp. 43–49. DOI: 10.1038/nrrheum.2010.197.

[7] T. D. Brown, E. L. Radin, R. B. Martin, and D. B. Burr. "Finite element studies of some juxtarticular stress changes due to localized subchondral stiffening." *Journal of biomechanics* 17.1 (1984), pp. 11–24.

[8] J. L. Berry, D. A. Thaeler-Oberdoerster, and A. S. Greenwald. "Subchondral pathways to the superior surface of the human talus." *Foot & ankle* 7.1 (1986), pp. 2–9.

[9] H Imhof, M Breitenseher, F Kainberger, T Rand, and S Trattnig. "Importance of subchondral bone to articular cartilage in health and disease." *Topics in magnetic resonance imaging : TMRI* 10.3 (1999), pp. 180–92.

[10] T. J. Lyons, S. F. McClure, R. W. Stoddart, and J. McClure. "The normal human chondro-osseous junctional region: evidence for contact of uncalcified cartilage with subchondral bone and marrow spaces". *BMC Musculoskeletal Disorders* 7.1 (2006), p. 52. DOI: 10.1186/1471-2474-7-52.

[11] D. Prieto-Alhambra, A. Judge, M. K. Javaid, C. Cooper, A. Diez-Perez, and N. K. Arden. "Incidence and risk factors for clinically diagnosed knee, hip and hand osteoarthritis: influences of age, gender and osteoarthritis affecting other joints". *Annals of the Rheumatic Diseases* 73.9 (2014), pp. 1659–1664. DOI: 10.1136/annrheumdis-2013-203355.

[12] A. Erdemir, T. F. Besier, J. P. Halloran, C. Imhauser, P. J. Laz, T. Morrison, and K. B. Shelburne. "Deciphering the ?Art? in Modeling and Simulation of the Knee Joint". *Journal of Biomechanical Engineering* (2019). DOI: 10.1115/1.4043346.

[13] K Yamada, R Healey, D Amiel, M Lotz, and R Coutts. "Subchondral bone of the human knee joint in aging and osteoarthritis". *Osteoarthritis and Cartilage* 10.5 (2002). Publisher: Elsevier, pp. 360–369. DOI: 10.1053/joca.2002.0525.

[14] A. J. Sophia Fox, A. Bedi, and S. A. Rodeo. "The basic science of articular cartilage: structure, composition, and function". eng. *Sports health* 1.6 (2009). Publisher: SAGE Publications, pp. 461–468. DOI: 10.1177/1941738109350438.

[15] J. T. A. Mäkelä, S.-k. Han, W Herzog, and R. K. Korhonen. "Very early osteoarthritis changes sensitively fl uid fl ow properties of articular cartilage". 48 (2015), pp. 3369–3376. DOI: 10.1016/j.jbiomech.2015.06.010.

[16] M. E. Mononen, P. Tanska, H. Isaksson, and R. K. Korhonen. "New algorithm for simulation of proteoglycan loss and collagen degeneration in the knee joint: Data from the osteoarthritis initiative". *Journal of Orthopaedic Research®* 36.6 (2018), pp. 1673–1683. DOI: 10.1002/jor.23811.

[17] L. A. Setton, V. C. Mow, F. J. Müller, J. C. Pita, and D. S. Howell. "Mechanical Properties of Canine Articular Cartilage Are Significantly Altered Following Transection of the Anterior Cruciate Ligament". *Journal of Orthopaedic Research* 12.4 (1994), pp. 451–463. DOI: 10.1002/jor.1100120402.

[18] W. Wilson, C. van Donkelaar, B. van Rietbergen, and R. Huiskes. "A fibril-reinforced poroviscoelastic swelling model for articular cartilage". *Journal of Biomechanics* 38.6 (2005), pp. 1195–1204. DOI: 10.1016/j.jbiomech.2004.07.003.

[19] G. A. Orozco, P. Tanska, C. Florea, A. J. Grodzinsky, and R. K. Korhonen. "A novel mechanobiological model can predict how physiologically relevant dynamic loading causes proteoglycan loss in mechanically injured articular cartilage". *Scientific Reports* 8.1 (2018), p. 15599. DOI: 10.1038/s41598-018-33759-3.

[20] S. Saarakkala, P. Julkunen, P. Kiviranta, J. Mäkitalo, J. Jurvelin, and R. Korhonen. "Depth-wise progression of osteoarthritis in human articular cartilage: investigation of composition, structure and biomechanics". *Osteoarthritis and Cartilage* 18.1 (2010), pp. 73–81. DOI: 10.1016/j.joca.2009.08.003.

[21] J. Fick, A. P. Ronkainen, R. Madden, A. Sawatsky, V. Tiitu, W. Herzog, and R. Korhonen. "Early in situ changes in chondrocyte biomechanical responses due to a partial meniscectomy in the lateral compartment of the mature rabbit knee joint". *Journal of Biomechanics* 49.16 (2016), pp. 4057–4064. DOI: 10.1016/j.jbiomech.2016.10.039.

[22] J. Rieppo, J. Töyräs, M. T. Nieminen, V. Kovanen, M. M. Hyttinen, R. K. Korhonen, J. S. Jurvelin, and H. J. Helminen. "Structure-Function Relationships in Enzymatically Modified Articular Cartilage". *Cells Tissues Organs* 175.3 (2003), pp. 121–132. DOI: 10.1159/000074628.

[23] M. Thibault, A. Robin Poole, and M. D. Buschmann. "Cyclic compression of cartilage/bone explants in vitro leads to physical weakening, mechanical breakdown of collagen and release of matrix fragments". *Journal of Orthopaedic Research* 20.6 (2002), pp. 1265–1273. DOI: 10.1016/S0736-0266(02)00070-0.

[24] S. Hosseini, W. Wilson, K. Ito, and C. van Donkelaar. "A numerical model to study mechanically induced initiation and progression of damage in articular cartilage". *Osteoarthritis and Cartilage* 22.1 (2014), pp. 95–103. DOI: 10.1016/j.joca.2013.10.010.

[25] M. E. Mononen, M. T. Mikkola, P. Julkunen, R. Ojala, M. T. Nieminen, J. S. Jurvelin, and R. K. Korhonen. "Effect of superficial collagen patterns and fibrillation of femoral articular cartilage on knee joint mechanics-A 3D finite element analysis". *Journal of Biomechanics* 45.3 (2012). Publisher: Elsevier, pp. 579–587. DOI: 10.1016/j.jbiomech.2011.11.003.

[26] W. Wilson, N. J. Driessen, C. C. van Donkelaar, and K. Ito. "Prediction of collagen orientation in articular cartilage by a collagen remodeling algorithm". *Osteoarthritis and Cartilage* 14.11 (2006), pp. 1196–1202. DOI: 10.1016/j.joca.2006.05.006.

[27] R. A. Bank, M. Soudry, A. Maroudas, J. Mizrahi, and J. M. TeKoppele. "The increased swelling and instantaneous deformation of osteoarthritic cartilage is highly correlated with collagen degradation". *Arthritis & Rheumatism* 43.10 (2000), pp. 2202–2210. DOI: 10.1002/1529-0131(200010)43:10<2202::AID-ANR7>3.0.CO;2-E.

[28] J. Clouet, C. Vinatier, C. Merceron, M. Pot-vaucel, Y. Maugars, P. Weiss, G. Grimandi, and J. Guicheux. "From osteoarthritis treatments to future regenerative therapies for cartilage". *Drug Discovery Today* 14.19-20 (2009), pp. 913–925. DOI: 10.1016/j.drudis.2009.07.012.

[29] L Lippiello, D Hall, and H. J. Mankin. "Collagen synthesis in normal and osteoarthritic human cartilage." *Journal of Clinical Investigation* 59.4 (1977), pp. 593–600. DOI: 10.1172/JCI108676.

[30] F. Moldovan, J.-P. Pelletier, J. Hambor, J.-M. Cloutier, and J. Martel-Pelletier. "Collagenase-3 (matrix metalloprotease 13) is preferentially localized in the deep layer of human arthritic cartilage in situ. In vitro mimicking effect by transforming growth factor $\beta$". *Arthritis & Rheumatism* 40.9 (1997), pp. 1653–1661. DOI: 10.1002/art.1780400915.

[31] Y Okada, M Shinmei, O Tanaka, K Naka, A Kimura, I Nakanishi, M. T. Bayliss, K Iwata, and H Nagase. "Localization of matrix metalloproteinase 3 (stromelysin) in osteoarthritic cartilage and synovium." *Laboratory investigation; a journal of technical methods and pathology* 66.6 (1992), pp. 680–90.

[32] C.-T. Chen, M. Bhargava, P. M. Lin, and P. A. Torzilli. "Time, stress, and location dependent chondrocyte death and collagen damage in cyclically loaded articular cartilage". *Journal of Orthopaedic Research* 21.5 (2003), pp. 888–898. DOI: 10.1016/S0736-0266(03)00050-0.

[33] H. Kim and F. Blanco. "Cell Death and Apoptosis in Ostearthritic Cartilage". *Current Drug Targets* 8.2 (2007), pp. 333–345. DOI: 10.2174/138945007779940025.

[34] J Alvarez, M Balbín, F Santos, M Fernández, S Ferrando, and J. M. López. "Different bone growth rates are associated with changes in the expression pattern of types II and X collagens and collagenase 3 in proximal growth plates of the rat tibia." *Journal of bone and mineral research : the official journal of the American Society for Bone and Mineral Research* 15.1 (2000), pp. 82–94. DOI: 10.1359/jbmr.2000.15.1.82.

[35] T Kirsch and K von der Mark. "Remodelling of collagen types I, II and X and calcification of human fetal cartilage." *Bone and mineral* 18.2 (1992), pp. 107–17.

[36] M Nurminskaya and T. F. Linsenmayer. "Identification and characterization of up-regulated genes during chondrocyte hypertrophy." *Developmental dynamics : an official publication of the American Association of Anatomists* 206.3 (1996), pp. 260–71. DOI: 10.1002/(SICI)1097-0177(199607)206:3<260::AID-AJA4>3.0.CO;2-G.

[37] R. Dreier. "Hypertrophic differentiation of chondrocytes in osteoarthritis: the developmental aspect of degenerative joint disorders." *Arthritis research & therapy* 12.5 (2010), p. 216. DOI: 10.1186/ar3117.

[38] P. van der Kraan and W. van den Berg. "Chondrocyte hypertrophy and osteoarthritis: role in initiation and progression of cartilage degeneration?" *Osteoarthritis and Cartilage* 20.3 (2012), pp. 223–232. DOI: 10.1016/j.joca.2011.12.003.

[39] K von der Mark, T Kirsch, A Nerlich, A Kuss, G Weseloh, K Glückert, and H Stöss. "Type X collagen synthesis in human osteoarthritic cartilage. Indication of chondrocyte hypertrophy." *Arthritis and rheumatism* 35.7 (1992), pp. 806–11. DOI: 10.1002/art.1780350715.

[40] E. Hargrave-Thomas, F. van Sloun, M. Dickinson, N. Broom, and A. Thambyah. "Multi-scalar mechanical testing of the calcified cartilage and subchondral bone comparing healthy vs early degenerative states". *Osteoarthritis and Cartilage* 23.10 (2015), pp. 1755–1762. DOI: 10.1016/j.joca.2015.05.012.

[41] T. R. Oegema, R. J. Carpenter, F. Hofmeister, and R. C. Thompson. "The interaction of the zone of calcified cartilage and subchondral bone in osteoarthritis". *Microscopy Research and Technique* 37.4 (1997), pp. 324–332. DOI: 10.1002/(SICI)1097-0029(19970515)37:4<324::AID-JEMT7>3.0.CO;2-K.

[42] T. R. Oegema, S. L. Johnson, T. Meglitsch, and R. J. Carpenter. "Prostaglandins and the Zone of Calcified Cartilage in Osteoarthritis." *American journal of therapeutics* 3.2 (1996), pp. 139–149.

[43] A. Thambyah and N. Broom. "On how degeneration influences load-bearing in the cartilage–bone system: a microstructural and micromechanical study". *Osteoarthritis and Cartilage* 15.12 (2007), pp. 1410–1423. DOI: 10.1016/j.joca.2007.05.006.

[44] D. A. Walsh, D. F. McWilliams, M. J. Turley, M. R. Dixon, R. E. Fransès, P. I. Mapp, and D. Wilson. "Angiogenesis and nerve growth factor at the osteochondral junction in rheumatoid arthritis and osteoarthritis." *Rheumatology (Oxford, England)* 49.10 (2010), pp. 1852–61. DOI: 10.1093/rheumatology/keq188.

[45] B Li and R. M. Aspden. "Composition and mechanical properties of cancellous bone from the femoral head of patients with osteoporosis or osteoarthritis." eng. *Journal of bone and mineral research : the official journal of the American Society for Bone and Mineral Research* 12.4 (1997). Place: United States, pp. 641–651. DOI: 10.1359/jbmr.1997.12.4.641.

[46] C. Buckland-Wright. "Subchondral bone changes in hand and knee osteoarthritis detected by radiography". *Osteoarthritis and Cartilage* 12 (2004). Publisher: Elsevier, pp. 10–19. DOI: 10.1016/j.joca.2003.09.007.

[47] J. M. Clark and J. D. Huber. "The structure of the human subchondral plate". *The Journal of Bone and Joint Surgery. British volume* 72-B.5 (1990). Publisher: The British Editorial Society of Bone & Joint Surgery, pp. 866–873. DOI: 10.1302/0301-620X.72B5.2211774.

[48] M. D. Grynpas, B Alpert, I Katz, I Lieberman, and K. P. H. Pritzker. "Subchondral bone in osteoarthritis". *Calcified Tissue International* 49.1 (1991), pp. 20–26. DOI: 10.1007/BF02555898.

[49] S Milz and R Putz. "Quantitative morphology of the subchondral plate of the tibial plateau". eng. *Journal of anatomy* 185 ( Pt 1.Pt 1 (1994), pp. 103–110.

[50] O.-M. Aho, M. Finnilä, J. Thevenot, S. Saarakkala, and P. Lehenkari. "Subchondral bone histology and grading in osteoarthritis". eng. *PloS one* 12.3 (2017). Publisher: Public Library of Science, e0173726–e0173726. DOI: 10.1371/journal.pone.0173726.

[51] S. R. Goldring. "Alterations in periarticular bone and cross talk between subchondral bone and articular cartilage in osteoarthritis". eng. *Therapeutic advances in musculoskeletal disease* 4.4 (2012). Publisher: SAGE Publications, pp. 249–258. DOI: 10.1177/1759720X12437353.

[52] Y. Li, E. H. Frank, Y. Wang, S. Chubinskaya, H.-H. Huang, and A. J. Grodzinsky. "Moderate dynamic compression inhibits pro-catabolic response of cartilage to mechanical injury, tumor necrosis factor-$\alpha$ and interleukin-6, but accentuates degradation above a strain threshold". English. *Osteoarthritis and Cartilage* 21.12 (2013). Publisher: Elsevier, pp. 1933–1941. DOI: 10.1016/j.joca.2013.08.021.

[53] K Choi, J. L. Kuhn, M. J. Ciarelli, and S. A. Goldstein. "The elastic moduli of human subchondral, trabecular, and cortical bone tissue and the size-dependency of cortical bone modulus". *Journal of Biomechanics* 23.11 (1990), pp. 1103–1113. DOI: https://doi.org/10.1016/0021-9290(90)90003-L.

[54] B. Li and R. M. Aspden. "Mechanical and material properties of the subchondral bone plate from the femoral head of patients with osteoarthritis or osteoporosis". *Annals of the Rheumatic Diseases* 56.4 (1997), 247 LP –254. DOI: 10.1136/ard.56.4.247.

[55] J. D. Johnston, S. A. Kontulainen, B. A. Masri, and D. R. Wilson. "Predicting subchondral bone stiffness using a depth-specific CT topographic mapping technique in normal and osteoarthritic proximal tibiae". *Clinical Biomechanics* 26.10 (2011). Publisher: Elsevier, pp. 1012–1018. DOI: 10.1016/j.clinbiomech.2011.06.009.

[56] M. ?Amini. "Stiffness of the Proximal Tibial Bone in Normal and Osteoarthritic Conditions: A Parametric Finite Element Simulation Study". PhD Thesis. University of Saskatchewan, 2013.

[57] S. M. Bentzen, I Hvid, and J Jorgensen. "Mechanical strength of tibial trabecular bone evaluated by X-ray computed tomography". *Journal of Biomechanics* 20.8 (1987), pp. 743–752. DOI: https://doi.org/10.1016/0021-9290(87)90053-4.

[58] J. S. Day, M Ding, J. C. van der Linden, I Hvid, D. R. Sumner, and H Weinans. "A decreased subchondral trabecular bone tissue elastic modulus is associated with pre-arthritic cartilage damage". *Journal of Orthopaedic Research* 19.5 (2001). Publisher: John Wiley & Sons, Ltd, pp. 914–918. DOI: 10.1016/S0736-0266(01)00012-2.

[59] J. B. Finlay, R. B. Bourne, W. J. Kraemer, T. K. Moroz, and C. H. Rorabeck. "Stiffness of bone underlying the tibial plateaus of osteoarthritic and normal knees." eng. *Clinical orthopaedics and related research* 247 (1989). Place: United States, pp. 193–201.

[60] P. K. Zysset, M Sonny, and W. C. Hayes. "Morphology-mechanical property relations in trabecular bone of the osteoarthritic proximal tibia." eng. *The Journal of arthroplasty* 9.2 (1994). Place: United States, pp. 203–216.

[61] L Kamibayashi, U. P. Wyss, T. D. V. Cooke, and B Zee. "Trabecular microstructure in the medial condyle of the proximal tibia of patients with knee osteoarthritis". *Bone* 17.1 (1995), pp. 27–35. DOI: https://doi.org/10.1016/8756-3282(95)00137-3.

[62] J. H. Keyak, I. Y. Lee, and H. B. Skinner. "Correlations between orthogonal mechanical properties and density of trabecular bone: use of different densitometric measures." eng. *Journal of biomedical materials research* 28.11 (1994). Place: United States, pp. 1329–1336. DOI: 10.1002/jbm.820281111.

[63] E. F. Morgan, H. H. Bayraktar, and T. M. Keaveny. "Trabecular bone modulus-density relationships depend on anatomic site." eng. *Journal of biomechanics* 36.7 (2003). Place: United States, pp. 897–904.

[64] A. M. Coats, P Zioupos, and R. M. Aspden. "Material properties of subchondral bone from patients with osteoporosis or osteoarthritis by microindentation testing and electron probe microanalysis." eng. *Calcified tissue international* 73.1 (2003). Place: United States, pp. 66–71.

[65] E. Dall'Ara, C. Ohman, M. Baleani, and M. Viceconti. "Reduced tissue hardness of trabecular bone is associated with severe osteoarthritis." eng. *Journal of biomechanics* 44.8 (2011). Place: United States, pp. 1593–1598. DOI: 10.1016/j.jbiomech.2010.12.022.

[66] C Chappard, F Peyrin, A Bonnassie, G Lemineur, B Brunet-Imbault, E Lespessailles, and C.-L. Benhamou. "Subchondral bone micro-architectural alterations in osteoarthritis: a synchrotron micro-computed tomography study." eng. *Osteoarthritis and cartilage* 14.3 (2006). Place: England, pp. 215–223. DOI: 10.1016/j.joca.2005.09.008.

[67] L. G. E. Cox, C. C. van Donkelaar, B van Rietbergen, P. J. Emans, and K Ito. "Decreased bone tissue mineralization can partly explain subchondral sclerosis observed in osteoarthritis." eng. *Bone* 50.5 (2012). Place: United States, pp. 1152–1161. DOI: 10.1016/j.bone.2012.01.024.

[68] M Ding, C. C. Danielsen, and I Hvid. "Bone density does not reflect mechanical properties in early-stage arthrosis." eng. *Acta orthopaedica Scandinavica* 72.2 (2001). Place: England, pp. 181–185. DOI: 10.1080/000164701317323444.

[69] M Ding, A Odgaard, and I Hvid. "Changes in the three-dimensional microstructure of human tibial cancellous bone in early osteoarthritis." eng. *The Journal of bone and joint surgery. British volume* 85.6 (2003). Place: England, pp. 906–912.

[70] D. K. Dedrick, S. A. Goldstein, K. D. Brandt, B. L. O'Connor, R. W. Goulet, and M Albrecht. "A longitudinal study of subchondral plate and trabecular bone in cruciate-deficient dogs with osteoarthritis followed up for 54 months." eng. *Arthritis and rheumatism* 36.10 (1993). Place: United States, pp. 1460–1467.

[71] D. L. Batiste, A. Kirkley, S. Laverty, L. M. F. Thain, A. R. Spouge, and D. W. Holdsworth. "Ex vivo characterization of articular cartilage and bone lesions in a rabbit ACL transection model of osteoarthritis using MRI and micro-CT." eng. *Osteoarthritis and cartilage* 12.12 (2004). Place: England, pp. 986–996. DOI: 10.1016/j.joca.2004.08.010.

[72] M Ding, M Dalstra, F Linde, and I Hvid. "Changes in the stiffness of the human tibial cartilage-bone complex in early-stage osteoarthrosis." eng. *Acta orthopaedica Scandinavica* 69.4 (1998). Place: England, pp. 358–362.

[73] F Intema, H. A. W. Hazewinkel, D Gouwens, J. W. J. Bijlsma, H Weinans, F. P. J. G. Lafeber, and S. C. Mastbergen. "In early OA, thinning of the subchondral plate is directly related to cartilage damage: results from a canine ACLT-meniscectomy model." eng. *Osteoarthritis and cartilage* 18.5 (2010). Place: England, pp. 691–698. DOI: 10.1016/j.joca.2010.01.004.

[74] D. B. Burr and M. B. Schaffler. "The involvement of subchondral mineralized tissues in osteoarthrosis: quantitative microscopic evidence." eng. *Microscopy research and technique* 37.4 (1997). Place: United States, pp. 343–357. DOI: 10.1002/(SICI)1097-0029(19970515)37:4<343::AID-JEMT9>3.0.CO;2-L.

[75] J. D. Johnston, B. A. Masri, and D. R. Wilson. "Computed tomography topographic mapping of subchondral density (CT-TOMASD) in osteoarthritic and normal knees: methodological development and preliminary findings." eng. *Osteoarthritis and cartilage* 17.10 (2009). Place: England, pp. 1319–1326. DOI: 10.1016/j.joca.2009.04.013.

[76] E. L. Radin, I. L. Paul, and M. J. Tolkoff. "Subchondral bone changes in patients with early degenerative joint disease." eng. *Arthritis and rheumatism* 13.4 (1970). Place: United States, pp. 400–405.

[77] E. L. Radin, I. L. Paul, and R. M. Rose. "Role of mechanical factors in pathogenesis of primary osteoarthritis." eng. *Lancet (London, England)* 1.7749 (1972). Place: England, pp. 519–522. DOI: 10.1016/s0140-6736(72)90179-1.

[78] E. L. Radin and R. M. Rose. "Role of subchondral bone in the initiation and progression of cartilage damage." eng. *Clinical orthopaedics and related research* 213 (1986). Place: United States, pp. 34–40.

[79] V. B. Shim, P. J. Hunter, P. Pivonka, and J. W. Fernandez. "A Multiscale Framework Based on the Physiome Markup Languages for Exploring the Initiation of Osteoarthritis at the Bone–Cartilage Interface". *IEEE Transactions on Biomedical Engineering* 58.12 (2011). Conference Name: IEEE Transactions on Biomedical Engineering, pp. 3532–3536. DOI: 10.1109/TBME.2011.2165955.

[80] D. Simon, R. Mascarenhas, B. M. Saltzman, M. Rollins, B. R. Bach, and P. MacDonald. "The Relationship between Anterior Cruciate Ligament Injury and Osteoarthritis of the Knee". *Advances in Orthopedics* 2015 (2015), pp. 1–11. DOI: 10.1155/2015/928301.

[81] M. Englund and L. S. Lohmander. "Meniscectomy and osteoarthritis: what is the cause and what is the effect?" *Future Rheumatology* 1.2 (2006), pp. 207–215. DOI: 10.2217/17460816.1.2.207.

[82] S. Farrokhi, M. O'Connell, A. B. Gil, P. J. Sparto, and G. K. Fitzgerald. "Altered Gait Characteristics in Individuals With Knee Osteoarthritis and Self-Reported Knee Instability". *Journal of Orthopaedic & Sports Physical Therapy* 45.5 (2015), pp. 351–359. DOI: 10.2519/jospt.2015.5540.

[83] J. Favre and B. M. Jolles. "Gait analysis of patients with knee osteoarthritis highlights a pathological mechanical pathway and provides a basis for therapeutic interventions". *EFORT Open Reviews* 1.10 (2016), pp. 368–374. DOI: 10.1302/2058-5241.1.000051.

[84] A. J. Baliunas, D. E. Hurwitz, A. B. Ryals, A Karrar, J. P. Case, J. A. Block, and T. P. Andriacchi. "Increased knee joint loads during walking are present in subjects with knee osteoarthritis." *Osteoarthritis and cartilage* 10.7 (2002), pp. 573–9.

[85] R. E. Richards, M. S. Andersen, J. Harlaar, and J. C. van den Noort. "Relationship between knee joint contact forces and external knee joint moments in patients with medial knee osteoarthritis: effects of gait modifications". *Osteoarthritis and Cartilage* 26.9 (2018). Publisher: Elsevier Ltd, pp. 1203–1214. DOI: 10.1016/j.joca.2018.04.011.

[86] S. Meireles, M. Wesseling, C. R. Smith, D. G. Thelen, S. Verschueren, and I. Jonkers. "Medial knee loading is altered in subjects with early osteoarthritis during gait but not during step-up-and-over task." *PloS one* 12.11 (2017), e0187583. DOI: 10.1371/journal.pone.0187583.

[87] L. Scheys, A. Spaepen, P. Suetens, and I. Jonkers. "Calculated moment-arm and muscle-tendon lengths during gait differ substantially using MR based versus rescaled generic lower-limb musculoskeletal models". *Gait & Posture* 28.4 (2008), pp. 640–648. DOI: 10.1016/j.gaitpost.2008.04.010.

[88] A. S. D. J. S. V. Z. J. Killen B. "Creating subject specific tibiofemoral articular cartilage from population data using the Musculoskeletal Atlas Project Client". *Proceedings of the 8th World Congress of Biomechanics, Dublin, Ireland, 8-12 July 2018* (2018).

[89] K. S. Halonen, M. E. Mononen, J. S. Jurvelin, J. Töyräs, J. Salo, and R. K. Korhonen. "Deformation of articular cartilage during static loading of a knee joint - Experimental and finite element analysis". *Journal of Biomechanics* 47.10 (2014), pp. 2467–2474. DOI: 10.1016/j.jbiomech.2014.04.013.

[90] K. S. Halonen, M. E. Mononen, J. S. Jurvelin, J. Töyräs, and R. K. Korhonen. "Importance of depth-wise distribution of collagen and proteoglycans in articular cartilage-A 3D finite element study of stresses and strains in human knee joint". *Journal of Biomechanics* 46.6 (2013), pp. 1184–1192. DOI: 10.1016/j.jbiomech.2012.12.025.

[91] M. E. Mononen, J. S. Jurvelin, and R. K. Korhonen. "Implementation of a gait cycle loading into healthy and meniscectomised knee joint models with fibril-reinforced articular cartilage". *Computer Methods in Biomechanics and Biomedical Engineering* 18.2 (2015). Publisher: Taylor & Francis, pp. 141–152. DOI: 10.1080/10255842.2013.783575.

[92] M. E. Mononen, P. Tanska, H. Isaksson, and R. K. Korhonen. "A novel method to simulate the progression of collagen degeneration of cartilage in the knee: Data from the osteoarthritis initiative". *Scientific Reports* 6.June 2015 (2016), pp. 1–14. DOI: 10.1038/srep21415.

[93] S. Bonaretti, G. E. Gold, and G. S. Beaupre. "pyKNEEr : An image analysis workflow for open and reproducible research on femoral knee cartilage". *bioRxiv=10.1101/556423* (2019), pp. 1–19.

[94] E. B. Dam, M. Lillholm, J. Marques, and M. Nielsen. "Automatic segmentation of high- and low-field knee MRIs using knee image quantification with data from the osteoarthritis initiative". *Journal of Medical Imaging* 2.2 (2015), p. 024001. DOI: 10.1117/1.JMI.2.2.024001.

[95] J. G. Lee, S. Gumus, C. H. Moon, C. K. Kwoh, and K. T. Bae. "Fully automated segmentation of cartilage from the MR images of knee using a multi-atlas and local structural analysis method". *Medical Physics* 41.9 (2014), pp. 1–9. DOI: 10.1118/1.4893533.

[96] K Marstal, H Gudbergsen, M Boesen, O Kubassova, R Bouert, and H Bliddal. "Semi-automatic segmentation of knee osteoarthritic cartilage in magnetic resonance images". *ELMAR, 2011 Proceedings* September (2011). ISBN: 1334-2630 VO - Publisher: IEEE, pp. 385–388.

[97] T. Ye, X. Cui, and H. Kim. "Fully automated segmentation of cartilage from magnetic resonance images using improved 3D shape context and active shape model". *Osteoarthritis and Cartilage* 23.2015 (2015), A301–A302. DOI: 10.1016/j.joca.2015.02.546.

[98] P. Julkunen, W. Wilson, H. Isaksson, J. S. Jurvelin, W. Herzog, and R. K. Korhonen. "A Review of the Combination of Experimental Measurements and Fibril-Reinforced Modeling for Investigation of Articular Cartilage and Chondrocyte Response to Loading". *Computational and Mathematical Methods in Medicine* 2013 (2013), pp. 1–23. DOI: 10.1155/2013/326150.

[99] J. MacKay, S. Low, T. Smith, A. Toms, A. McCaskie, and F. Gilbert. "Systematic review and meta-analysis of the reliability and discriminative validity of cartilage compositional MRI in knee osteoarthritis". *Osteoarthritis and Cartilage* 26.9 (2018), pp. 1140–1152. DOI: 10.1016/j.joca.2017.11.018.

[100] M. H. Chen and N Broom. "On the ultrastructure of softened cartilage: a possible model for structural transformation." *Journal of anatomy* 192 ( Pt 3 (1998), pp. 329–41. DOI: 10.1046/j.1469-7580.1998.19230329.x.

[101] A. S. Eskelinen, M. E. Mononen, M. S. Venäläinen, R. K. Korhonen, and P. Tanska. "Maximum shear strain-based algorithm can predict proteoglycan loss in damaged articular cartilage". *Biomechanics and Modeling in Mechanobiology* 0123456789 (2019). ISBN: 0123456789 Publisher: Springer Berlin Heidelberg. DOI: 10.1007/s10237-018-01113-1.

[102] G. Pijaudier-Cabot and Z. P. Bažant. "Nonlocal Damage Theory". EN. *Journal of Engineering Mechanics* 113.10 (1987). Publisher: American Society of Civil Engineers, pp. 1512–1533. DOI: 10.1061/(ASCE)0733-9399(1987)113:10(1512).

[103] J. H. P. de Vree, W. A. M. Brekelmans, and M. A. J. van Gils. "Comparison of nonlocal approaches in continuum damage mechanics". *Computers & Structures* 55.4 (1995), pp. 581–588. DOI: 10.1016/0045-7949(94)00501-S.

[104] R. H. J. Peerlings, R. de Borst, W. A. M. Brekelmans, and M. G. D. Geers. "Localisation issues in local and nonlocal continuum approaches to fracture". *European Journal of Mechanics - A/Solids* 21.2 (2002), pp. 175–189. DOI: 10.1016/S0997-7538(02)01211-1.

[105] J. M. Párraga Quiroga, W. Wilson, K. Ito, and C. C. van Donkelaar. "The effect of loading rate on the development of early damage in articular cartilage". *Biomechanics and Modeling in Mechanobiology* 16.1 (2017). Publisher: Springer Berlin Heidelberg, pp. 263–273. DOI: 10.1007/s10237-016-0815-0.

[106] M. K. Liukkonen, M. E. Mononen, O. Klets, J. P. Arokoski, S. Saarakkala, and R. K. Korhonen. "Simulation of subject-specific progression of knee osteoarthritis and comparison to experimental follow-up data: Data from the osteoarthritis initiative". *Scientific Reports* 7.1 (2017). Publisher: Springer US, pp. 1–14. DOI: 10.1038/s41598-017-09013-7.

[107] W. Wilson, C. van Burken, C. van Donkelaar, P. Buma, B. van Rietbergen, and R. Huiskes. "Causes of mechanically induced collagen damage in articular cartilage". *Journal of Orthopaedic Research* 24.2 (2006), pp. 220–228. DOI: 10.1002/jor.20027.

[108] U. Ferizi, I. Rossi, Y. Lee, M. Lendhey, J. Teplensky, O. D. Kennedy, T. Kirsch, J. Bencardino, and J. G. Raya. "Diffusion tensor imaging of articular cartilage at 3T correlates with histology and biomechanics in a mechanical injury model". *Magnetic Resonance in Medicine* 78.1 (2017), pp. 69–78. DOI: 10.1002/mrm.26336.

[109] P. Tanska, P. Julkunen, and R. K. Korhonen. "A computational algorithm to simulate disorganization of collagen network in injured articular cartilage". *Biomechanics and Modeling in Mechanobiology* 17.3 (2018). Publisher: Springer Berlin Heidelberg, pp. 689–699. DOI: 10.1007/s10237-017-0986-3.

[110] T. P. Andriacchi, A. Mündermann, R. L. Smith, E. J. Alexander, C. O. Dyrby, and S. Koo. "A framework for the in vivo pathomechanics of osteoarthritis at the knee." *Annals of biomedical engineering* 32.3 (2004), pp. 447–57.

[111] I. Argatov and G. Mishuris. "A phenomenological model of damage in articular cartilage under impact loading". *Mechanics Research Communications* 69 (2015), pp. 87–90. DOI: 10.1016/j.mechrescom.2015.06.013.

[112] N. S. Landinez-Parra, D. A. Garzón-Alvarado, and J. C. Vanegas-Acosta. "A phenomenological mathematical model of the articular cartilage damage". *Computer Methods and Programs in Biomedicine* 104.3 (2011). Publisher: Elsevier Ireland Ltd, e58–e74. DOI: 10.1016/j.cmpb.2011.02.003.

[113] J. Meng, F. Boschetto, S. Yagi, E. Marin, T. Adachi, X. Chen, G. Pezzotti, S. Sakurai, H. Yamane, and H. Xu. "Design and manufacturing of 3D high-precision micro-fibrous poly (l-lactic acid) scaffold using melt electrowriting technique for bone tissue engineering". *Materials & Design* 210 (2021), p. 110063. DOI: 10.1016/j.matdes.2021.110063.

[114] R. B. Little, H. W. Wevers, D Siu, and T. D. V. Cooke. "A Three-Dimensional Finite Element Analysis of the Upper Tibia". *Journal of Biomechanical Engineering* 108.2 (1986). Publisher: ASME, pp. 111–119.

[115] S. M. Nazemi, M. Amini, S. A. Kontulainen, J. S. Milner, D. W. Holdsworth, B. A. Masri, D. R. Wilson, and J. D. Johnston. "Prediction of local proximal tibial subchondral bone structural stiffness using subject-specific finite element modeling: Effect of selected density-modulus relationship." eng. *Clinical biomechanics (Bristol, Avon)* 30.7 (2015). Place: England, pp. 703–712. DOI: 10.1016/j.clinbiomech.2015.05.002.

[116] S. M. Nazemi, S. M. H. Kalajahi, D. M. L. Cooper, S. A. Kontulainen, D. W. Holdsworth, B. A. Masri, D. R. Wilson, and J. D. Johnston. "Accounting for spatial variation of trabecular anisotropy with subject-specific finite element modeling moderately improves predictions of local subchondral bone stiffness at the proximal tibia." eng. *Journal of biomechanics* 59 (2017). Place: United States, pp. 101–108. DOI: 10.1016/j.jbiomech.2017.05.018.

[117] S. J. Matzat, F. Kogan, G. W. Fong, and G. E. Gold. "Imaging strategies for assessing cartilage composition in osteoarthritis". eng. *Current rheumatology reports* 16.11 (2014), p. 462. DOI: 10.1007/s11926-014-0462-3.

[118] M. E. Stender, R. D. Carpenter, R. A. Regueiro, and V. L. Ferguson. "An evolutionary model of osteoarthritis including articular cartilage damage, and bone remodeling in a computational study". *Journal of Biomechanics* 49.14 (2016). Publisher: Elsevier, pp. 3502–3508. DOI: 10.1016/j.jbiomech.2016.09.024.

[119] M. E. Stender, R. A. Regueiro, and V. L. Ferguson. "A poroelastic finite element model of the bone–cartilage unit to determine the effects of changes in permeability with osteoarthritis". *Computer Methods in Biomechanics and Biomedical Engineering* 20.3 (2017). Publisher: Taylor & Francis, pp. 319–331. DOI: 10.1080/10255842.2016.1233326.

[120] B. B. Aldridge, J. Saez-Rodriguez, J. L. Muhlich, P. K. Sorger, and D. A. Lauffenburger. "Fuzzy Logic Analysis of Kinase Pathway Crosstalk in TNF/EGF/Insulin-Induced Signaling". *PLoS Computational Biology* 5.4 (2009). Ed. by C. Rao, e1000340. DOI: 10.1371/journal.pcbi.1000340.

[121] J. Saez-Rodriguez, L. G. Alexopoulos, J. Epperlein, R. Samaga, D. A. Lauffenburger, S. Klamt, and P. K. Sorger. "Discrete logic modelling as a means to link protein signalling networks with functional analysis of mammalian signal transduction". *Molecular Systems Biology* 5 (2009). DOI: 10.1038/msb.2009.87.

[122] P. J. Woolf, W. Prudhomme, L. Daheron, G. Q. Daley, and D. A. Lauffenburger. "Bayesian analysis of signaling networks governing embryonic stem cell fate decisions". *Bioinformatics* 21.6 (2005), pp. 741–753. DOI: 10.1093/bioinformatics/bti056.

[123] K. Xia, H. Xue, D. Dong, S. Zhu, J. Wang, Q. Zhang, L. Hou, H. Chen, R. Tao, Z. Huang, Z. Fu, Y.-G. Chen, and J.-D. J. Han. "Identification of the Proliferation/Differentiation Switch in the Cellular Network of Multicellular Organisms". *PLoS Computational Biology* 2.11 (2006), e145. DOI: 10.1371/journal.pcbi.0020145.

[124] R. Lesage, J. Kerkhofs, and L. Geris. "Computational Modeling and Reverse Engineering to Reveal Dominant Regulatory Interactions Controlling Osteochondral Differentiation: Potential for Regenerative Medicine". *Frontiers in Bioengineering and Biotechnology* 6.November (2018), pp. 1–16. DOI: 10.3389/fbioe.2018.00165.

[125] M. K. Morris, J. Saez-Rodriguez, P. K. Sorger, and D. A. Lauffenburger. "Logic-based models for the analysis of cell signaling networks". *Biochemistry* 49.15 (2010), pp. 3216–3224. DOI: 10.1021/bi902202q.

[126] J. Kerkhofs, J. Leijten, J. Bolander, F. P. Luyten, J. N. Post, and L. Geris. "A qualitative model of the differentiation network in chondrocyte maturation: A holistic view of chondrocyte hypertrophy". *PLoS ONE* 11.8 (2016), pp. 1–27. DOI: 10.1371/journal.pone.0162052.

[127] J. Kerkhofs and L. Geris. "A Semiquantitative Framework for Gene Regulatory Networks: Increasing the Time and Quantitative Resolution of Boolean Networks". *PLOS ONE* 10.6 (2015). Ed. by M. Helmer-Citterich, e0130033. DOI: 10.1371/journal.pone.0130033.

[128] D. Hodgson, A. D. Rowan, F. Falciani, and C. J. Proctor. "Systems biology reveals how altered TGF$\beta$ signalling with age reduces protection against pro-inflammatory stimuli". *PLoS Computational Biology* 15.1 (2019). ISBN: 1111111111, pp. 1–26. DOI: 10.1371/journal.pcbi.1006685.

[129] W. Hui, D. A. Young, A. D. Rowan, X. Xu, T. E. Cawston, and C. J. Proctor. "Oxidative changes and signalling pathways are pivotal in initiating age-related changes in articular cartilage". *Annals of the Rheumatic Diseases* 75.2 (2016). ISBN: 2014206295, pp. 449–458. DOI: 10.1136/annrheumdis-2014-206295.

[130] C. J. Proctor, C Macdonald, J. M. Milner, A. D. Rowan, and T. E. Cawston. "A computer simulation approach to assessing therapeutic intervention points for the prevention of cytokine-induced cartilage breakdown". *Arthritis and Rheumatology* 66.4 (2014), pp. 979–989. DOI: 10.1002/art.38297.

[131] M. Segarra-Queralt, M. Neidlin, L. Tio, J. Monfort, J. C. Monllau, M. Á. González Ballester, L. G. Alexopoulos, G. Piella, and J. Noailly. "Regulatory network-based model to simulate the biochemical regulation of chondrocytes in healthy and osteoarthritic environments". en. *Sci Rep* 12.1 (2022). Publisher: Nature Publishing Group, p. 3856. DOI: 10.1038/s41598-022-07776-2.

[132] M. Segarra-Queralt, G. Piella, and J. Noailly. "Network-based modelling of mechano-inflammatory chondrocyte regulation in early osteoarthritis". English. *Front. Bioeng. Biotechnol.* 11 (2023). Publisher: Frontiers. DOI: 10.3389/fbioe.2023.1006066.

[133] S. Khurana, S. Schivo, J. R. M. Plass, N. Mersinis, J. Scholma, J. Kerkhofs, L. Zhong, J. van de Pol, R. Langerak, L. Geris, M. Karperien, and J. N. Post. "An ECHO of Cartilage: In Silico Prediction of Combinatorial Treatments to Switch Between Transient and Permanent Cartilage Phenotypes With Ex Vivo Validation". *Front Bioeng Biotechnol* 9 (2021), p. 732917. DOI: 10.3389/fbioe.2021.732917.

[134] D. L. Bader, D. M. Salter, and T. T. Chowdhury. "Biomechanical Influence of Cartilage Homeostasis in Health and Disease". *Arthritis* 2011 (2011), p. 979032. DOI: 10.1155/2011/979032.

[135] T. M. Quinn, A. J. Grodzinsky, M. D. Buschmann, Y. J. Kim, and E. B. Hunziker. "Mechanical compression alters proteoglycan deposition and matrix deformation around individual cells in cartilage explants". *Journal of Cell Science* 111.5 (1998), 573 LP –583.

[136] R. L.-Y. Sah, Y.-J. Kim, J.-Y. H. Doong, A. J. Grodzinsky, A. H. K. Plass, and J. D. Sandy. "Biosynthetic response of cartilage explants to dynamic compression". en. *Journal of Orthopaedic Research* 7.5 (1989). _eprint: https://onlinelibrary.wiley.com/doi/pdf/10.1002/jor.1100070502, pp. 619–636. DOI: 10.1002/jor.1100070502.

[137] J. P. Halloran, S. Sibole, C. C. van Donkelaar, M. C. van Turnhout, C. W. J. Oomens, J. A. Weiss, F. Guilak, and A. Erdemir. "Multiscale Mechanics of Articular Cartilage: Potentials and Challenges of Coupling Musculoskeletal, Joint, and Microscale Computational Models". *Ann Biomed Eng* 40.11 (2012), pp. 2456–2474. DOI: 10.1007/s10439-012-0598-0.

[138] G. I. Kapitanov, X. Wang, B. P. Ayati, M. J. Brouillette, and J. A. Martin. "Linking Cellular and Mechanical Processes in Articular Cartilage Lesion Formation: A Mathematical Model" (2016). _eprint: 1601.01288, pp. 1–22.

[139] M. G. D. Geers, V. G. Kouznetsova, and W. A. M. Brekelmans. "Multi-scale computational homogenization: Trends and challenges". *Journal of Computational and Applied Mathematics*. Fourth International Conference on Advanced COmputational Methods in ENgineering (ACOMEN 2008) 234.7 (2010), pp. 2175–2182. DOI: 10.1016/j.cam.2009.08.077.

[140] S. C. Sibole and A. Erdemir. "Chondrocyte Deformations as a Function of Tibiofemoral Joint Loading Predicted by a Generalized High-Throughput Pipeline of Multi-Scale Simulations". *PLoS ONE* 7.5 (2012). Ed. by H. A. Awad, e37538. DOI: 10.1371/journal.pone.0037538.

[141] S. C. Sibole, S. Maas, J. P. Halloran, J. A. Weiss, and A. Erdemir. "Evaluation of a post-processing approach for multiscale analysis of biphasic mechanics of chondrocytes". *Computer Methods in Biomechanics and Biomedical Engineering* 16.10 (2013). Publisher: Taylor & Francis _eprint: https://doi.org/10.1080/10255842.2013.809711, pp. 1112–1126. DOI: 10.1080/10255842.2013.809711.

[142] P. Tanska, M. E. Mononen, and R. K. Korhonen. "A multi-scale finite element model for investigation of chondrocyte mechanics in normal and medial meniscectomy human knee joint during walking". en. *Journal of Biomechanics* 48.8 (2015), pp. 1397–1406. DOI: 10.1016/j.jbiomech.2015.02.043.

[143] J. W. Fernandez, V. B. Shim, and P. J. Hunter. "Integrating degenerative mechanisms in bone and cartilage: A multiscale approach". *Proceedings of the Annual International Conference of the IEEE Engineering in Medicine and Biology Society, EMBS* (2012). ISBN: 9781424441198 Publisher: IEEE, pp. 6616–6619. DOI: 10.1109/EMBC.2012.6347511.

[144] D. Nickerson and P. Hunter. "Using CellML in Computational Models of Multiscale Physiology". *2005 IEEE Engineering in Medicine and Biology 27th Annual Conference*. IEEE, 2005, pp. 6096–6099. ISBN: 0-7803-8741-4. DOI: 10.1109/IEMBS.2005.1615884.

[145] P. Pivonka, J. Zimak, D. W. Smith, B. S. Gardiner, C. R. Dunstan, N. A. Sims, T. John Martin, and G. R. Mundy. "Model structure and control of bone remodeling: A theoretical study". *Bone* 43.2 (2008), pp. 249–263. DOI: 10.1016/j.bone.2008.03.025.

[146] J. Nam, B. D. Aguda, B. Rath, and S. Agarwal. "Biomechanical Thresholds Regulate Inflammation through the NF-$\kappa$B Pathway: Experiments and Modeling". *PLoS One* 4.4 (2009), e5262. DOI: 10.1371/journal.pone.0005262.

[147] Y. Du, R. Almajalid, J. Shan, and M. Zhang. "A novel method to predict knee osteoarthritis progression on MRI using machine learning methods". *IEEE Transactions on Nanobioscience* 17.3 (2018). Publisher: IEEE, pp. 228–236. DOI: 10.1109/TNB.2018.2840082.

[148] A. Jamshidi, J. P. Pelletier, and J. Martel-Pelletier. "Machine-learning-based patient-specific prediction models for knee osteoarthritis". *Nature Reviews Rheumatology* 15.1 (2019). Publisher: Springer US, pp. 49–60. DOI: 10.1038/s41584-018-0130-5.

[149] A. Nelson, F. Fang, R. Cleveland, T. Schwartz, L. Callahan, J. Marron, and R. Loeser. "A machine learning approach to knee OA phenotyping". *Osteoarthritis and Cartilage* 26.2018 (2018). Publisher: Elsevier Ltd, S236–S237. DOI: 10.1016/j.joca.2018.02.491.

[150] B. G. Ashinsky, M. Bouhrara, C. E. Coletta, B. Lehallier, K. L. Urish, P. C. Lin, I. G. Goldberg, and R. G. Spencer. "Predicting early symptomatic osteoarthritis in the human knee using machine learning classification of magnetic resonance images from the osteoarthritis initiative". *Journal of Orthopaedic Research* 35.10 (2017), pp. 2243–2250. DOI: 10.1002/jor.23519.

[151] M. J. Long, E. Papi, L. D. Duffell, and A. H. McGregor. "Predicting knee osteoarthritis risk in injured populations". *Clinical Biomechanics* 47.March 2016 (2017), pp. 87–95. DOI: 10.1016/j.clinbiomech.2017.06.001.

[152] N. Lazzarini, J. Runhaar, A. C. Bay-Jensen, C. S. Thudium, S. M. Bierma-Zeinstra, Y. Henrotin, and J. Bacardit. "A machine learning approach for the identification of new biomarkers for knee osteoarthritis development in overweight and obese women". *Osteoarthritis and Cartilage* 25.12 (2017). Publisher: Elsevier Ltd, pp. 2014–2021. DOI: 10.1016/j.joca.2017.09.001.

[153] A. V. 40-2018. *Assessing Credibility Of Computational Modeling Through Verification And Validation: Application To Medical Devices*. Tech. rep.

[154] C. Kuemmel, Y. Yang, X. Zhang, J. Florian, H. Zhu, M. Tegenge, S.-M. Huang, Y. Wang, T. Morrison, and I. Zineh. "Consideration of a Credibility Assessment Framework in Model-Informed Drug Development: Potential Application to Physiologically-Based Pharmacokinetic Modeling and Simulation". *CPT: Pharmacometrics & Systems Pharmacology* (2019), psp4.12479. DOI: 10.1002/psp4.12479.

[155] B. Parvinian, P. Pathmanathan, C. Daluwatte, F. Yaghouby, R. A. Gray, S. Weininger, T. M. Morrison, and C. G. Scully. "Credibility Evidence for Computational Patient Models Used in the Development of Physiological

Closed-Loop Controlled Devices for Critical Care Medicine". *Frontiers in Physiology* 10 (2019). DOI: 10.3389/fphys.2019.00220.

[156] D. A. Steinman and F. Migliavacca. "Editorial: Special Issue on Verification, Validation, and Uncertainty Quantification of Cardiovascular Models: Towards Effective VVUQ for Translating Cardiovascular Modelling to Clinical Utility". *Cardiovascular Engineering and Technology* 9.4 (2018), pp. 539–543. DOI: 10.1007/s13239-018-00393-z.

[157] B. J. Fregly, T. F. Besier, D. G. Lloyd, S. L. Delp, S. A. Banks, M. G. Pandy, and D. D. D'Lima. "Grand challenge competition to predict in vivo knee loads". *Journal of Orthopaedic Research* 30.4 (2012), pp. 503–513. DOI: 10.1002/jor.22023.

[158] J. L. Hicks, T. K. Uchida, A. Seth, A. Rajagopal, and S. L. Delp. "Is My Model Good Enough? Best Practices for Verification and Validation of Musculoskeletal Models and Simulations of Movement". *Journal of Biomechanical Engineering* 137.2 (2015). DOI: 10.1115/1.4029304.

[159] A. Erdemir, T. M. Guess, J. Halloran, S. C. Tadepalli, and T. M. Morrison. "Considerations for reporting finite element analysis studies in biomechanics". *Journal of Biomechanics* 45.4 (2012), pp. 625–633. DOI: 10.1016/j.jbiomech.2011.11.038.

[160] A. C. Jones and R. K. Wilcox. "Finite element analysis of the spine: Towards a framework of verification, validation and sensitivity analysis". *Medical Engineering & Physics* 30.10 (2008), pp. 1287–1304. DOI: 10.1016/j.medengphy.2008.09.006.

[161] E. K. Moo, S. C. Sibole, S. K. Han, and W. Herzog. "Three-dimensional micro-scale strain mapping in living biological soft tissues". *Acta Biomaterialia* 70 (2018), pp. 260–269. DOI: 10.1016/j.actbio.2018.01.048.

[162] A. Erdemir, C. Bennetts, S. Davis, A. Reddy, and S. Sibole. "Multiscale cartilage biomechanics: Technical challenges in realizing a high-throughput modelling and simulation workflow". *Interface Focus* 5.2 (2015). DOI: 10.1098/rsfs.2014.0081.

[163] M. K. Honkanen, H. Matikka, J. T. Honkanen, A. Bhattarai, M. W. Grinstaff, A. Joukainen, H. Kröger, J. S. Jurvelin, and J. Töyräs. "Imaging of proteoglycan and water contents in human articular cartilage with full-body CT using dual contrast technique". *Journal of Orthopaedic Research* 37.5 (2019), pp. 1059–1070. DOI: 10.1002/jor.24256.

[164] K. D. Jadin, W. C. Bae, B. L. Schumacher, and R. L. Sah. "Three-dimensional (3-D) imaging of chondrocytes in articular cartilage: Growth-associated changes in cell organization". *Biomaterials* 28.2 (2007), pp. 230–239. DOI: 10.1016/j.biomaterials.2006.08.053.

[165] Y. Xia, E. M. Darling, and W. Herzog. "Functional properties of chondrocytes and articular cartilage using optical imaging to scanning probe microscopy". *Journal of Orthopaedic Research* 36.2 (2018), pp. 620–631. DOI: 10.1002/jor.23757.

[166] T. M. Griffin and F. Guilak. "The role of mechanical loading in the onset and progression of osteoarthritis". eng. *Exerc Sport Sci Rev* 33.4 (2005), pp. 195–200. DOI: 10.1097/00003677-200510000-00008.

[167] S. J. Gilbert and E. J. Blain. "Chapter 4 - Cartilage mechanobiology: How chondrocytes respond to mechanical load". *Mechanobiology in Health and Disease*. Ed. by S. W. Verbruggen. Academic Press, 2018, pp. 99–126. ISBN: 978-0-12-812952-4. DOI: 10.1016/B978-0-12-812952-4.00004-0.

[168] J. Natenstedt, A. C. Kok, J. Dankelman, and G. J. Tuijthof. "What quantitative mechanical loading stimulates in vitro cultivation best?" *Journal of Experimental Orthopaedics* 2.1 (2015), p. 15. DOI: 10.1186/s40634-015-0029-x.

[169] W. Gao, H. Hasan, D. E. Anderson, and W. Lee. "The Role of Mechanically-Activated Ion Channels Piezo1, Piezo2, and TRPV4 in Chondrocyte Mechanotransduction and Mechano-Therapeutics for Osteoarthritis". en. *Front. Cell Dev. Biol.* 10 (2022), p. 885224. DOI: 10.3389/fcell.2022.885224.

[170] E. Y. Salinas, J. C. Hu, and K. Athanasiou. "A Guide for Using Mechanical Stimulation to Enhance Tissue-Engineered Articular Cartilage Properties". en. *Tissue Engineering Part B: Reviews* 24.5 (2018), pp. 345–358. DOI: 10.1089/ten.teb.2018.0006.

[171] L. Geris, T. Lambrechts, A. Carlier, and I. Papantoniou. "The future is digital: *In silico* tissue engineering". *Current Opinion in Biomedical Engineering*. Tissue Engineering and Regenerative Medicine / Biomaterials 6 (2018), pp. 92–98. DOI: 10.1016/j.cobme.2018.04.001.

[172] C. R. Hassan, Y.-X. Qin, D. E. Komatsu, and S. M. Uddin. "Utilization of Finite Element Analysis for Articular Cartilage Tissue Engineering". *Materials (Basel)* 12.20 (2019), p. 3331. DOI: 10.3390/ma12203331.

[173] O. M. Babalola and L. J. Bonassar. "Parametric Finite Element Analysis of Physical Stimuli Resulting From Mechanical Stimulation of Tissue Engineered Cartilage". *Journal of Biomechanical Engineering* 131.061014 (2009). DOI: 10.1115/1.3128672.

[174] ZahedmaneshHouman, StoddartMartin, LezuoPatrick, ForkmannChristoph, W. A, AliniMauro, and V. OosterwyckHans. "Deciphering Mechanical Regulation of Chondrogenesis in Fibrin–Polyurethane Composite Scaffolds Enriched with Human Mesenchymal Stem Cells: A Dual Computational and Experimental Approach". en. *https://home.liebertpub.com/tea*

(2014). Publisher: Mary Ann Liebert, Inc. 140 Huguenot Street, 3rd Floor New Rochelle, NY 10801 USA. DOI: 10.1089/ten.tea.2013.0145.

[175] C. Bandeiras, A. Completo, and A. Ramos. "Compression, shear and bending on tissue-engineered cartilage: a numerical study". *Computer Methods in Biomechanics and Biomedical Engineering* 17.sup1 (2014). Publisher: Taylor & Francis, pp. 2–3. DOI: 10.1080/10255842.2014.931047.

[176] A. Erdemir. "Open Knee: Open Source Modeling & Simulation to Enable Scientific Discovery and Clinical Care in Knee Biomechanics". *J Knee Surg* 29.2 (2016), pp. 107–116. DOI: 10.1055/s-0035-1564600.

[177] B. Zielinska and T. L. Haut Donahue. "3D Finite Element Model of Meniscectomy: Changes in Joint Contact Behavior". *Journal of Biomechanical Engineering* 128.1 (2005), pp. 115–123. DOI: 10.1115/1.2132370.

[178] W. Wilson, C. C. van Donkelaar, B. van Rietbergen, K. Ito, and R. Huiskes. "Stresses in the local collagen network of articular cartilage: a poroviscoelastic fibril-reinforced finite element study". *Journal of Biomechanics* 37.3 (2004), pp. 357–366. DOI: 10.1016/S0021-9290(03)00267-7.

[179] J. M. P. Quiroga, W. Wilson, K. Ito, and C. C. van Donkelaar. "Relative contribution of articular cartilage's constitutive components to load support depending on strain rate". en. *Biomech Model Mechanobiol* 16.1 (2017), pp. 151–158. DOI: 10.1007/s10237-016-0807-0.

[180] A. Heuijerjans, W. Wilson, K. Ito, and C. C. Van Donkelaar. "Osteochondral resurfacing implantation angle is more important than implant material stiffness". en. *Journal Orthopaedic Research* 36.11 (2018), pp. 2911–2922. DOI: 10.1002/jor.24101.

[181] H Stolze, J. P Kuhtz-Buschbeck, C Mondwurf, A Boczek-Funcke, K Jöhnk, G Deuschl, and M Illert. "Gait analysis during treadmill and overground locomotion in children and adults". *Electroencephalography and Clinical Neurophysiology/Electromyography and Motor Control* 105.6 (1997), pp. 490–497. DOI: 10.1016/S0924-980X(97)00055-6.

[182] A. Schwab, A. Buss, O. Pullig, and F. Ehlicke. "*Ex vivo* osteochondral test system with control over cartilage defect depth – A pilot study to investigate the effect of oxygen tension and chondrocyte based treatments in chondral and full thickness defects in an organ model". *Osteoarthritis and Cartilage Open* 3.2 (2021), p. 100173. DOI: 10.1016/j.ocarto.2021.100173.

[183] M. W. A. Kleuskens, C. C. van Donkelaar, L. M. Kock, R. P. A. Janssen, and K. Ito. "An ex vivo human osteochondral culture model". en. *Journal of Orthopaedic Research* 39.4 (2021). _eprint: https://onlinelibrary.wiley.com/doi/pdf/10.1002/jor.24789, pp. 871–879. DOI: 10.1002/jor.24789.

[184] L. A. E. Evans and A. A. Pitsillides. "Structural clues to articular calcified cartilage function: A descriptive review of this crucial interface tissue". en. *Journal of Anatomy* 241.4 (2022). _eprint: https://onlinelibrary.wiley.com/doi/pdf/10.1111/joa.13728, pp. 875–895. DOI: 10.1111/joa.13728.

[185] S. Rapagna, B. C. Roberts, L. B. Solomon, K. J. Reynolds, D. Thewlis, and E. Perilli. "Tibial cartilage, subchondral bone plate and trabecular bone microarchitecture in varus- and valgus-osteoarthritis versus controls". en. *Journal of Orthopaedic Research* 39.9 (2021). _eprint: https://onlinelibrary.wiley.com/doi/pdf/10.1002/jor.24914, pp. 1988–1999. DOI: 10.1002/jor.24914.

[186] J. M. Patel, B. C. Wise, E. D. Bonnevie, and R. L. Mauck. "A Systematic Review and Guide to Mechanical Testing for Articular Cartilage Tissue Engineering". en. *Tissue Engineering Part C: Methods* 25.10 (2019), pp. 593–608. DOI: 10.1089/ten.tec.2019.0116.

[187] F. Guilak. "The slippery slope of arthritis". en. *Arthritis & Rheumatism* 52.6 (2005), pp. 1632–1633. DOI: 10.1002/art.21051.

[188] S. Grad, M. Loparic, R. Peter, M. Stolz, U. Aebi, and M. Alini. "Sliding motion modulates stiffness and friction coefficient at the surface of tissue engineered cartilage". *Osteoarthritis and Cartilage* 20.4 (2012), pp. 288–295. DOI: 10.1016/j.joca.2011.12.010.

[189] M. L. Vainieri, D. Wahl, M. Alini, G. J. V. M. van Osch, and S. Grad. "Mechanically stimulated osteochondral organ culture for evaluation of biomaterials in cartilage repair studies". *Acta Biomaterialia* 81 (2018), pp. 256–266. DOI: 10.1016/j.actbio.2018.09.058.

[190] M. D. Buschmann, Y. A. Gluzband, A. J. Grodzinsky, J. H. Kimura, and E. B. Hunziker. "Chondrocytes in agarose culture synthesize a mechanically functional extracellular matrix". en. *Journal of Orthopaedic Research* 10.6 (1992), pp. 745–758. DOI: 10.1002/jor.1100100602.

[191] M. Khoshgoftar, C. C. van Donkelaar, and K. Ito. "Mechanical stimulation to stimulate formation of a physiological collagen architecture in tissue-engineered cartilage: a numerical study". *Computer Methods in Biomechanics and Biomedical Engineering* 14.2 (2011). Publisher: Taylor & Francis _eprint: https://doi.org/10.1080/10255842.2010.519335, pp. 135–144. DOI: 10.1080/10255842.2010.519335.

[192] L. Geurds, Y. Xu, and J. R. Stokes. "Friction of lubricated hydrogels: Influence of load, speed and lubricant viscosity". *Biotribology* 25 (2021), p. 100162. DOI: 10.1016/j.biotri.2021.100162.

[193] E. Hodder, F. Guppy, D. Covill, and P. Bush. "The effect of hydrostatic pressure on proteoglycan production in articular cartilage in vitro: a meta-analysis". en. *Osteoarthritis and Cartilage* 28.8 (2020), pp. 1007–1019. DOI: 10.1016/j.joca.2020.03.021.

[194] B. D. Elder and K. A. Athanasiou. "Hydrostatic Pressure in Articular Cartilage Tissue Engineering: From Chondrocytes to Tissue Regeneration". en. *Tissue Engineering Part B: Reviews* 15.1 (2009), pp. 43–53. DOI: 10.1089/ten.teb.2008.0435.

[195] F. Chariyev-Prinz, A. Szojka, N. Neto, R. Burdis, M. G. Monaghan, and D. J. Kelly. "An assessment of the response of human MSCs to hydrostatic pressure in environments supportive of differential chondrogenesis". en. *Journal of Biomechanics* 154 (2023), p. 111590. DOI: 10.1016/j.jbiomech.2023.111590.

[196] K. M. Durney, C. A. Shaeffer, B. K. Zimmerman, R. J. Nims, S. Oungoulian, B. K. Jones, J. F. Boorman-Padgett, J. T. Suh, R. P. Shah, C. T. Hung, and G. A. Ateshian. "Immature bovine cartilage wear by fatigue failure and delamination". *Journal of Biomechanics* 107 (2020), p. 109852. DOI: 10.1016/j.jbiomech.2020.109852.

[197] C. P. Neu, M. L. Hull, and J. H. Walton. "Heterogeneous three-dimensional strain fields during unconfined cyclic compression in bovine articular cartilage explants". eng. *J Orthop Res* 23.6 (2005), pp. 1390–1398. DOI: 10.1016/j.orthres.2005.03.022.1100230622.

[198] C. A. Petersen, C. V. Sise, J. X. Dewing, J. Yun, B. K. Zimmerman, X. E. Guo, C. T. Hung, and G. A. Ateshian. "Immature bovine cartilage wear is due to fatigue failure from repetitive compressive forces and not reciprocating frictional forces". *Osteoarthritis and Cartilage* 31.12 (2023), pp. 1594–1601. DOI: 10.1016/j.joca.2023.08.008.

[199] E Tanck, W. D van Driel, J. W Hagen, E. H Burger, L Blankevoort, and R Huiskes. "Why does intermittent hydrostatic pressure enhance the mineralization process in fetal cartilage?" *Journal of Biomechanics* 32.2 (1999), pp. 153–161. DOI: 10.1016/S0021-9290(98)00165-1.

[200] V. Jönsson, G. A. Orozco, M. Pierantoni, H. Dejea, A. Gustafsson, L. Grassi, and H. Isaksson. "Influence of articular cartilage sample geometry on mechanical response and properties using finite element simulation". *Journal of Biomechanics* 176 (2024), p. 112323. DOI: 10.1016/j.jbiomech.2024.112323.

[201] B. G. Sengers, C. W. J. Oomens, and F. P. T. Baaijens. “An Integrated Finite-Element Approach to Mechanics, Transport and Biosynthesis in Tissue Engineering”. en. *Journal of Biomechanical Engineering* 126.1 (2004), pp. 82–91. DOI: 10.1115/1.1645526.

[202] G. A. Orozco, P. Bolcos, A. Mohammadi, M. S. Tanaka, M. Yang, T. M. Link, B. Ma, X. Li, P. Tanska, and R. K. Korhonen. “Prediction of local fixed charge density loss in cartilage following ACL injury and reconstruction: A computational proof-of-concept study with MRI follow-up”. en. *Journal of Orthopaedic Research* 39.5 (2021). _eprint: https://onlinelibrary.wiley.com/doi/pdf/10.1002/jor.24797, pp. 1064–1081. DOI: 10.1002/jor.24797.

[203] S. D. Thorpe, T. Nagel, S. F. Carroll, and D. J. Kelly. “Modulating Gradients in Regulatory Signals within Mesenchymal Stem Cell Seeded Hydrogels: A Novel Strategy to Engineer Zonal Articular Cartilage”. en. *PLOS ONE* 8.4 (2013). Publisher: Public Library of Science, e60764. DOI: 10.1371/journal.pone.0060764.

[204] A. J. Steward, S. D. Thorpe, T. Vinardell, C. T. Buckley, D. R. Wagner, and D. J. Kelly. “Cell–matrix interactions regulate mesenchymal stem cell response to hydrostatic pressure”. *Acta Biomaterialia* 8.6 (2012), pp. 2153–2159. DOI: 10.1016/j.actbio.2012.03.016.

[205] E. G. Meyer, C. T. Buckley, A. J. Steward, and D. J. Kelly. “The effect of cyclic hydrostatic pressure on the functional development of cartilaginous tissues engineered using bone marrow derived mesenchymal stem cells”. *Journal of the Mechanical Behavior of Biomedical Materials* 4.7 (2011), pp. 1257–1265. DOI: 10.1016/j.jmbbm.2011.04.012.

[206] M. P. Kadaba, H. K. Ramakrishnan, and M. E. Wootten. “Measurement of lower extremity kinematics during level walking”. en. *Journal of Orthopaedic Research* 8.3 (1990), pp. 383–392. DOI: 10.1002/jor.1100080310.

[207] G. A. Ateshian. “The role of interstitial fluid pressurization in articular cartilage lubrication”. *Journal of Biomechanics* 42.9 (2009), pp. 1163–1176. DOI: 10.1016/j.jbiomech.2009.04.040.

[208] Y. Gao, S. Liu, J. Huang, W. Guo, J. Chen, L. Zhang, B. Zhao, J. Peng, A. Wang, Y. Wang, W. Xu, S. Lu, M. Yuan, and Q. Guo. “The ECM-Cell Interaction of Cartilage Extracellular Matrix on Chondrocytes”. *Biomed Res Int* 2014 (2014), p. 648459. DOI: 10.1155/2014/648459.

[209] J. D. Steinmetz et al. “Global, regional, and national burden of osteoarthritis, 1990–2020 and projections to 2050: a systematic analysis for the Global Burden of Disease Study 2021”. *The Lancet Rheumatology* 5.9 (2023), e508–e522. DOI: 10.1016/S2665-9913(23)00163-7.

[210] A. Cui, H. Li, D. Wang, J. Zhong, Y. Chen, and H. Lu. "Global, regional prevalence, incidence and risk factors of knee osteoarthritis in population-based studies". English. *eClinicalMedicine* 29 (2020). Publisher: Elsevier. DOI: 10.1016/j.eclinm.2020.100587.

[211] R. F. Loeser. "Integrins and chondrocyte–matrix interactions in articular cartilage". *Matrix Biology* 39 (2014), pp. 11–16. DOI: 10.1016/j.matbio.2014.08.007.

[212] C. J. O'Conor, H. A. Leddy, H. C. Benefield, W. B. Liedtke, and F. Guilak. "TRPV4-mediated mechanotransduction regulates the metabolic response of chondrocytes to dynamic loading". eng. *Proc Natl Acad Sci U S A* 111.4 (2014), pp. 1316–1321. DOI: 10.1073/pnas.1319569111.

[213] W. Lee, H. A. Leddy, Y. Chen, S. H. Lee, N. A. Zelenski, A. L. McNulty, J. Wu, K. N. Beicker, J. Coles, S. Zauscher, J. Grandl, F. Sachs, F. Guilak, and W. B. Liedtke. "Synergy between Piezo1 and Piezo2 channels confers high-strain mechanosensitivity to articular cartilage". en. *Proc. Natl. Acad. Sci. U.S.A.* 111.47 (2014). DOI: 10.1073/pnas.1414298111.

[214] A. P. Hollander, I. Pidoux, A. Reiner, C. Rorabeck, R. Bourne, and A. R. Poole. "Damage to type II collagen in aging and osteoarthritis starts at the articular surface, originates around chondrocytes, and extends into the cartilage with progressive degeneration". eng. *J Clin Invest* 96.6 (1995), pp. 2859–2869. DOI: 10.1172/JCI118357.

[215] J. H. Rosenberg, V. Rai, M. F. Dilisio, and D. K. Agrawal. "Damage Associated Molecular Patterns in the Pathogenesis of Osteoarthritis: Potentially Novel Therapeutic Targets". *Mol Cell Biochem* 434.1-2 (2017), pp. 171–179. DOI: 10.1007/s11010-017-3047-4.

[216] Z. Fan, S. Söder, S. Oehler, K. Fundel, and T. Aigner. "Activation of Interleukin-1 Signaling Cascades in Normal and Osteoarthritic Articular Cartilage". *Am J Pathol* 171.3 (2007), pp. 938–946. DOI: 10.2353/ajpath.2007.061083.

[217] M. Neidlin, S. Dimitrakopoulou, and L. G. Alexopoulos. "Multi-tissue network analysis for drug prioritization in knee osteoarthritis". en. *Sci Rep* 9.1 (2019). Publisher: Nature Publishing Group, p. 15176. DOI: 10.1038/s41598-019-51627-6.

[218] M. Kapoor, J. Martel-Pelletier, D. Lajeunesse, J.-P. Pelletier, and H. Fahmi. "Role of proinflammatory cytokines in the pathophysiology of osteoarthritis". en. *Nat Rev Rheumatol* 7.1 (2011). Publisher: Nature Publishing Group, pp. 33–42. DOI: 10.1038/nrrheum.2010.196.

[219] V. D. Sree and A. B. Tepole. "Computational systems mechanobiology of growth and remodeling: Integration of tissue mechanics and cell regulatory network dynamics". *Current Opinion in Biomedical Engineering*. Biomechanics and Mechanobiology: Growth and remodeling in both mechanics and mechanobiology 15 (2020), pp. 75–80. DOI: 10.1016/j.cobme.2020.01.002.

[220] P. Julkunen, W. Wilson, J. S. Jurvelin, and R. K. Korhonen. "Composition of the pericellular matrix modulates the deformation behaviour of chondrocytes in articular cartilage under static loading." *Medical & biological engineering & computing* 47.12 (2009), pp. 1281–90. DOI: 10.1007/s11517-009-0547-8.

[221] F. Guilak, W. R. Jones, H. Ting-Beall, and G. M. Lee. "The deformation behavior and mechanical properties of chondrocytes in articular cartilage". *Osteoarthritis and Cartilage* 7.1 (1999), pp. 59–70. DOI: 10.1053/joca.1998.0162.

[222] M. Kääb, R. Richards, K. Ito, I. ap Gwynn, and H. Nötzli. "Deformation of Chondrocytes in Articular Cartilage under Compressive Load: A Morphological Study". *Cells Tissues Organs* 175.3 (2003), pp. 133–139. DOI: 10.1159/000074629.

[223] C. A. POOLE. "Review. Articular cartilage chondrons: form, function and failure". *J Anat* 191.Pt 1 (1997), pp. 1–13. DOI: 10.1046/j.1469-7580.1997.19110001.x.

[224] C. A. Poole, S. Ayad, and R. T. Gilbert. "Chondrons from articular cartilage: V.* Immunohistochemical evaluation of type VI collagen organisation in isolated chondrons by light, confocal and electron microscopy". *Journal of Cell Science* 103.4 (1992), pp. 1101–1110. DOI: 10.1242/jcs.103.4.1101.

[225] I. Youn, J. Choi, L. Cao, L. Setton, and F. Guilak. "Zonal variations in the three-dimensional morphology of the chondron measured in situ using confocal microscopy". en. *Osteoarthritis and Cartilage* 14.9 (2006), pp. 889–897. DOI: 10.1016/j.joca.2006.02.017.

[226] H. Guo and P. A. Torzilli. "Shape of chondrocytes within articular cartilage affects the solid but not the fluid microenvironment under unconfined compression". *Acta Biomater* 29 (2016), pp. 170–179. DOI: 10.1016/j.actbio.2015.10.035.

[227] A. Saraswathibhatla, D. Indana, and O. Chaudhuri. "Cell-extracellular matrix mechanotransduction in 3D". eng. *Nat Rev Mol Cell Biol* 24.7 (2023), pp. 495–516. DOI: 10.1038/s41580-023-00583-1.

[228] R. Lesage, M. N. Ferrao Blanco, R. Narcisi, T. Welting, G. J. V. M. van Osch, and L. Geris. "An integrated in silico-in vitro approach for identifying therapeutic targets against osteoarthritis". en. *BMC Biol* 20.1 (2022), p. 253. DOI: 10.1186/s12915-022-01451-8.

[229] A. Mobasheri, C. Matta, I. Uzielienè, E. Budd, P. Martín-Vasallo, and E. Bernotiene. "The chondrocyte channelome: A narrative review". eng. *Joint Bone Spine* 86.1 (2019), pp. 29–35. DOI: 10.1016/j.jbspin.2018.01.012.

[230] R. J. Nims, L. Pferdehirt, and F. Guilak. "Mechanogenetics: harnessing mechanobiology for cellular engineering". en. *Current Opinion in Biotechnology* 73 (2022), pp. 374–379. DOI: 10.1016/j.copbio.2021.09.011.

[231] S. Madhavan, M. Anghelina, D. Sjostrom, A. Dossumbekova, D. C. Guttridge, and S. Agarwal. "Biomechanical Signals Suppress TAK1 Activation to Inhibit NF-$\kappa$B Transcriptional Activation in Fibrochondrocytes1". *The Journal of Immunology* 179.9 (2007), pp. 6246–6254. DOI: 10.4049/jimmunol.179.9.6246.

[232] P. S. Chang and R. H. Brophy. "As Goes the Meniscus Goes the Knee: Early, Intermediate, and Late Evidence for the Detrimental Effect of Meniscus Tears". English. *Clinics in Sports Medicine* 39.1 (2020). Publisher: Elsevier, pp. 29–36. DOI: 10.1016/j.csm.2019.08.001.

[233] L. S. Lohmander, P. M. Englund, L. L. Dahl, and E. M. Roos. "The Long-term Consequence of Anterior Cruciate Ligament and Meniscus Injuries: Osteoarthritis". en. *Am J Sports Med* 35.10 (2007). Publisher: SAGE Publications Inc STM, pp. 1756–1769. DOI: 10.1177/0363546507307396.

[234] M. Englund and L. S. Lohmander. "Risk factors for symptomatic knee osteoarthritis fifteen to twenty-two years after meniscectomy". en. *Arthritis & Rheumatism* 50.9 (2004), pp. 2811–2819. DOI: 10.1002/art.20489.

[235] H. Roos, M. Laurén, T. Adalberth, E. M. Roos, K. Jonsson, and L. S. Lohmander. "Knee osteoarthritis after meniscectomy: prevalence of radiographic changes after twenty-one years, compared with matched controls". eng. *Arthritis Rheum* 41.4 (1998), pp. 687–693. DOI: 10.1002/1529-0131(199804)41:4<687::AID-ART16>3.0.CO;2-2.

[236] A. De Roover, A. Escribano-Núñez, S. Monteagudo, and R. Lories. "Fundamentals of osteoarthritis: Inflammatory mediators in osteoarthritis". *Osteoarthritis and Cartilage* 31.10 (2023), pp. 1303–1311. DOI: 10.1016/j.joca.2023.06.005.

[237] M. Segarra-Queralt, K. Crump, A. Pascuet-Fontanet, B. Gantenbein, and J. Noailly. "The interplay between biochemical mediators and mechanotransduction in chondrocytes: Unravelling the differential responses in primary knee osteoarthritis". *Physics of Life Reviews* 48 (2024), pp. 205–221. DOI: 10.1016/j.plrev.2024.02.003.

[238] T. Hodgkinson, D. C. Kelly, C. M. Curtin, and F. J. O'Brien. "Mechanosignalling in cartilage: an emerging target for the treatment of osteoarthritis". en. *Nat Rev Rheumatol* 18.2 (2022). Publisher: Nature Publishing Group, pp. 67–84. DOI: 10.1038/s41584-021-00724-w.

[239] Z. Karagöz, L. Rijns, P. Y. W. Dankers, M. van Griensven, and A. Carlier. "Towards understanding the messengers of extracellular space: Computational models of outside-in integrin reaction networks". *Computational and Structural Biotechnology Journal* 19 (2021), pp. 303–314. DOI: 10.1016/j.csbj.2020.12.025.

[240] M. Almonte-Becerril, M. Costell, and J. B. Kouri. "Changes in the integrins expression are related with the osteoarthritis severity in an experimental animal model in rats". en. *Journal of Orthopaedic Research* 32.9 (2014). _eprint: https://onlinelibrary.wiley.com/doi/pdf/10.1002/jor.22649, pp. 1161–1166. DOI: 10.1002/jor.22649.

[241] W. Lee, R. J. Nims, A. Savadipour, Q. Zhang, H. A. Leddy, F. Liu, A. L. McNulty, Y. Chen, F. Guilak, and W. B. Liedtke. "Inflammatory signaling sensitizes Piezo1 mechanotransduction in articular chondrocytes as a pathogenic feed-forward mechanism in osteoarthritis". en. *Proc. Natl. Acad. Sci. U.S.A.* 118.13 (2021), e2001611118. DOI: 10.1073/pnas.2001611118.

[242] A. S. A. Eskelinen, P. Tanska, C. Florea, G. A. Orozco, P. Julkunen, A. J. Grodzinsky, and R. K. Korhonen. "Mechanobiological model for simulation of injured cartilage degradation via pro-inflammatory cytokines and mechanical stimulus". eng. *PLoS Comput Biol* 16.6 (2020), e1007998. DOI: 10.1371/journal.pcbi.1007998.

[243] X. Fan, A. R. Sun, R. S. E. Young, I. O. Afara, B. R. Hamilton, L. J. Y. Ong, R. Crawford, and I. Prasadam. "Spatial analysis of the osteoarthritis microenvironment: techniques, insights, and applications". en. *Bone Res* 12.1 (2024). Publisher: Nature Publishing Group, pp. 1–19. DOI: 10.1038/s41413-023-00304-6.

[244] C. A. Paggi, B. Venzac, M. Karperien, J. C. H. Leijten, and S. Le Gac. "Monolithic microfluidic platform for exerting gradients of compression on cell-laden hydrogels, and application to a model of the articular cartilage". *Sensors and Actuators B: Chemical* 315 (2020), p. 127917. DOI: 10.1016/j.snb.2020.127917.

[245] C. A. Paggi, L. M. Teixeira, S. Le Gac, and M. Karperien. "Joint-on-chip platforms: entering a new era of in vitro models for arthritis". en. *Nat Rev Rheumatol* 18.4 (2022), pp. 217–231. DOI: 10.1038/s41584-021-00736-6.

[246] P. Occhetta, A. Mainardi, E. Votta, Q. Vallmajo-Martin, M. Ehrbar, I. Martin, A. Barbero, and M. Rasponi. "Hyperphysiological compression of articular cartilage induces an osteoarthritic phenotype in a cartilage-on-a-chip model". en. *Nat Biomed Eng* 3.7 (2019). Publisher: Nature Publishing Group, pp. 545–557. DOI: 10.1038/s41551-019-0406-3.

[247] A. Komeili, B. S. Otoo, Z. Abusara, S. Sibole, S. Federico, and W. Herzog. "Chondrocyte Deformations Under Mild Dynamic Loading Conditions". en. *Ann Biomed Eng* 49.2 (2021), pp. 846–857. DOI: 10.1007/s10439-020-02615-9.

[248] S. C. Sibole, E. K. Moo, S. Federico, and W. Herzog. "Dynamic Deformation Calculation of Articular Cartilage and Cells Using Resonance-Driven Laser Scanning Microscopy". *Journal of Biomechanical Engineering* 145.021005 (2022). DOI: 10.1115/1.4055308.

[249] B. S. Otoo, E. Kuan Moo, A. Komeili, D. A. Hart, and W. Herzog. "Chondrocyte deformation during the unloading phase of cyclic compression loading". *Journal of Biomechanics* 171 (2024), p. 112179. DOI: 10.1016/j.jbiomech.2024.112179.

[250] V. G. Kouznetsova, M. G. D. Geers, and W. A. M. Brekelmans. "Multi-scale second-order computational homogenization of multi-phase materials: a nested finite element solution strategy". *Computer Methods in Applied Mechanics and Engineering*. Advances in Computational Plasticity 193.48 (2004), pp. 5525–5550. DOI: 10.1016/j.cma.2003.12.073.

[251] R. L. Mauck, M. A. Soltz, C. C. B. Wang, D. D. Wong, P.-H. G. Chao, W. B. Valhmu, C. T. Hung, and G. A. Ateshian. "Functional Tissue Engineering of Articular Cartilage Through Dynamic Loading of Chondrocyte-Seeded Agarose Gels". *Journal of Biomechanical Engineering* 122.3 (2000), pp. 252–260. DOI: 10.1115/1.429656.

[252] C. J. O'Conor, N. Case, and F. Guilak. "Mechanical regulation of chondrogenesis". *Stem Cell Research & Therapy* 4.4 (2013), p. 61. DOI: 10.1186/scrt211.

[253] P. Cope, K. Ourradi, Y. Li, and M. Sharif. "Models of osteoarthritis: the good, the bad and the promising". *Osteoarthritis Cartilage* 27.2 (2019), pp. 230–239. DOI: 10.1016/j.joca.2018.09.016.

[254] C. A. Paggi, J. Hendriks, M. Karperien, and S. L. Gac. "Emulating the chondrocyte microenvironment using multi-directional mechanical stimulation in a cartilage-on-chip". en. *Lab Chip* 22.9 (2022). Publisher: The Royal Society of Chemistry, pp. 1815–1828. DOI: 10.1039/D1LC01069G.

[255] S. A. Elahi, P. Tanska, S. Mukherjee, R. K. Korhonen, L. Geris, I. Jonkers, and N. Famaey. "Guide to mechanical characterization of articular cartilage and hydrogel constructs based on a systematic *in silico* parameter sensitivity analysis". *Journal of the Mechanical Behavior of Biomedical Materials* 124 (2021), p. 104795. DOI: 10.1016/j.jmbbm.2021.104795.

[256] M. Khoshgoftar, K. Ito, and C. C. van Donkelaar. "The Influence of Cell-Matrix Attachment and Matrix Development on the Micromechanical Environment of the Chondrocyte in Tissue-Engineered Cartilage". *Tissue Engineering Part A* 20.23-24 (2014). Publisher: Mary Ann Liebert, Inc., publishers, pp. 3112–3121. DOI: 10.1089/ten.tea.2013.0676.

[257] A. Jorge-Peñas, A. Izquierdo-Alvarez, R. Aguilar-Cuenca, M. Vicente-Manzanares, J. M. Garcia-Aznar, H. V. Oosterwyck, E. M. de Juan-Pardo, C. Ortiz-de Solorzano, and A. Muñoz-Barrutia. "Free Form Deformation–Based Image Registration Improves Accuracy of Traction Force Microscopy". en. *PLOS ONE* 10.12 (2015). Publisher: Public Library of Science, e0144184. DOI: 10.1371/journal.pone.0144184.

[258] F. Buggenthin, C. Marr, M. Schwarzfischer, P. S. Hoppe, O. Hilsenbeck, T. Schroeder, and F. J. Theis. "An automatic method for robust and fast cell detection in bright field images from high-throughput microscopy". en. *BMC Bioinformatics* 14.1 (2013), p. 297. DOI: 10.1186/1471-2105-14-297.

[259] Y. Fu, B. Zoetebier, S. Both, P. J. Dijkstra, and M. Karperien. "Engineering of Optimized Hydrogel Formulations for Cartilage Repair". en. *Polymers* 13.9 (2021). Number: 9 Publisher: Multidisciplinary Digital Publishing Institute, p. 1526. DOI: 10.3390/polym13091526.

[260] N. Petitjean, P. Canadas, P. Royer, D. Noël, and S. Le Floc'h. "Cartilage biomechanics: From the basic facts to the challenges of tissue engineering". en. *Journal of Biomedical Materials Research Part A* 111.7 (2023). _eprint: https://onlinelibrary.wiley.com/doi/pdf/10.1002/jbm.a.37478, pp. 1067–1089. DOI: 10.1002/jbm.a.37478.

[261] M. E. Mononen, M. K. Liukkonen, and R. K. Korhonen. "Utilizing Atlas-Based Modeling to Predict Knee Joint Cartilage Degeneration: Data from the Osteoarthritis Initiative". eng. *Ann Biomed Eng* 47.3 (2019), pp. 813–825. DOI: 10.1007/s10439-018-02184-y.

# Statement on the use of Generative AI

I did not use generative AI assistance tools during the research/writing process of my thesis.
The text, code, and images in this thesis are my own (unless otherwise specified). Generative AI has only been used in accordance with the KU Leuven guidelines and appropriate references have been added. I have reviewed and edited the content as needed and I take full responsibility for the content of the thesis.

# Curriculum Vitae

## Contact Information


| | |
|---|---|
| **Name:** | Satanik Mukherjee |
| **Email:** | satanikmukherjeeju@gmail.com |
| **Work address:** | Biomechanics Section<br>Department of Mechanical Engineering<br>KU Leuven<br>Celestijnenlaan 300C - 2419<br>3001 Leuven, Belgium |


## Research Interests

Regenerative medicine, Cartilage Mechanobiology, Synthetic Biology, Multiscale Modeling, Finite Element Analysis, Systems Biology, Organ-on-Chip

## Education

2018–2025 **Doctoral Student (Marie Curie Early Stage Researcher)**
Biomechanics Section, KU Leuven, Belgium
Thesis title: *Multiscale modeling of cartilage mechanobiology: insights into degeneration and regeneration*
Supervisor: Prof. Liesbet Geris

| | |
|---|---|
| 2015–2017 | **Master of Technology in Applied Mechanics (CGPA : 9.327/10)**<br>Department of Applied Mechanics, Indian Institute of Technology Delhi, India<br>Thesis title: *Simulation of cutting of human brain tissue*<br>Supervisor: Prof. Puneet Mahajan and Prof. Sanjeev Sanghi |
| 2011–2015 | **Bachelor of Engineering in Mechanical Engineering (CGPA: 8.65/10, First Class Honours)**<br>Department of Mechanical Engineering, Jadavpur University, Kolkata, India<br>Thesis title: *Analysis of two simple configurations of hexapod walking machine using multi-body dynamics software MSC ADAMS*<br>Supervisor: Prof. Arghya Nandi and Prof. Sumanta Neogy |

## Research Projects

| | |
|---|---|
| 2023–2025 | Implementation of a parallelized cartilage multiscale modeling workflow in a Model Execution Environment (in collaboration with SANO Science, Poland in the context of the In-Silico World project) |
| 2022–2025 | Multiscale modeling and validation of a cartilage on chip setup for cartilage regeneration (as Visiting Researcher in the University of Twente, The Netherlands under Prof. Marcel Karperien) |
| 2020–2022 | Development of a stabilizer for scaffolds to repair large bone defects, KU Leuven, Belgium (in collaboration with Maastricht University under BONE InterReg project) |
| 2020–2021 | An in-silico approach to optimize the design of TimoD injector, KU Leuven, Belgium (in collaboration with EYED Pharma, Belgium). |
| 2018–2019 | In-silico modeling of scaffolds for repair of large articular cartilage defects in the knee joint, KU Leuven, Belgium. |

| | |
|---|---|
| 2018–2025 | Multiscale modeling of experimental regeneration setups in Skeletal Tissue Engineering, KU Leuven, Belgium. (As an ESR in the CarBon consortium, a Marie Curie ITN) |
| 2016–2017 | Simulation of cutting of brain tissue, IIT Delhi, India. |
| 2014–2015 | Analysis of two simple configurations of hexapod walking machine using multi-body dynamics software MSC ADAMS, Jadavpur University, India |
| 2014 | Study of vibration and acoustics of a violin by varying the position of violin soundpost, IIT Kanpur, India |
| 2013–2015 | ADAMS as an aid for teaching undergraduate dynamics, Jadavpur University, India |

# Publications

## Journal Articles (Published)

1. Elahi, S.A., Tanska, P., **Mukherjee, S.**, Korhonen, R.K., Geris, L., Jonkers, I., Famaey, N. (2021). "Guide to mechanical characterization of articular cartilage and hydrogel constructs based on a systematic in silico parameter sensitivity analysis." Journal of Mechanical Behavior of Biomedical Materials, 124,104795,2021.
2. **Mukherjee, S.**, Nazemi, M., Jonkers, I. and Geris, L. (2020). "Use of Computational Modeling to Study Joint Degeneration: A Review". Frontiers in Bioengineering and Biotechnology, 8:93.
3. **Mukherjee, S.**, Neogy, S., and Nandi, A. (2018). "ADAMS as an aid for teaching undergraduate dynamics". Computer Applications in Engineering Education, 26(2), 239-258.

## Journal Articles (In Preparation)

1. **Mukherjee, S.**, Senol, S., Hegde, S., Chandrakar, A., Wieringa, A., Geris, L."Experimentally-informed in silico design of melt-electrowritten scaffolds for tissue engineering applications." Materials and Design (Under review).
2. **Mukherjee, S.**, Lesage, R., Spoelstra, L., Le, T., Paggi, C.A., Karperien, M., and Geris, L. "A multiscale approach to study chondrocyte mechanobiology using a cartilage-on-chip setup." (In preparation)

3. **Mukherjee, S.**, Zajac, K., Nowakowski, P., Malawski. M., and Geris, L. "Implementation of a multiscale model of articular cartilage in a Model Execution Environment."(In preparation)
4. **Mukherjee, S.**,Wilson, W., and Geris, L. "From Human Joints to Bioreactor Setups: Quantifying Mechanical Stimuli in Cartilage Physiology and Regeneration." (In preparation)
5. **Mukherjee, S.**, Lesage, R., and Geris, L. "A multiscale modeling approach to study the role of mechanics and inflammation in pathophysiology of articular cartilage." (In preparation)

## Conference Abstracts

1. Mukherjee, S., Spoelstra, L., Le, T., Serrano, C., Paggi, C.A., Lesage, R., Fano, J.B., van Oosterwyck, H., Karperien, M., Geris, L. (2025). "Exploring the Multiscale Mechanobiology of Articular Cartilage: Insights from Computational and Experimental Approaches" *byteMAL 2025*, Leuven, Belgium (Oral presentation award)
2. Mukherjee, S., Spoelstra, L., Le, T., Serrano, C., Paggi, C.A., Lesage, R., Fano, J.B., van Oosterwyck, H., Karperien, M., Geris, L. (2025). "Multiscale Mechanobiology of Articular Cartilage: Insights From In Silico and In Vitro Approaches" *Gordon Research Conference in Cartilage Biology and Pathology*, Pomona, USA (Oral presentation)
3. Mukherjee, S., Spoelstra, L., Le, T., Serrano, C., Paggi, C.A., Lesage, R., Fano, J.B., van Oosterwyck, H., Karperien, M., Geris, L. (2024). "A combinatorial in silico and in vitro approach to study cartilage mechanobiology using a cartilage-on-chip setup." *IUTAM Symposium on Theoretical and Numerical Developments in Cellular Mechanobiology 2024*, Seville, Spain (Oral presentation)
4. Mukherjee, S., Spoelstra, L., Le, T., Serrano, C., Paggi, C.A., Lesage, R., Fano, J.B., van Oosterwyck, H., Karperien, M., Geris, L. (2024). "Study of chondrocyte mechanobiology using a cartilage-on-chip device: a multiscale approach." *ORS Annual Meeting 2024*, Long Beach, California, USA (Poster presentation)
5. Mukherjee, S., Spoelstra, L., Le, T., Serrano, C., Paggi, C.A., Lesage, R., Fano, J.B., van Oosterwyck, H., Karperien, M., Geris, L. (2023). "A multiscale approach to study chondrocyte mechanobiology using a Cartilage on Chip setup." *28th Congress of the European Society Biomechanics 2022*, Maastricht, the Netherlands (Winner of the ESB Student Award 2023)

6. Mukherjee, S., Lesage, R., Geris, L. (2023). "Multiscale model to elucidate the role of mechanics in cartilage degeneration and regeneration." *GRS/GRC on Cartilage Biology and Pathology 2023*, Italy (Oral presentation award in GRS)

7. Mukherjee, S., Lesage, R., Geris, L. (2023). "A calibrated multiscale model to study the crosstalk between inflammation and mechanics in the pathophysiology of articular cartilage." *ORS Annual Meeting 2023*, Dallas, Texas, USA (Poster presentation)

8. Mukherjee, S., Lesage, R., Geris, L. (2022). "Calibration and validation of a multiscale model to study the role of mechanics and inflammation in osteoarthritis." *VPH 2022 Conference*, Porto, Portugal (Podium presentation, runner up of student awards)

9. Mukherjee, S., Lesage, R., Geris, L. (2022). "A multi-scale analysis of cartilage pathophysiology: interplay of mechanoregulatory and inflammatory pathways." *9th World Congress of Biomechanics 2022*, Taipei (Podium presentation, virtual)

10. Mukherjee, S., Lesage, R., Geris, L. (2022). "A coupled finite element and systems biology model to study the role of mechanics and inflammation in knee OA." *27th Congress of the European Society Biomechanics 2022*, Porto (Podium presentation)

11. Mukherjee, S., Lesage, R., Geris, L. (2021). "Multiscale modeling of knee joint pathophysiology: combined effect of mechanics and inflammation." *12th Australasian Biomechanics Conference, 2021* (Podium presentation, virtual)

12. Mukherjee, S., Lesage, R., Geris, L. (2021). "Interplay of mechanical and inflammatory cues in osteoarthritis: a multiscale in-silico approach." *26th Congress of the European Society of Biomechanics 2021* (Podium presentation, virtual)

13. Mukherjee, S., Lesage, R., Geris, L. (2021). "Induction of a pathological phenotype in articular chondrocyte through inflammatory and mechanical stimuli: a multiscale in silico approach." *6th TERMIS World Congress, 2021* (Podium presentation, shortlisted for best podium presentation)

14. Mukherjee, S., Lesage, R., Geris, L. (2021). "Multiscale modeling of the knee joint pathophysiology: differential effect of mechanical loading on the cartilage zones." *17th International Symposium on Computer Methods in Biomechanics and Biomedical Engineering, 2021* (Oral Presentation, virtual)

15. Mukherjee, S., Lesage, R., Geris, L. (2021). "Predicting chondrocyte hypertrophy due to mechanical and inflammatory cues: a multiscale in-silico approach." *ORS 2021 Annual Meeting* (Oral presentation, virtual)

16. Mukherjee, S., Lesage, R., Wilson, W., Geris, L. (2021). "Multiscale modeling to investigate the role of mechanical loading in articular cartilage." *14th World Congress in Computational Mechanics (WCCM) and ECCOMAS Congress* (Oral presentation, virtual)

17. Mukherjee, S., Lesage, R., Geris, L. (2020). "Interplay of Mechanical and Inflammatory Cues in Osteoarthritis: A Multiscale In-silico Study." *19th National Day on Biomedical Engineering, Belgium* (Oral presentation, virtual)

18. Mukherjee, S., Lesage, R., Wilson, W., Geris, L. (2020). "A coupled multiscale model to determine the fate of stable articular chondrocytes due to mechanical loading." *VPH 2020 Conference* (Oral presentation, virtual)

19. Mukherjee, S., Puricelli, M., Kock, L., Geris, L. (2019). "Comparison of mechanical stresses between in-silico models of an osteochondral setup and the human knee joint." *Conference of the International Society of Biomechanics*, Calgary, Canada (Poster presentation)

20. Mukherjee, S., Puricelli, M., Kock, L., Geris, L. (2019). "Quantification of physiological loading regimes in an ex vivo osteochondral setup for cartilage regeneration." *Conference of the European Society of Biomechanics*, Vienna, Austria (Poster presentation)

21. Mukherjee, S., Mahajan, P. (2017). "Cohesive zone model of simulation of cutting of brain tissue." *Indian Conference on Applied Mechanics*, Allahabad, India (Oral presentation)

## Invited Talks / Seminars

1. Multiscale modeling of articular cartilage: from knee joint mechanics to cellular mechano-transduction for osteoarthritis and tissue engineering applications.Texas A&M Institute of Data Science - Digital Twin Lab Virtual Workshop Series. 8th October, 2024.

2. Can Digital Twins help in treatment of Osteoarthritis? DigitalTwins4Health, a meeting of the Belgian ecosystem for digital twins in healthcare, Leuven, 29 September 2023.

3. Multiscale Modeling to Elucidate the Role of Mechanics in Degeneration and Regeneration of Articular Cartilage, Washington University in St. Louis, 24 August 2023 (virtual).

4. From Mechanics to Mechanobiology: Understanding How Mechanical Forces Modulate Cell Behaviour, Jadavpur University Mechanical Engineering Seminar, India, 10 January 2023.

5. Use of Computational Modeling to Define Bioreactor Protocols, OJO Bioreactor Workshop, KU Leuven, 4-5 June 2019.

6. In-Silico Modeling of Scaffolds for Repair of Large Articular Cartilage Defects, EuroMech 604 Meeting, Mathematical Institute, University of Oxford, 23-25 September 2019.

## Grants and Awards

| | |
|---|---|
| 2025 | Rita Levi-Montalcini Post-doctoral Fellowship, Washington University in St. Louis |
| 2025 | Best Oral Presentation Award, byteMAL 2025, Leuven |
| 2023 | Winner of European Society of Biomechanics Student Award |
| 2023 | GRS Cartilage Biology and Pathology Oral Presentation Award |
| 2023 | ON Education Grant to attend ORS Annual Meeting, 2023 |
| 2022 | Runner-up of VPHI Student Award |
| 2022 | Long Stay Travel Grant from Research Foundation Flanders (FWO) (3432 euros) |
| 2022 | European Society of Biomechanics Mobility Award 2022 (4000 euros) |
| 2022 | Travel Award to attend World Conference of Biomechanics 2022, Taiwan |
| 2021 | Shortlisted for Best Podium Presentation Award for 6th TERMIS World Congress |
| 2021 | Travel Award to attend 12th Australasian Society of Biomechanics Conference |

| | |
|---|---|
| 2018 | Best Hands-on Project Award: "Analysis of Normal and Altered Gait Analysis and Consequences on Cartilage Biology and Mechanobiology", VPHI Summer School, Barcelona |
| 2018–2022 | Marie Curie Fellowship as Early Stage Researcher for the CarBon ITN Project under the Marie Sklodowska-Curie Grant Agreement No 721432 |
| 2015–2017 | MHRD Postgraduate Fellowship, Government of India |
| 2014 | First Runner-up in Student Quiz Competition organized by Indian Society of Heating, Refrigeration and Air Conditioning (I.S.H.R.A.E.) |

## Teaching and Supervision

| | |
|---|---|
| 2022–2023 | Supervision of Bachelor's Internship project (Shrivatsa Hegde, NIT Surathkal, India)<br>Project Title: In-silico modeling of melt electrowritten scaffolds. |
| 2021–2022 | Supervision of Bachelor's Internship project (Ayush Agarwal, MANIT, India)<br>Project Title: In-silico model of cartilage regeneration in a hybrid scaffold. |
| 2020–2021 | Daily supervision of a Master's Thesis student (Simay Şenol)<br>Thesis title: Development of a stabilizer for scaffolds to repair large bone defects. |
| 2019–2020 | Daily supervision for industrial project of the 3rd Bachelor major Mechanical Engineering for the academic year 2019-20 consisting of a group of 16 students.<br>Project Title: Automation of a tensile testing machine. |
| 2018–2019 | Daily supervision of a Master's Thesis student (Rithika Gidijala)<br>Thesis title: In-silico modeling of scaffolds for repair of large articular cartilage defects in the knee joint. |
| 2016–2017 | Teaching Assistant for Fluid Mechanics and Computer Aided Design courses, IIT Delhi, India. |

## Service and Outreach

**Journal Reviewer:** BMC Musculoskeletal Disorders, Frontiers in Bioengineering and Biotechnology, eLife Journal, Computer Applications in Engineering Education, Biomechanics and Modeling in Mechanobiology

**Grant Reviewer:** Austrian Science Fund (FWF)

**Leadership Roles:**

| | |
|---|---|
| 2025 | Chair of Gordon Research Seminar on Cartilage Biology and Pathology |
| 2024 | Rotating group leader in ORS Open Door Event |
| 2024–2025 | Member of ORS Social Media Committee |
| 2022 | Student committee member of Virtual Physiological Human Institute (VPHi) |
| 2021 | Co-chairing multiple sessions in VPH 2022 Conference, Porto, Portugal |
| 2020–ongoing | Organizing and chairing VPHi keynote webinar by Prof. Gerard Ateshian from Columbia University |
| 2020–ongoing | Member of Tissue Characterization Task Force, VPHi |
| 2020–ongoing | Member of Good Simulation Practices (GSP) working group, VPHi |

## Memberships and Affiliations

European Society of Biomechanics (ESB) since 2021
Tissue Engineering and Regenerative Medicine International Society (TERMIS), since 2021
Orthopedic Research Society (ORS), since 2020
Virtual Physiological Human Institute (VPHi), since 2018
European Calcified Tissue Society (ECTS), since 2018
Prometheus, an interdisciplinary platform for skeletal tissue engineering research in KU Leuven, since 2018

## Relevant Skills

**Programming:** Fortran, Python
**Scientific Computing:** Matlab
**Software:** Abaqus, FEBio, ScanIP, MSC Adams, Pro-Engineer, ANSA, SolidWorks
**Other Tools:** GitHub, Mendeley, OneNote
**Experimental:** Cartilage-on-chip, Bioreactor systems
**Languages:** English, Bengali, Hindi, Dutch (limited proficiency)

FACULTY OF ENGINEERING SCIENCE
DEPARTMENT OF MECHANICAL ENGINEERING
Celestijnenlaan 300A box 2402
B-3001 Leuven
first.last@cs.kuleuven.be

